Orbit and Attitude Control for (non-) Rotating Space-Based Telescopes Utilizing Reflectivity Control Devices

by

Alejandro D. Cabrales Hernandez

S.B., Massachusetts Institute of Technology (2018)
S.M., Massachusetts Institute of Technology (2020)

Submitted to the Department of Aeronautics and Astronautics
in partial fulfillment of the requirements for the degree of

Doctor of Philosophy in Aeronautics and Astronautics

at the

MASSACHUSETTS INSTITUTE OF TECHNOLOGY

May 2023

Certified by: David W. Miller
Jerome C. Hunsaker Professor, MIT
Thesis Supervisor

Matteo Ceriotti
Senior Lecturer in Space Systems Engineering, University of Glasgow
Thesis Committee Member

Richard Linares
Rockwell International Career Development Professor, MIT
Thesis Committee Member

Rebecca Masterson
Principal Research Scientist, MIT
Thesis Committee Member

Accepted by: Jonathan P. How
R. C. Maclaurin Professor of Aeronautics and Astronautics
Chair, Graduate Program Committee

Orbit and Attitude Control for (non-) Rotating Space-Based Telescopes Utilizing Reflectivity Control Devices

by

Alejandro D. Cabrales Hernandez

Submitted to the Department of Aeronautics and Astronautics
on May 23, 2023, in partial fulfillment of the
requirements for the degree of
Doctor of Philosophy in Aeronautics and Astronautics

Abstract

Satellite-based imaging has allowed for advancements in knowledge of Earth's environment, the Solar System, and the cosmos that were otherwise not possible using ground-based counterparts. It is no surprise that scientists call for advancements in telescope technology that allow for longer-lasting and larger apertures to improve the quantity and quality of data. An increase in the aperture's diameter and fuel capacity coincides with an increase in satellite size and mass that may be incompatible with current and proposed launch systems. Mission lifetime limitations due to propellant is of particular concern for satellites operating in unstable orbits such as the Sun-Earth Lagrange points. Therefore, there exists a need for novel methods that allow space telescopes to reduce fuel usage *and* satellite's volume and mass.

To address fuel reduction and increase mission lifetime, reflectivity control devices (RCDs), or devices that are capable of regulating the effective force produced by Solar radiation pressure on a surface, are utilized in conjunction with the dynamics around the Sun-Earth Lagrange Points to provide a method of fuel-free orbit and attitude control. Additionally, RCDs produce lower actuator disturbances compared to traditional spacecraft actuators leading to a reduction in line-of-sight jitter. To address satellite's volume and mass limitations, Rotating Synthetic Apertures (RSA) are analyzed as a potential technology that enables larger apertures due to the reduction in mirror surface area compared to traditional satellites RSA satellites consist of a thin strip aperture which is rotated about an axis normal to the aperture plane. As the satellite rotates, multiple images are taken that are combined to recover the full image as if it was taken from a circular aperture. This dissertation presents the methodology of achieving fuel-free orbit and attitude control via reflectivity control devices; this enables long-mission lifetime, large-aperture sizing, and low disturbances for non-rotating and rotating space-based apertures.

Although reflectivity control devices have been demonstrated in orbit and extensively studied, no previous method has shown the ability to obtain full six degrees of freedom with RCDs as the satellite's only actuators. An allocation algorithm for utilizing RCDs that can be continuously switched from a specular reflective state to an

absorptive state is presented along with an analysis of the impact of satellite attitude on the control envelope of an aggregate RCD configuration. Regarding the operation of space telescopes, the field of regard region, or the region in which a satellite with RCDs can maintain combined orbit and attitude control, is derived for both RSA-like and non-rotating telescope configurations. An optimization scheme for the placement of RCD cells in a given configuration to maximize the control authority over different attitudes is also presented. Additionally presented in this work is the development of a dynamically similar testbed to allow for the testing of pointing control algorithms for rotating synthetic apertures. The testbed serves as a method of testing conceptual RSA satellites at lower orbital regimes where the RCDs are not able to provide control, but still correspond to regions of interest for the operation of RSA satellites for Earth science observation. The derivation of scaling laws for the testbed and hardware-based results for RSA satellites ranging from low Earth orbit to medium Earth orbit are demonstrated.

Thesis Supervisor (Chair): David W. Miller
Title: Jerome C. Hunsaker Professor, MIT

Thesis Committee Member: Matteo Ceriotti
Title: Senior Lecturer in Space Systems Engineering, University of Glasgow

Thesis Committee Member: Richard Linares
Title: Rockwell International Career Development Professor, MIT

Thesis Committee Member: Rebecca Masterson
Title: Principal Research Scientist, MIT

Acknowledgments

This work was primarily supported by the National Science Foundation Graduate Research Fellowships Program (# 2141064), The GEM Fellowship, the MIT AeroAstro Department, and the MIT Office of Graduate Education. Additional support and funding sources for this work were from NASA Space and Earth Sciences Office Astrophysics Research and Analysis Program (# 80NSSC20K0400), and the Massachusetts Space Grant Consortium. The author is extremely grateful for the support from all the sponsors that enabled this research.

First and foremost, I want to thank my advisor, Prof. David Miller, for supporting me and guiding my research for the past five years. Your guidance and mentorship, both professionally and personally have made me a better researcher, engineer, and person. Thank you Dr. Rebecca Masterson for serving on my committee and working with you in Spin Ap. I now significantly appreciate hardware development and testing, and I am glad I had the chance to experience a small glimpse of that process. Thank you so much Dr. Matteo Ceriotti for your willingness to serve on my committee. Your insights and recommendations regarding RCDs are key reasons why I was able to finish this thesis. Thank you Prof. Richard Linares for being a committee member, and always allowing me to be part of ARCLab. I would also like to thank my thesis readers: Dr. Tupper Hyde and Dr. Paul Mason. Dr. Tupper Hyde, thank you for being willing to be an MIT Office of Minority EMAP mentor throughout my undergrad. You inspired me not only to work at NASA Goddard but also to decide to apply to graduate school. Dr. Paul Mason, thank you so much for being one of the best mentors and supervisors I have ever had. I loved my time working for you and all my friends at the ACS Branch.

Thank you to Prof. Paulo Lozano, Prof. Karen Willcox, Dr. Alice Liu, and every amazing mentor I have had in undergrad and graduate school. Thank you to Marilyn, Corrine, Todd, Dave, Marie, and MIT Staff for all you do. Thank you to all the professors I have had at MIT.

There are so many people that have supported me throughout this journey and

am extremely grateful for having them in my life. To the SSL: Michael (I will miss our countless loops around MIT, all the movie/TV show references, and the SSL Swim Team), Hailee (the best officemate I could ever ask for), Keenan (the rumpus room was not the same without you, and we still need to get tacos in LA), Tonio (a hero of the SSL, and the best Ragnar/Charles running buddy), Evan (I could not imagine how Spin Ap would have ended up without you, and the SSL Swim Team), Rosemary (thank you for the SSL Labsgiving drinks and all you do for SSL and the Dept.), Charlotte (the soul of the SSL and organizer of the muddy). To all my friends: Oliver, Annika, Rachel, Adriana, Daniel, Rahul, Carla, Michael, Katie, Juju, David, Cynthia, Antoni, and so so many more. Thank you my students in New Vassar Section 3C. Thank you, Mr. Chun, Mrs. Gubbins, Mr. Seagle, and so many other teachers.

Thank you to my family. Thank you, Beto for all our chats and your support and confidence in me being able to graduate. Thank you, Bertha and Hugo. Finally, thank you so much to my mom, Cecilia, who has supported me every single day of my life. Without your love and support, we would not be in the United States, not to mention being able to graduate with my Ph.D.

This thesis is dedicated to my grandparents:

Sofia Hernandez Ruiz and Maximiliano Cabrales Vasquez

Contents

List of Figures

List of Tables

Acronyms

ACS	Atittude Control System
ADT	Attitude Determination Testbed
AFoR	Annual Field of Regard
AU	Astronomical Unit
CM	Center of Mass
COTS	Commercial Off the Shelf
CR	Center of Rotation
CR3BP	Circular Restricted Three Body Problem
DCT	Dynamics and Control Testbed
DOF	Degrees of Freedom
ECI	Earth-Centered Inertial frame
FoR	Field of Regard
GNC	Guidance, Navigation, and Control
ICRF	International Celestial Reference System frame
IFoR	Instantaneous Field of Regard
IKAROS	Interplanetary Kitecraft Accelerated by Radiation Of the Sun
IMU	Inertial Measurement Unit
JAXA	Japan Aerospace Exploration Agency
JWST	James Webb Space Telescope
LEO	Low Earth Orbit
LQR	Linear Quadratic Regulator
LVLH	Local Vertical Local Horizontal frame

NASA National Aeronautics and Space Administration

OD Orbit Determination

RCD Reflectivity Control Device

ROS Robot Operating System

RSA Rotating Synthetic Aperture

RWA Reaction Wheel Assembly

SEL2 Sun-Earth Lagrange Point 2

SRP Solar Radiation Pressure

SVD Singular Value Decomposition

Symbols

$\mathcal{F}^{\#}$	Frame definition
ϕ	Vector representing linear combinations of the columns of the nullspace matrix V_{null}
$\Phi(t, t_0)$	State transition matrix for the Circular Restricted Three Body Problem
$\mu_{\#}$	Gravitational parameter for system, e.g. μ_{SE} is for Sun-Earth system
$\tau_{\#}$	Torque vector, subscript # indicates where it comes from
ρ_a	Absorptivity coefficient
ρ_d	Coefficient of diffuse reflectivity
β_{rcd}	Vector of force and torque produce when all RCDs in a given configuration are at their 50%
ρ_s	Coefficient of specular reflectivity
ω_{syn}	Angular velocity of Synodic Rotating Frame
A_{rcd}	Matrix of force and torques by an RCD configuration that is linearly depenent on the reflectivity coefficient vector
G_{opt}	Composite matrix used in the linear SVD problem for RCD coefficient allocations
N_{rcd}	Number of RCD cells in each configuration
Q_{att}	Linear Quadratic Regulator Q gain positive semi-definite matrix for attitude controller
Q_{orb}	Linear Quadratic Regulator Q gain positive semi-definite matrix for position controller
R_{att}	Linear Quadratic Regulator R gain positive definite matrix for attitude

	controller
R_{orb}	Linear Quadratic Regulator R gain positive definite matrix for position controller
S_{rcd}	Singular value decomposition S matrix. Size is $6 \times N_{rcd}$
T_{per}	Period of the halo orbit in s
U_{rcd}	Singular value decomposition U matrix. Size is 6×6
V_{null}	Nullspace matrix of A_{rcd}
V_{rcd}	Singular value decomposition S matrix. Size is $N_{rcd} \times N_{rcd}$
a_{cell}	Area of each RCD cell in m^2
$a_{rcd,50\%}$	Acceleration produced by RCD configuration at 50% control when at nominal attitude
b_{rcd}	Column vector of force and torque by an RCD configuration that is not dependent on reflectivity coefficient
$f_{\#}$	Force vector, subscript # indicates where it comes from
g_{opt}	Composite vector used in the linear SVD problem for RCD coefficient allocations
l_{au}	Average distances between Sun and Earth, 1 AU, in m
m_{sc}	Mass of the spacecraft system in kg
p_{sun}	Solar radiation pressure in N/m^2
q	Attitude quaternion from inertial to body frame

Chapter 1

Introduction

Space telescopes and Earth observation satellites provide an invaluable avenue for obtaining science and gathering data from Earth, our Solar System, and the cosmos. Earth observation satellites enable the ability for sensing and imaging remote areas and have provided global coverage that was not possible with traditional aerial imaging [5, 6]. Additionally, space telescopes yield measurements that would otherwise not be possible, or not as high quality if they were taken through the Earth's atmosphere by ground-based counterparts [7]. Thus, the quality of the images, namely a higher angular resolution and signal-to-noise ratio, is of the utmost importance when designing a space-based telescope. It can be shown that higher angular resolution and signal-to-noise ratio are proportional to an increase in the aperture size of the primary mirror [8].

Unsurprisingly, larger apertures are shown by the current and proposed space-based telescopes by the National Aeronautics and Space Administration (NASA). The Hubble Space Telescope, one of NASA's most famous telescopes responsible for many astrophysics discoveries, has an aperture diameter of 2.4 m. James Webb Space Telescope (JWST), launched in 2021, has an aperture size of 6.5 meters[1] [9]. Following this pattern, NASA has proposed several flagship missions for the 2020 Astrophysics Decadal survey including the Habitable Exoplanet Observatory (HabEx) with a 4 m

[1]The James Webb Space Telescope will operate in the infrared spectrum while Hubble operates in IR, Optical, and UV imaging which makes them not a one-to-one comparison, however, the idea of a larger aperture having higher angular resolution still applies

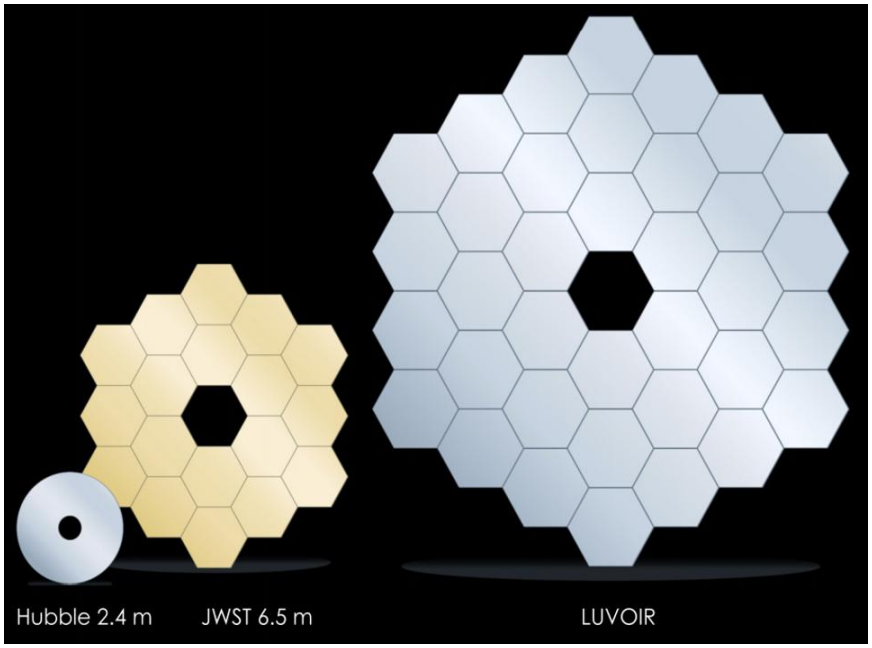

Figure 1-1: Proposed aperture diameter for NASA's Large UV/Optical/IR Surveyor (LUVOIR) as compared to Hubble and James Webb Space Telescope (JWST) [1]

mirror diameter [10], and the Large UV/Optical/IR Surveyor (LUVOIR) with an 8 m to 15 m mirror diameter [11]. LUVOIR will have around six times the angular resolution and around 40 times the sensitivity compared to Hubble and is shown compared to the JWST and Hubble in Figure 1-1 [12, 13]. More recently, NASA has proposed a hybrid between the proposed LUVOIR and HabEx coined as the Habitable Worlds Observatory (HWO) (previously called IROUV) that could enable the detection of atmospheric constituents that could potentially support life [14, 15].

As aperture systems become bigger, launch volume and weight limitations present one of the biggest obstacles for future space telescopes. Unlike Hubble, JWST is a segmented mirror as the fully deployed mirror would not fit on the launch vehicle. It is estimated that the largest aperture diameter telescope with a segmented mirror that can be launched on the Space Launch System is around 15m or just enough for LUVOIR [16]. Due to this limitation, there is a current interest in advancing the next generation of space-based telescopes through new technologies. For example, in-space assembly avoids the launch mass and volume limitation by launching individual components and assembling them in space [17–19]. Studies have been conducted

on how to pack each launch vehicle [20], the location of assembly [21], as well as the development of the algorithms required for robotic assembly of such telescopes [22, 23]. Nevertheless, in-space assembly represents a complex system with several open areas of research [17]. Several advancements such as wavefront stability, robotics, and trajectory generation must be made before having the ability to execute the construction of such a system.

Another important challenge present for space-based aperture systems is that of their mission lifetime. Flagship missions such as JWST, LUVOIR, HabEx, Nancy Grace Roman Space Telescope, and HWO tend to cost on the order of billions of dollars due in part to their one-of-a-kind technology required to make the mission successful. Therefore there is a desire for the missions to have a long mission lifetime in order to maximize the amount of science the observatory can provide. One of the main constraints on mission lifetime for space telescopes is the onboard propellant carried. Most satellites spend fuel either by performing momentum desaturation maneuvers, orbit maintenance, or for attitude control and can only carry a limited amount of fuel based on the aforementioned mass and volume constraints. This is especially true for JWST, LUVOIR, HabEx, Nancy Grace Roman Space Telescope, and HWO as they are all designed to maintain orbit in the Sun-Earth Lagrange point 2 where constant orbit maintenance is needed due to the unstable nature of orbits in this region [24, 25]. As such, advancements in trajectory design, novel efficient propulsion systems, and utilization of orbital perturbations for reduction in fuel usage are current and rich research problems [12, 25, 26].

In order to advance our understanding of the cosmos, it is clear that technological advancements are needed to allow for an increase in a satellite's aperture size and mission lifetime. For the former, one method to achieve this is by exploring a different telescope configuration known as a Rotating Synthetic Aperture (RSA) that utilizes *less* volume and mass for the primary mirror compared to traditional circular apertures. For the latter, exploring the ability to use Solar Radiation Pressure (SRP), the biggest natural dynamics and perturbation present in the Sun-Earth Lagrange points, rather than treat it as a disturbance could allow for a decrease in fuel usage

and longer mission lifetimes.

1.1 Reducing Space-Aperture Size and Mass Constraints: Rotating Synthetic Aperture Telescopes

First developed by Rafanelli and Rehfield, RSA telescopes consist of a strip aperture that is rotated about the axis normal to the aperture plane, known as the primary optical axis or spin axis [27]. An example of an artist's rendition of an RSA telescope is shown in Figure 1-2. As the aperture performs a half rotation, several images are taken and then combined to reconstruct the full image as shown in Figure 1-3. As is common for synthetic aperture systems, an RSA telescope is capable of super-

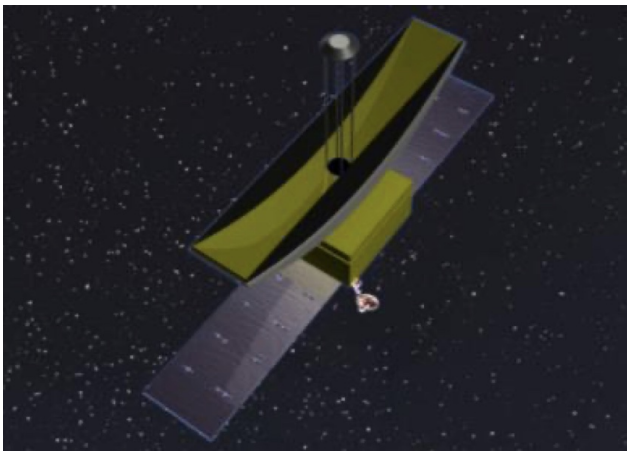

Figure 1-2: Artist rendition of an RSA telescope [2]. The primary mirror corresponds to the rectangular golden mirror while the secondary mirror is shown at the center top. The bus and solar panels are shown behind the system. The spin axis is given as the axis that is normal to the primary mirror in the direction of the secondary mirror.

resolving an image or going beyond the diffraction limit of a given aperture, which when compared to an equivalent diameter-filled circular aperture yields around a 20% increase in resolution. [2,3,28]. One of their drawbacks, however, is higher integration times than filled apertures with a similar diameter.

Furthermore, depending on the aspect ratio of the strip aperture, an RSA telescope is expected to have a reduction in mirror mass by upwards of 75% [2]. This reduction

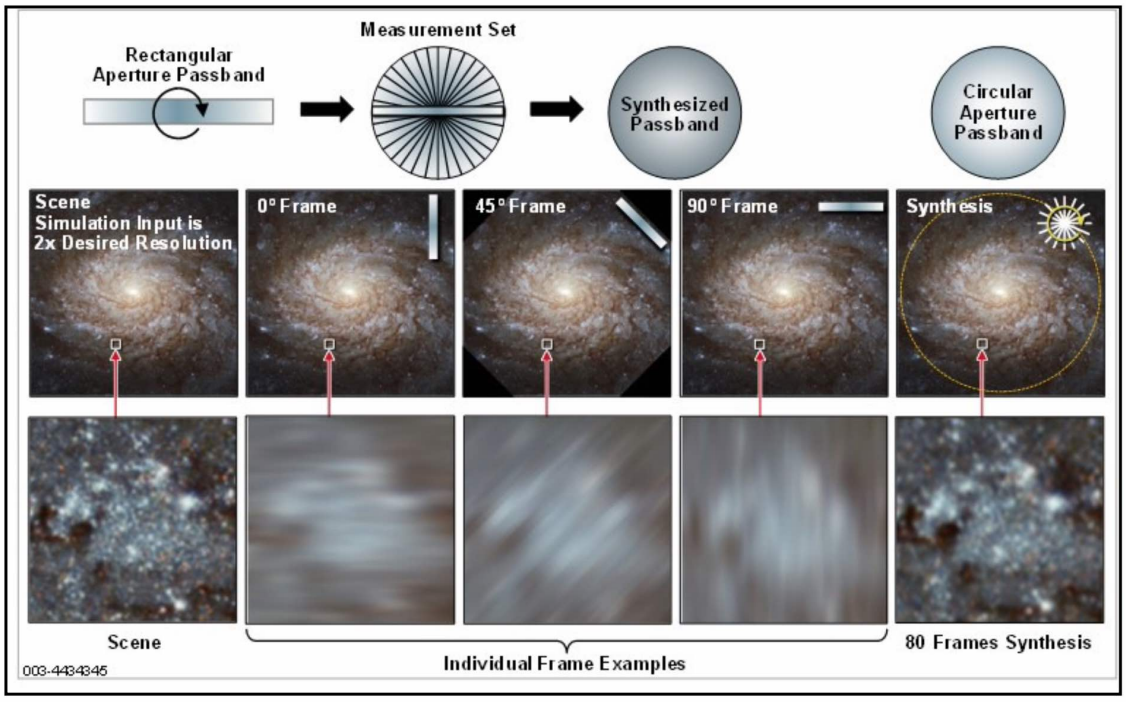

Figure 1-3: Visualization of image processing method for an RSA telescope, source: [3]. As the strip aperture rotates, several images are taken and then processed to recover the original image. Note that higher contrast on each individual image is along the long axis of the strip aperture

in mass translates into also a reduction in volume and complexity for the optical assembly. This could allow for satellites with an effective aperture diameter that would otherwise not be permitted using existing and proposed launch vehicles.

RSA telescopes can have multiple applications whether it is for Earth observation, Solar system observation, or astrophysics, and as such, their operating regimes can vary. For astrophysics, RSA telescopes, like their circular aperture counterparts, benefit from being operated in the Sun-Earth Lagrange points to ensure thermal stability during operation. For Solar system observation, RSA telescopes provide an excellent alternative for lightweight and compact imagers for orbiters around other planets such as Mars. For Earth science observation, RSA telescopes could operate in low to medium Earth orbit. Due to the reduction in mass and volume, an RSA telescope in a 3U or 6U CubeSat form factor could deploy an aperture diameter that would rival current commercial imaging satellites [29]. These telescopes, however,

would require spin rates of up to 15°/s about the optical axis in order to acquire an image. This presents several technical challenges in the area of attitude control that must be overcome to make RSA telescopes a reality.

RSA satellites could bring a fundamental paradigm shift in the development of future space telescopes. Larger aperture Earth-observing satellites could enable imaging of natural disasters, resource management, and 3D photographic images with higher resolution than many of the current commercial satellites [30, 31]. Due to the ability to enable larger apertures, satellites could be positioned at higher orbits allowing for a larger field of view (FOV) and global coverage. For astrophysics, RSA satellites could enable massive aperture telescopes that could be used for direct exoplanet imaging [32]. Currently, technology maturation in vibration and pointing control to satisfy stringent pointing requirements, as well as image processing are needed to enable this technology [2, 33]. Additionally, there is a need to validate these pointing controls by developing a testbed that is dynamically similar to that of an RSA in order to mature the technology.

1.2 Increasing Mission Lifetime: Reflectivity Control Devices

One potential way to reduce the need for fuel and thus increase mission lifetime is utilizing the orbital perturbations in the environment. For the Sun-Earth Lagrange 2 point region, Solar Radiation Pressure (SRP) is the main source of disturbance [34,35]. Satellites have previously demonstrated the ability to treat this disturbance as an actuator. Most famously between these satellites is Japan Aerospace Exploration Agency's (JAXA) Interplanetary Kite-Craft Accelerated by Radiation of the Sun (IKAROS) mission.

IKAROS was the first mission that utilized SRP as its main method for propulsion [36, 37]. IKAROS shown in Figure 1-4 consisted of a large 196 m^2 sail, compared to JWST's 163 m^2 sunshield. In the sail, a series of liquid crystal panels–shown by the

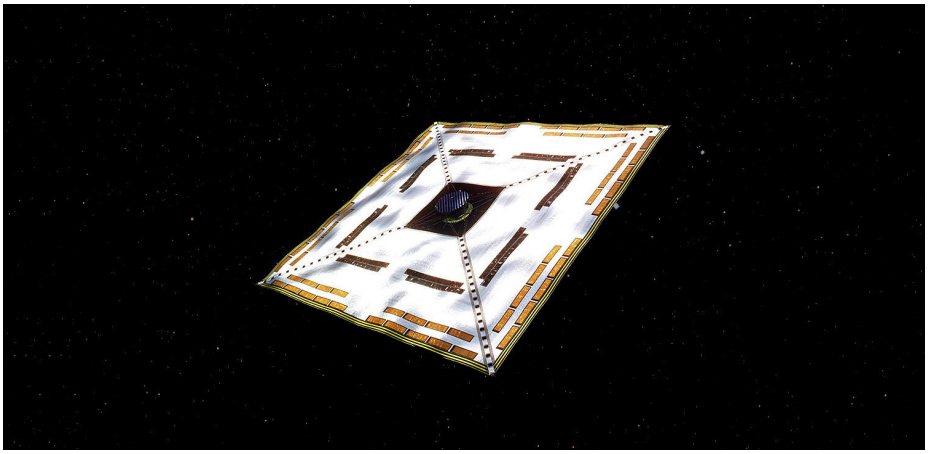

Figure 1-4: Artist rendition of JAXA's IKAROS satellite. Orange rectangles along the edge of the sail correspond to reflectivity control devices. Image Credit: JAXA

orange cells at the edge of the sail in Figure 1-4–acted as Reflectivity Control Devices (RCDs), or devices that could regulate their surface reflectivity properties and thus the force generated by SRP. These devices are controlled via an application of voltage and do not have any expendables [38]. The spacecraft was able to demonstrate tip and tilt attitude control utilizing only RCDs on-orbit. This opens the possibility for fuel-free control for larger satellite systems such as RSA telescopes or non-rotating designs *if* the additional degrees of freedom can be controlled through the use of RCDs. Beyond increasing the mission lifetime, RCDs present a unique opportunity of also reducing the actuator disturbances created by typical spacecraft actuators due to their mechanical simplicity.

1.2.1 Improving Pointing Performance by Reducing Actuator Disturbances

Future space telescopes demand increasingly stringent pointing requirements that would enable improvement in wavefront stability and an overall increase in instrument performance. For space-based telescopes, disturbances from onboard actuators are one of the main sources of line-of-sight jitter [39,40]. State-of-the-art attitude control actuators such as Reaction Wheel Assembly (RWA) are one of the largest sources of disturbances [41]. Microthrusters present a novel alternative for future space tele-

scopes' actuators [42]. Although still relying on expendable fuel, microthrusters could provide longer mission lifetime and low jitter compared to RWA [42, 43]. The use of thrusters in space telescopes, however, could potentially impact science collection due to surface contamination of the mirrors [44], or sunlight glinting [45] from thruster plumes[2]. RCDs, therefore, are an attractive actuator as they do not produce plumes, nor do they produce large disturbances due to their lack of moving mechanical components.

1.3 Thesis Statement

The utilization of reflectivity control devices for space telescopes could provide an opportunity for reducing or even eliminating the fuel usage of space telescopes thereby increasing the mission lifetime. A longer lifetime would ensure an increase in the total science produced by space telescopes. Additionally, rotating synthetic aperture systems would allow larger effective apertures than those possible with traditional circular apertures which is of interest to the science community. RSA accomplishes this at the cost of requiring highly-dynamic maneuvers when taking images compared to traditional space telescopes, so there is a need to validate and demonstrate the ability to maintain pointing accuracy through the use of a dynamically similar testbed. The combination of these two concepts would allow not only for an increase in the *quantity* but also the *quality* of the data produced by space-based aperture systems. This dissertation presents the methodology of achieving fuel-free orbit and attitude control via reflectivity control devices; this enables long-mission lifetime, large-aperture sizing, and low disturbances for rotating synthetic apertures.

Alternatively, the thesis statement can be summarized as follows:

The goal of this thesis is **to** enable a large-aperture and a long-mission lifetime of rotating and non-rotating telescopes **by** developing a methodology of achieving orbit

[2]Methods exists to reduce the impact of thruster plumes such as maintaining the optical components at certain temperatures to reduce surface collection [44] or coordinating thruster firings with instrument observation to avoid glinting [45]

and attitude control using only RCDs **while** demonstrating hardware-based results of a dynamically similar testbed of an RSA at different orbital regimes.

Chapter 2

Literature Review and Thesis Roadmap

This chapter covers an overview of relevant literature for the development of the work in this thesis. Additionally, the research gap for this work is identified alongside the expected contributions and overview of the thesis structure.

This work spans several fields of study and research areas including the utilization of rotating synthetic aperture telescopes for science gathering, the use of SRP for orbit and attitude control, and the development of dynamically similar testbeds. A survey of relevant literature that covers the three mentioned areas is presented. First, an introduction of rotating synthetic aperture telescopes including an overview of previous usage of spinning telescopes, and an overview of synthetic aperture systems is presented in order to highlight the proposed benefits that these systems would have compared to traditional space telescopes. The utilization of SRP for orbit and attitude control follows. This section covers the current state of the art of reflectivity control devices for use in the control of satellites. Finally, a survey of testbed development with a focus on methods of scaling between testbed systems and flight systems will be shown.

2.1 Use of Rotating Synthetic Aperture Telescopes for Science Collection

This section goes over technology development for Rotating Synthetic Aperture telescopes and its potential benefits as an alternative to traditional circular aperture configurations

Before going over RSA technology it is important to define and highlight one of the main benefits of synthetic aperture systems. Synthetic aperture optics is a broad and well-researched area. Synthetic aperture is defined as "any technique for achieving with one or more small apertures the resolution normally associated with a single large aperture" [46]. This includes sparse apertures, interferometry, sparse aperture radar, and Rotating Synthetic Apertures [27, 47, 48]. One of the main attractions of synthetic aperture optics is the ability to super-resolve images despite utilizing less optical area, which is capable due to the oversampling of regions between each image composite [49]. A current open research area is the development of new image processing algorithms such as by utilizing physics-based models of the imager and target area rather than typical Fourier transform techniques [50].

2.1.1 Utilization of Spinning Satellites for Science Gathering

Spinning satellites have a long history in spaceflight as attractive architectures for Earth-observing satellites. Spinning satellites can provide attitude stabilization, gyroscopic stiffness, and the ability to scan large areas in celestial space or on the ground [51, 52]. Different configurations exist such as single spinners, dual spinners, tri-axial spinners, etc. Single spinners correspond to single-body spinning, while dual spinners, also known as gyrostats, operate by having two modules free to spin relative to each other about a joint axis. Both single and dual spinners can either have net-zero or nonzero system angular momentum. For example, in a nonzero angular momentum case one of the modules of the dual spinner might not be spinning relative to an inertial frame, while the second module spins. Alternatively, a system can be

designed so that each module spins in an opposite direction at rates such that their angular momentum cancels the other module's to yield a zero net angular momentum system. Examples of these types of satellites can be shown in Figure 2-1.

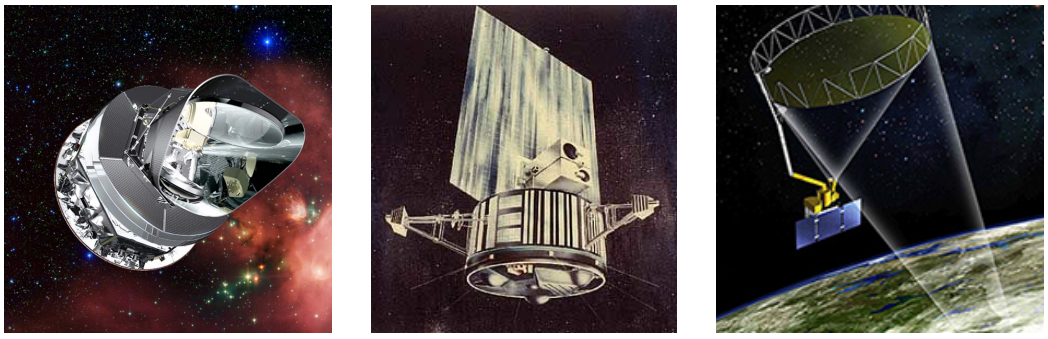

(a) Plank Satellite (b) OSO-1 Satellite (c) SMAP Satellite

Figure 2-1: Examples of (a) a spin stabilized satellite, (b) a dual-spinner gyrostat, and (c) a three-axis stabilized satellite as a dual-spinner. Credit: NASA

The history of spin-stabilized satellites goes back to one of the first satellites ever launched and the first one by the U.S.: *Explorer 1*. Explorer 1 was a cosmic ray detector satellite that was spin-stabilized along the smallest moment of inertia; the satellite, due to energy dissipation by the antennas, began to rotate about its largest moment of inertia [53]. The fate of this satellite demonstrated the importance of energy dissipation and stability analyses of rotating bodies. Additionally, NASA's Wilkinson Microwave Anisotropy Probe (WMAP), which was the first satellite to use Earth-Sun Lagrange point L2 as its orbit location, was operated with stringent attitude knowledge requirements while spinning at a nominal rate of 2.8 °/s [54]. Improving on WMAP, ESA's Plank satellite was also a single spinner operating at 6 °/s ±0.06 °/s with an impressive pointing accuracy of fewer than 10 arcseconds. WMAP represented an ambitious breakthrough in terms of science return as well the performance in attitude control for spinning satellites [55]. Operating at a higher spinning rate and more comparable to an LEO RSA satellite, the Magnetospheric Multiscale Mission (MMS) operated at 18 °/s rate with a pointing performance requirement less than 0.5 ° [56]. Overall, spin-stabilized satellites have a rich history and flight heritage and represent a viable architecture for an RSA satellite provided that energy dissipation concerns are addressed as well as the fuel allocation for slewing the angular

momentum vector while reorienting the spacecraft.

Dual-spinner satellites present an attractive alternative to spin-stabilized satellites. One of the main challenges with spin-stabilized satellites is that due to stability requirements, a spin-stabilized satellite must be oblate (spinning about its largest moment of inertia) [52]. Dual-spinners, however, add gyroscopic stiffness and stability to the satellite [57, 58]. Wang demonstrated that the stability of the Hamiltonian system of a dual-spinner increased by the addition of a rotor in a similar way as the addition of a moment of inertia about the spinning axis. Due to these benefits, several spacecraft have flown using this architecture. The Orbiting Solar Observatory (OSO-1) shown in Figure 2-1b was not only the first dual-spinner but also the first satellite with a pointing instrument [59]. More recently, MicroMas-1, a dual-spinning 3U CubeSat microwave spectrometer was designed to operate at 60 RPM (360 °/s) with a pointing accuracy requirement of 30 arcmin [60, 61]. MicroMas-1 suffered a communication anomaly and was unable to demonstrate its science operation [62]. Its successor MicroMas-2 contained improved sensors with a lower spin requirement to 30 RPM [63].

A more relevant comparison for a LEO-based RSA telescope is NASA's Soil Moisture Active Passive (SMAP) Satellite shown in Figure 2-1c. An Earth-observation satellite tasked to provide global coverage for soil moisture measurements, SMAP is a dual-spinner satellite composed of a radio antenna rotating nominally at 14.6 RPM (87.6 $^\circ/s$), and a static module that has a full three-axis attitude control system [64]. The on-orbit performance of the satellite surpassed the pointing requirement of 0.8 $^\circ/s$ spin accuracy and 0.1 ° pointing accuracy for Attitude Control System (ACS) and instead was capable of maintaining pointing accuracy within 0.002 ° while spinning [65]. Additionally, the satellite experienced a wobble with a radius of $< 0.035^\circ$ due to the motor spin axis not being aligned with the principal axis of the rotating module. The looser requirements from that of an RSA are expected due to SMAP operating at a different wavelength than an optical satellite. Since the spinning module inertia was almost equal to the nonspinning satellite any dynamic imbalances on the spin module affected the control accuracy [64]. This effect can be expected in an RSA satellite as

the majority of the inertia will consist of the primary mirrors as well as the rest of the optical system and instruments.

Several challenges are present in the use of a dual-spinner for a CubeSat-size RSA for LEO. First, dual-spinners require a slip ring for transferring power and data between each module [60]. The slip rings have been known to be a source of failure for satellites, especially at high RPMs [66–68], and on rare occasions, cold welding has affected dual spinners and Solar Array Drive Mechanisms (SADA) [69]. Due to its important use in SADA mechanisms, advancements in slip rings are a current research topic in literature and could present a reliable venue for high power and high-speed mechanisms [70, 71]. Furthermore, to avoid large loads in the slip rings and attitude disturbances in the nonspinning module, modules on dual-spinners must be carefully balanced to ensure minimum static and dynamic imbalance. This process is similar to traditional approaches for balancing reaction wheels which can result in large delays and be significantly costly [39]. Finally, one of the main sources of errors in an optical telescope is optics and instrument misalignments [72]. Adjustments for those misalignments might require expensive and numerous actuators that raise the overall cost of the program. Due to this, it is recommended that the entire optical train (primary mirror, secondary mirror, and instruments) be located on the same module to resemble a rigid mirror. Having the entire optical train will produce a large moment of inertia on the spinning module that is similar or larger to the nonspinning module, and may present similar challenges as SMAP. Alternatively, a single spinner can be designed so that the optical train, ACS, power system, etc are all contained on a single module, reducing risks of misalignments while at the same time reducing the overall volume[1].

[1]By removing the second module of a dual-spinner and compacting the overall system, the observatory would have a smaller moment of inertia about an axis normal to the optical axis. This will aid in either reducing or eliminating the effect of the spinning optical axis being the minor or intermediate axis of inertia which corresponds to an unstable axis of rotation.

2.1.2 Rotating Synthetic Apertures

Rotating synthetic apertures provide the ability to super-resolve images utilizing a single aperture and a lower areal mass than traditional circular apertures. An additional advantage over traditional circular apertures is that rectangular apertures offer higher contrast due to a narrower Point Spread Function (PSF) along the major axis of the aperture compared to a circular aperture [73]. This makes RSA telescopes an ideal candidate for exoplanet detection, as the strength of an exoplanet PSF will vary depending on the aperture rotation [3, 74]. Current research focuses on the development of new methods for image reconstruction [28, 75], and analyzing the impact of dynamic disturbances on measurements [76]. The maximum allowed parallax, or the difference in the apparent position of the object, is one of the main drivers for the spin requirement of the RSA. Spinning rate stability and pointing error will be primarily driven by the ability to perform feature recognition and satisfy the assumptions for the imaging algorithms.

2.2 Utilization of Solar Radiation Pressure for Orbit and Attitude Control

Knowledge of the environmental disturbances and perturbations is crucial to understanding the state evolution of the spacecraft in what is known as the orbit-attitude problem. The effects of these orbital perturbations on satellites are well studied including in-depth analysis of the effect of these disturbances on the control authority of the satellites [35, 77]. However, the question arises of whether it is possible to utilize this disturbance rather than rejecting them. By exploiting these disturbances, satellites can benefit from a reduction in fuel expenditure. This could significantly extend the lifetime of missions for both rotating and non-rotating telescope configurations.

SRP has been used widely for spacecraft orbit and attitude control [78]. As photons from the Sun hit a surface momentum is exchanged, and the photon can then the absorbed or reflected providing a force that can be used [78]. Reflection

can either be diffuse or specular. In diffuse reflection, incoming light is scattered in random directions. In contrast, in specular reflection, the incoming photons are reflected along a parallel direction. Specular diffusion, therefore, yields greater SRP force.

Solar sails provide a stabilization effect for certain orbits in the Earth-Moon [79], and Sun-Earth system [80, 81]. Techniques can additionally be used for controlling the orbit of a satellite with a solar sail in these regimes [82]. Bookless developed station-keeping techniques by utilizing pitch and yaw angle variations of the solar sail to produce the desired control force [83]. The techniques utilized to analyze the stability as well as find the initial conditions of the orbits will be useful for this project. Similar to that proposed for this thesis, Pande [84] demonstrated the benefit of utilizing environmental forces, rather than treating them as simple disturbances, by the use of controlling surfaces for spinning satellites for attitude control.

Beyond stability, the orbit and/or attitude control of satellites has been successfully demonstrated through various techniques including control of the effective solar sail area, moving mass, or control vanes, among others [85–87]. Firuzi and Gong [87] show the importance of having a high-fidelity model of the sail deformation when calculating sail disturbances and developed a method of control attitude control using sliding masses. Sail deformation itself can be utilized as a method of controlling the coupled orbit and attitude dynamics as seen in [88], where piezo-electric actuators are utilized to deform the structural booms of the sail itself resulting in a change of force produced by the sail. The control about the rotational axis was normal to the sail, however, still required another actuator. Solar vanes have also been explored for both SRP disturbance rejection and attitude control. NASA's Mariner IV utilized solar vanes for disturbance rejection of SRP which allowed the minimization of fuel usage [89]. Furthermore, Lee and Singh [90], developed an adaptive control law that used solar vanes for three DOF attitude control; the proposed solar vane design in [90] would still require the use of mechanical actuators to move and orient the solar vanes which produce actuator disturbances that could impact line of sight jitter. Nevertheless, Mariner IV and work by Lee and Singh demonstrate that having multiple solar

vanes canted at different angles relative to the Sun direction allows for torques to be produced in all rotational axes.

2.2.1 Reflective Control Devices

Traditional techniques for orbit and attitude control through SRP rely on changing the center of mass, changing in surface area or shape of the sail, or changing the angle of the satellite altogether. These techniques prove to be incredibly useful for many applications such as earth orbiting and solar system exploration, but may not be suitable for space telescopes where low disturbances and high accuracy pointing at specific targets are needed. RCDs are an alternative SRP-driven actuator that may prove useful for space-based telescope applications. RCDs control the amount of absorption and reflection (including the type of reflection such as diffuse vs. specular) of photons [85, 91]. As mentioned before, JAXA's Interplanetary Kite-craft Accelerated by Radiation of the Sun (IKAROS) successfully demonstrated the ability to use RCDs for attitude control by turning on and off liquid-crystal displays (LCDs) [37]. Materials that can change the optical properties when voltage is applied such as electrochromic can provide significant advantages to techniques that rely on just an "on or off" condition [92]. Electrochromic material has been successfully demonstrated for spacecraft thermal management by changing the reflectivity of the coated surface [93]. Proposals have been made for utilizing electrochromic materials for orbit or attitude control due to their efficient compact form [91].

In terms of controllability, Mu et al. first analyzed the coupled effect of attitude and orbit control for satellites using RCDs [94]. The controller demonstrated a completely propellent-free approach for satellite formation flying. The ability for combined orbit and attitude control using RCDs has been demonstrated on solar sails where a portion of its area is covered by RCDs [95]. Previous work has additionally compared the effect of controllability of switching RCD states between specular to diffuse reflectivity, and specular reflectivity to absorption, where it was determined that the latter provides higher differences in forces [96]. Furthermore, Biggs and Negri demonstrated a novel approach for orbit-attitude control using RCDs using a

computationally efficient control algorithm and RCDs torque allocation [97]. Biggs and Negri's approach relied on the symmetric property of the sail for a fast allocation of which RCDs to turn on or off; they demonstrated that as the number of RCD control surfaces increased the torque and force produced by them approached the ideal desired torque. A commonality between these approaches is the assumption of either the sail spinning or an additional actuator, typically a reaction wheel, provides control over the axis normal to the sail.

2.3 Testbed Development and Scaling Analysis

Testbeds have been widely used as part of the development and testing of control algorithms. Satellite testbeds can be characterized by the number of degrees of freedom (DOF) [98]. Air bearings have been widely used for attitude control systems by providing three rotational DOF [98–101]. For six DOF testbeds, the most dynamically realistic testbeds are microgravity-free flyers such as Synchronized Position Hold Engage Re-orient Experimental Satellites (SPHERES) and NASA's Astrobee [102, 103]; these testbeds are capable of testing attitude control algorithms, formation flying, or in the case of Astrobee serve as an assistant free-flyer for astronauts. For ground-based testbeds, the use of a spherical air bearing, as well as smooth granite floors, are popular among the literature [104, 105]. Furthermore, having similar actuators as those present in satellites allow for a greater confidence in the evaluation of the control algorithms being developed. For example, the POSEIDYN testbed utilizes similar spacecraft components such as reaction wheels, solenoid-actuated thrusters, and onboard computers with similar capacity and performance as satellite onboard processors [100]. In terms of RSA telescopes, Raytheon developed a full-scale RSA telescope testbed for a 12m aperture capable of spinning at 1.5 RPM. The testbed was inertially pointing without slewing since it was constrained by the testbed setup, nevertheless, it demonstrated the feasibility of controlling and stabilizing an RSA satellite with low jitter in the order of hundreds of nano radians [3].

Scaling analysis has been an invaluable tool in the design of satellite testbeds. A

powerful scaling law known as the Buckingham-π Theorem has extensively been used for performing similarity analysis [106–108]. The Buckingham-π relies on identifying the number of nondimensional parameters possible given a set of variables and fundamental units used in a system (e.g. mass, length, temperature, time, etc.). From this, scaling ratios can be generated, and if two systems share the same value for each ratio, the two systems are said to be dynamically similar. Ciarcia et al. utilized the Buckingham-π theorem to demonstrate proximity operations between satellites in the POSEIDYN testbed by "scaling down" the motion of the satellite into the equivalent motion on the ground testbed [109].

2.4 Thesis Roadmap

This section describes the identified research gap, the thesis contribution, and the outline of the thesis.

2.4.1 Research Gap

The utilization of orbital perturbations such as SRP has been an active and rich area of interest. Utilizing these ever-present perturbations could pave the way for satellites with longer mission lifetimes as there is no dependency on consumables for propulsion. Furthermore, using SRP via actuators such as RCDs would reduce actuator disturbances, as RCDs operate without moving parts that typically produce jitter. This increase in mission lifetime and increase in pointing performance is of particular importance to space telescopes where longer operation times lead to an increase in the quantity of science collected, and a reduction in line of sight jitter leads to an improvement in the quality of said data.

RCDs are promising actuators that could enable these longer mission lifetimes and no disturbances. Currently, RCDs have been successfully tested in orbit and have shown the ability to influence and control the attitude of a satellite. Additionally, work has been done to demonstrate the ability to have either orbit-only or also orbit and attitude control using RCDs. Nevertheless, these techniques still rely on an

additional actuator such as a reaction wheel or thruster to attain full control authority over the axis normal to the solar sail leading to at most five degrees of freedom control from RCDs alone. Therefore, three main questions remain from this gap: Is it possible to attain full orbit and attitude control using only RCDs? If so, what are the limits of controllability for satellites utilizing RCDs, and could RCDs be used for space telescopes operating in the Lagrange points? A contribution of this thesis is to demonstrate the full six degrees of freedom (6 DOF) control using RCDs while exploiting the dynamics of the Circular Restricted Three Body Problem (CR3BP) with SRP present and analyze the resultant controllability in the context of RSA-type satellites as well as other space telescope configurations.

An additional gap exists on maturing rotating synthetic aperture satellites, particularly regarding demonstrating effective pointing control of the satellites. Current testbeds do not have the ability either in degrees of freedom or operational envelope to perform an imaging maneuver for an RSA satellite. Additionally, the testbed demonstration developed by Rafanelli et al. could not tip and tilt for large angles as that testbed was developed for operation in the SEL2 point rather than in LEO or MEO orbit. RSA systems operating at lower altitudes pose unique control challenges due to their simultaneous spinning and slewing mode of observation compared to satellites operating in SEL2. Therefore, there is a need for developing a hardware-flexible three-degree-of-freedom rotating synthetic aperture testbed that demonstrates motion consistent with an RSA satellite operating in LEO to MEO. This includes an ability to scale the testbed using similarity laws to obtain the performance and behavior of satellites at different orbital altitudes. This thesis will also leverage the analysis presented in Reference 110 regarding the effect of parallax, location access, and smear requirements to generate slew and spin commands for the testbed that would be consistent with RSA satellite systems operating at different orbital regimes.

2.4.2 Contributions

The contributions for this thesis are divided into three main categories for developing no-fuel control for RSA satellites in the Sun-Earth Lagrange point as well as in low

Earth orbit. The first two contributions and categories focus on the controllability and operationality of RCDs and their use for space telescopes in SEL2. The last contribution is about testability and scalability and it focuses on low Earth orbit where RCDs are unable to provide attitude control and zero momentum systems such as reaction wheels are needed to accomplish the motion of RSA satellites. The contributions of this thesis are:

1. *Controllability*: The creation of a methodology for utilizing RCDs for combined orbit-attitude (6 DOF) control that provides no-to-low fuel consumption and low disturbances in rotating and non-rotating telescopes operating in the Sun-Earth Lagrange Points

    - Allocation algorithm for using RCD that ensures directionality preservation
    - Analysis of force and torque envelope for RCD configurations highlighting the region of controllability as a function of Sun-Direction
    - Generation of nominal orbits for satellites with RCDs in the CR3BP

2. *Operationability*: The formulation of design tools and computation of region of operation for different telescope configurations utilizing RCDs as actuators

    - Field of regard analysis for different telescope configurations using RCDs as its primary actuators
    - Optimization of RCD configuration that maximizes the total control authority over different satellite attitudes
    - Analysis of operational torque and force available in the presence of disturbances

3. *Scalability*: The development of a dynamically similar testbed for modeling LEO RSA telescopes

- Development and testing of a hardware-based testbed to demonstrate the operational motion of RSA satellites while maintaining code flexibility for different GNC testbed configurations
- Generation of scaling laws to allow for the testbed to be scaled to different RSA satellites
- Demonstration of scaling laws for LEO and MEO satellites using the dynamically similar testbed, and analysis of testbed scalability limits

2.4.3 Thesis Outline

This structure of the thesis follows the list of contributions shown in the previous section. Chapter 1 introduced and motivated the problem of enabling larger telescopes with longer mission lifetimes through the development of orbit and attitude control using RCDs and orbital dynamics, and the maturing testbed technology for rotating synthetic aperture telescopes. Chapter 2 went over relevant literature for RSA telescopes, testbed development, solar sails, and RCDs. Chapter 2 also contained the identified research gaps and the thesis contributions are listed. Chapter 3-5 are the main body chapters of the thesis that show the developed contributions of this work.

Chapter 3 develops the methodology needed to use RCDs as the only actuator to provide orbit and attitude control via exploiting the dynamics of the CR3BP with SRP directly addressing Contribution 1. An analysis of the possible force and torque envelope for a satellite with multiple RCD cells is presented. Additionally, an allocation algorithm is derived that achieves direction preservation when the commanded force or torque lies outside the control envelope of the aggregate RCD configuration. Finally, the dynamics of the CR3BP are utilized to design reference orbits for telescopes with RCDs to demonstrate the ability to point and perform orbit maintenance using only these actuators.

Chapter 4 addresses Contribution 2 by analyzing the operability of space telescopes using RCDs as actuators. This Chapter introduces the concept of the field of regard for a satellite, or the region in which combined orbit and attitude control is

maintained. This is a useful metric for space telescopes as it informs designers of the available region from which space telescopes can collect science. The field of regard is shown for different space telescope configurations including RSA telescopes as well as more traditional satellite configurations such as the James Webb Space Telescope (JWST) or the future Habitable Worlds Observatory (HWO). Additionally, a method to optimize the placement of RCDs is presented in this Chapter. The optimization algorithm considers the volume of the control envelope for an aggregate RCD configuration at its nominal attitude as well as different operational attitudes to ensure that the operationality of the configuration is maximized. Finally, environmental disturbances are considered; this demonstrates that the force and torque available allow for the successful operation of space telescopes.

Chapter 5 goes over the development of a dynamics and control testbed (DCT) that simulates the motion of an RSA telescope. The testbed uses the Robot Operating System (ROS) and is designed to allow for ease of improvements and additions to the algorithms, sensors, and actuators as needed. Scaling laws are derived to allow for the testbed to be made dynamically similar to telescopes operating in LEO, and MEO, along with a discussion on how the testbed can be extended to operations in the Lagrange points. This chapter addressed the scalability component of Contribution 3.

Chapter 6 revisits the contributions and presents possible future work for this thesis. This thesis also includes two Appendixes that complement the work shown in the other chapters. Appendix A presents the generation of guidance reference functions that were used throughout the thesis for both telescopes operating in SEL2 with RCDs, and for the DCT testbed. These trajectories ensure a smooth commanded angular velocity and quaternion vector that minimize the control input required to achieve the desired motion of the systems. Appendix B shows how gravity gradient torque in low Earth Orbit can spin a satellite under certain assumptions without the need for any additional external or control torques and could potentially serve as a way to offset the energy required to spin RSA telescopes.

Chapter 3

Reflectivity Control Devices for Orbit and Attitude Control in SEL2

This Chapter develops the framework and algorithms needed to demonstrate the ability to use RCDs for full six DOF control. Alongside, some of the main challenges of using RCDs as actuators are highlighted by presenting how the controllability of these actuators changes as a function of the attitude of the satellites, as well as the need for careful design of the satellite's nominal orbit for station keeping.

Section 3.1 covers an overview of the orbit and attitude dynamics model used in this work. Section 3.2 gives an overview of the SRP force model, as well as the allocation algorithm developed to obtain the commands needed on each RCD cell to generate the desired force and torque. Section 3.3 presents the method for obtaining the control envelope for a given aggregate RCD configuration. Finally, Section 3.4 covers the satellite orbit and attitude controller with an emphasis on the generation of the reference periodic orbits used for station keeping in the Sun-Earth Lagrange points.

3.1 Orbit and Attitude Dynamics

This section covers the dynamics model used including the Newton-Euler dynamics and kinematic formulation for attitude as well as the CR3BP dynamics for the

satellite's position.

3.1.1 Circular Restricted Three Body Problem

The CR3BP is a useful formulation of the dynamics of orbits near Lagrange points that are used by multiple space telescopes.

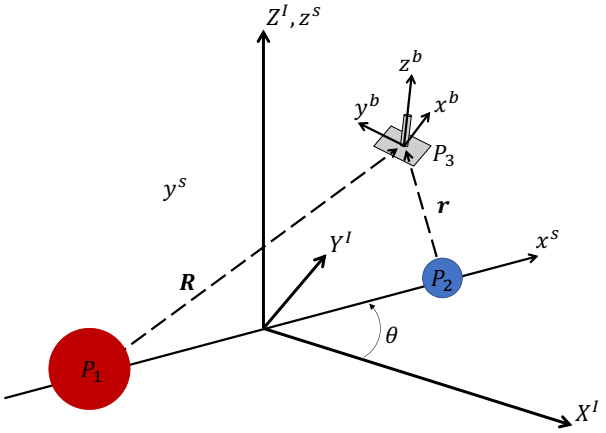

Figure 3-1: Diagram of the CR3BP. The inertial, synodic, and body-fixed frames are shown.

Figure 3-1 shows a diagram of a satellite moving in the CR3BP along with three frames corresponding to the inertial, synodic, and body-fixed frame. The model consists of two primary bodies located at P_1 and P_2, representing the Sun and Earth and their corresponding masses m_1 and m_2. A third body, P_3, corresponds to a satellite and it is assumed that its mass is insignificant compared to the primaries. The inertial frame $\mathcal{F}^I = \{X^I, Y^I, Z^I\}$ is defined with the origin at the barycenter of the Sun-Earth system, the X^I-axis aligned towards the vernal equinox, the Z^I-axis normal to the plane defined by the motion of the Sun and Earth around the barycenter, and with the Y^I-axis completing the right-hand coordinate system. The synodic rotating frame $\mathcal{F}^s = \{x^s, y^s, z^s\}$ is a rotating frame with its origin also at the barycenter of the Sun-Earth system, the x^s-axis aligned along the Sun-Earth line as shown in Figure 3-1, the z^s-axis is collinear with the Z^I-axis, and the y^s-axis completing the right-hand coordinate system and is also pointing towards the velocity direction of the Sun-Earth line. The synodic frame rotates around about the Z^I-axis

for a period of one year. Finally, the body-fixed frame $\mathcal{F}^b = \{x^b, y^b, z^b\}$ is a frame that is fixed to the third body, or the satellite, in the CR3BP. This frame is used for attitude dynamics and kinematics with its origin at the satellite's center of mass.

The orbital dynamics of the satellite with a state vector $\mathbf{x}^s_{orb} = [x^s,\ y^s,\ z^s,\ \dot{x}^s,\ \dot{y}^s,\ \dot{z}^s]^T$ expressed in the synodic frame are given by,

$$\begin{aligned} \ddot{x}^s - 2\omega_{syn}\dot{y}^s &= \frac{\partial U}{\partial x^s} + a^s_{ext,x} \\ \ddot{y}^s + 2\omega_{syn}\dot{x}^s &= \frac{\partial U}{\partial y^s} + a^s_{ext,y} \\ \ddot{z}^s &= \frac{\partial U}{\partial z^s} + a^s_{ext,z} \end{aligned} \tag{3.1}$$

where ω_{syn} is the angular rate of the synodic frame, $\mu_{SE} = \frac{m_2}{m_1+m_2}$ is the gravitational parameter, $\mathbf{a}^s_{ext} = [a^s_{ext,\ x}, a^s_{ext,\ y}, a^s_{ext,\ z}]^T$ is the external acceleration including SRP, and U represents the potential energy of the system from gravity given by,

$$U = \frac{1}{2}(x^2 + y^2) + \frac{1-\mu_{SE}}{((x+\mu_{SE})^2 + y^2 + z^2)^{1/2}} + \frac{\mu_{SE}}{((x-1+\mu_{SE})^2 + y^2 + z^2)^{1/2}} \tag{3.2}$$

where the superscripts indicating that x^s, y^s, and z^s are expressed in the synodic frame were dropped for clarity. Note that in Equation (3.1) the angular rate of the synodic frame is traditionally nondimensionalized such that its value is set equal to 1 [111]. The conversion between the nondimensionalized values in Equation 3.1 and values in SI units are given in Table 3.1.

It is well known that Equation (3.1) when $\mathbf{a}_{ext} = \mathbf{0}$ permits five equilibrium points known as Libration or Lagrange points [111, 112]. Further analysis shows that there exist periodic orbit solutions around these points even for cases with $\mathbf{a}_{ext} \neq \mathbf{0}$ such as the halo orbits, or quasi-halo orbits used for the JWST [113, 114][1]. To obtain the periodic solutions a state transition matrix, $\mathbf{\Phi}(t, t_0)$, given by,

$$\frac{d}{dt}\mathbf{\Phi}(t, t_0) = F(t)\mathbf{\Phi}(t, t_0) \tag{3.3}$$

[1]JWST's orbit does account for SRP when designing the reference trajectory

where $F(t) = \begin{pmatrix} 0_{3\times3} & I_{3\times3} \\ U_{xx} & 2\Omega \end{pmatrix}$ and $\Omega = \begin{pmatrix} 0 & 1 & 0 \\ -1 & 0 & 0 \\ 0 & 0 & 0 \end{pmatrix}$. Equation 3.3 is integrated from an initial condition at time t_0 that represents an initial guess of a specific periodic orbit to half a period of the halo orbit, T_{per} –or until the trajectory crosses the synodic xy^s-plane [115, 116]. In the case of halo orbits, Richardson's third order initial guess of the form $\mathbf{x}(t_0) = [x_0, 0, z_0, 0, \dot{y}_0, 0]^T$ is propagated with Equations 3.1 and 3.3 until the trajectory crosses the xy-synodic plane, $\mathbf{x}(T/2)$ [117].

Due to nonlinearities, the initial solution must then be refined through the use of differential correctors. Howell proposed a differential corrector that takes the value of the trajectory at the xy-plane intersection of the form $x(T_{per}/s) = [x(T_{per}/2),\ 0,\ z(T_{per}/2), \delta\dot{x},\ \dot{y}(T_{per}/2),\ \delta\dot{z}]^T$, and applies the correction Δx_0 and $\Delta\dot{y}_0$ through

$$\begin{bmatrix} \Delta x \\ \Delta\dot{y} \end{bmatrix} = \begin{bmatrix} \Phi_{41} - \delta\dot{x}/\ddot{y}\Phi_{21} & \Phi_{45} - \delta\dot{x}/\ddot{y}\Phi_{25} \\ \Phi_{61} - \delta\dot{z}/\ddot{y}\Phi_{21} & \Phi_{65} - \delta\dot{z}/\ddot{y}\Phi_{25} \end{bmatrix}^{-1} \begin{bmatrix} -\delta\dot{x} \\ -\delta\dot{z} \end{bmatrix} \tag{3.4}$$

The differential corrector repeats until the values for $\delta\dot{x}$ and $\delta\dot{z}$ are below a threshold tolerance, after which the initial solution is then used to create a halo orbit. For example, a $120,000$ $[km]$ amplitude halo-orbit produced by the above differential corrector is shown in Figure 3-2. The origin for the three plots corresponds to the SEL2 point, the views from the ecliptic plane (xy^S-plane), the plane formed by the Sun-Earth line and the ecliptic normal (xz^s-plane), and isometric view are shown. Plotted in the figures is the location of the SEL2 point noted by a black asterisk. The period for this orbit is approximately 178.3 ($days$).

One of the main challenges when operating within the CR3BP and having a low Δv actuator is the difference in the scales of units (e.g. the distance between the two primaries being measured in AUs while the delta-v produced by thrusters being in cm/s or mm/s). When using a traditional Runge-Kutta method, for example, sub-mm/s error in integration requires the relative tolerance to be in the order of 1×10^{-15}. A way to mitigate this issue is by utilizing different base units rather

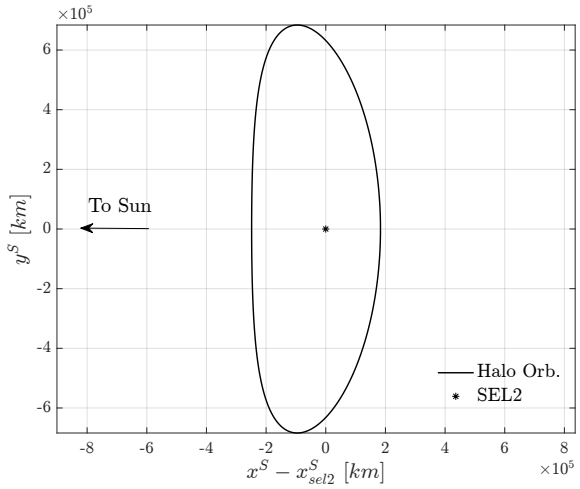

(a) xy^s-plane view about SEL2

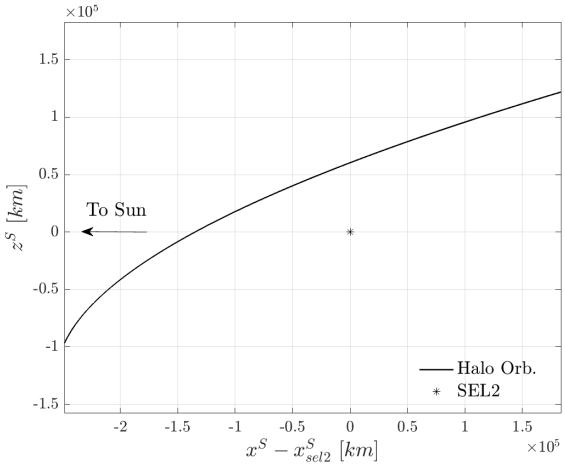

(b) xz^s-plane view about SEL2

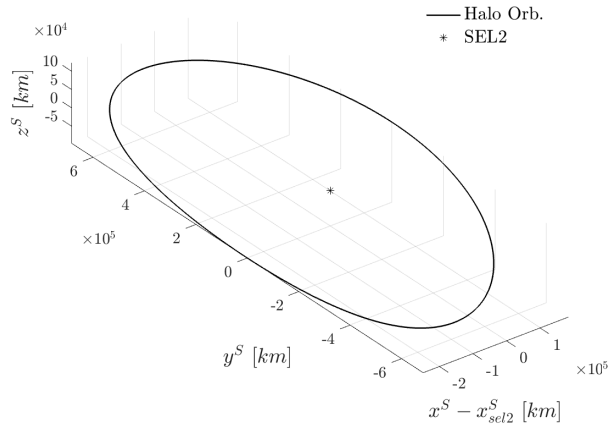

(c) Isometric view about SEL2

Figure 3-2: Example SEL2 halo orbit through differential corrector as seen relative to SEL2 point in the synodic rotating frame.

than the traditional SI units for distance and time. The scaling and conversion factors for position and velocities in the CR3BP are shown in Table 3.1, where m_{sc} is the total mass of the satellite in kg, t_{per} is the period of the halo orbit in seconds, and l_{au} is the average distance between the Earth and Sun or 1 AU in $[m]$. For example, $v_{non} = (T_{per}/(2\pi l_{au}))\, v_{dim}$ converts a dimensionalized velocity into a non-dimensionalized velocity to be used in Equation (3.1).

A future extension to this work that would further improve the relative tolerances used in numerical integration is to reformulate Equation (3.1) about the Lagrange point of interest instead the barycenter of the Sun-Earth system.

Table 3.1: Table for converting dimensional and nondimensional values in the CR3BP

Physical Quantity	**Conversion Factor (dim. $\rightarrow$ Nondim.)**
Time	$2\pi/T_{per}$
Mass	$1/m_{sc}$
Length	$1/l_{au}$
Velocity	$T_{per}/(2\pi l_{au})$
Acceleration	$T_{per}^2/(4\pi^2 l_{au})$

3.1.2 Attitude Dynamics and Kinematics

In terms of attitude dynamics, the satellite is assumed to be a rigid body with an attitude state vector given by $\mathbf{x}_{att}^b = [\mathbf{q},\ \boldsymbol{\omega}]^T$ where $\mathbf{q} = [q_w,\ q_x,\ q_y,\ q_z]^T$ is the unit quaternion that represents the coordinate axes transformation *from* the inertial frame *to* the body-fixed frame, and $\boldsymbol{\omega} = [\omega_x, \omega_y, \omega_z]^T$ represents the angular velocity vector relative to the inertial frame expressed in the body-fixed frame. The attitude dynamics of the system are given by the standard Newton-Euler dynamics equations,

$$I_{sc}^b \dot{\boldsymbol{\omega}}^b + \boldsymbol{\omega}^b \times I_{sc}^b \boldsymbol{\omega}^b = \boldsymbol{\tau}_{ext}^b \tag{3.5}$$

where, I_{sc} is the inertia tensor of the body, and $\boldsymbol{\tau}_{ext}^b$ is the external torque on the system and all are expressed in the body frame. The external forces include any disturbance torques as well as the control torques due to the RCDs.

The equation for the rate of change of angular velocity is given by,

$$\dot{\omega}^b = I_{sc}^{b-1}\left(-\boldsymbol{\omega}^b \times I_{sc}^b \boldsymbol{\omega}^b + \boldsymbol{\tau}_{ext}^b\right) \tag{3.6}$$

The rate of change of quaternion is obtained by [118],

$$\dot{\mathbf{q}} = \frac{1}{2}\Omega\mathbf{q} = \begin{pmatrix} 0 & \omega_z & -\omega_y & \omega_x \\ -\omega_z & 0 & \omega_x & \omega_y \\ \omega_y & -\omega_x & 0 & \omega_z \\ -\omega_x & \omega_y & \omega_z & 0 \end{pmatrix} \mathbf{q} \tag{3.7}$$

The full equations of motion for the attitude dynamics is then $\dot{\mathbf{x}}_{att}^b = [\dot{\mathbf{q}}, \dot{\boldsymbol{\omega}}]^T$ given by Equations (3.7) and (3.6). Both the position and attitude equations of motion

must be integrated at the same time, however, the base units may be different as long the integration timestep is consistent for each set of equations. For example, the non-dimensional units for the position vector given by Table (3.1) can be used while SI units $[kg,\ m,\ s]$ can be used for the attitude dynamics. Using multiple base units leads to better numerical conditioning for the integrator.

This section covered the main dynamics present in satellites operating in the SEL2 environment. Having the combined equations of motion, the next step is to formulate how to use RCDs for full 6 DOF in this environment.

3.2 Reflectivity Control Devices Allocation Algorithm

This section goes over the SRP force model and the allocation algorithm used to select the specular reflectivity coefficients (henceforth called simply reflectivity coefficients) for a given RCD configuration.

3.2.1 Solar Radiation Pressure Force Model

The Solar radiation pressure model presented in this subsection is the main perturbation force used to control the satellite.

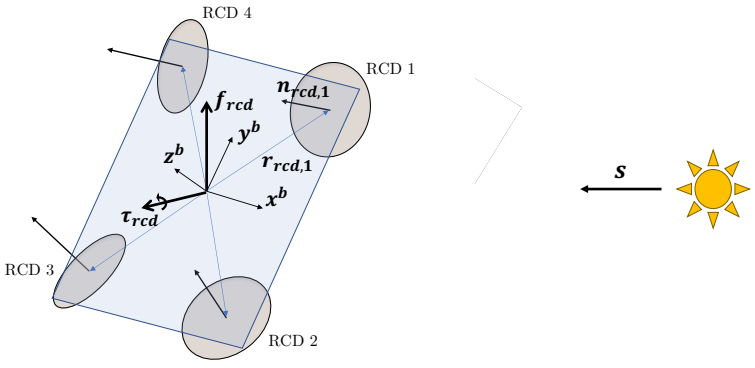

Figure 3-3: Notional satellite with four reflectivity control devices cells.

Figure 3-3 shows a notional satellite with four RCD cells (shown as light orange disks) along with the body fixed frame $\mathcal{F}^B$, and the Sun vector $\mathbf{s}$. It is assumed that the RCDs are allowed to be canted at a fixed angle relative to the $x^B y^B$ plane. The force produced by SRP on a given surface is given by [119],

$$\mathbf{f}_{rcd} = p_{sun}\ a_{cell}\,(\mathbf{s}\cdot\mathbf{n})\left[(\rho_d+\rho_a)\mathbf{s} + \left(2\rho_s\,(\mathbf{s}\cdot\mathbf{n}) + \frac{2}{3}\rho_d\right)\mathbf{n}\right] \tag{3.8}$$

where $p_{sun} = 4.56\times10^{-6}$ N/m^2 is the solar radiation pressure at SEL2 due to the Solar flux, and it is assumed to be constant, a_{cell} is the area of the surface of each RCD, $\mathbf{s}$ is the Sun unit vector, $\mathbf{n}$ is the unit normal to the surface of an RCD cell, ρ_a is the absorptivity coefficient, ρ_d is the coefficient of diffuse reflectivity, and ρ_s is the coefficient of specular reflectivity.[2] The reflectivity coefficients are constrained to each be greater than zero, and their sum be equal to one, $\rho_s+\rho_d+\rho_a = 1$. The torque produced by SRP is then $\boldsymbol{\tau}_{rcd} = \mathbf{r}\times\mathbf{f}_{rcd}$, where $\mathbf{r}$ is the vector from the satellite's center of mass to the geometric center of the RCD cell.

For each RCD cell it is assumed that there is no diffuse reflectivity $\rho_d = 0$ which is consistent with previous works [97, 120]. That is, the RCD can vary from fully absorptive $\rho_s = 0$ to fully specular reflectivity ρ_s; in other words, it is assumed that the specular reflectivity coefficient, ρ_s, can be varied continuously between $[0, 1]$.

The force and torque produced by an individual RCD from Equation 3.8 can be rewritten in affine form to separate the components that are dependent on the reflectivity coefficients as

$$\begin{aligned}\mathbf{f}_{rcd} &= \big(p_{sun}\ a_{cell}\,(\mathbf{s}\cdot\mathbf{n})\left[-\mathbf{s} + 2\big(\mathbf{s}\cdot\mathbf{n}\big)\,\mathbf{n}\right]\big)\ \rho_s + p_{sun}a_{cell}\,(\mathbf{s}\cdot\mathbf{n})\,\mathbf{s}\\ &= \mathbf{f}_{lin}\ \rho_s + \mathbf{f}_{const}\end{aligned} \tag{3.9}$$

where, $\mathbf{f}_{lin}$ is the component linearly dependent on the ρ_s and $\mathbf{f}_{const}$ is the constant

[2]Note that some photons that are absorbed will be re-emitted as heat and produce a force on a non-ideal sail. However, the force produced by this re-emission is orders of magnitude lower than the force by absorption or reflection, and can be treated as a disturbance and is therefore ignored in this force model [78].

component regardless of the reflectivity coefficient. Similarly, for the torque:

$$\begin{aligned}\boldsymbol{\tau}_{rcd} &= \mathbf{r} \times \left(p_{sun} a_{cell} \left(\mathbf{s} \cdot \mathbf{n}\right) \left[-\mathbf{s} + 2\big(\mathbf{s} \cdot \mathbf{n}\big)\, \mathbf{n}\right]\right)\, \rho_s + \mathbf{r} \times p_{sun} a_{cell} \left(\mathbf{s} \cdot \mathbf{n}\right) \mathbf{s} \\ &= \boldsymbol{\tau}_{lin}\, \rho_s + \boldsymbol{\tau}_{const}\end{aligned} \tag{3.10}$$

$\boldsymbol{\tau}_{lin}$ and $\boldsymbol{\tau}_{const}$ are both column vectors. Given an RCD configuration on a satellite with N_{rcd} coefficients, it is possible to write the total force and torque produced by the given configuration. Let, the matrix A_{rcd} be defined as,

$$A_{rcd} = \begin{pmatrix} \mathbf{f}_{lin,1} & \dots & \mathbf{f}_{lin,N_{rcd}} \\ \boldsymbol{\tau}_{lin,1} & \dots & \boldsymbol{\tau}_{lin,N_{rcd}} \end{pmatrix} \tag{3.11}$$

where $A_{rcd} \in \mathcal{R}^{6 \times N_{rcd}}$, N_{rcd} is the number of RCD cells, $\mathbf{f}_{lin,i}$ and $\boldsymbol{\tau}_{lin,i}$ are from Equation 3.9 and 3.10, respectively. Given a vector of reflectivity coefficients $\boldsymbol{\rho}_s \in \mathcal{R}^{N_{rcd} \times 1}$ the total force and torque produced by this configuration is then,

$$\boldsymbol{f}_{tot} = \begin{bmatrix} \mathbf{f}_{tot} \\ \boldsymbol{\tau}_{tot} \end{bmatrix} = A_{rcd} \boldsymbol{\rho}_s + \mathbf{b}_{rcd} \tag{3.12}$$

where,

$$\mathbf{b}_{rcd} = \begin{pmatrix} \sum_{i=1}^{N_{rcd}} \mathbf{f}_{const,i} \\ \sum_{i=1}^{N_{rcd}} \boldsymbol{\tau}_{const,i} \end{pmatrix} \tag{3.13}$$

A precondition for matrix A_{rcd} to be full row-rank and have controllability about the satellite's 6 DOF is to have at least six RCDs in a given configuration. Additional controllability issues arise due to the reflectivity coefficients being constrained to $0 \leq \boldsymbol{\rho}_{s,i} \leq 1$, and that the direction of the force produced by SRP is limited to be at an angle within $\pm 90^\circ$ from the Sun direction, $\mathbf{s}$, or $\mathbf{f}_{rcd} \cdot \mathbf{s} \geq 0$. Therefore, to obtain full 6 DOF control, the relative force produced by RCDs in a satellite is measured from the force produced when *all* the RCDs are at a nominal reflectivity value.

3.2.2 Force and Torque Allocation Algorithm

Given a desired generalized control vector $\boldsymbol{f}_{des} = [\mathbf{f}_{des},\ \boldsymbol{\tau}_{des}]^T$, the objective is to find a set of reflective coefficients that generates a force and torque that matches as closely as possible. Unfortunately, RCDs, like many satellite actuators, have a limit on the magnitude of force and torque that can be generated, known as saturation. For RCDs, saturation occurs when a non-physical value of ρ_s that is not between [0, 1] is needed to generate the desired generalized control vector. In the case where the requested force, torque, or both is beyond the limitations of the actuator, a compromise must be made in trying to match the desired control inputs as closely as possible. An optimization problem that achieves the objective of generating a desired input is given by,

$$\begin{aligned} \min \quad & \|\mathbf{f}_{des} - \mathbf{f}_{tot}\|_2 + \|\boldsymbol{\tau}_{des} - \boldsymbol{\tau}_{tot}\|_2 \\ s.t. \quad & 0 \leq \rho_i \leq 1 \quad \forall i \in \{1, \ldots, n_{rcd}\} \end{aligned} \tag{3.14}$$

where each of the RCD cells is constrained to be within the physically realizable limit between zero and one. Equation (3.14) does not impose any directionality constraints on the output produced by the RCDs. However, matching directionality in the control inputs is paramount for ensuring the satellite maintains the desired trajectory as it maintains the effective plant gain for the controller [121]. Preservation of directionality in the controller output can be added as a nonlinear constraint on the dot product between the desired and total force and torque:

$$\begin{aligned} \hat{\mathbf{f}}_{des} \cdot \hat{\mathbf{f}}_{tot} = 1 \\ \hat{\boldsymbol{\tau}}_{des} \cdot \hat{\boldsymbol{\tau}}_{tot} = 1 \end{aligned} \tag{3.15}$$

A simple strategy for solving the optimization problem in Equation (3.14) is using a pseudoinverse $\boldsymbol{\rho}_s = A^{\#}_{rcd}(\boldsymbol{f}_{des} - \mathbf{b}_{rcd})$. However, the pseudoinverse solves the least squares problem that minimizes the values of $\boldsymbol{\rho}_s$ without accounting for the constraint that the reflectivity coefficients must be between zero and one. In practice, this will result in values for reflective coefficients that are negative, or greater than one. A

well-known strategy to overcome this is to bias the reflectivity coefficients by the average of their allowable range [122]. Instead, an approach that utilizes the Singular Value Decomposition (SVD) is used for obtaining the coefficients. First, a vector $\boldsymbol{\beta}_{rcd}$ is defined as the force and torque produced when all the reflectivity coefficients are at 50%,

$$\boldsymbol{\beta}_{rcd} = A_{rcd}(0.5(\mathbf{1}_{N_{rcd}})) + \mathbf{b}_{rcd} \tag{3.16}$$

where $\mathbf{1}_{N_{rcd}} = [1, 1, \ldots, 1]^T \in \mathcal{R}^{N_{rcd} \times 1}$. Let,

$$A_{rcd} = U_{rcd} S_{rcd} V_{rcd}^T \tag{3.17}$$

be the SVD of matrix A_{rcd} where $U_{rcd} \in \mathcal{R}^{6\times 6}$, $V_{rcd} \in \mathcal{R}^{N_{rcd}\times N_{rcd}}$, and $S_{rcd} \in \mathcal{R}^{6\times N_{rcd}}$. Note that S_{rcd} is a matrix of the form $(diag(\boldsymbol{\sigma}), \mathbf{0})$ where $diag(\boldsymbol{\sigma}) \in \mathcal{R}^{6\times 6}$ is a diagonal matrix of the singular values.

The matrix V_{rcd} corresponds to a set of orthonormal vectors that are the generalization of the eigenvectors for a rectangular matrix, and physically correspond to values of reflective coefficients, $\boldsymbol{\rho}'$. The values in V_{rcd}, however, will normally be within [-1,1] rather than the physical limit of [0, 1]. The matrix U_{rcd} corresponds to a square matrix such that $\mathbf{u}_i \sigma_i = A_{rcd}\mathbf{v}_i$. That is, each of the columns of $\mathbf{u}_i$ show the principal component direction of force and torque, scaled by σ_i, produced by the RCD configuration when multiplied by the reflectivity coefficient values given by $\mathbf{v}_i$, where i indicates the column number of the diagonal matrix part of S_{rcd}.

Therefore, the set of linear combinations of columns in V_{rcd} so that it produces the vector equal to $\boldsymbol{f}_{des} - \boldsymbol{\beta}_{rcd}$ can be obtained using the pseudo inverse,

$$\boldsymbol{\alpha} = (U_{rcd} S_{rcd})^{\#} (\boldsymbol{f}_{des} - \boldsymbol{\beta}_{rcd}) \tag{3.18}$$

The values for the reflectivity coefficients can then be recovered by

$$\begin{aligned} \boldsymbol{\rho}' &= V_{rcd}\boldsymbol{\alpha} \\ \boldsymbol{\rho}_s &= \boldsymbol{\rho}' + 0.5(\mathbf{1}_{N_{rcd}}) \end{aligned} \tag{3.19}$$

The values in Equation 3.19 are still not guaranteed to satisfy the constraint of $0 \leq \boldsymbol{\rho}_{s,i} \leq 1$ which either means that the magnitude and direction of $\boldsymbol{f}_{des}$ lies outside the control envelope of the aggregate RCD configuration *or* there is a need to operate in the nullspace of matrix A_{rcd} to find a set of reflectivity coefficients so that none of the RCDs are saturated. The second case can only be possible when $N_{rcd} > 6$ as otherwise the matrix A_{rcd} will not have a nullspace and full 6 DOF controllability.

The problem of allocation of the reflectivity coefficients fall then into two cathegories:

1. Reflectivity coefficients from Equation (3.19) are *valid* (i.e. $0 \leq \rho_{s,i} \leq 1$)
2. Reflectivity coefficients from Equation (3.19) are *invalid* and non-physical (i.e. $\rho_{s,i} < 0$ or $\rho_{s,i} > 1$)

In case 2, when the resultant reflective coefficient values from Equation (3.19) are invalid, an additional optimization problem has to be solved to ensure that the reflective coefficients are constrained to be within [0, 1], or $||\boldsymbol{\rho}'||_\infty \leq 0.5$, while preserving the force and torque directionality. A method for preserving direction relies on finding the minimum scaling value of the generalized control vector $\boldsymbol{f}_{des}$ such that the values of the RCDs reflectivity coefficients remain within their physical limit. This can be accomplished by an optimization problem given by:

$$\begin{aligned} \min_{\gamma,\boldsymbol{\phi}} \quad & [1, \mathbf{0}] \begin{bmatrix} \gamma \\ \boldsymbol{\phi} \end{bmatrix} \\ \text{subject to} \quad & ||V_{rcd}\ \boldsymbol{\alpha} + V_{null}\ \boldsymbol{\phi}||_\infty \leq 0.5\mathbf{1}_{N_{rcd}\times 1} \\ & \boldsymbol{\alpha} = (U_{rcd}S_{rcd})^{\#}\Big((1-\gamma)f_{des} - \boldsymbol{\beta}_{rcd}\Big) \\ & 0 \leq \gamma \leq 1 \\ & \boldsymbol{\phi}\ \textit{free} \end{aligned} \tag{3.20}$$

where $\|\#\|_\infty$ is the infinity-norm, $\mathbf{1}_{N_{rcd}\times 1}$ is a column vector of ones with length N_{rcd}, and $V_{null} \in \mathcal{R}^{N_{rcd}\times(N_{rcd}-6)}$ represents the nullspace of the matrix A_{rcd} and is already computed during the SVD and it represents the seventh to N_{rcd} columns in the V_{rcd}

matrix. The vector $\boldsymbol{\phi} \in \mathcal{R}^{(N_{rcd}-6)\times 1}$ is a decision variable that corresponds to a set of linear combinations of the matrix V_{null}. When $\gamma = 0$ the algorithm is able to find a set of values for the RCD through the nullspace so that the desired force is matched perfectly. Note that unlike in Equation (3.19), the null vector of the RCD configuration V_{null} is utilized to allow for a reduction in the reflectivity coefficient values, and is similar to the strategy employed in reaction wheels of offloading momentum between them to have more balanced speeds.

The optimization problem in Equation (3.20) is nonlinear due to the infinity-norm constraint, however, it is possible to convert it into a linear optimization problem. To do so, it is possible to define a matrix G_{opt}, and $\mathbf{g}_{opt}$ given by,

$$G_{opt} = \begin{pmatrix} -V_{rcd}(U_{rcd}S_{rcd})^{\#}f_{des}, & V_{null} \\ V_{rcd}(U_{rcd}S_{rcd})^{\#}f_{des}, & -V_{null} \end{pmatrix} \tag{3.21}$$

$$\mathbf{g}_{opt} = \begin{pmatrix} 0.5\mathbf{1}_{N_{rcd}\times 1} - \boldsymbol{\beta}_{rcd} \\ 0.5\mathbf{1}_{N_{rcd}\times 1} + \boldsymbol{\beta}_{rcd} \end{pmatrix} \tag{3.22}$$

where, $G_{opt} \in \mathcal{R}^{2N_{rcd}\times(N_{rcd}-5)}$, and $\mathbf{g}_{opt} \in \mathcal{R}^{2N_{rcd}\times 1}$. The optimization problem in Equation (3.20) can then be written as,

$$\begin{aligned} \min_{\gamma,\boldsymbol{\phi}} \quad & [1, \mathbf{0}] \begin{bmatrix} \gamma \\ \boldsymbol{\phi} \end{bmatrix} \\ s.t. \quad & G_{opt}[\gamma,\ \boldsymbol{\phi}]^T \leq \mathbf{g}_{opt} \\ & 0 \leq \gamma \leq 1 \end{aligned} \tag{3.23}$$

The optimization problem in Equation (3.23) can easily be solved for the optimal γ^* and $\boldsymbol{\phi}^*$ by any linear problem solver such as dual-simplex method, or through MATLAB's *linprog* function [123].

The new reflectivity coefficients can then be found by Equations (3.24) and (3.25)

which will satisfy the [0,1] value constraint.

$$\boldsymbol{\alpha}_{opt} = (U_{rcd}S_{rcd})^{\#}\Big((1-\gamma^*)f_{des} - \boldsymbol{\beta}_{rcd}\Big) \tag{3.24}$$

$$\begin{aligned} \boldsymbol{\rho}^{*\prime} &= V_{rcd}\boldsymbol{\alpha}_{opt} + V_{null,rcd}\ \boldsymbol{\phi}^* \\ \boldsymbol{\rho}_s^* &= \boldsymbol{\rho}^{*\prime} + 0.5(\mathbf{1}_{N_{rcd}}) \end{aligned} \tag{3.25}$$

Allocation Algorithm Diagram

Figure 3-4 shows a visual representation of the allocation algorithm for RCD reflectivity coefficients. Given the desired $\boldsymbol{f}_{des} = [\mathbf{f}_{des},\ \boldsymbol{\tau}_{des}]^T$, the SVD matrices for the configuration at the current Sun direction are computed. The reflective coefficients are then obtained by Equations (3) and (3.19). If any of those values are beyond the range [-0.5, 0.5] the optimization problem in Equation (3.23) must then be solved, and the reflective coefficients can be recovered via Equation (3.25). It is recommended that the matrix $(U_{rcd}S_{rcd})^{\#}$ is computed once and used throughout the allocation algorithm for computational efficiency.

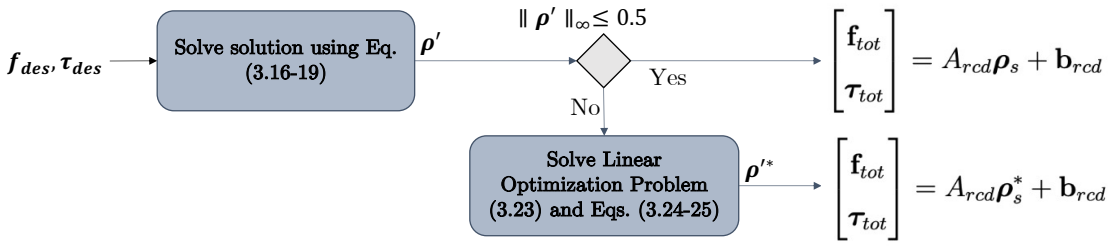

Figure 3-4: Diagram of allocation algorithm for RCDs. The inputs of the algorithms are the desired force and torque, $\mathbf{f}_{des}$ and $\boldsymbol{\tau}_{des}$ respectively. If the infinite norm of ρ' is not within 0.5, the reflective coefficients are then solved via linear optimization.

This section presented the allocation algorithm that allows for the computation of the reflectivity coefficients needed to produce the desired control vectors. However, it is also important to understand what control authority exits for a specific configuration.

3.3 Control Envelope for RCDs

Devices that utilize SRP for actuation, like solar sails or RCDs, have a state-dependent control authority, unlike traditional satellite actuators such as thrusters or reaction wheels. Due to this, the force and torque authority changes in both magnitude and shape as the Sun vector changes with respect to the satellite's z^b-axis. A method to characterize this control authority is by generating the control envelope of the actuators [122, 124]. The envelope represents the set of achievable forces and torques that the RCD configuration can produce at any direction on a unit sphere direction. This section covers how the force and torque authority is characterized which aids in quantifying the effectiveness of a given aggregate RCD configuration. Aggregate RCD configuration refers in this context to the orientation and position of all the RCD present in a satellite or space-based telescope.

There are several characteristics of good aggregate RCD configurations. First, it is desired that the control authority not be biased to a specific orientation of the satellite relative to the Sun direction. This property of the control authority can be accomplished by ensuring that there is symmetry in the RCD placements. Furthermore, when the Sun direction, $\mathbf{s}$, is along the satellite's z^b-axis and all the RCDs are at the same percentage of reflectivity, there should be no torques about any axis, and the force produced should be along the z^b-axis. This torque condition ensures that the satellite has no external torques at its nominal attitude while the force condition will be useful when designing the nominal orbits as shown in the next section. Finally, a good aggregate RCD configuration should have enough control authority to combat the expected environmental disturbances and performance requirements plus any desired operational margin.

For this work, it will be assumed that a given RCD configuration follows the aforementioned characteristics. Namely, when the Sun direction is aligned with the z^b-axis, $\hat{\mathbf{s}} = [0, 0, 1]^T$, the **nominal force** of the RCD configuration is defined as the force produced when the RCD are at 50% of their capacity,

$$\begin{aligned}\mathbf{f}_{nom} &= A_{rcd}(0.5\mathbf{1}_{N_{rcd}\times,1}) + b_{rcd} \\ &= p_{sun}a_{cell}\mathbf{a}_{rcd,50\%} \\ &= p_{sun}a_{cell}[0,0,a_{rcd,50\%}]^T\end{aligned} \tag{3.26}$$

The nominal force is used to generate the reference orbit of the RCDs to maintain orbit, and it is the *relative* forces between the output of the RCD and the nominal force that allows the satellite to move in a controllable maner. Furthermore, the nominal torque, $\boldsymbol{\tau}_{rcd,50\%}$, will be equal to zero.

3.3.1 Generation of the Force and Torque Envelope

Given a desired force and torque direction, $\hat{f}_{des}$ and $\hat{\tau}_{des}$ respectively, it is possible to find the maximum force that can be produced by an RCD configuration by utilizing the SVD matrices,

$$\begin{aligned}\max \quad & \gamma \\ s.t \quad & \|V\left[(US)^{\#}\left(\gamma[\hat{\mathbf{f}}_{des},\hat{\boldsymbol{\tau}}_{des}] - (\boldsymbol{\beta} - \|F_{nom}\|[s,\mathbf{0}]^T)\right)\right]\|_{\infty} \leq 0.5\end{aligned} \tag{3.27}$$

In Equation (3.27), the value of gamma–or the magnitude of the generalized control vector direction–is maximized until the value of the reflective coefficients is no longer feasible. Given the optimal cost found from Equation (3.27), γ^*, the reflectivity coefficients and force and torque can be obtained by,

$$\begin{aligned}\boldsymbol{\rho}_s &= V_{rcd}(U_{rcd}S_{rcd})^{\#}\left[(US)^{\#}\left(\gamma^*[\hat{\mathbf{f}}_{des},\hat{\boldsymbol{\tau}}_{des}] - (\boldsymbol{\beta} - \|F_{nom}\|[s,\mathbf{0}]^T)\right)\right]^T \\ \begin{bmatrix}\mathbf{f}_{tot} \\ \boldsymbol{\tau}_{tot}\end{bmatrix} &= A_{rcd}\boldsymbol{\rho}_s + \boldsymbol{\beta}_{rcd}\end{aligned} \tag{3.28}$$

The relative force is then obtained by computing $\delta f_{tot} = f_{tot} - \|F_{nom}\|\hat{\boldsymbol{s}}$, and this is the force that can be used to operate and station keep. The force and torque envelopes can then be obtained by plotting the value of γ for each direction in a unit sphere.

As the Sun direction changes, it might be of interest to find the maximum and minimum force allowable for each control axis $(f_x, f_y, f_z, \tau_x, \tau_y, \tau_z)$ in the body frame. Solving Equation (3.27) when $\arccos(\boldsymbol{s} \cdot z^b)$ is larger than $\approx 10^\circ$ sometimes leads to the matrix $(US)^\#$ bein ill-conditioned. Therefore, a different method needs to be used for computing the maximum and minimum control values at these high angles.[3]

As the Sun angle changes, the nominal force produced by the aggregate RCD configuration must still point in the same direction relative to the synodic frame (i.e. $\|F_{nom}\mathbf{s}$). The generalized control vector relative to this nominal force is then $\delta \boldsymbol{f}_{tot} = \boldsymbol{f}_{tot} - \|F_{nom}\|[\mathbf{s}, \mathbf{0}]^T$. The goal for the computation of the control envelope is then to maximize each component of the generalized control vector when all the other values are set to zero, or,

$$\begin{aligned} \max_{\rho_s, i} \quad & \delta \boldsymbol{f}_{tot,i} \\ s.t. \quad & \delta \boldsymbol{f}_{tot} = \boldsymbol{f}_{tot} - \|F_{nom}\|[\mathbf{s}, \mathbf{0}]^T \\ & \boldsymbol{f}_{tot} = A_{rcd}\boldsymbol{\rho}_s + b_{rcd} \\ & \delta \boldsymbol{f}_{tot,k} = 0 \quad \forall k \neq i, k \in (1, \ldots, 6) \\ & 0 \leq \rho_{s,k} \leq 1 \quad \forall k \in (1, \ldots, 6) \end{aligned} \tag{3.29}$$

where i represents the axis of interest. For example, if we want to maximize the force along the y-direction, $i = 2$ while the torque about the y-direction will be $i = 5$.

3.3.2 Example of Sun Direction Impact on Force and Torque Envelope

An example of an RCD configuration is shown in Figure 3-5. The configuration assumed that the cells could be placed within a 50×50 meter area or roughly the area for the IKAROS mission [37]. Each of the twelve RCD cells has its normal vector shown by a black arrow. Eight of the twelve RCD cells are located at the extremes of the 50×50 square, as shown in the figure, and are placed on top of one another.

[3]The Sun angle for which the matrix $(US)^\#$ is ill-conditioned depends on the RCD configuration itself and due to this it is recommended always use the alternative approach .

There is an assumption that RCDs can be placed on top of one another just for this analysis. An improved placement that is more realistic would be to have the RCD placed as close to the corner as possible without interacting or bouncing light from one another. The remaining four RCDs are placed closer to the origin.

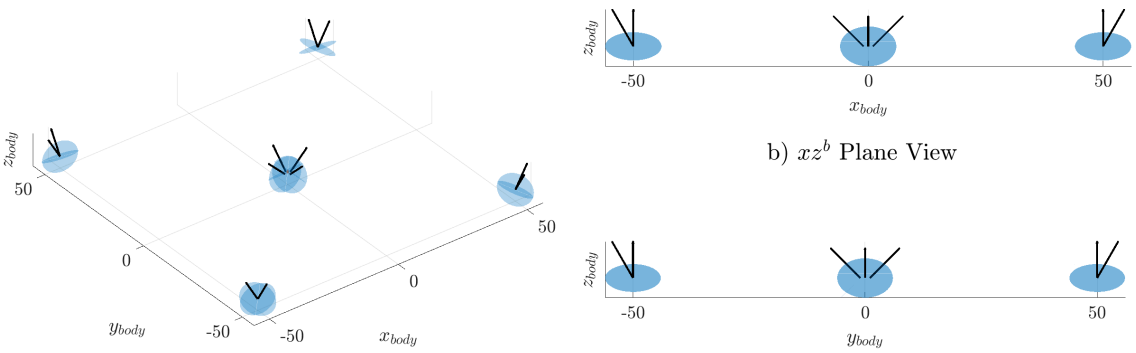

a) Isometric View

b) xz^b Plane View

c) yz^b Plane View

Figure 3-5: Placement location and orientation of a 12 cell RCD configuration.

The full orientation and locations of this RCD placement are shown in Table 3.2. The elevation angle is defined as the angle between the $\mathbf{z}^b$-axis and the axis normal to an RCD cell. The azimuth angle is defined as the angle between the projection of the axis normal to the RCD cell onto the xy^b-plane and the x^b-axis.

Table 3.2: RCD configuration with 12 Cells

Cell ID	**Elevation (deg)**	**Azimuth (deg)**	$\boldsymbol{x^b}$ **Pos. (m)**	$\boldsymbol{y^b}$ **Pos. (m)**
1	30	-90	-50	-50
2	30	180	-50	-50
3	30	180	-50	50
4	30	90	-50	50
5	30	90	50	50
6	30	0	50	50
7	30	0	50	-50
8	30	-90	50	-50
9	45	-90	0	-1
10	45	180	-1	0
11	45	90	0	1
12	45	0	1	0

The force and torque envelope for the twelve RCD cell configurations when the Sun direction is perfectly aligned with the $\mathbf{z}^b$-axis is shown in Figure 3-6 and 3-7,

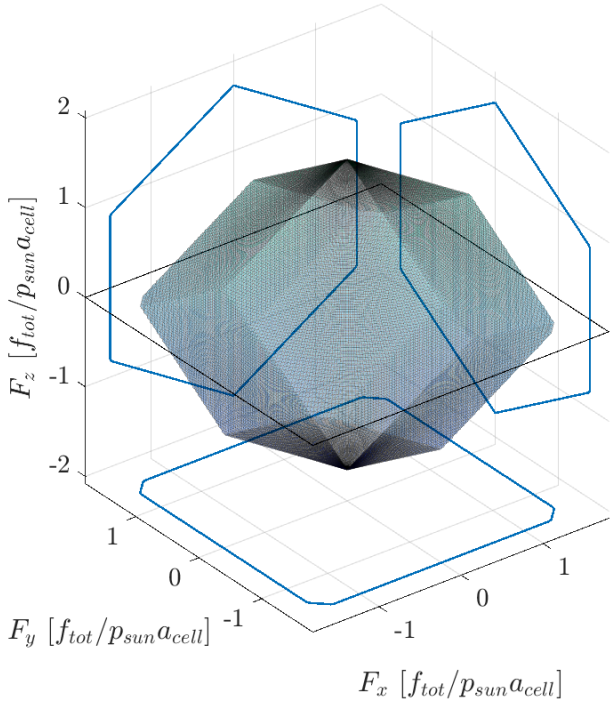

Figure 3-6: Force Envelope for RCD configuration with 12 RCD Cells at nominal Sun direction

respectively. The values are nondimensionalized by the solar pressure at SEL2, p_{sun}, and the area of the RCDs cells, a_{cell}. For both figures, the solid blue lines in the background plane represent a projection of the force and torque envelope onto that plane. Additionally, a thin black plane representing the $\mathbf{xy}^b$-plane is plotted.

The force envelope shown in Figure 3-6 is relative to the nominal force produced by the RCD when all the cells are as described earlier in Equation (3.26). The geometry of the envelopes for both the force and the torque is due to the number of RCDs as well as the orientation of all the configurations. For example, it is expected that given that most of the RCD's normal axes have a significant component projected along the $\mathbf{z}^b$-axis, the maximum range for the forces is along the z^b-axis. It is also worth noting that by canting the RCDs we are able to not only obtain torque authority about the z^b axis, but that axis is the one with the highest control authority. The high control range of τ_z can be explained by visual inspection of the configuration in Figure 3-5. By increasing the reflectivity coefficients on four of the RCD cells that

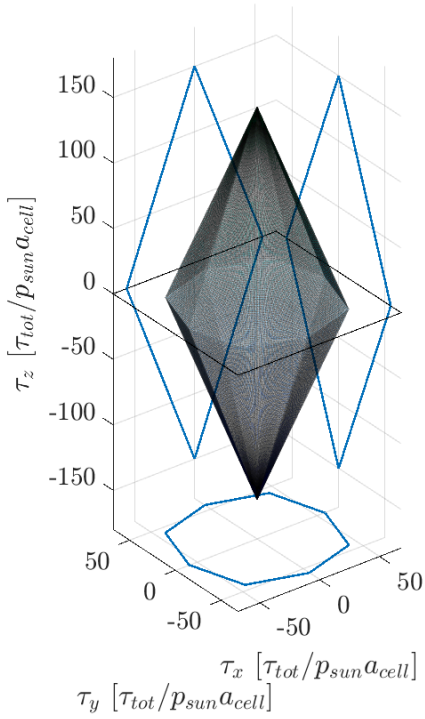

Figure 3-7: Torque Envelope for RCD configuration with 12 RCD Cells at nominal Sun direction

are in the extremities whose normal vector faces to the right of the position vector, a pure torque and force parallel to the $\mathbf{z}^b$-axis is produced. The additional force about the $\mathbf{z}^b$-axis can be eliminated by reducing the reflectivity of the four RCDs close to the origin. Altogether, eight of the twelve RCDs must change in order to produce a pure torque about the z-axis. However, in order to produce a pure torque about the $\mathbf{y}^b$ or $\mathbf{x}^b$ direction, all twelve RCDs must have a change in their coefficients; this results in a less efficient torque per change in reflective coefficient values and a limit on the amount of torque the aggregate RCD configuration before some of the RCD cells saturates.

Impact of Sun Direction

As the Sun direction changes, however, the control envelope like the one shown in Figure 3-6 will change in shape. Notably, it is expected that the control envelope will decrease in size as the angle of the Sun's direction relative to the satellite $\mathbf{z}^b$ axis

increases. To see this the maximum force produced by the RCD configuration in the $\mathbf{z}^b$ direction is plotted in Figure 3-8. The force plotted here is equivalent to the range of the allowable forces along the z^b-axis in Figure 3-6 as a function of Sun direction.

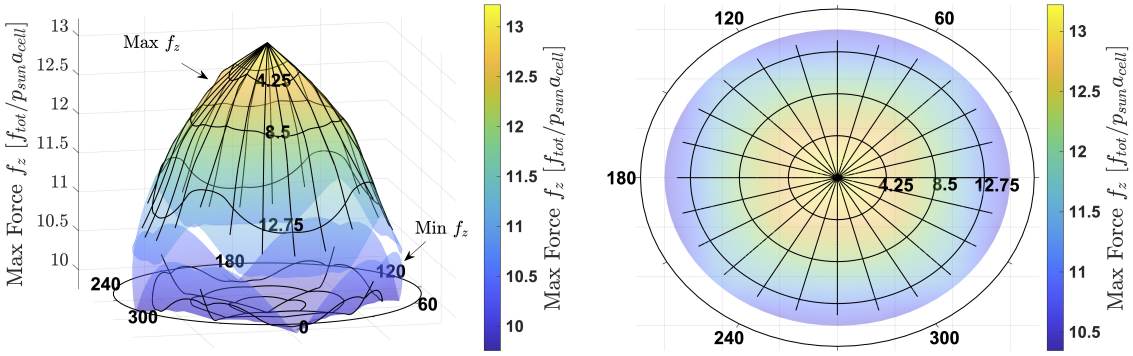

(a) Max min force F_z^b envelope

(b) Max force F_z^b envelope XY plane projection

Figure 3-8: F_z^b force envelope as a function of Sun azimuth and elevation angle.

Figure 3-8a shows the maximum f_z^b surface on the top, and the minimum f_z^b on the bottom. Figure 3-8b shows the XY plane projection of the maximum surface on the plot, the spokes on the figure correspond to the azimuth angles of the sun, while the rings correspond to the elevation angles. The plot is produced while enforcing that the force on x and y and torque in x, y, and z is at zero and the angle between the Sun and the z_b-axis changes from 0° to 18° and the azimuth angle changing from 0° to 360°. As expected, that maximum force is produced when the Sun's direction is parallel with the z^b. The z^b direction also has the highest range of allowable forces.

As the satellite tilts (or the Sun's direction relative to the body axes changes), the range of allowable forces decreases until you lose controllability. Figure 3-9 shows the max f_z^b force (top solid line), and min f_z^b force (bottom solid line) and correspond to a cut view of the surfaces in Figure 3-8a at zero azimuth angle. The allowable f_z^b force from the aggregate RCD configuration is shown in the light blue region. The dashed black line corresponds to the force produced by the configuration when all the RCDs are at 50% and the Sun direction is parallel with the z^b-axis. three regions are labeled in the Figure corresponding to areas with different controllability.

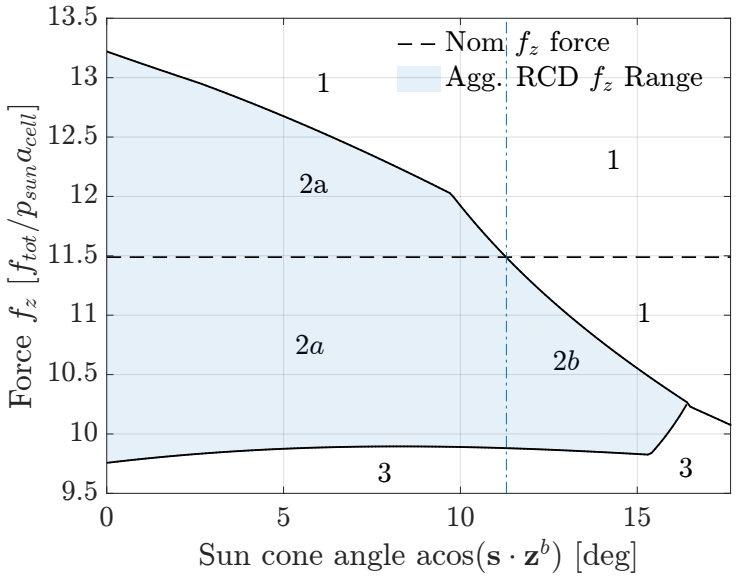

Figure 3-9: Twelve cell RCD configuration f_z^b range as a function of Sun angle at zero azimuth

Region 1 represents the set of forces in the z^b direction that are *not* attainable by the configuration because the force values in this region are above the maximum possible force authority of the aggregate RCD configuration. Similarly, Region 3, corresponds to the set of forces that are not reachable due to them being too low in magnitude. Region 2 corresponds to the set of achievable forces or the controllable region of relative forces along the $\mathbf{z}^b$-axis. However, region 2a is defined where it is possible to produce a force either above or below the magnitude of the dashed line which occurs at angles below 11.47°. Region 2b lies between Sun direction angles of $[11.47°, 16.40°]$ and is the region where there is still some level of controllability, however, the maximum possible force that is attainable is less than the nominal force. Finally, after the Sun angle of 16.40° the maximum and minimum force lines collapse into a single line; this indicates that it is no longer possible to produce a range of z forces while keeping the other forces and torques at zero, and there is a loss in controllability about this axis.

Obtaining the force and torque envelope for an RCD configuration is a necessary step for understanding the controllability of the satellite. Due to operational margin requirements on the control authority, a satellite might need to have requirements on

the maximum azimuth and elevation orientation relative to the Sun direction where it can operate.

For completeness, Figure 3-10 shows the same cut in the surface as in Figure 3-9 but for each control axis. Similar to the case of Figure 3-9, the figures were generated by finding the maximum (top black line) and minimum (bottom black line) force or torque while the other axes were commanded to zero. Additionally, for each figure, a negative Sun direction corresponds to a Sun azimuth angle of 180°, which means that the Sun direction vector will be tilted towards the $-x^b$-axis. A positive Sun direction angle corresponds to an azimuth angle of 0°, and the Sun direction vector is tilted towards x^b-axis.

In Figure 3-10a, which corresponds to the maximum and minimum force in the x^b-direction, two key characteristics are present: the envelope appears to be tilted, and, similarly to Figure 3-9, there is a point in which the two lines join. As the Sun's direction tilts towards the x^b-axis, some of the RCD cells' surface normal vectors begin to align with the Sun, this allows a larger effective force to be produced in that direction. However, there is a limit to this behavior, due to the need to keep the rest of the relative force and torque axis to be equal to zero. At angles $-15.4°$ and $15.4°$, the range between maximum and minimum force along the x^b-axis goes to zero, represented by the two lines joining. At angles below $-15.4°$ or above $15.4°$, the aggregate RCD configuration can no longer produce the nominal force vector pointed along the Sun direction. Additionally, the noise that appears on the edges of $\pm 20°$ are only due to numerical error from solving Equation (3.29).

The plot for τ_y, Figure 3-10d, is unique among the other axes in that there is no observable angle at which the maximum torque and minimum torque collapse into a single line. For this aggregate RCD configuration, it is possible to still provide a torque along the y^b axis until the Sun direction angle hits 31°. Nevertheless, after 12.3° it is no longer possible to provide a positive τ_y which would qualify as another instance of the system being underactuated, even though there is still controllability along the $-\tau_y$ axis. A similar behavior occurs at angles less than $-12.3°$.

For τ_x, δf_y, δf_z, and $\delta \tau_z$ shown in Figures 3-10b, 3-10c, 3-10e, and 3-10f respec-

tively, the relative forces and torques are symmetric about the vertical zero axis. Additionally, each figure also has a point at which the controllability about that axis is lost.

Overall, one of the main challenges for satellites using SRP or RCDs is the limited region in which the system is fully controllable, in the sense of having actuator authority greater than zero for each of the control axes. Even with these constraints, and as shown in the next section, it is still possible to attain orbit and attitude control using only RCDs as actuators. In practice, there must be a requirement for a maximum Sun angle allowable by the satellite to ensure that there is sufficient margin to reject disturbances as well as maintain some form of orbit control.

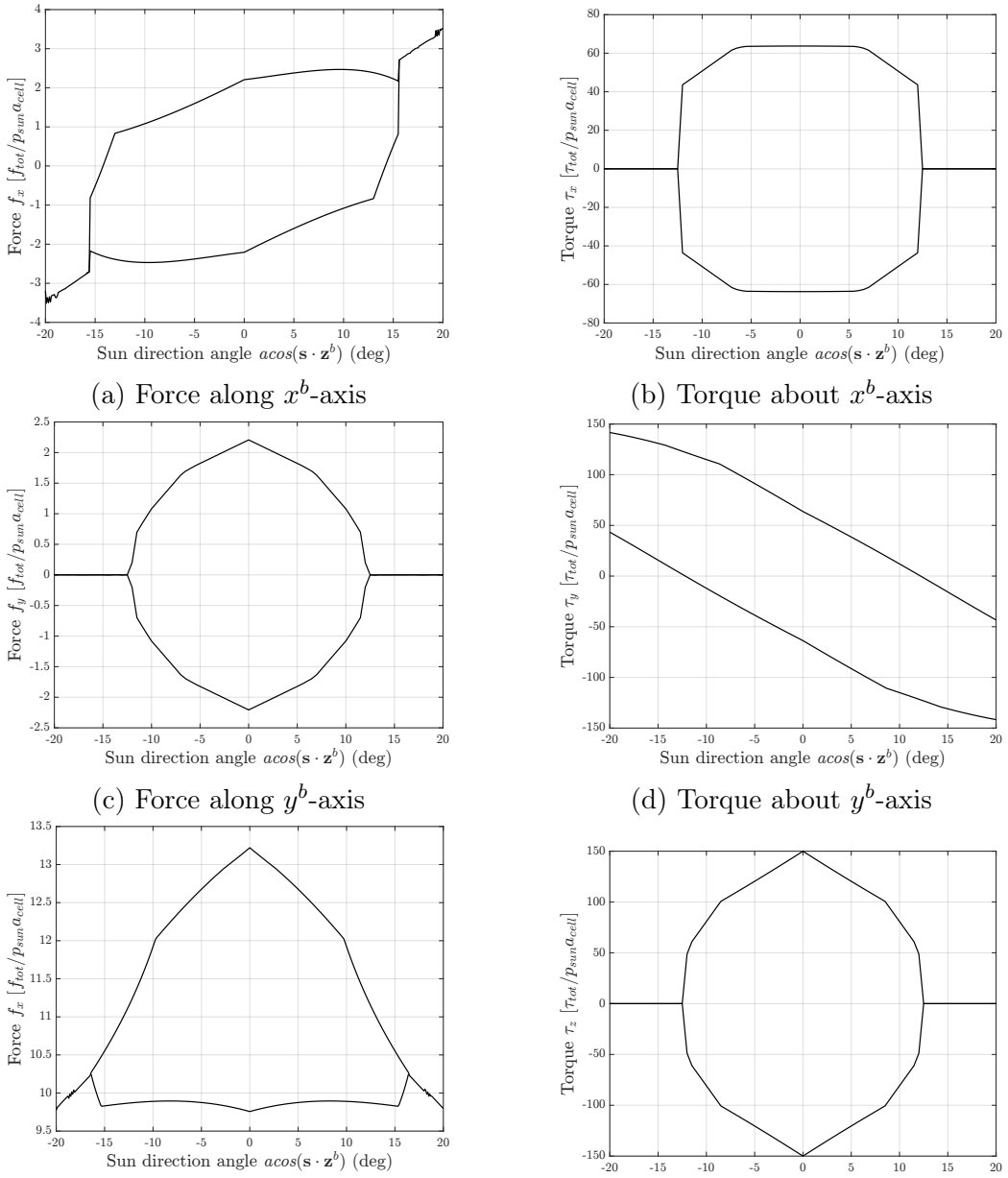

(a) Force along x^b-axis

(b) Torque about x^b-axis

(c) Force along y^b-axis

(d) Torque about y^b-axis

(e) Force along z^b-axis

(f) Torque about z^b-axis

Figure 3-10: Maximum and minimum force and torque as a function of Sun Angle. Positive values correspond to azimuth angle of 0, negative values correspond to azimuth angle of 180°. The top line corresponds to the maximum possible force or torque attained in each corrensponding axis, while the bottom line corresponds to the minimum value. A loss of controllability occurs when the lines meet.

3.4 Orbit-Attitude Controller

This section covers the orbit and attitude controllers that generate the control force and torque that must be provided by the RCDs. The orbit and attitude dynamics are assumed to be decoupled and two independent controllers are described. This assumption relies on the attitude and orbit dynamics evolving slowly enough to permit the separation of the degrees of freedom. Additionally, an example of 6 DOF control is presented to demonstrate the ability to use RCDs for combined orbit and attitude control.

3.4.1 Orbit Control

For orbit control, a reference orbit for the satellite must first be found. This process expands to that described in Section 3.1 by including the effect of SRP produced by the RCDs.

Reference Halo orbits

This work uses the technique explained in Reference [125] where a continuation algorithm is used to find an orbit with a desired SRP acceleration by incrementally increasing the acceleration present in the dynamics. As described in the previous section, the nominal force produced by the RCD configuration is defined when the satellite's z^b-axis is aligned with the Sun direction. Therefore, the desired orbit is a halo orbit that is produced when there is an SRP acceleration equivalent to the acceleration produced by the RCD configuration when all the reflectivity coefficients are at 50%, $a_{rcd,50\%}$. Substituting $\mathbf{a}^s_{ext} = [a_{rcd,50\%}, 0, 0]^T$ in Equation 3.1 yields,

$$\begin{aligned} \ddot{x}^s - 2\dot{y}^s &= \frac{\partial U}{\partial x^s} + a^s_{rcd,50\%} \\ \ddot{y}^s + 2\dot{x}^s &= \frac{\partial U}{\partial y^s} + 0 \\ \ddot{z}^s &= \frac{\partial U}{\partial z^s} + 0 \end{aligned} \tag{3.30}$$

The continuation algorithm will start with an initial condition solution for when no RCD acceleration is present, and increase the acceleration by Δa in the model. A differential corrector will then be used to find the initial condition by enforcing the periodicity constraint, and the process will be repeated until the acceleration present on the model matches $a_{rcd,50\%}$. Figure 3-11 shows the result of this algorithm where

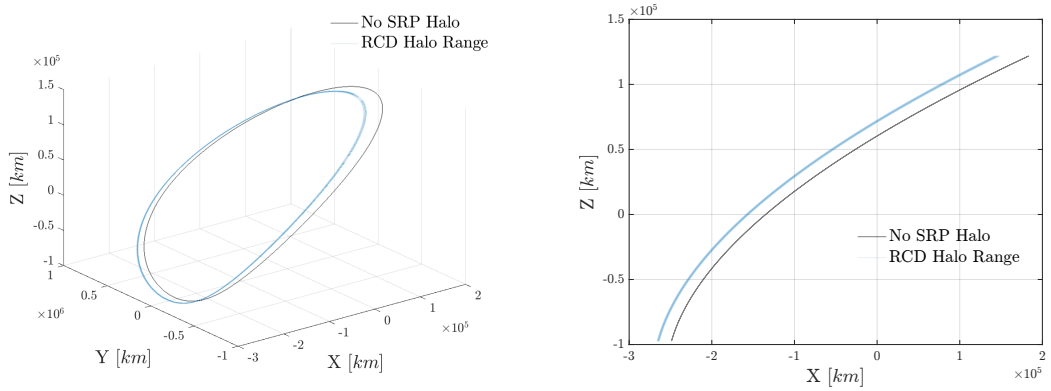

(a) Isometric view (b) XZ-plane view

Figure 3-11: Reference halo orbits about SEL2 point in the synodic reference frame. The solid black line corresponds to a halo orbit where no SRP is present, blue range lines correspond to halo orbits that are possible with a 12-cell RCD configuration.

the halo orbit with no SRP is shown in a solid black line, and a continous range of possible halo orbits when a_{rcd} is at different percentages is shown in the light blue manifold.The gap between the blue region and the no SRP halo is due to $a_{rcd,0\%} \neq 0$ (or the case where all RCDs are fully absorptive). Furthermore, the results shown in Figure 3-11 assumed that the desired halo orbit had an amplitude of 120,000 (km), and the area for each RCD was 10 (m^2). For station keeping, an orbit from the allowable RCD orbit manifold must be chosen. To increase the possible range of operation for satellites using RCDs, it is recommended that the reference orbit for a satellite with an aggregate RCD configuration is the orbit that is generated when all the RCDs in a given configuration are at 50%, or the orbit that matches an SRP acceleration of $a_{rcd,50\%}$.

Orbit guidance and control

The orbit control relies on linearizing the equation of motion to the form,

$$\delta\dot{\mathbf{x}}^s_{orb} = F\delta\mathbf{x}^s_{orb} + B_{orb}\mathbf{f}_{ctrl} \tag{3.31}$$

where F is the matrix from Equation 3.3, and $B_{orb} = (\mathbf{0}_{3\times3}, \text{eye}(3))^T$. A full-state feedback Linear Quadratic Regulator can be used to produce the optimal control policy for the control force $\boldsymbol{f}_{ctrl}$ that will have to be produced by the RCDs [126]. The control feedback is given by,

$$\boldsymbol{f}_{ctrl} = K_{orb}\delta\mathbf{x}_{orb,err} + a_{rcd,50\%} \tag{3.32}$$

where $a_{rcd,50\%}$ is feed-forward to the controller, $\delta\mathbf{x}_{orb,err} = \mathbf{x}_{orb,des} - \mathbf{x}_{orb}$, and $K_{orb} = R^{-1}_{orb}B^T_{orb}P_{orb}$ is the solution to the steady-state algebraic Riccati equation,

$$F^T P_{orb} + P_{orb}F + Q_{orb} - P_{orb}B_{orb}R^{-1}B^T_{orb}P_{orb} = 0 \tag{3.33}$$

The matrices $Q_{orb} \succeq \mathbf{0}$ and $R_{orb} \succ \mathbf{0}$ are weighting matrices that can be used to prioritize between error reduction or small force inputs.

The desired orbit state $\mathbf{x}_{orb,des}$ is obtained by using the reference orbit with a desired $a_{rcd,\#\%}$ acceleration–nominally this is at 50% to ensure the maximum force and torque range. At each time step, t, the state of the desired orbit is obtained using linear interpolation from a lookup table with the full state vector $\mathbf{x}_{orb,des}(t)$ that was obtained by integrating the initial condition produced by the continuation algorithm over a full orbital period, T_{per}. Alternatively, the value for $\mathbf{x}_{orb,des}(t)$ can be obtained by finding the closest point of the desired orbit with the current orbital state vector $\mathbf{x}_{orb}$. The former method ensures that the satellite follows the phase angle of the desired orbit, while the latter method ensures that the satellite follows the trajectory of a halo orbit. For satellites that have requirements of orbit position for communications and data transfer, the former method is recommended and will be the one used in this thesis.

3.4.2 Attitude Control

The quaternion-based attitude control follows that of Reference [4]. The attitude dynamics and kinematics in Equations 3.5 and 3.7 are linearized about the nominal equilibrium point $\mathbf{x}_{att} = [\mathbf{q}_0,\ \boldsymbol{\omega}_0]^T = [1,0,0,0,0,0,0]^T$ to be in the form $\delta\dot{\mathbf{x}}'_{att} = A_{att}\delta\mathbf{x}'_{att} + b_{att}\boldsymbol{\tau}_{ctrl}$, where $\delta\dot{\mathbf{x}}'_{att}$ represents a vector with only the vector component of the quaternion and the angular velocity. Matrices A_{att}, and b_{att} are given by,

$$A_{att} = \begin{pmatrix} \mathbf{0}_{3\times3}, & \frac{1}{2}\text{eye}(3) \\ \mathbf{0}_{3\times3}, & \mathbf{0}_{3\times3} \end{pmatrix}$$
$$b_{att} = \begin{pmatrix} \mathbf{0}_{3\times3} \\ I_{sc}^{-1} \end{pmatrix} \tag{3.34}$$

where eye(#) is the MATLAB function of the same name and represents an identity matrix of size given by the value inside the parenthesis.

Similar to the orbit case, an LQR controller can be used to produce the control torque policy and is given by,

$$\boldsymbol{\tau}_{ctrl} = K_{att,lqr}\delta\mathbf{x}_{att,err} \tag{3.35}$$

where $K_{att} = R_{att}^{-1}B_{att}^T P_{att}$ is the solution to a similar algebraic Riccati equation,

$$A_{att}^T P_{att} + P_{att}A_{att} + Q_{att} - P_{att}B_{att}R^{-1}B_{att}^T P_{att} = 0 \tag{3.36}$$

The matrices $Q_{att} \succeq \mathbf{0}$ and $R_{att} \succ \mathbf{0}$ behave in the same way as the orbit case. For completeness, given a desired kinematically consistent quaternion and angular velocity $\mathbf{x}_{att,des} = [\mathbf{q}_{des}, \boldsymbol{\omega}_{des}]^T$ the attitude error can be computed as follows:

$$\begin{aligned} \mathbf{q}_{err} &= \mathbf{q}^{-1} \otimes \mathbf{q}_{des} \\ \mathbf{q}'_{err} &= \text{sign}(\mathbf{q}_{err,w})[\mathbf{q}_{err,x},\ \mathbf{q}_{err,y},\ \mathbf{q}_{err,z}]^T \end{aligned} \tag{3.37}$$

where $q_1 \otimes q_2$ represents the standard quaternion multiplication between q_1 and q_2. The error in angular velocity is simply $\boldsymbol{\omega}_{err} = \boldsymbol{\omega}_{des} - \boldsymbol{\omega}$, yielding $\delta \mathbf{x}_{att,err} = [\mathbf{q}'_{err},\ \boldsymbol{\omega}_{err}]^T$. The generation of $\boldsymbol{\omega}_{des}$ and $\mathbf{q}_{des}$ is presented in Appendix A.

3.4.3 Example of Orbit and Attitude Control Using RCDs

To demonstrate full orbit and attitude control via RCD the reference configuration in Table 3.2 is used. Additionally, the satellite mass properties and controller parameters for the simulation are given by Table 3.3 and represent the values of the IKAROS satellite [37]. Note that Δt_{ctrl} corresponds to the controller time step of the simulation

Table 3.3: Satellite mass properties and controller parameters.

Parameter	**Value**
Mass (kg)	100
Inertia (kgm^2)	diag([33801, 33801, 67602])
RCD Cell Area (m^2)	10
Δt_{ctrl} (hr)	3
ζ_1, ζ_2	1
Q_{orb}	eye(6)
R_{orb}	eye(3)
Q_{att}	eye(6)
R_{att}	1×10^{-3}eye(3)

Rejection of Initial Position Error

Rejection of an initial offset error is an important test to do for any control system. A simulation in which the position of the satellite is perturbed away from its nominal orbit is shown in example case. The nominal trajectory was the 120,000 km amplitude halo orbit from the previous section. In terms of attitude control, the satellite is commanded to have its z^b-axis pointed along the synodic x^S-axis. The simulation ran with an initial offset of $x_{offset} = [100, -300, 500]^T(km)$. The initial attitude error $\delta \mathbf{x}_{err}$ was set to zero. No disturbances were present in the simulation, and the simulation was run for 400 days which corresponds to almost three revolutions of the halo orbit.

Figure 3-12 shows the result of this test case. Figure 3-12a shows an isometric projection of the nominal reference orbit with an SRP acceleration of $a_{rcd,50\%}$. The

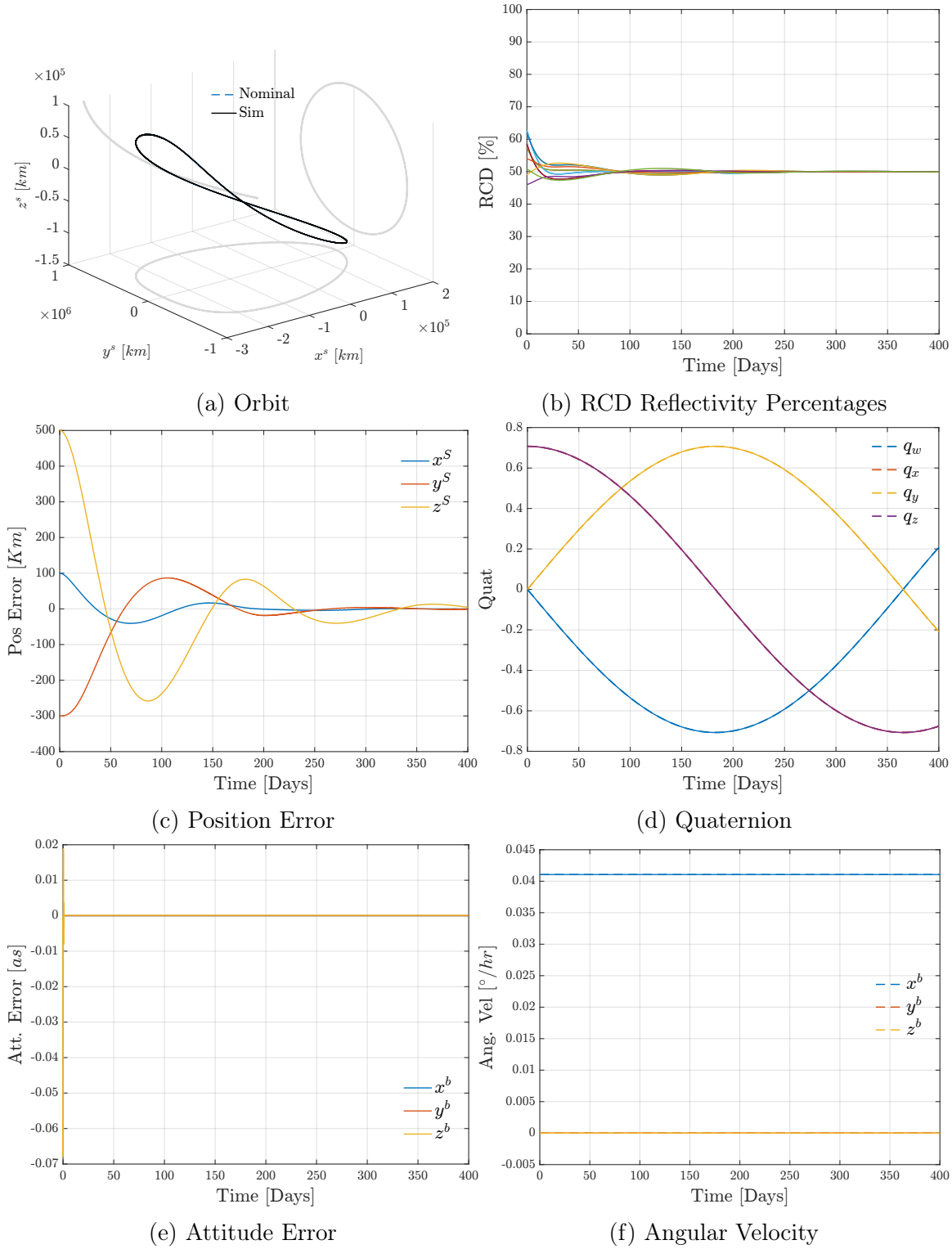

(a) Orbit

(b) RCD Reflectivity Percentages

(c) Position Error

(d) Quaternion

(e) Attitude Error

(f) Angular Velocity

Figure 3-12: Results for initial position error rejection. The satellite is commanded to follow the reference orbit from an initial position offset while maintaining pointing along the synodic x^S-axis.

nominal halo orbit in the blue dashed line as well as the satellite trajectory in solid black line. Additionally plotted is the shadow of the nominal orbit on the background planes. The initial offset represents less than 1% of the amplitude of the orbit and as such is not clearly seen in the figure.

The position error shown in Figure 3-12c is constantly decreasing, however, it takes approximately 321 days for the position error to go below 10 (km) in magnitude. This highlights one of the main downsides of using RCD or solar sails in that they are an extremely low thurst actuator. Depending on the mission, the satellite might need to have a backup propulsion system to perform major course corrections in relatively short periods of time. Alternatively, the magnitude of each value in R_{orb} and Q_{orb} may also be altered to place more importance on position error rejection at the cost of higher ranges of RCD reflectivity percentages.

Figure 3-12b shows the percentage of the reflectivity coefficients for all the 12 cells where 100% indicates the cell is completely reflective, while 0% is purely absorptive. As expected, all of the RCDs settle close to 50% which is consistent with the reference orbit being designed for $a_{rcd,50\%}$.

Although the ability to perform orbit maintenance and reject an initial position offset were the main objectives of this simulation, it is also important to look at how the attitude evolved. Figure 3-12d shows the evolution of the quaternion. Throughout the trajectory the satellite had to maintain a constant angular velocity so that its z^b-axis was always aligned with the Sun-Earth line as shown in Figure 3-12f. The attitude error throughout the simulation is given in Figure 3-12e measured in arcseconds.

To aid in understanding how the attitude of the satellite evolved, a polar plot of the orientation of the z^b-axis was expressed in both the synodic rotating frame and inertial frame and is shown in Figure 3-13. Both frames are plotted from the perspective of someone looking along the Sun-Earth line. However, for the synodic rotating frame the person is always aligned with the Sun-Earth line, while in the inertial frame the view is represented from t_0 at which point the Sun-Earth line in the inertial and rotating frame matched. The circles represent the angle between the satellite z^b-axis and the Sun-Earth line, while the spokes represent the azimuth

angle. For reference, the 270° azimuth angle represents the direction of the velocity of Sun-Earth, (or towards the y^s-axis). The 0° azimuth angle represents the direction towards the ecliptic (or towards the z^s, Z^I-axis). The initial and final orientations are plotted with a red asterisk, and blue triangle symbols, respectively.

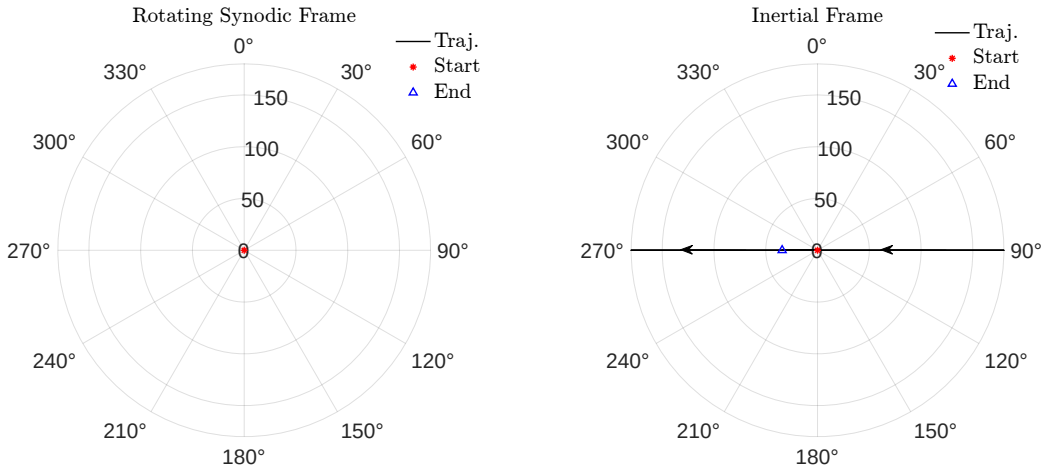

(a) Rotating Synodic Frame

(b) Inertial Frame

Figure 3-13: Representation of satellite's z^b-axis orientation in synodic rotating frame and inertial frame for initial position error rejection. The frame is seen from the perspective of looking along the Sun-Earth Line. For the Inertial frame, the origin represents the instant at t_0 where the Sun-Earth line for the rotating frame matches that of the inertial frame. Rings correspond to elevation, spokes correspond to azimuth angles.

In Figure 3-13a, the trajectory is always at the origin, as expected because the satellite was commanded to track the Sun-Earth line. For the inertial frame in Figure 3-13b the trajectory is moving towards the left along the 270° azimuth, wrapping around the polar plot along the 90° azimuth angle. The Sun-Earth line moves approximately at the rate of $1°/day$ so after 400 days of simulation we expect the end of the trajectory to be $\approx 35°$ degrees ahead of the start position along the 270° azimuth direction, and it is shown in the figure by the blue triangle being ahead of the red asterisk by about that magnitude.

Attitude Pointing in Inertial Frame: Imaging Maneuver

A more challenging example to show RCD potential as actuators for large space telescopes is the ability to maintain inertial pointing while following the nominal halo orbit. A simulation was run where a satellite using the mass properties from Table 3.3 performs four maneuvers to demonstrate a completion of an image maneuver. Each of the four maneuvers are described as follows:

1. Slew the satellite's z^b-axis inertially to a point in space that is 10°, elevation and 24° azimuth about the Sun-Earth line at t_0
2. Maintain inertial pointing for 8 days to simulate an image-taking maneuver
3. Slew back to point the satellite's z^b-axis towards the Sun-Earth line
4. Maintain pointing of the satellite's z^b-axis to Sun-Earth line

The duration of the simulation was 20 days, where the first three days were used to perform the slew towards the target (maneuver 1), eight days for imaging (maneuver 2), 3 days for return (maneuver 3), and six days to demonstrate maintaining pointing to the Sun-Earth line (maneuver 4). The same initial offset in position as the last case of $[100, -300, 500](km)$ was used. Figure 3-14 shows the results of the simulation. Similar to the previous case Figure 3-14a shows the halo orbit in space, with the blue dashed line being the nominal orbit. Since this simulation only lasted 20 days, only a part of the halo orbit was traversed as seen in the solid black line. Figure 3-14c shows the position error, with its behavior similar to the first 20 days of Figure 3-12c.

The RCD reflectivity coefficients are shown in Figure 3-14b. Compared to the initial position rejection example, this maneuver utilizes more of the RCD envelope. Of note, between day three to eleven, the overall magnitude of the RCD begin to move towards the 50% mark. This is expected as the satellite is pointing ahead of the Sun-Earth line, and as time moves on the Sun-Earth line, as seen in the rotating frame, catches up to the satellite. At the start of maneuver (4) which occurs when $t = 14$ $(days)$, the satellite is commanded to align its z^b-axis with the Sun-Earth line, and as expected the RCD coefficients are close to 50%.

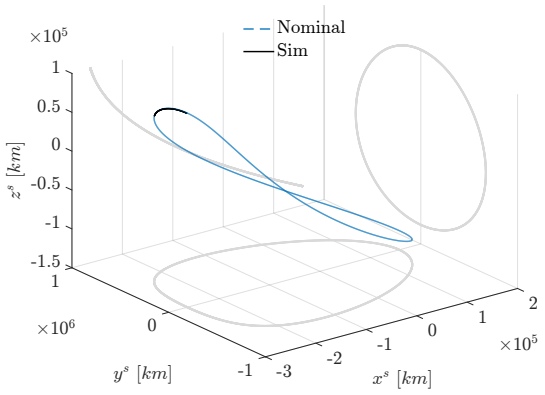

(a) Orbit

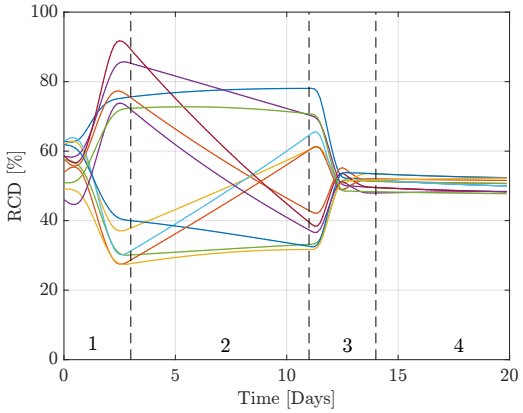

(b) RCD Reflectivity Percentages

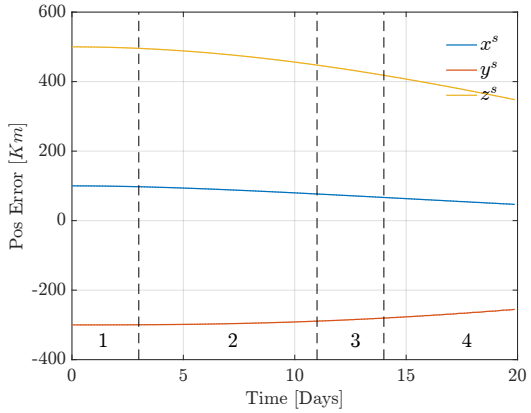

(c) Position Error

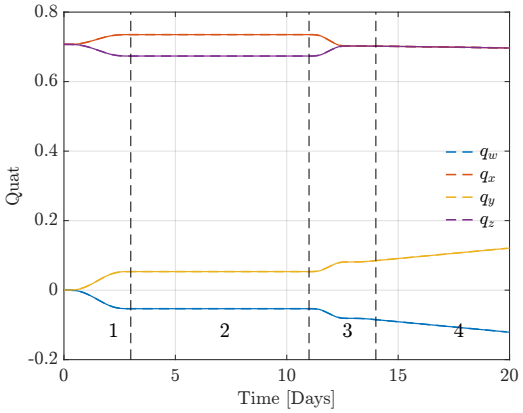

(d) Quaternion

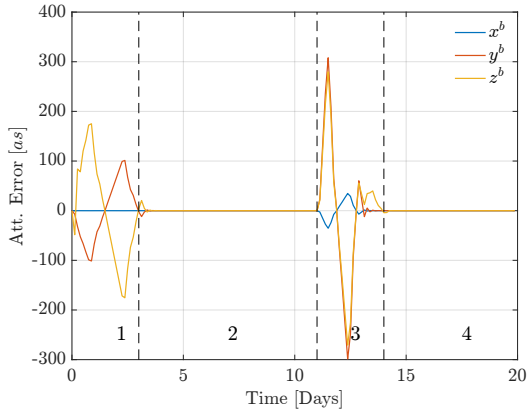

(e) Attitude Error

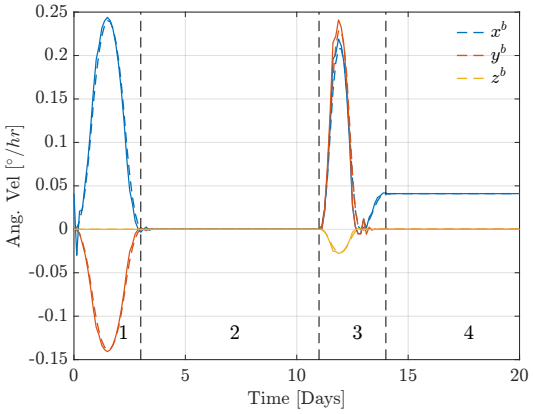

(f) Angular Velocity

Figure 3-14: Results for imaging maneuver. The satellite is commanded to point its z^b-axis inertially to a target for 8 days ($t \in (3, 11)$ $(days)$), and then proceed to return to point towards the Sun-Earth line.

The quaternion and angular velocity time history are shown in Figure 3-14d and 3-14f, respectively. The four maneuvers can be seen in each of the plots, During the first maneuver a slew about the x^b and y^b axis occurs. The slew is twice differentiable and ensures a smooth movement and low commanded torques by the attitude controller. During maneuver (2), the inertial pointing and image-taking period, the angular velocity is zero, and the quaternion remains the same for the 8-day duration. During the return to the Sun-Earth axis, two steps occur a reorientation step, as well as a ramp-up step about the x^b-axis. The latter is to ensure that the angular velocity of the satellite is such that its z^b-axis moves with the Sun-Earth line. During the entire simulation, the attitude error, seen in Figure 3-14e is within 300 (as). More crucially, during the image-taking part of the maneuver which occurs between the period of [3, 11] days, the attitude error falls below $0.02(as)$.

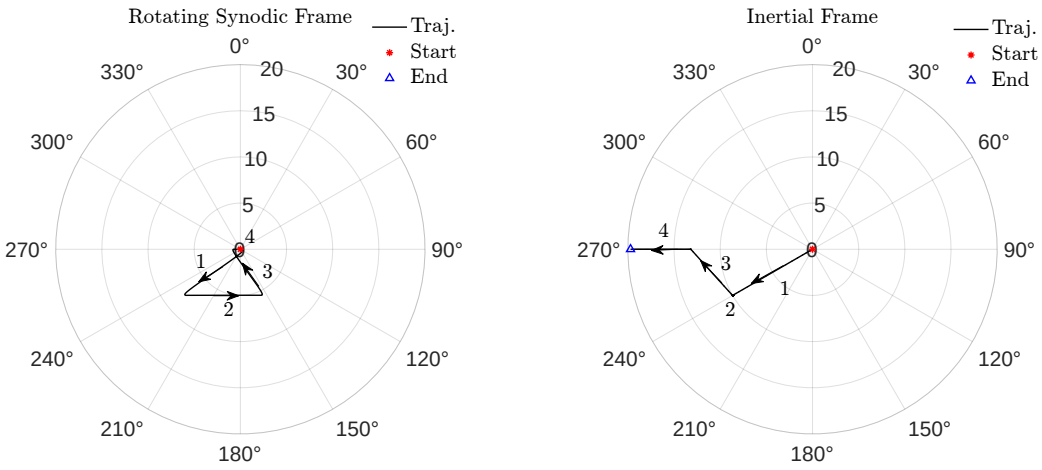

(a) Rotating Synodic Frame

(b) Inertial Frame

Figure 3-15: Representation of satellite's z^b-axis orientation in the synodic rotating frame and inertial frame for imaging maneuver. The frame is seen from the perspective of looking along the Sun-Earth Line. For the Inertial frame, the origin represents the instant at t_0 where the Sun-Earth line for the rotating frame matches that of the inertial frame. Rings correspond to elevation, spokes correspond to azimuth angles.

As with the initial error rejection example, two polar plots representing the view of the satellite's z^b-axis in the inertial and synodic rotating framea were plotted and are shown in Figure 3-15. The four maneuvers are labeled as well the start and end positions of the trajectories. For maneuver (1) the satellite is commanded to

move towards the point 8° elevation, and 240° azimuth. Afterward, the maneuver (2) relies on maintaining that position on the inertial frame which is why it appears stationary in Figure 3-15b, but moving towards the 90° line in the rotating frame on Figure 3-15a. Maneuver (3) is the return to pointing along the Sun-Earth line which corresponds to the origin in the rotating frame, after which it remains there as part of maneuver (4). In the case of the view from the inertial frame, maneuver (3) appears to look as if the satellite is moving towards the 270° azimuth line, and then maneuver (4) continues moving along the 270° azimuth.

Overall the two examples showcase the different capabilities of RCDs as an actuator such as the ability to inertially point and hold, while also the ability to demonstrate orbit maintenance. Both examples demonstrate that it is possible to have full 6 DOF control with only RCDs as actuators and pose a novel way that could be used for future space telescopes or satellites that require no consumables to enable an extended mission lifetime.

Chapter Summary

This chapter presented the main formulation needed to demonstrate the ability to have full orbit and attitude control using only RCDs and addresses Contribution 1. Contribution 1 focused on the creation of a methodology for using RCDs and orbital dynamics for combined orbit and attitude control. A description of the orbit and attitude dynamics, the main allocation algorithm, an analysis of the control envelopes for a given configuration, and a set of examples of a satellite achieving 6 DOF control was presented. The following chapter expands on this result and presents analysis needed to understand the limitation and capabilities for RCDs for use in space telescopes.

Chapter 4

Operability of RCDs for Space Telescopes at SEL2

This Chapter focuses on analyzing the capability of RCDs as actuators for space telescopes, or Contribution 2 of this thesis. The objective is to demonstrate the viability of RCDs as actuators as well as develop tools needed for designing an RCD configuration and understanding its performance for science collection.

Section 4.1 presents the concept of field of regard for space telescopes with RCDs, or the set of orientations where a satellite, utiltizing RCDs, can maintain orbit and attitude control for a long period of time. Section 4.2 goes over RCD placement optimization that maximizes the control authority for the aggregate RCD configuration. Section 4.3 shows an analysis of how expected disturbances compare to the operational envelope for RCDs in SEL2. The analysis of expected disturbances is needed for sizing the aggregate RCD configuration. Finally, Section 4.4 presents a case study of retrofitting JWST to study the performance of a non-rotating space satellite using RCDs.

4.1 Field of Regard Analysis

Beyond the control envelope discussed in Section 3.3, it is important to understand what is the allowable line-of-sight (LOS) pointing angles relative to the Sun-Earth

line of space telescopes using RCDs. The concept of field of regard (FOR) is a useful property to assess this region, and it is defined as the area that can be scanned or observed by a sensor [127]. For JWST, this is further defined as "the region of the sky where scientific observations can be conducted safely at a given time" [128]. Therefore, JWST restricts its field of regard further than what its actuators are capable of rotating and pointing due primarily to sunlight keep-out zones. This work utilizes a similar definition as JWST in that field of regard is defined as *the region for which it is possible to safely maintain both orbit and attitude control.* Safely is defined as ensuring that the maximum orbit position error and attitude error is within a threshold as discussed below.

4.1.1 Instantaneous Field of Regard

The computation for the Instantaneous Field of Regard (IFoR) relies on commanding a specific attitude for imaging and holding inertially that attitude for a predefined number of days as shown in Figure 4-1. Diagram is shown relative to the rotating synodic axis. A longer imaging time, t_{image}, corresponds to a space telescope imaging a dim object across the sky that requires a large integration time while having a low LOS pointing error. The term *instantaneous* refers to the field of regard being computed for a certain phase angle along the reference orbit. That is, at each location in a reference halo orbit a separate IFoR can be computed that looks at different locations in the celestial sphere.

For this analysis, the satellite's z^b-axis starts pointing at a specific azimuth and elevation relative to the Sun-Earth line and continues pointing inertially for a specific number of days. The simulation is repeated multiple times for different choices of azimuth and elevation angles. The azimuth and elevation angles for each simulation were obtained using MATLAB's meshgrid function to test all possible combinations within a cone centered around the Sun-Earth line, or x^s-axis. As before, the elevation is defined as the angle between the z^b-axis and the Sun-Earth line, or $\arccos(\hat{\mathbf{z}}^b \cdot \hat{\mathbf{x}}^s)$, and the azimuth is defined as the angle between the synodic z^s-axis and the projection of the z^b axis on the yz^s-plane. The orientation definition is more easily seen in Figure

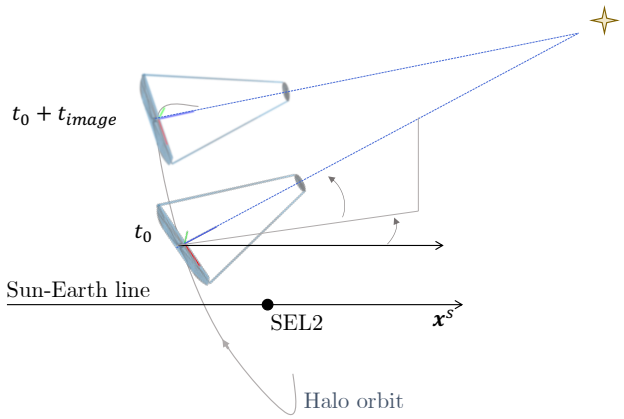

Figure 4-1: Telescope imaging diagram. Telescope maintains pointing on a target for a t_{image} duration. Diagram is shown relative to the rotating synodic frame.

4-2. The imaging location are mapped to a polar frame where the rings correspond to the elevation angles, and the azimuth angles correspond to the spokes.

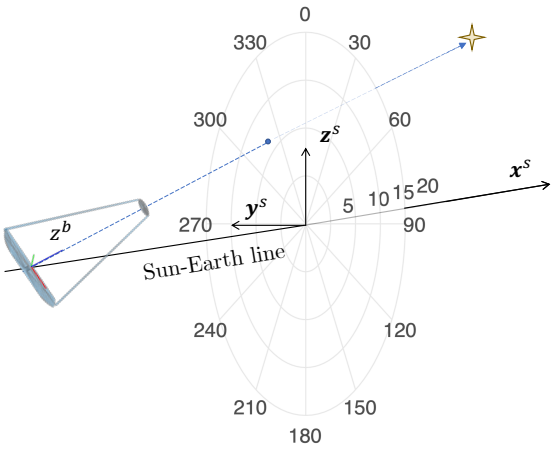

Figure 4-2: Definition of polar axes for IFoR analysis. Origin represents the direction of the Sun-Earth line.

This analysis utilized the same mass and controller properties from Table 3.3. The spacecraft is initialized with zero attitude error as well as zero position error. As the simulation proceeded the attitude and position error relative to the commanded quaternion and reference halo orbit is recorded. The simulation lasted for seven days

with a control period of 3 $[hrs]$. For this analysis, no disturbances were assumed as the goal is to obtain the region of control due only to the effect of having RCD actuators, not the impact of an orbit-attitude controller on disturbance rejection.

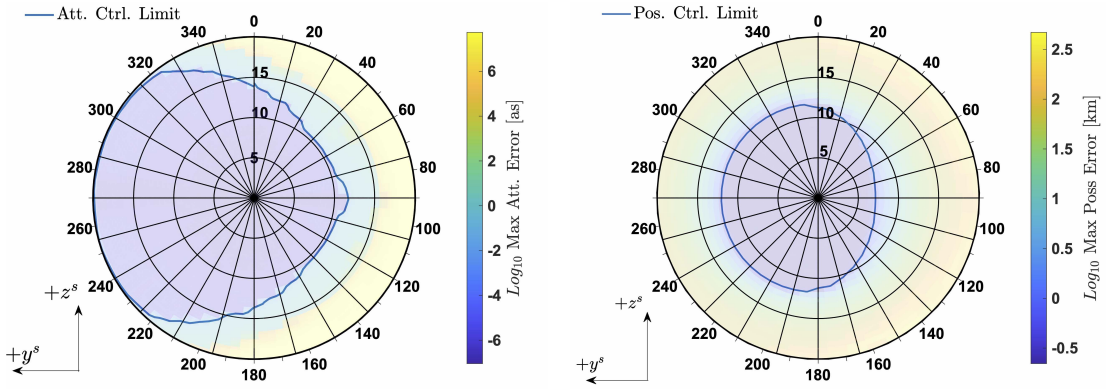

(a) Max Attitude Error

(b) Max Position Error

Figure 4-3: Polar surface of maximum attitude and position error as a function of initial pointing direction with 7-day imaging requirement. Spokes and rings correspond to the azimuth and elevation from the synodic x^S-axis, respectively.

The attitude error relative to the imaging target and position error relative to the reference halo orbit as a function of the imaging target is shown in Figure 4-3a and 4-3b, respectively. In both figures, the spokes correspond to the azimuth angle, while the rings correspond to the elevation angle, both in degrees, of the initial pointing direction from the x^S-axis at the start of the simulation. A zero elevation indicates that the spacecraft's z^b-axis is pointing along x^S-axis, an azimuth of 270° points toward the synodic y^S-axis which is also the velocity axis of the Sun-Earth line. These axes are plotted in both figures for reference.

For Figure 4-3a, the color of the surface corresponded to the magnitude, in log scale, of the maximum *attitude* error relative to the imaging target during the 7-day run expressed in arcseconds. The solid blue line contour represents the boundary when the attitude error is less than $0.1[as]$. Beyond this value, the attitude error appeared to grow unbounded suggesting that there is a bifurcation in the behavior of the system from a stable configuration to an unstable one, and is thus called the attitude control limit. The jaggedness of the boundary is due to both numerical error in the integration and a coarse meshgrid. For Figure 4-3b, the color of the surface

corresponded to the magnitude, also in log scale, of the maximum *position* error relative to the reference halo orbit during each 7-day simulation and is expressed in kilometers. The blue line contour represents the boundary when the position error is less than 1 $[km]$. The value is chosen for the same reason as the attitude plot and is called the position control limit.

The overall shape of the 1 (km) and 0.1 (as) contours are shifted towards the left of the plot, or the 270° direction. This is expected because, initially, the inertial axis and the synodic axis are aligned with each other. As time goes on, the satellite's z^b-axis will continue pointing inertially to the same point in space, however, relative to the synodic frame the satellite will rotate clockwise, and the angle between the z^b-axis and x^S-axis will decrease. For example, if the satellite starts pointing with an azimuth of 270°, and elevation of 7° from the x^S-axis, after seven days, the elevation angle should be close to zero. Compared to the position control limit, the attitude control limit in Figure 4-3a occupies a larger region of space. This is expected as the torque envelope for the configuration shown in Figure 3-5 is larger than the force envelope. Furthermore, during inertial pointing, no torques should be applied to the satellite compared to a force that must be applied to match the force needed to track the nominal halo orbit.

Since the IFoR is defined as the region in which it is possible to have combined orbit and attitude control, the IFoR for this configuration must be the intersection of the attitude and position control limit contours. Figure 4-4 shows the two contours overlaid. Similar to Figure 4-3, the spokes correspond to azimuth angles relative to the Sun-Earth line at the start of the simulation and the ring is the elevation angle measured about the same. In this configuration, the position control limit is the most constraining out of the two and its boundary lies completely inside the attitude control limit. Thus, the instantaneous field of regard is the position control limit region and is represented in the figure by a blue patch. Outside this region, the satellite may still perform an imaging maneuver as long as it lies within the attitude control-only region given by the light yellow patch. However, the position error will grow unbounded, and different actuators such as thrusters, are needed to bring the

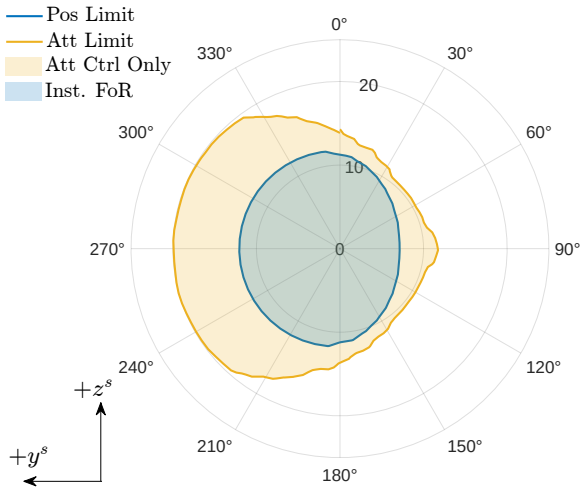

Figure 4-4: IFoR as a function of initial pointing direction relative to the Sun-Earth line for a 7-day imaging requirement. The blue region represents the imaging direction where there exits both orbital position and attitude control. Spokes and rings values in degrees correspond to the azimuth and elevation from the synodic x^S-axis, respectively.

satellite back to its reference orbit.

To demonstrate the different behavior between the IFoR region and the attitude control-only region, two simulations were run each with an initial pointing direction inside one of the two regions. The commanded azimuth and elevation for inside the FOR case and inside the attitude control only are $(293°, 10°)$ and $(90°, 10°)$, respectively. The results for this example are shown in Figure 4-5. The satellites were not commanded to spin about the z^b-axis like RSA telescope, however, to simplify the results for the RCD percentages and is done without loss of generality for RSA telescope motion. Figure 4-5a and 4-5b show the RCD percentage for both test cases. In the IFoR case, the RCD are not saturated, furthermore, the percentages decrease as time goes on as expected because the Sun-Earth line catches up to it. For the attitude control only case, however, some of the RCD cells start close to either 100% or 0%, and as time continues more of the RCD cells approach saturation this suggests that there is not enough control authority for the configuration. The position error time history is shown in 4-5c and 4-5d for both cases, respectively. As expected, the position for the IFoR case remains bounded within $[-1, 1]$ $[km]$, while in the attitude controller case, the position appears to grow unbounded and the RCDs tend

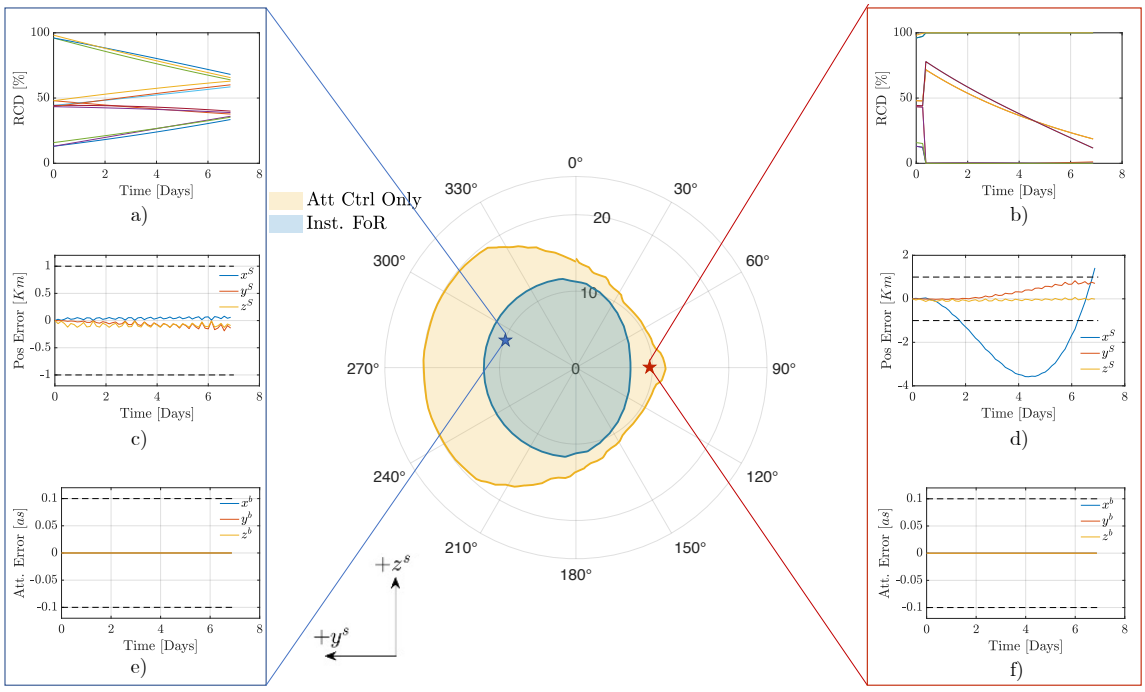

Figure 4-5: Comparison behavior between satellite pointing inside the IFoR region and the attitude control-only region. Spokes and rings values in degrees that correspond to the azimuth and elevation from the synodic x^S-axis, respectively.

to saturation. The small noise on the position error for the IFoR case is due to numerical integration issues. Finally, Figures 4-5e and 4-5f shows the attitude error time history with both being well within the attitude error limits.

Comparison of Instantaneous Field of Regard for various imaging times

The previous analysis had an imaging requirement of seven days. However, it is important to understand how the IFoR is affected by a shorter or longer imaging time. To do so, the same analysis as in the previous subsection was conducted which consisted of four steps:

1. A mesh is constructed to select various azimuths and elevations with respect to the Sun-Earth line

2. For each azimuth and elevation a simulation is run where the satellite is commanded to keep its z^b-axis pointed along the commanded angles for a predefined amount of time

3. Two contours are generated that corresponded to the maximum azimuth and elevation in which position and attitude control were maintained

4. The IFoR is produced which is the intersection of the two contours

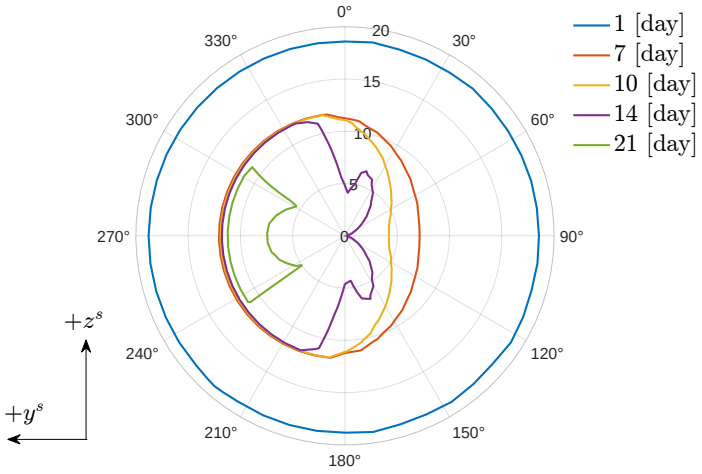

Figure 4-6: IFoR relative to the Sun-Earth line at the start of imaging as a function of imaging duration.

The IFoR is computed for 1, 7, 10, 14, and 21-day imaging times. The result of this analysis is shown in Figure 4-6. As in the previous figures, the rings represent elevation angles of the z^b-axis relative to the Sun-Earth line, and the spokes are the azimuth of that angle. Unsurprisingly, as the imaging time increases the field of regard shrinks. For all cases, the field of regard is shifted towards the 270° line, with the shift being more pronounced as the number of days increases. Again, the main contribution to this behavior is from the movement of the Sun-Earth line with respect to the z^b-axis. If the satellite starts ahead of the Sun-Earth line, or towards 270° azimuth, the Sun-Earth line will catch up to it at a rate of $\approx 1°/day$. Starting too far ahead from the Sun-Earth line, however, will have the RCDs start already saturated leading to a loss of control and onset of instability.

This subsection described the IFoR for satellites using RCDs as actuators. The IFoR is defined as the intersection of the attitude and position control limits of a satellite performing an imaging maneuver while maintaining orbit. The next step is to show the field of regard in the context of targets for space telescopes.

4.1.2 Field of Regard in Celestial Sphere for RSA and HWO Configurations

In the previous subsection, the field of regard computation did not assume that there was a pointing axis. Instead, it was assumed that the satellite z^b-axis was aligned with a target azimuth and elevation relative to the Sun-Earth line at the start of the imaging maneuver. If the satellite optical pointing axis was aligned along the z^b-axis then the IFoR would be the same as the previous subsection, but that is not always a practical design. For this reason, different configurations must be taken into account for computing what the field of regard looks like in terms of possible imaging targets in the celestial sphere.

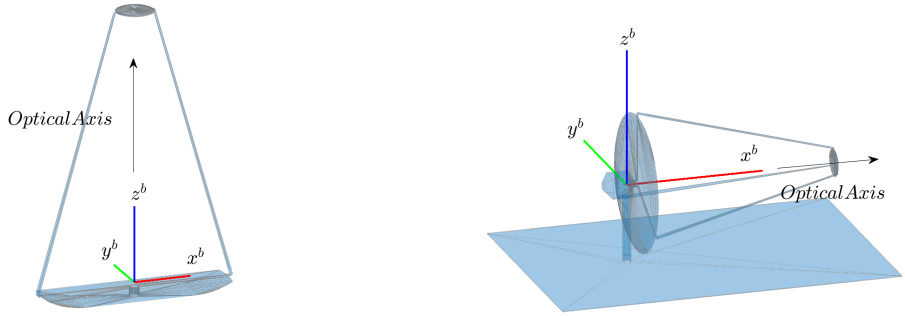

(a) RSA Configuration (b) HWO Configuration

Figure 4-7: Notional satellite configurations for computation of field of regard. The optical axis corresponds to the direction in which the science instrument points to obtain an image.

Two types of configurations were analyzed corresponding to an RSA-type satellite, and another corresponding to a typical observatory such as JWST or the Habitable Worlds Observatory (HWO) [14]. The two types of configurations are shown in Figure 4-7. For each configuration, the satellite's body axis x^b, y^b, and z^b are shown by the red, green, and blue axes, respectively. Since the RSA satellite, shown in Figure 4-7a, has to rotate about the optical axis, an obvious design is to have the optical axis align with the z^b-axis to ensure that at nominal attitude, the sunlight is coming from the $-z^b$ direction, away from the optics. The alternative configuration is to have the

optical axis aligned with an axis normal to the z^b-axis as shown in Figure 4-7b. The latter configuration is approximately the configuration utilized in the JWST as well as the upcoming HWO. This configuration allows for the addition of a sunshade to block all the Sun's light from the optical components. An additional benefit of this configuration is that it allows a 360° rotation about the z^b-axis while maintaining the same direction of the z^b-axis, and thus is a feasible orientation in terms of the IFoR[1].

The Annual Field of Regard (AFoR) for the optical axis of a satellite with any of the configurations in Figure 4-7 is expressed in the celestial sphere expressed in the International Celestial Reference Frame (ICRF). The ICRF frame is widely used in the astrophysics community to catalog candidate stars. The ICRF frame definition relies on carefully defining and cataloging various radio sources and their locations, but it can be understood to be aligned with the Z^{ICRF} axis pointing in the direction normal to the Earth's equatorial plane, the X^{ICRF} pointing towards the vernal equinox and the Y^{ICRF} completing the right-hand coordinate system [129, 130]. Thus, the difference between the inertial frame discussed in Section 3.1.1 and the ICRF frame is that the Z^I-axis is tilted 23.44° about the x^I-axis so that it points in the same direction as Earth's North Pole.

Annual Field of Regard for RSA Configuration in Celestial Sphere

The process for obtaining the AFoR plotted in the celestial sphere relied on computing the IFoR at different times during a year. For the RSA configuration, the optical axis matches the z^b-axis and the IFoR of the optical axis is equivalent to the IFoR of the satellite's z^b-axis. To plot it in the ICRF frame, each point along the IFoR must be converted to the correct frame.

Let (φ, ϑ) be the azimuth and elevation angles of a point inside the IFoR in Figure 4-4. The rotation matrix between the synodic frame and the satellite's body frame is

[1]Many additional possible configurations exits, however, one of the priorities for space telescopes is to ensure that no stray light from the sun hits the optical components. Thus, the optical axis should be limited to form an angle of 90° with respect to the z^b-axis and ensure that there exists a sunshade with a geometry that would block the sunlight at the operational field of regard.

given by,

$$ {}^{s}R^{b} = \begin{pmatrix} -\sin(\varphi), & 0, & \cos(\varphi) \\ -\cos(\varphi)\sin(\vartheta), & -\cos(\vartheta), & -\sin(\varphi)\sin(\vartheta) \\ \cos(\varphi)\cos(\vartheta), & -\sin(\vartheta), & \cos(\vartheta)\sin(\varphi) \end{pmatrix} \tag{4.1} $$

The optical axis in the synodic frame is then,

$$ \hat{\mathbf{z}}^{s}_{OptAxis} = {}^{s}R^{b}\hat{\mathbf{z}}^{b} \tag{4.2} $$

The axis can then be expressed in the ICRF frame by multiplying by the matrix ${}^{ICRF}R^{s}(t_{start})$. Matrix ${}^{ICRF}R^{s}(t_{start})$ represents a rotation matrix, as a function of time, between the synodic frame and the ICRF frame at the start of the imaging time. For this analysis, the rotation matrix between the inertial frame and synodic frame is given by,

$$ {}^{I}R^{s}(t) = \begin{pmatrix} \cos(\omega_{syn}(t)+\theta_{0,halo}), & -\sin(\omega_{syn}(t)+\theta_{0,halo}), & 0 \\ \sin(\omega_{syn}(t)+\theta_{0,halo}), & \cos(\omega_{syn}(t)+\theta_{0,halo}), & 0 \\ 0, & 0, & 1 \end{pmatrix} \tag{4.3} $$

where $\omega_{syn} = 1.9906\times10^{-6}\ rad/s$ represents the angular rate of the synodic frame relative to the inertial frame, and $\theta_{0,\ halo}$ represents the initial angle offset that accounts for where in the inertial frame is $t_{start} = 0$. Finally, the rotation matrix between the inertial axis and the ICRF frame is a rotation matrix about the x-axis,

$$ {}^{ICRF}R^{I} = \begin{pmatrix} 1, & 0, & 0 \\ 0, & \cos(23.44^{\circ}), & -\sin(23.44^{\circ}) \\ 0 & \sin(23.44^{\circ}), & \cos(23.44^{\circ}) \end{pmatrix} \tag{4.4} $$

where the 23.44° represents the rotation about the vernal equinox, X^{I}, by the inclination of Earth's North pole to match our definition for the ICRF frame. The pointing axis is then,

$$ \hat{\mathbf{z}}^{ICRF}_{OptAxis} = {}^{ICRF}R^{I}\ {}^{I}R^{s}(t)\hat{\mathbf{z}}^{s}_{OptAxis} \tag{4.5} $$

The optical axis $\hat{\mathbf{z}}_{OptAxis}^{ICRF}$ was computed for each (φ, ϑ) pair in the IFoR.

Figure 4-8 shows the IFoR with different start times for a 10-day imaging maneuver. The plot represents the celestial sphere in the ICRF frame. The origin points along the X^{ICRF}-axis. After the start time, the satellite will continue pointing at the target for 10 days. The start time of zero days corresponds to the satellite aligned with X^{ICRF} and is at the origin of the celestial sphere. The reference halo orbit is plotted using a black solid line, and also roughly represents the ecliptic plane as seen in the ICRF frame.

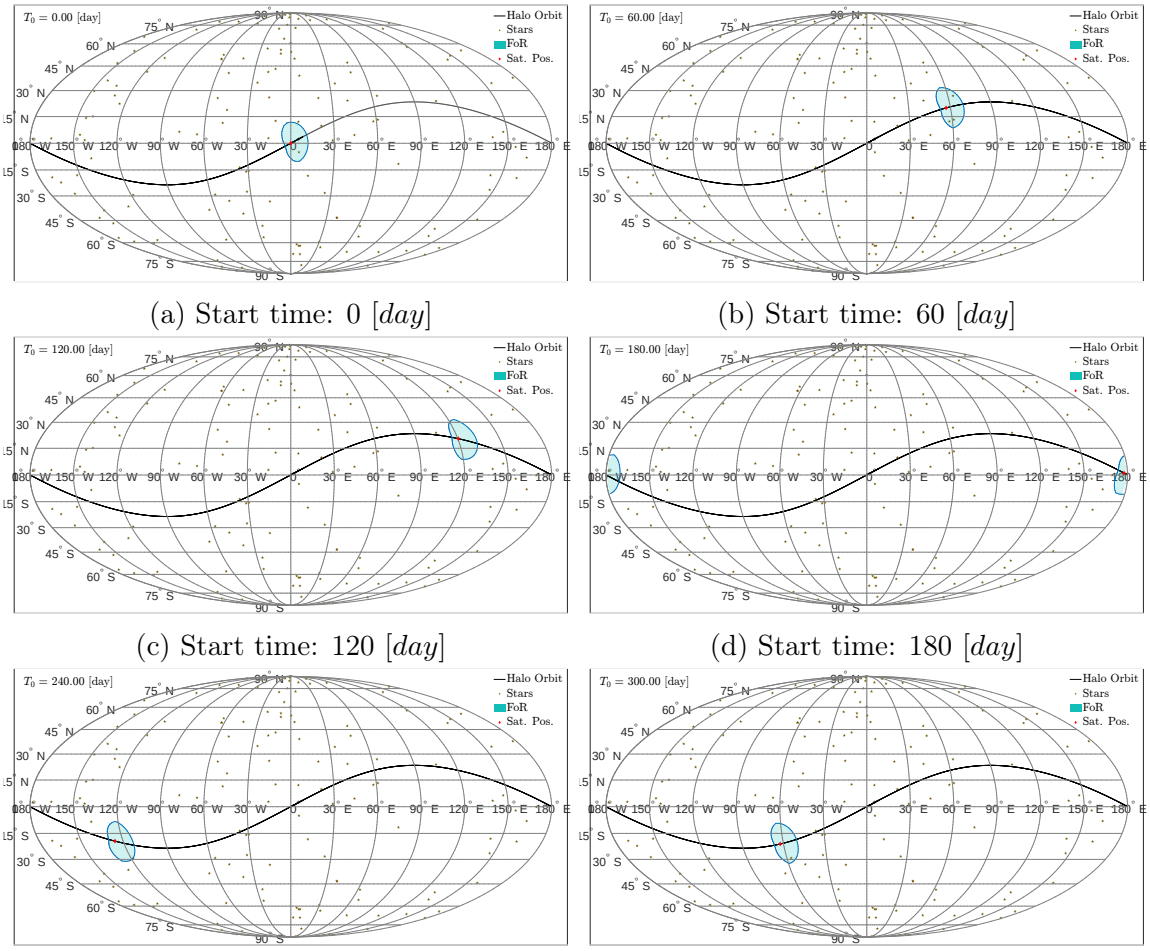

(a) Start time: 0 [*day*]

(b) Start time: 60 [*day*]

(c) Start time: 120 [*day*]

(d) Start time: 180 [*day*]

(e) Start time: 240 [*day*]

(f) Start time: 300 [*day*]

Figure 4-8: Plot of the IFoR at different points along the halo orbit for 10-day imaging time in the celestial sphere for the RSA telescope configuration. The start day corresponds to the day in the year at which imaging starts.

The satellite position is given by a red diamond, and as time progresses the satellite

moves east until it wraps to the longitude of 180° W. Also, plotted in Figure 4-8 are HabEx target stars in brown taken from HabEx's interim report [131]. The stars represent possible candidate stars that harbor exo-Earths. The overall shape of the IFoR does not change drastically as a function of the satellite's position in the halo orbit.

The IFoR at various points throughout the year can be extrapolated to create the AFoR. To do this, the maximum and minimum elevation angle relative to the Sun-Earth line is computed. This represents how far above and below the Earth's ecliptic plane to which the satellite can point. For example, in Figure 4-4, the maximum elevation for the field of regard is ±11.2°. An interpolated patch can be generated from this and plotted in the celestial sphere.

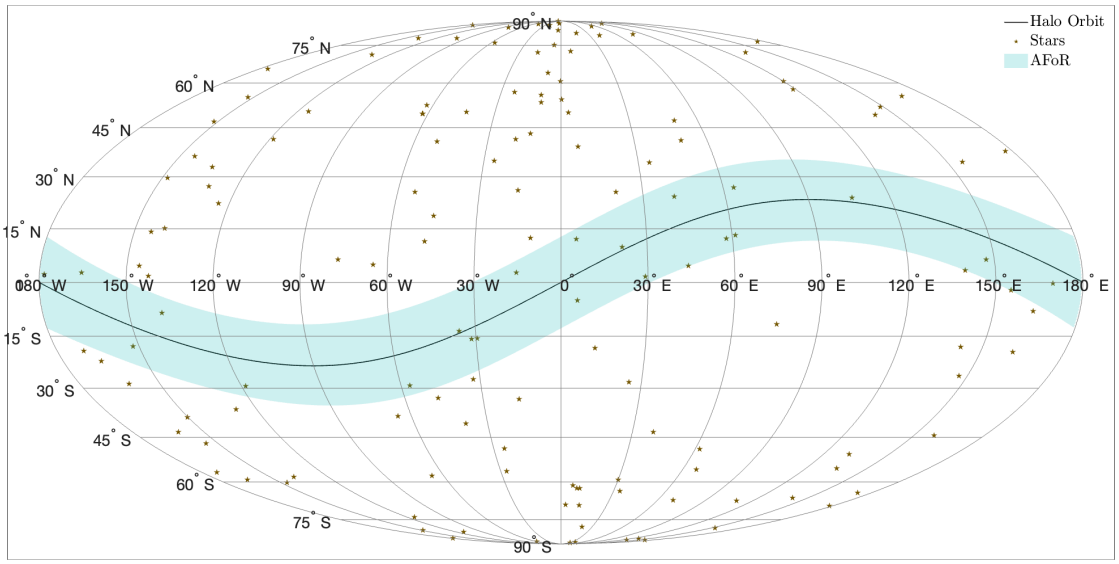

Figure 4-9: AFoR for a 10-day imaging period in ICRF frame. The blue region corresponds to any point in the celestial sphere at which the satellite can point inertially for seven days and maintain orbit control. The solid black line represents the ecliptic plane.

Figure 4-9 shows the AFoR for the 10-day imaging period case. The AFoR is plotted in an ICRF celestial sphere. Similarly to Figure 4-8, the solid black line represents the halo orbit. Furthermore, the HabEx target starts are also plotted in yellow stars. The light blue patch corresponds to the AFoR. Thus, the stars in the blue patch represent the possible target stars that an RSA satellite is able to image

if each imaging duration was less than or equal to 10-days.

Improvement on Total Field of Regard Coverage for RSA Configurations

The RSA AFoR in Figure 4-9 does not cover the entire celestial sphere, and as such is unable to image all the candidate stars. There exist several methods and techniques that can improve the coverage seen in Figure 4-9. For example, by decreasing the imaging period from 10-days to one day the total field of regard area would increase by 8° in width in each direction of the patch. This still is not enough to cover the entire celestial sphere. Alternatively, the satellite might be able to transition to the attitude control limit rather than the combined attitude and position control limit as mentioned in Section 4.1.1. Unfortunately, by switching to the attitude control limit only may require additional actuators such as low-thrust propulsion thrusters to bring the satellite back to the nominal halo orbit after imaging.

A different strategy is to design an RSA satellite with the same characteristics as the HWO configuration. That is, have the optical and spin axis be the x^b-axis. In this configuration, the RSA might become a dual spinner so that it still has a stationary sunshade and RCDs as the satellite's optical payload rotates. Alternatively, if the satellite remains a single spinner, the RCDs placement must be changed so that RCDs are able to be accessible as the satellite rotates in the x^b-axis. This may be accomplished by fitting RCD cells around a cylinder that surrounds the RSA optical payloads. The analysis for such configuration is left for future work.

Annual Field of Regard for HWO-like Configuration in Celestial Sphere

For the HWO satellite configuration shown in Figure 4-7b, the optical axis field of regard differs from the RSA's IFoR as the optical axis is not aligned with the z^b-axis. Assuming that the optical axis is along the x^b axis, the updated IFoR for an HWO-type satellite can be computed as follows,

$$\hat{\mathbf{x}}^{ICRF}_{OptAxis} = {}^{ICRF}R^b(t)\ {}^bR_z(\psi_z)\hat{\mathbf{x}}^b_{OptAxis} \tag{4.6}$$

where ${}^{ICRF}R^b(t) = {}^{ICRF}R^I\ {}^I R^s(t)\ {}^s R^b$ from previous, and ${}^b R_z(\psi_z)$ represents a rotation matrix about the z^b-axis. The field of regard for the optical axis is then the set of directions of $\hat{\mathbf{x}}^{ICRF}_{OptAxis}$ for each (φ, ϑ) pair in the IFoR, and each $\psi_z \in (0, 2\pi)$.

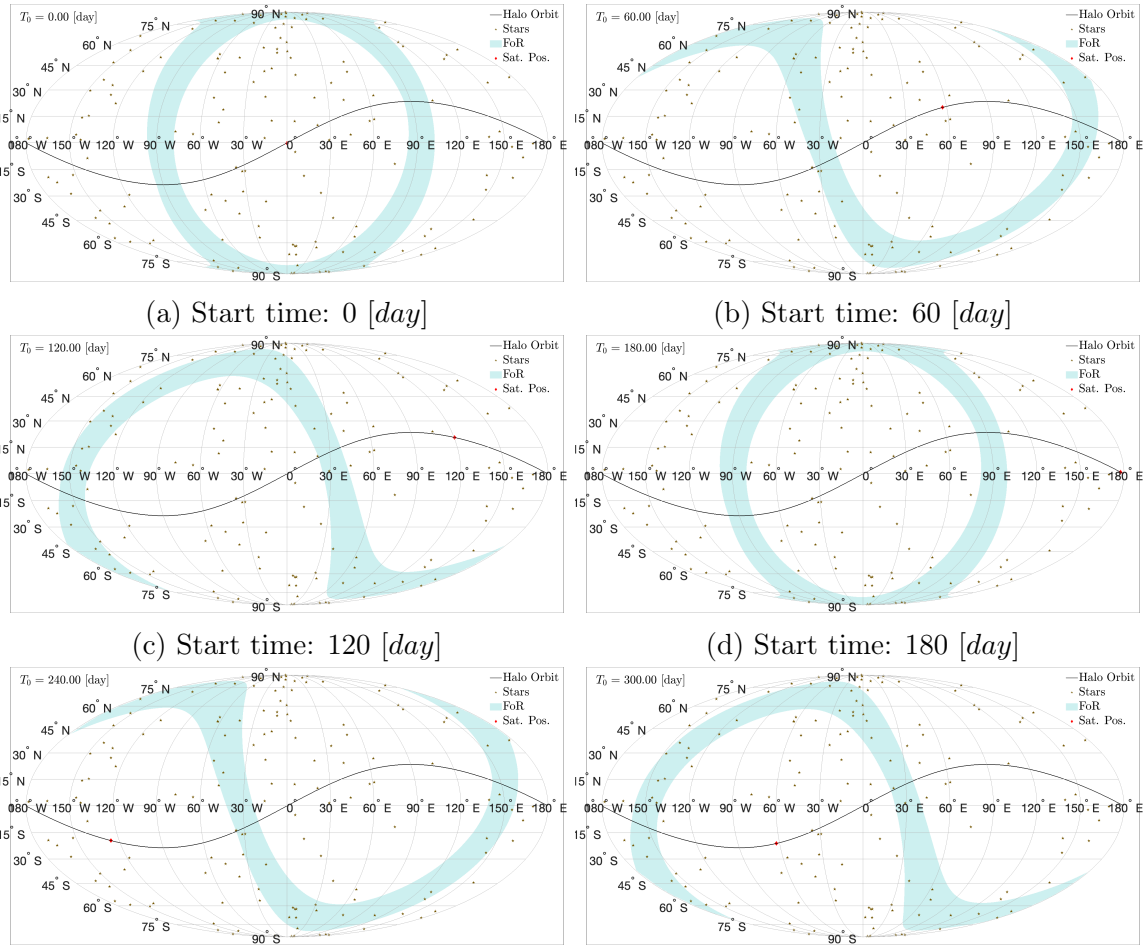

(a) Start time: 0 [*day*]

(b) Start time: 60 [*day*]

(c) Start time: 120 [*day*]

(d) Start time: 180 [*day*]

(e) Start time: 240 [*day*]

(f) Start time: 300 [*day*]

Figure 4-10: Plot of the IFoR at different points along the nominal halo orbit for 10-day imaging times in the celestial sphere for the HWO-like configuration. The start day corresponds to the day in the year at which imaging starts.

The resultant field of view plotted in the ICRF frame at various start times is shown in Figure 4-10. Similar to the RSA case, the halo orbit is plotted in a solid black line, and the satellite position was given by a red diamond. The same candidate stars from the HabEx report are shown as brown stars. Figure 4-10a, representing the IFoR at an imaging start time of zero, shows the overall shape of the field of regard to be a ring about the celestial sphere. This is consistent because the HWO-like configuration

is able to rotate a full 360° about the z^b-axis. As the start time increases, additional large regions of the celestial sky are accessible to this configuration, culminating in the ability to image the entire celestial sphere every half year. This is shown by the appearance of similar contours every 180 days. By inspecting all of the subplots in Figure 4-10 it can be seen that there exist two regions that are always accessible to this configuration, namely the north and south pole of the ecliptic plane. The north pole of the ecliptic plane is located between longitudes 90° W and 60° W at latitudes between 65° N and 78° N. A similar region exits for $-z^I$ direction.

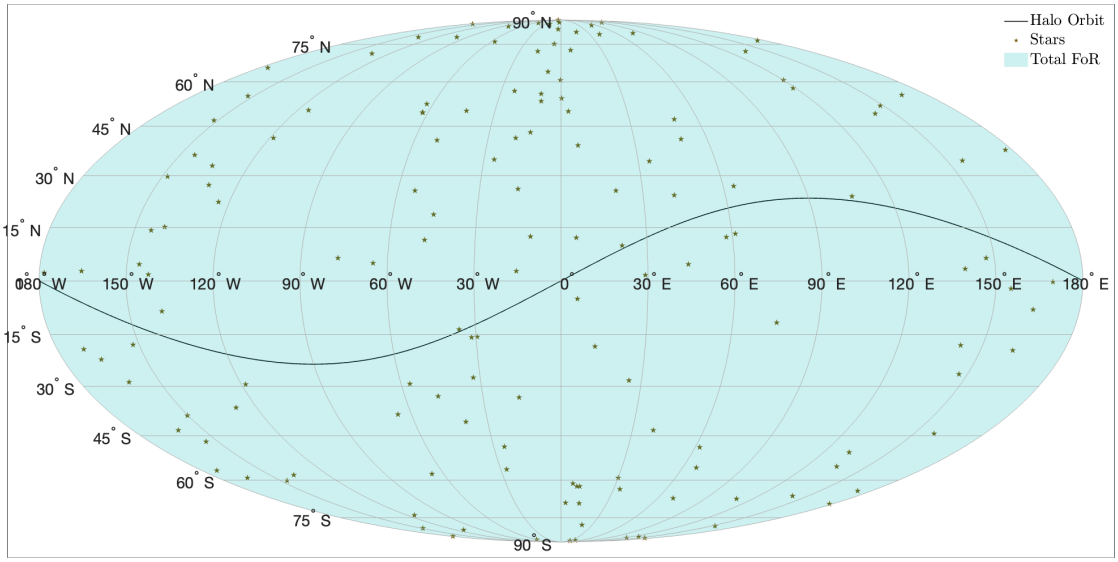

Figure 4-11: Full one-year Field of Regard for a 10-day imaging period in ICRF frame. The blue region corresponds to any point in the celestial sphere at which the satellite can point inertially for seven days and maintain orbit control. The solid black line represents the ecliptic plane.

The AFoR was obtained in a similar way as in the RSA case. Unsurprising, the AFoR is the complete celestial sphere as shown in Figure 4-11. For this reason, configurations like the HWO are very attractive as it allows full coverage of the sky while having a configuration where all the sunlight is in one direction which allows for light suppression designs like those used in the JWST.

This section covered the method of obtaining the IFoR and AFoR for space telescopes using RCDs as actuators and represents one of the main contributions of the thesis.

The IFoR is defined as the direction in which the satellite's LOS pointing has combined orbit and attitude control while conducting imaging for a defined number of days. As the imaging maneuver duration increases, the IFoR decreases and vice versa. Additionally, the AFoR was presented for two types of telescope configurations: an RSA-like telescope, and a HWO-like telescope. For HWO-like configuration, the optical axis is not collinear to the telescope's z^b-axis allowing for coverage over the entire celestial sphere.

4.2 Optimization of Aggregate RCD Configuration

This section focuses on the optimization of RCD cell placement for an aggregate RCD configuration. As defined before, the aggregate RCD configuration includes the location on the spacecraft plane where the RCD is to be located, as well as the orientation of each of the cells. One of the main challenges is the number of variables needed for optimization. As mentioned in Section 3.2, to have six DOF control there must be at least six RCD cells. Each RCD cell requires five values to set its location, namely three for position and two for orientation. In this work, the assumption, without loss of generality, is that the RCDs are placed on the xz^b plane, leading to only two values required for position per cell. This results in at least 24 continuous variables for optimization for a six-cell RCD configuration. Furthermore, for each configuration, it is desired to optimize the force and torque, representing six dependent variables, at various Sun angles which itself can be described by two variables. Thus, it becomes apparent that this type of optimization suffers from the well-known *curse of dimensionality* that makes optimization problems challenging, if not, practically impossible [132].

When looking for an optimal aggregate RCD configuration, it is important to define the cost function of the aggregate RCD configuration. For traditional satellite actuators such as thrusters or reaction wheels, an optimal configuration maximizes the torque or force envelope, momentum capacity envelope, agility envelope, or one that minimizes the power consumption [122, 133, 134]. For RCDs a similar approach

is taken in that the objective is to maximize the torque and force envelope shown in Section 3.3. The chosen cost function, known as the authority function, for a given configuration of RCDs is then

$$c_{auth} = \max \prod_{i=1}^{3} \text{range}(f_i)\text{range}(\tau_i) \tag{4.7}$$

where range(f_i) and range(τ_i) represent the allowable force and torque ranges about the ith axis. Multiplying the product of the ranges ensures that the configuration always has controllability about all axes. If there is no controllability about one axis, the product of the range will be zero causing the authority of that given configuration to also be zero. This is akin to trying to optimize the volume of a 6th-dimensional parallelotope that corresponds to the control authority envelope.

Note that alternative authority functions exist that can be used to Equation (4.7). For example, rather than having the product of ranges, one can have the sum of the square of the ranges,

$$c_{auth} = \max \sum_{i=1}^{3} \text{range}(f_i)^2 + \text{range}(\tau_i)^2 \tag{4.8}$$

where squaring the ranges makes the authority function convex. One of the drawbacks of this alternative authority function is that there are instances in which the RCDs can maximize the authority by increasing the range over only one axis while leaving another axis without any range. Other authority functions such as scaling Equation (4.8) by the corresponding mass or inertia products exits. However, similar drawbacks exist for cases in which there is no penalty for lack of control range about any degree of freedom.

To solve this optimization problem, the main problem of six DOF optimization of six plus cells was divided into three sub-problems: two DOF case, three DOF case, six DOF case. The insights gathered from the simplified problem were utilized to solve the subsequent ones.

4.2.1 Optimization for Two DOF Configuration: Two Cell Case

The first simplified problem solved was the case of optimizing two cells for a two-degree of freedom displacement control in a plane. In this case, the x and z position axis were the targets of the control and reduces the system to just simple planar motion in a Cartesian frame.

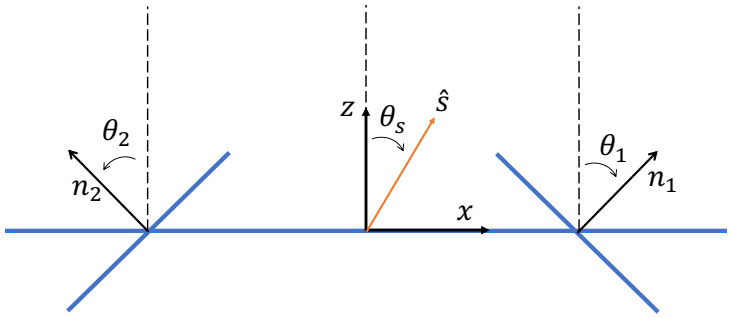

Figure 4-12: Notional satellite with two reflective control devices for two degrees of freedom control

The setup for this problem can be seen in Figure 4-12. The image is a representation of an "edge-on" view of a satellite with two RCD Cells. The two inclined blue lines are edge-on views of two RCDs that are assumed to be placed along the x-axis and are canted at angles θ_1 and θ_2, respectively. Note that a positive angle is clockwise about the y-axis pointing out of the page. The normal vector for the RCDs is given by,

$$\mathbf{n}_1 = \begin{pmatrix} \sin(\theta_1) \\ \cos(\theta_1) \end{pmatrix}, \quad \mathbf{n}_2 = \begin{pmatrix} \sin(\theta_2) \\ \cos(\theta_2) \end{pmatrix} \tag{4.9}$$

The Sun vector is given by $\mathbf{s}$ and is also determined by a single angle θ_s. The Sun

direction vector is given by,

$$\hat{\mathbf{s}} = \begin{pmatrix} \sin(\theta_s) \\ \cos(\theta_s) \end{pmatrix} \tag{4.10}$$

Using the same function for the SRP force from RCDs as in Equation (3.8), and assuming without loss of generality that $P = 1, A_{rcd} = 1, \rho_d = 0$, the force of each RCD is given by,

$$\begin{aligned} \mathbf{f}_1 &= \begin{pmatrix} \cos(\theta_s - \theta_1)(\sin(\theta_1) - \rho_1 \sin(\theta_s - 2\theta_1)) \\ 0 \\ \cos(\theta_s - \theta_1)(\cos(\theta_1) + \rho_1 \cos(\theta_s - 2\theta_1)) \end{pmatrix} \\ \mathbf{f}_2 &= \begin{pmatrix} \cos(\theta_s - \theta_2)(\sin(\theta_2) - \rho_2 \sin(\theta_s - 2\theta_2)) \\ 0 \\ \cos(\theta_s - \theta_2)(\cos(\theta_2) + \rho_2 \cos(\theta_s - 2\theta_2)) \end{pmatrix} \end{aligned} \tag{4.11}$$

where, $\rho_1, \rho_2 \in [0, 1]$ are the reflectivity coefficients of their respective RCD cells. A further assumption can be made by setting $\theta_2 = -\theta_1$ which reduces the number of variables for the problem by one. This assumption is desired as it leads to symmetry in the force authority about the angle θ_s. That is, the magnitude of the force authority for θ_s is the same as when $\theta_s' = -\theta_s$.

With the $\theta_1 = -\theta_2$ assumption, it is possible to compute the *nominal force* of this configuration. The nominal force is defined similarly to the normal force definition in the previous chapter, and it is the force produced by the configuration when $\theta_s = 0$, and the reflectivity coefficients are $\rho_1 = \rho_2 = 0.5$. This yields,

$$\mathbf{f}_{nom} = \begin{pmatrix} 0 \\ 0 \\ \cos(\theta_1) + 2\cos(\theta_1)^3 \end{pmatrix} \tag{4.12}$$

The maximum force happens when $\theta_1 = 0$, and the force equals zero when $\theta_1 = \pi/2$

as expected. The relative force produced by the two RCD cells is then given by,

$$\mathbf{f}^b_{rel} = \mathbf{f}_1 + \mathbf{f}_2 - {}^bR^I_y(\theta_s)\mathbf{f}_{nom} = \begin{pmatrix} f_{1,x} + f_{2,x} - \sin(\theta_s) f_{nom,z} \\ 0 \\ f_{1,z} + f_{2,z} - \cos(\theta_s) f_{nom,z} \end{pmatrix} \tag{4.13}$$

where the rotation matrix ${}^bR^I_y(\theta_s)$ transforms a vector pointing from the inertial frame to the body frame which in this case is a simple passive rotation about the y^b-axis. The reason for having ${}^bR^I_y(\theta_s)$ multiply the nominal force rather than just subtract it by the vector $\mathbf{f}_{nom}$ is to take into account that the force required to maintain an orbit is always pointing along the Sun-direction as described in Section 3.4.

To obtain the net force that can be generated along the z^b-axis, a constraint on ρ_1 and ρ_2 needs to be placed such that the net force along the x^b-axis is equal to zero. In other words, the constraint on ρ_1 and ρ_2 such that $f_{1,x} + f_{2,x} - \sin(\theta_s) f_{nom,z} = 0$ needs to be found. For this simple configuration, the condition is given by,

$$\rho_{1,x\ cond} = \frac{w_1 + \rho_2 w_2}{\sin(2\theta_s - 3\theta_1) - \sin(\theta_1)} \tag{4.14}$$

where,

$$\begin{aligned} w_1 &= 2\cos(\theta_1)\sin(\theta_s) + 4\cos(\theta_1)^3\sin(\theta_s) - 2\sin(2\theta_s)\cos(\theta_1) \\ w_2 &= \sin(2\theta_s + 3\theta_1) + \sin(\theta_1) \end{aligned} \tag{4.15}$$

The condition depends on the angle θ_s, and has a term that is linearly dependent on ρ_2 and another one that is purely a function of θ_s and θ_1. However, when the z^b-axis is aligned with the Sun axis and $\theta_s = 0$, the condition simplifies as $\rho_1 = \rho_2$. This is expected as in the special case $\theta_s = 0$ the forces produced by the cells will only be along the z^b-axis if their RCD reflectivity coefficients are the same.

Pluging in the condition in Equation (4.14) into Equation (4.13) to obtain the possible forces on the z^b-direction. This gives the equation

$$f_{rel,z} = \frac{n_1\rho_2 + n_2}{d_1} + q_1 \tag{4.16}$$

where,

$$
\begin{aligned}
n_1 &= -\sin(4\theta_1)(\cos(2\theta_s) + \cos(2\theta_1)) \\
n_2 &= -2\cos(\theta_s - \theta_1)\cos(\theta_s - 2\theta_1)\cos(\theta_1)\sin(\theta_s)(2\cos(\theta_1)^2 - 2\cos(\theta_s) + 1) \\
q_1 &= \cos(\theta_s - \theta_1)\cos(\theta_s) + \cos(\theta_s + \theta_1)\cos(\theta_s) - \cos(\theta_s)\cos(\theta_1)(2\cos(\theta_1)^2 + 1) \\
d_1 &= \sin(2\theta_s - 3\theta_1) - \sin(\theta_1)
\end{aligned}
\tag{4.17}
$$

Equation (4.16) was obtained using algebraic manipulators using the symbolic toolbox of MATLAB. When the angle $\theta_s = 0$ Equation (4.16) is simplified to

$$
f_{rel,z}|_{\theta_s=0} = (2\cos(\theta_1)^3 - \cos(\theta_1))(2\rho_2 - 1) \tag{4.18}
$$

The maximum range can then be obtained by substituting ρ_2 for one and zero, and subtracting the result, leading to a total range in the z^b-direction when $\theta_s = 0$ of,

$$
\text{range}(f_{rel,z}) = |4\cos(\theta_1)^3 - 2\cos(\theta_1)| \tag{4.19}
$$

where, $|\#|$ represents the absolute value of the function.

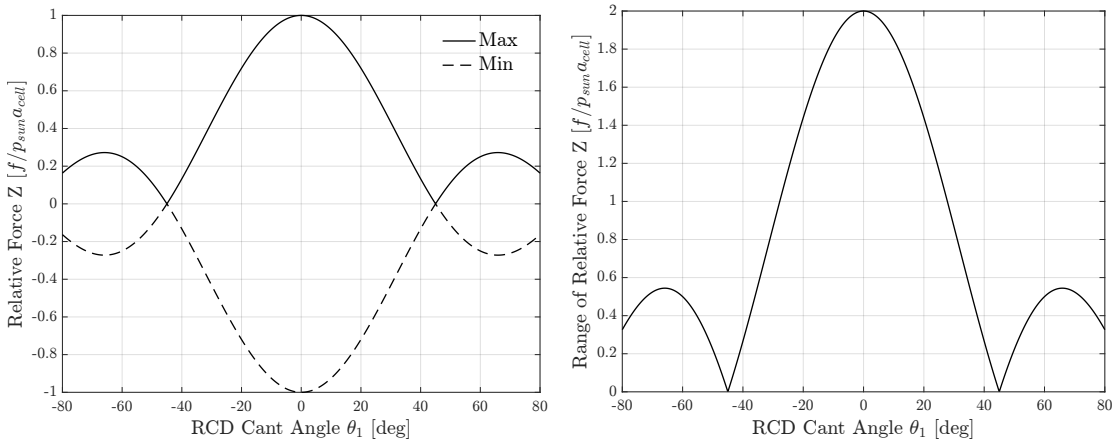

(a) Max and min z force

(b) Range z force

Figure 4-13: Relative z force capability as a function of RCD cant angle for two cells, two DOF optimization at $\theta_s = 0°$.

The maximum and minimum relative force, as well as its range from Equation (4.18) and (4.19), are plotted in Figure 4-13. Note that maximum ranges occur at

$\theta_1 = 0°$ and $\theta_1 = \pm 65.91°$. Furthermore, the range goes to zero when the cant angle is $\theta_1 = \pm 45°$. At this angle the coefficient dependent on ρ_1 and ρ_2 for f_1 and f_2, respectively, becomes zero leading to no possible force change by modifying the reflectivity coefficient.

The same process can be used to find the ranges along the x^b-direction by enforcing $f_{1,z} + f_{2,z} - cos(\theta_s) f_{z,nom} = 0$. For completeness, the condition that guarantees that the force in the z direction is zero is given by,

$$\rho_{1,z\ cond} = -\frac{w_3 \rho_2 + w_4}{\cos(2\theta_s - 3\theta_1) + \cos(\theta_1)} \tag{4.20}$$

where,

$$\begin{aligned} w_3 &= \cos(2\theta_s + 3\theta_1) + \cos(\theta_1) \\ w_4 &= \cos(3\theta_1) - 4\cos(\theta_1)\cos(\theta_s)^2 + 5\cos(\theta_1) \end{aligned} \tag{4.21}$$

The special case of $\theta_s = 0$ yields $\rho_{1,z\ cond} = 1 - \rho_2$. Plugging Equation (4.20) into Equation (4.13) yields the net force in the x^b-direction and is given by,

$$f_{rel,x} = \frac{n_3 \rho_2 + n_4}{d_2} \tag{4.22}$$

where,

$$\begin{aligned} n_3 &= -(2\sin(2\theta_1) + 2\sin(6\theta_1) - 2\sin(2\theta_s - 4\theta_1) + 2\sin(2\theta_s + 4\theta_1)) \\ n_4 &= \sin(2\theta_s) + 2\sin(2\theta_1) + \sin(4\theta_1) - \sin(2\theta_s - 2\theta_1) \\ &\quad - 3\sin(2\theta_s - 4\theta_1) + 2\sin(4\theta_s - 2\theta_1) - \sin(2\theta_s - 6\theta_1) + 2\sin(4\theta_s - 4\theta_1) \\ d_2 &= 4(\cos(2\theta_s - 3\theta_1) + \cos(\theta_1)) \end{aligned} \tag{4.23}$$

When θ_1 is equal to zero, the Equation (4.22) simplifies to,

$$f_{rel,x} = 2(2\rho_2 - 1)\sin(\theta_1)\left(\sin(\theta_1)^2 - 1\right) \tag{4.24}$$

The possible range as a function of θ_1 is simply,

$$\text{range}(f_{rel,x}) = |4\left(sin(\theta_1)^3 - sin(\theta_1)\right)| \tag{4.25}$$

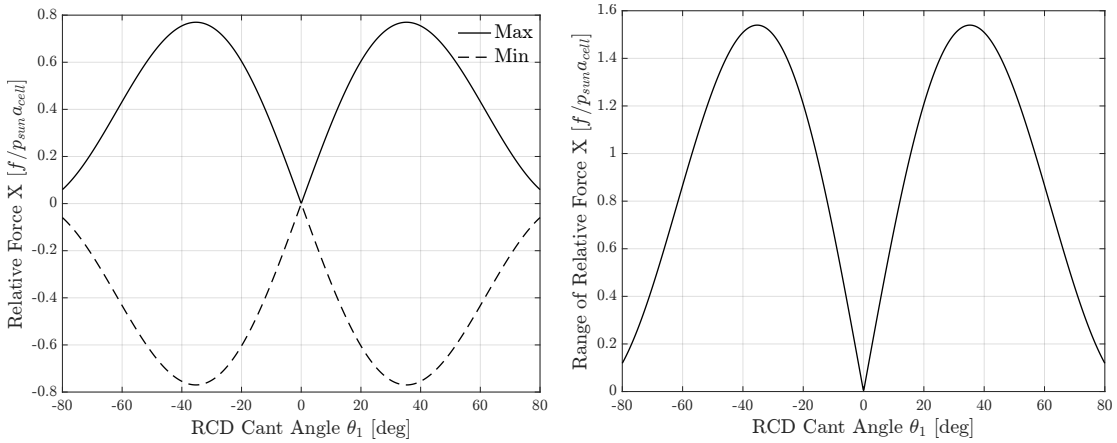

(a) Max and min x force

(b) Range x force

Figure 4-14: Relative x force capability as a function of RCD cant angle for two cells, two DOF optimization at $\theta_s = 0°$.

Similar to the z^b-direction, the possible x^b-force and the range can be plotted and are shown in Figure 4-14. The magnitude of the relative x-force is less than that of the z^b-force. Furthermore, the range of forces goes to zero when $\theta_1 = 0°$ and it is maximum at $\theta_1 = 35.26°$. Similar to the plot for the z^b-direction, there exists symmetry about the vertical axis, and about the horizontal axis. This is expected due to the symmetry argument earlier.

Having the ranges of relative forces for both the x and z direction, we can compute the authority at $\theta_s = 0$ over cant angles ranging from $[-80°, 80°]$ by multiplying them together as in Equation (4.7). Figure 4-15 shows the authority function. The horizontal axis represents the change in the RCD cant angle, while the left vertical corresponds to the authority of that RCD configuration. The solid black line is the authority function and it is associated with the left vertical axis. Alongside the authority function, the ranges of the relative forces z^b and x^b in Figure 4-13b and 4-14b, respectively, were plotted in solid and dashed light blue with the values of the function given by the right vertical axis. From here, it is clear that two absolute

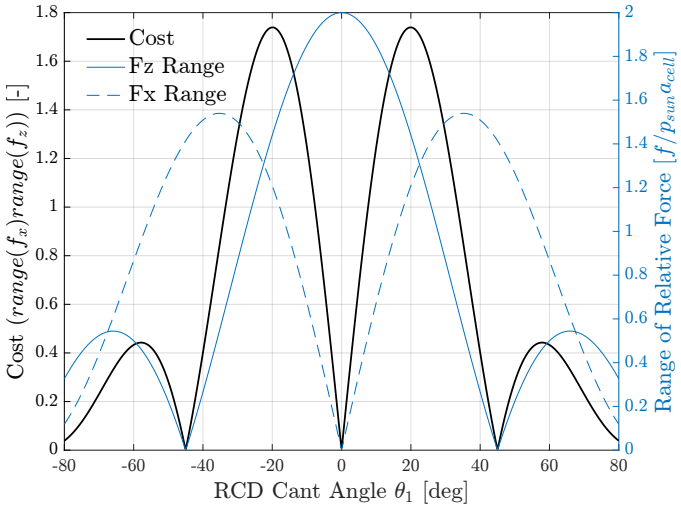

Figure 4-15: RCD configuration authority function as a function of RCD cant angle, θ_1 at Sun angle $\theta_s = 0°$. The ranges of the relative force in x and z are also plotted on the right y-axis

maximum points exist, at $\theta_1 = \pm 19.94°$. Two additional local maximum authority exit when $\theta_1 = \pm 57.89°$. This plot additionally helps show that when θ_1 is close to zero, the authority function has a steep decline due to the range in the x-force quickly going to zero even though the controllability about the z-direction is maximum. Multiplying the ranges ensures that there always exists controllability along both axis.

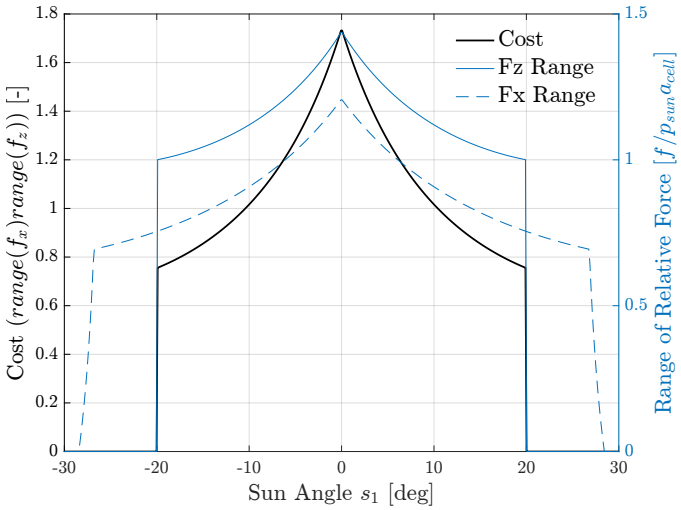

Figure 4-16: RCD configuration authority function as a function of Sun Angle, θ_s at RCD cant angle $\theta_1 = 19.94°$. The ranges of the relative force in x^b and z^b are also plotted on the right vertical axes.

In the previous analysis, the Sun angle, θ_s was set to zero, however, as mentioned

in Section 3.3, the control envelope dramatically changes with the Sun direction. To observe this, the optimal cant angle, $\theta_1^* = 19.94°$ is selected for the RCD configuration and the Sun angle is varied. The authority function is plotted in Figure 4-16, where the horizontal axis indicates the change in the Sun angle. Similar to Figure 4-15 the solid black line represents the authority function, while the thin solid and dashed blue line represent the range in the relative force for z^b and x^b, respectively. The maximum authority for the optimization occurs at $\theta_s = 0°$, as expected as this is the angle where it is easiest to produce the required nominal force. As the Sun angle increases, the authority function monotonically decreases until it hits a Sun angle of $\theta_s = 19.94°$. At this Sun angle, there is no solution for the $\rho_{1,x\ cond}$ in Equation (4.14) in the range [0, 1] which means that there is no way to obtain a pure net force along the z^b-axis. Since the authority function is the product of the ranges, the authority at this angle and greater is zero, even though the range in the x^b-direction continues to be nonzero.

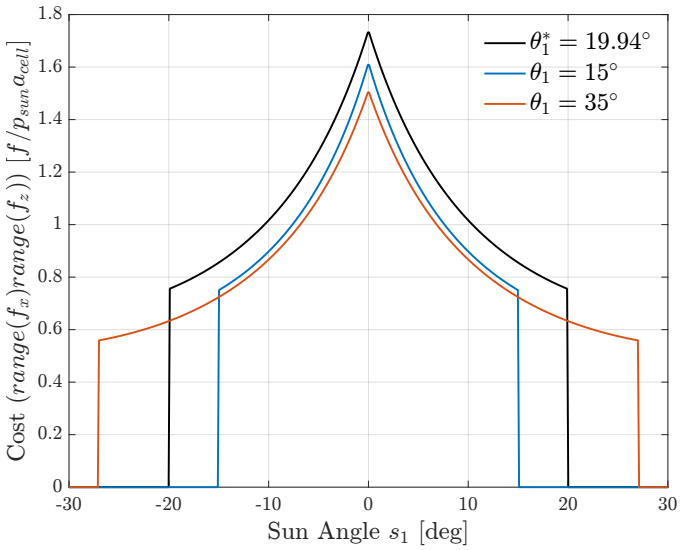

Figure 4-17: RCD configuration authority function as a function of Sun Angle, θ_s at RCD Cant angle $\theta_1 = 19.93°$. The ranges of the relative force in x and z are also plotted on the right y-axis.

Figure 4-17 shows the same authority function as a function of Sun angles for three different RCD cant angles. From here we see that as the cant angle increases the region for which you have control authority increases, however, the maximum

authority decreases relative to the optimal cant angle $\theta_s^* = 19.93°$. Thus, a larger cant angle results in an *increase* in operational Sun angles but it lowers the *maximum* authority at a nominal attitude of $\theta_s = 0°$. Therefore, two authority functions can be utilized for RCD configurations, one that maximizes the maximum authority similar to Equation 4.7, and one that takes into account the operational angles. For the two degrees of freedom case, the two objectives can be stated as,

$$\begin{aligned} c_{opt}(\theta_1) &= \max \quad \text{range}(f_z)\text{range}(f_x) \\ c_{int,opt}(\theta_1, \theta_s) &= \max \quad \int c_{opt}(\theta_1, \theta_s) d\theta_s \end{aligned} \tag{4.26}$$

where the second objective seeks to maximize the area under the curve of the authority function, which is akin to measuring the authority optimization over the entire operation region for an RCD configuration. These competing objectives lead to a case of multi-objective optimization. An strategy to find the non-dominant set of solutions for multi-objective optimization is by obtaining the Pareto front.

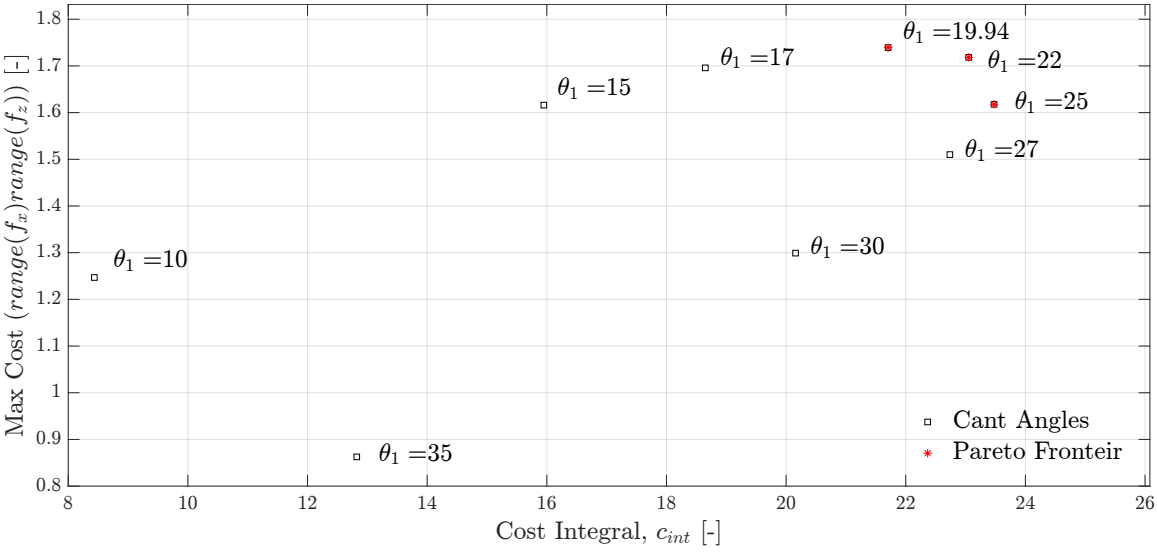

Figure 4-18: Pareto Front for the two DOF RCD optimization placement. The black squares represent dominated solutions for configurations at a given RCD cant angle, and the red asterisk corresponds to the non-dominated solutions, i.e. the Pareto front.

Figure 4-18 shows the Pareto front for the two DOF case. The utopia point for the multi-objective optimization is the top right corner of the plot. The horizontal

axis represents the value for the authority integral, while the vertical axis represents the maximum authority value when the Sun angle is zero. In the plot, nine points are shown each representing an individual RCD configuration where the RCDs were canted at the angles in degrees shown in the text next to the points. The three cant angles 19.94°, 22°, and 25° lay on the Pareto Frontier and represent the non-dominated solutions. Values either below or above those angles have lower integral authority *and* nominal authority.

This subsection covered the optimization of RCD placement for the two DOF case. The analysis produced by this example case gave various insights into the main RCD optimization for the full six DOF case, namely,

1. Symmetry in RCD placement yields symmetric control authority
2. A small RCD cant angle increases force authority along the axis aligned with the Sun direction but reduces (or eliminates for $\theta_1 = 0°$) authority about normal to the Sun direction
3. An increase in RCD cant angle allows for control authority over larger Sun angles
4. There exists a competing authority function between the maximum authority that can be produced at the nominal Sun direction and the integral authority over the range of Sun angles

These insights will be utilized for the three DOF case and six DOF case.

4.2.2 Optimization for Three DOF RCD Configuration: Four Cell Case

The next problem corresponds to a three DOF case, namely the positional x^b and z^b directions, and the torque about the y^b-axis. A simplified model for this configuration is shown in Figure 4-19. Each RCD is represented by a solid blue inclined line with a corresponding black arrow normal to that surface. In contrast to the two DOF case,

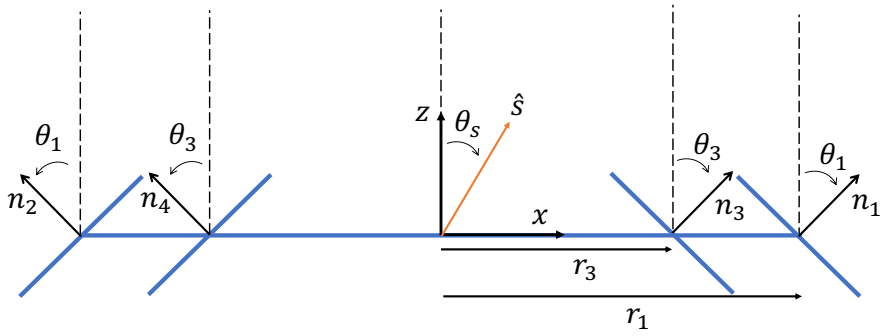

Figure 4-19: Notional satellite with four reflective control devices for three degrees of freedom control. Each RCD cell is represented by the inclined blue line. Additionally, the Sun's direction is represented by the orange arrow.

the location along the x^b-axis of each of the cells matters in terms of the lever arm for the torque about the y^b-axis, and thus additional variables indicating the position of the cells are shown as $r_{\#}$.

The same symmetry argument as in the two 2 DOF case was used for this case, enforcing $\theta_2 = -\theta_1$ and $\theta_4 = -\theta_1$, and $r_2 = -r_1$ and $r_4 = -r_3$. Furthermore, the same process as in the two DOF case was employed to find the relative force and torque. Namely, a set of conditions on the reflectivity coefficients was found such that the force or torque in the direction that is not being used to compute the range is set to equal that of the nominal force. For example, when finding the range in the x^b-direction, the relative force in the z-direction was set to zero, $f_{1,z} + f_{2,z} + f_{3,z} + f_{4,z} - \cos(\theta_s) f_{nom,z} = 0$, and the torque was set to zero, $\tau_{1,y} + \tau_{2,y} + \tau_{3,y} + \tau_{4,y} = 0$. For the z-direction the constraints where $f_{1,x} + f_{2,x} + f_{3,x} + f_{4,x} - \sin(\theta_s) f_{nom,z} = 0$, and $\tau_{1,y} + \tau_{2,y} + \tau_{3,y} + \tau_{4,y} = 0$. Finally for the torque about y the constraints where $f_{1,x} + f_{2,x} + f_{3,x} + f_{4,x} - \sin(\theta_s) f_{nom,z} = 0$ and $f_{1,z} + f_{2,z} + f_{3,z} + f_{4,z} - \cos(\theta_s) f_{nom,z} = 0$. For this case, the optimization function for the max authority and max integral was defined as

$$\begin{aligned} c_{opt}(\theta_1, \theta_3) &= \max \quad \text{range}(f_x)\text{range}(f_z)\text{range}(\tau_y) \\ c_{int,opt}(\theta_1, \theta_3, \theta_s) &= \max \quad \int c_{opt}(\theta_1, \theta_3, \theta_s) d\theta_s \end{aligned} \tag{4.27}$$

where for this case an additional variable on the authority function corresponding to the cant angles for RCD 3 and 4 was added. To illustrate how the choice of angles θ_1

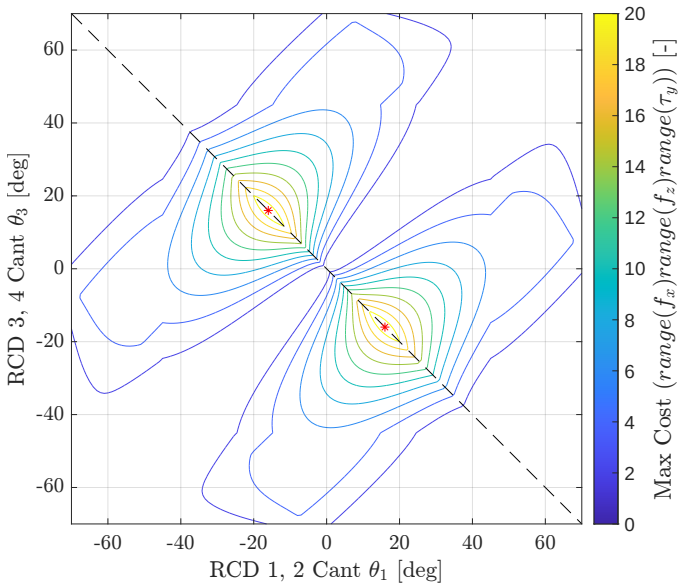

Figure 4-20: Four RCD cells, 3 DOF optimization over nominal Sun direction

and θ_3 influence the maximum authority, a surface contour was generated in Figure 4-20. The surface was obtained by creating a meshgrid of θ_1 and θ_3 angles and then computing the ranges for f_x, f_z, and τ_y for each combination of RCD cant angles. For this analysis, it was assumed. that RCD 1 and 3 were placed along the same direction with the same magnitude of the lever arm. RCD 2 and 4 were similarly placed with the same lever arm, but in opposite directions than RCD 1 and 3. The horizontal axis represents the value for θ_1 in degrees, the vertical axis is the value of θ_3 in degrees, and the color represents the maximum authority at the nominal Sun direction. Alongside the plot, a black dashed line with a slope of $-\theta_1$ was plotted. The surface has symmetry along this axis, and by looking at the contour values along the dashed line we see a resemblance of Figure 4-15. For example, the values are zero as you get close to the origin and increase to a maximum and subsequently fall off as the angles increase. The maximum points were plotted with red asterisks and are located at $(\theta_1, theta_3) = \pm(16°, -16°)$. Due to the symmetry, this indicates that for a given θ_1, the optimal max authority angle for θ_3 is equal and opposite.

Additionally, the three DOF case shares the same behavior as in the 2 DOF in that larger angles have lower max authority but have higher authority over larger Sun angles. To see this behavior two RCD configurations were plotted in Figure 4-21.

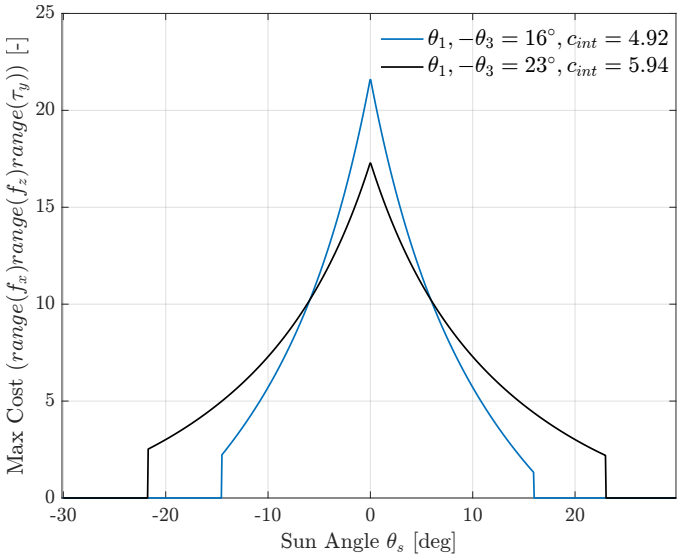

Figure 4-21: Four cell RCD configuration authority as a function of Sun Angle, 3 DOF case

The horizontal axis represents the Sun angle, θ_s, and the vertical axis shows the authority of the ranges of f_x, f_z, and τ_y at that current Sun angle. A configuration with angles $(\theta_1, \theta_3) = (16°, -16°)$ is shown in the solid blue line. This configuration corresponds to one of the maximum points in Figure 4-20. The black line corresponds to a configuration with $(\theta_1, \theta_3) = (23°, -23°)$. This configuration has a higher Sun angle for which there exists a non-zero level of control authority about all axis. Another similarity with the 2 DOF case is that the point at which the authority goes to zero equals the cant angle of the RCD configuration.

Figure 4-21 also highlights an important aspect of multi-objective optimization. For example. if the telescope was only to operate at Sun angles less than 7° then the 16° degree configuration would be better since it has higher operation control over all the angles. However, if the telescope needs to operate at Sun angles of at least ±20°, then only the 23° configuration meets this requirement.

The Pareto front for the RCD 3 DOF Configuration: multi-objective case in Equation (4.27) is shown in Figure 4-22. The Pareto plot was generated by evaluating RCD configurations at various θ_1, θ_3 angles as well as changing the lever arm r_1, and r_3 with the constraint that both $|r_1| < 1, |r_3| < 1$. Each solution is represented by a black dot in the figure. The configurations closer to the Pareto front correspond to

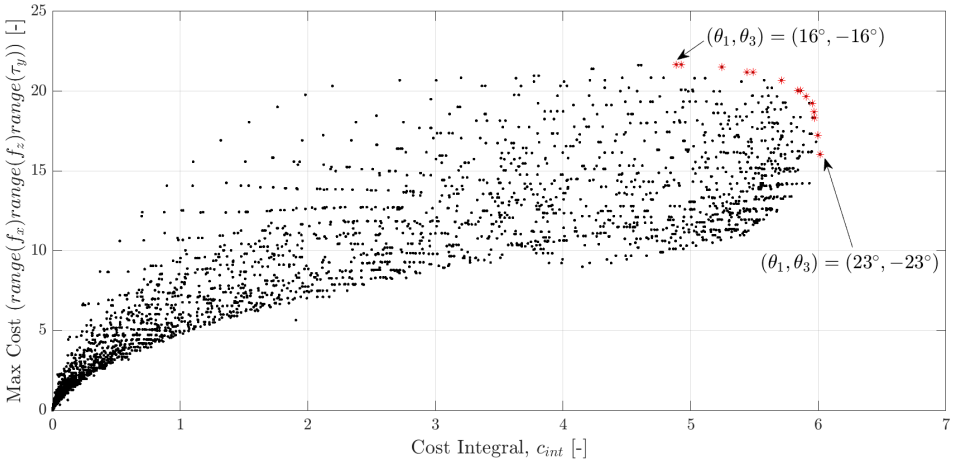

Figure 4-22: Pareto front for the three DOF RCD Optimization placement. The horizontal axis represents the integral authority of the configuration over multiple Sun directions, and the vertical axis represents the authority at the nominal Sun direction. Red asterisks correspond to the Pareto Front. Utopia point is in the upper right corner

instances in which $r_1 = r_3$. The solutions in the Pareto front are the configurations where $\theta_1 = -\theta_2$ and angles between 16° and 23°. The Pareto front configurations are shown by red asterisks.

The RCD placement optimization for three DOF looks very much to that of the two DOF as expected. There exist similar arguments of symmetry that are applied on this case. Namely, RCD 2 is a mirror about the z-axis of RCD 1, and RCD 3 and 4 are a mirror of each other. The other important takeaways that were used for the full six DOF case was,

1. Larger lever arm leads to an increase in authority, thus, the RCDs must be placed with the maximum lever arm as possible

2. The values in the Pareto front all have the same magnitude of cant angle

3. Similar to the 2 DOF case, the larger the cant angle leads to control over a larger span of Sun angles

4.2.3 Optimization for Six DOF Configuration: Six-Plus Cell Case

This subsection presents the RCD cell optimization for the full six degrees of freedom case. As mentioned before, this case requires at least six RCD cells in any configuration. The insights gained from the two and three DOF cases were used to aid in the optimization scheme for this case.

The description and variable convention of RCD cells for 6 DOF is shown in Figure 4-23. At the center of the figure lies the body frame shown in medium-thickness black

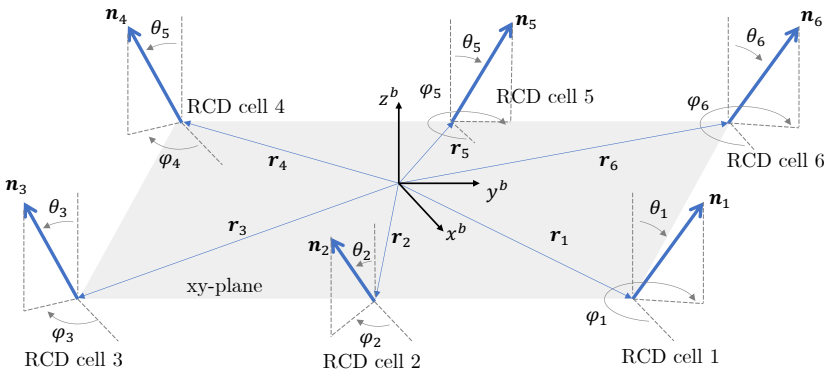

Figure 4-23: Notional six-cell RCD configuration. RCDs are assumed to lie on the xy-body frame. Each normal vector to the cell is shown in a thick blue arrow. The body frames are also shown in the figure.

arrows. The xy^b-plane is shown with the light gray parallelogram for reference. Each RCD has four variables associated with it: the vector normal to the surface of the cell (the surface is not pictured for the sake of clarity) given by $\mathbf{n}_{\#}$, the vector from the frame origin to the location of the RCD, $\mathbf{r}_{\#}$, the cant angle $\theta_{\#}$, and the azimuth angle $\phi_{\#}$. The $\#$ symbol indicates the ID of the corresponding cell. The cant angle is defined as the angle of the normal vector of the cell relative to the z^b-axis with possible values between $(0, 90°)$. The azimuth angle corresponds to the angle measured from the x^b-axis to the xy^b plane projection of the normal vector. The azimuth angle can vary between $(0, 360°)$.

As mentioned at the start of the section, a large number of continuous variables are needed for the optimization, and it is expected that there exist many local maxima

as was shown in the 2 DOF case. Furthermore, the large number of variables hinders the ability to solve the optimization analytically. Thus, the main strategy utilized for this case relied on providing good initial solutions for the optimizer to reduce the possibility of the optimizer getting stuck at a local maximum. These initial solutions were guided by the insights gained from the previous schemes, namely that the initial guess had a symmetric aggregate RCD configuration, the RCDs had the highest possible lever arm, and the cant angle for all RCD cells was between $(10°, 30°)$ and equal to each other.

The multi-objective authority function used for the optimization was given by,

$$\begin{aligned} c_{opt}(\boldsymbol{\theta}, \boldsymbol{\phi}, \boldsymbol{r}) &= \max \quad \prod_{i=1}^{3} \text{range}(f_i)\text{range}(\tau_i) \\ c_{sum,opt}(\boldsymbol{\theta}, \boldsymbol{\phi}, \boldsymbol{r}, \hat{\boldsymbol{s}}) &= \max \quad \sum_{i=1}^{n_{sun}} c_{opt}(\boldsymbol{\theta}, \boldsymbol{\phi}, \boldsymbol{r})|_{\hat{\boldsymbol{s}}} \end{aligned} \tag{4.28}$$

where, unlike in the two or three DOF sections, the c_{int} was changed to a sum of the authority at various Sun directions rather than integral. This was done to reduce the computational authority of evaluating a single RCD configuration. The Sun direction was selected to be three sets of ten equally spaced angles around the z^b-axis each with an elevation of 5°, 10°, and 15°.

The solver for the Pareto Front was MATLAB's gamultobj function [135]. The solver uses a modified genetic algorithm to find solutions that lie in the Pareto front of the multi-objective authority function. As an example, an eight-cell RCD configuration was selected for the optimization. This number of cells was chosen not only because it is greater than the minimum number of cells required, but also because it represents a natural extension of the three DOF case by having four extra RCDs for the other axis. The solution on the Pareto front for the optimization only varied in terms of the cant angle. This is expected as we saw in the three DOF that the cant angle was the main driver of values in the Pareto front. Each configuration shared the same azimuth angle as well as position in x and y. The values shared are shown in Table 4.1. Note that for each RCD cell, the norm of its position was one indication

that the cell has the maximum possible lever arm, as expected. The values of the cant

Table 4.1: Shared RCD eight cell configuration values in the Pareto front.

Cell ID	**Azimuth ϕ**	$\mathbf{r_x}$	$\mathbf{r_y}$
1	135	0.71	0.71
2	45	0.71	-0.71
3	315	-0.71	-0.71
4	45	-0.71	0.71
5	225	0.71	-0.71
6	225	-0.71	0.71
7	315	0.71	0.71
8	135	-0.71	-0.71

angles in the Pareto Front are shown in Table 4.2. Similar to the simplified problem, as the cant angle increases the value for the integral authority increases while the maximum authority decreases.

Table 4.2: Pareto Front solutions for eight cell configuration.

Cant Angle θ_1	**Sum authority** $\mathbf{c}_{sum}$ $[-]$	**Max authority** $\mathbf{c}_{max}$ $[-]$
20.00	1.70e+04	5.39e+03
20.63	1.75e+04	5.36e+03
21.45	1.81e+04	5.28e+03
22.26	1.83e+04	5.15e+03
23.00	1.84e+04	4.99e+03

An example of an optimal solution in the 6 DOF Pareto Front is shown in Figure 4-24. Each blue semi-transparent disk represents an RCD cell and a black arrow represents the normal vector defined by the cant and azimuth angles. The overall configuration has a circular symmetry about the z^b axis. Additionally, the RCDs are placed on top of each other in pairs. This behavior was also seen in the three DOF case where the optimal position of the cells was to be placed on top of one another with opposite θ_1, and θ_3 angles.

One of the main drawbacks of the optimal configurations shown in Table 4.2 is that it requires pairs of RCD cells to be placed on top of one another. Given that from an engineering point of view, this is impossible, a new constraint was added to the multi-objective optimization function that represented the inability of two cells to be placed on top of one another. The constraint was defined by a new angle ψ that defined the half angle from where two RCD can be placed from one another. For example, the same RCD configuration in Figure 4-24 is shown in Figure 4-25.

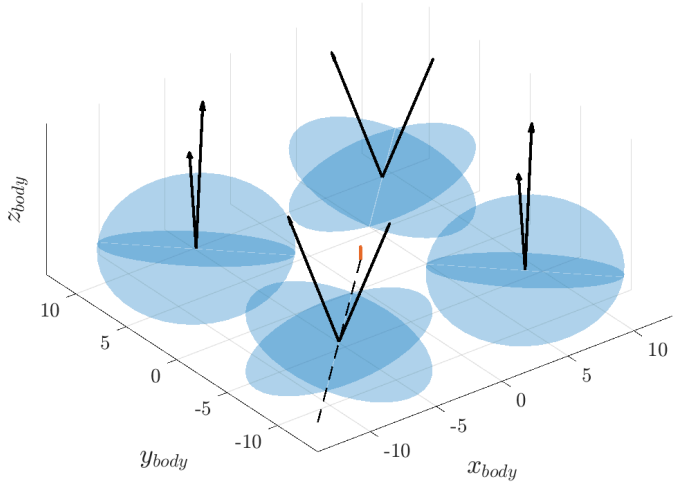

Figure 4-24: Example of 8-cell configuration on the Pareto front. Each of the cells has a black line representing the normal vector of that cell.

Again, in this figure, the magenta circles correspond to each of the cells. The angle ψ represents the half-angle between two adjacent cells. For example, for a value of $\psi = 10°$, and an RCD cell with an area of 10 $[m^2]$ with a cant angle of 20°, a lever arm greater than 9.66 $[m]$ is required for the RCDs to not intersect with each other.

Unfortunately, as the angle ψ increases the values on the Pareto Front decrease. Figure 4-26 shows this behavior. The horizontal axis represents the sum of authoritys over different Sun directions, and the vertical axis represents the maximum authority at the nominal Sun direction. The optimal Pareto Front without any RCD location constraints and given by Table 4.2 are shown in the blue asterisks at the top right of the plot. Plotted alongside is the Pareto front for different configurations when the position constraint angle, ψ increases. The red, yellow, and magenta asterisks correspond to the Pareto Front for $\psi = 1°,\ 5°$, and 10°, respectively. Additionally, other non-optimal configurations for the constraint of $\psi = 10°$ are shown by the grey dots.

It is possible to find a bound on the sum and max authority of all possible RCD configurations at a given ψ angle. All the values on the Pareto plot for $\psi = 10°$ share

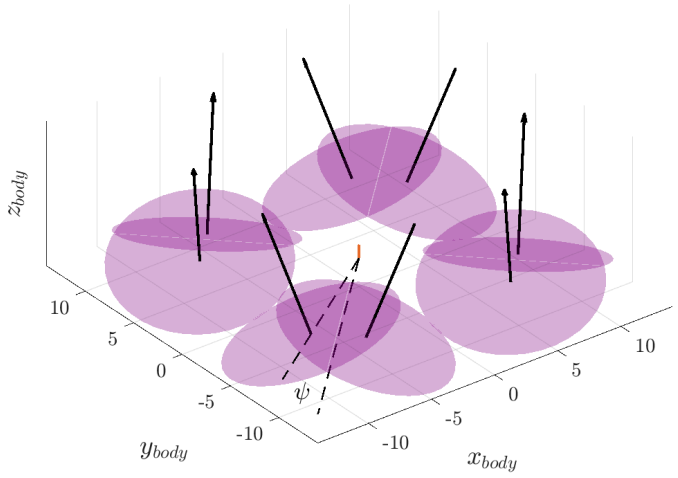

Figure 4-25: Example of 8-cell configuration on the Pareto front with a $\psi = 10°$ constraint on the position between two adjacent RCDs. Each of the cells has a black line representing the normal vector of that cell.

the same azimuth and position angles as in Table 4.3[2]. However, the values on the Pareto plot have a RCD cant angle between $(20°, 23°)$. The values for the Pareto plot

Table 4.3: Shared RCD eight cell configuration values in the Pareto front for $\psi = 10°$.

Cell ID	**Azimuth ϕ**	$\mathbf{r_x}$	$\mathbf{r_y}$
1	125	0.57	0.82
2	35	0.82	-0.57
3	305	-0.57	-0.82
4	35	-0.57	0.82
5	235	0.57	-0.82
6	235	-0.82	0.57
7	325	0.82	0.57
8	145	-0.82	-0.57

are shown in Table 4.4. If the cant angle is greater than 23° the RCD configuration has a reduction in both maximum and sum authority, and is the lower bound of the Pareto plot as shown by the upside down magenta triangles in Figure 4-26. When the cant angle is less than 20° the same behavior happens however, they form the upper bound of the Pareto plot as shown by the right side up magenta triangles in the figures. For both of these cases the same shared values in Table 4.3 were used.

[2]Note that given the circular symmetry of the configurations, it is possible to find an infinite number of configurations with the same performance by rotating the azimuth, and position angles about the z^b-axis.

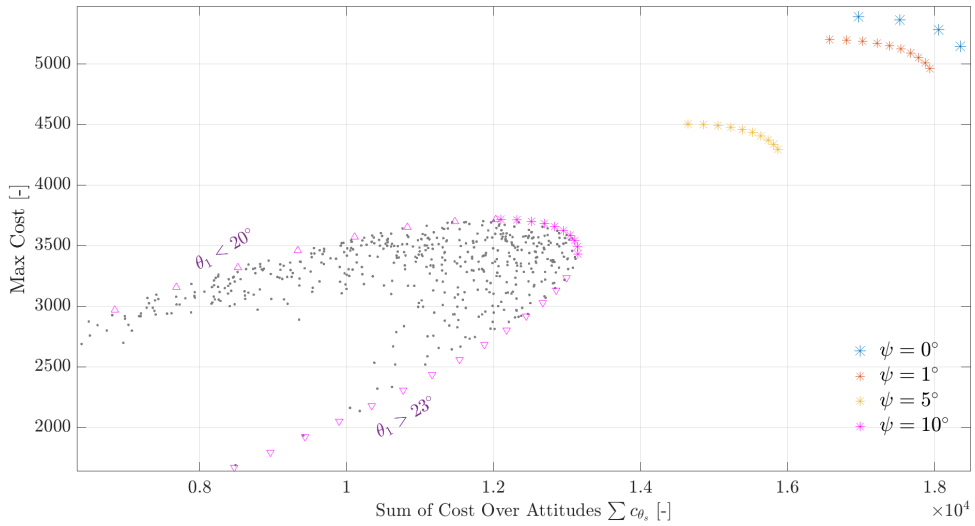

Figure 4-26: Eight RCD placement Pareto plot. The horizontal axis represents the integral authority of the configuration over multiple Sun directions, and the vertical axis represents the authority at a nominal attitude. Utopia point is in the upper right corner

Thus, it is possible to analytically determine the boundary of the Pareto plot and the Pareto frontier for any ψ angle for the eight-cell case. Similar results may be obtained for RCD configuration with a higher or lower number of cells.

Table 4.4: Pareto Front solutions for eight cell configuration with $\psi = 10°$ constraint.

Cant Angle θ_1	**Sum authority** $\mathbf{c}_{sum}$ $[-]$	**Max authority** $\mathbf{c}_{max}$ $[-]$
20.00	1.210e+04	3.718e+03
20.50	1.242e+04	3.708e+03
21.00	1.269e+04	3.682e+03
21.50	1.289e+04	3.641e+03
22.00	1.304e+04	3.586e+03
22.50	1.312e+04	3.516e+03
23.00	1.314e+04	3.434e+03

This section presented the methodology used to find the optimal placement of RCD configurations that maximized the control authority over the nominal attitude and over multiple Sun directions. The results showed that an optimal cant angle for the RCDs exists for which the configuration maximizes the authority of the force and

torque envelopes. Additionally, it was found that by increasing the cant angle, to an extent, it is possible to increase the operational envelope for the RCD at the authority of a reduction in the maximum control envelope at the nominal attitude. This analysis can help in the design of satellites by figuring out the optimal placement of RCD cells to ensure the satellite is able to have full orbit maintainance and attitude control.

4.3 Disturbance analysis for RCDs

This section goes over types of disturbances that affect satellites with RCDs as actuators. The main disturbances analyzed are due to Sun direction and orbit determination error. The section does not go over an exhaustive list of uncertainties that may be present, however, it still provides an initial analysis of how much of the RCDs actuators have to be dedicated to disturbance rejection.

4.3.1 Sun Direction Error

The RCD force model (Equation 3.9) relies on knowledge of several parameters inherent to the configuration such as the position of each RCD cell, the normal vector of the cell, and its area. Additionally, two parameters that are independent of the configuration, namely the solar radiation pressure at SEL2, p_{sun}, and the Sun direction $\hat{\mathbf{s}}$ are present. In reality, all of these parameters, and the model itself are prone to uncertainty and errors. This section covers an example of how to analyze the source of error from these parameters by focusing on the Sun direction vector.

The Monte Carlo method was utilized in order to determine how a given magnitude of Sun direction error translated into torque and force error for an RCD configuration. The simulation consisted of selecting a value of Sun direction error standard deviation (sd), $\sigma_{sun,err}$, which was defined as the expected standard deviation of an angle error between the true Sun direction and the estimated Sun direction. Then, N Sun directions were sampled from a uniform distribution for azimuth and elevation angles. Additionally, N RCD $\boldsymbol{\rho}_s$ vectors were also sampled from a uniform distribution. The force and torque from the $\boldsymbol{\rho}_s$ were computed using the true Sun direction,

as well as from a randomly generated Sun direction error that was sampled from a normal distribution with a standard deviation given by $\sigma_{sun,err}$. The error between the computed forces and torques from the truth and estimated Sun direction was computed along with its standard deviation. This analysis was repeated for different Sun direction error sd values.

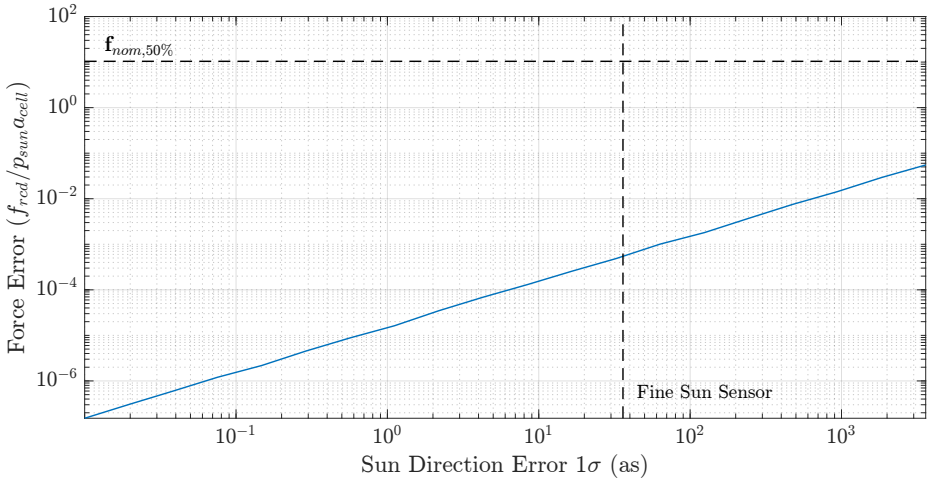

(a) Force Error

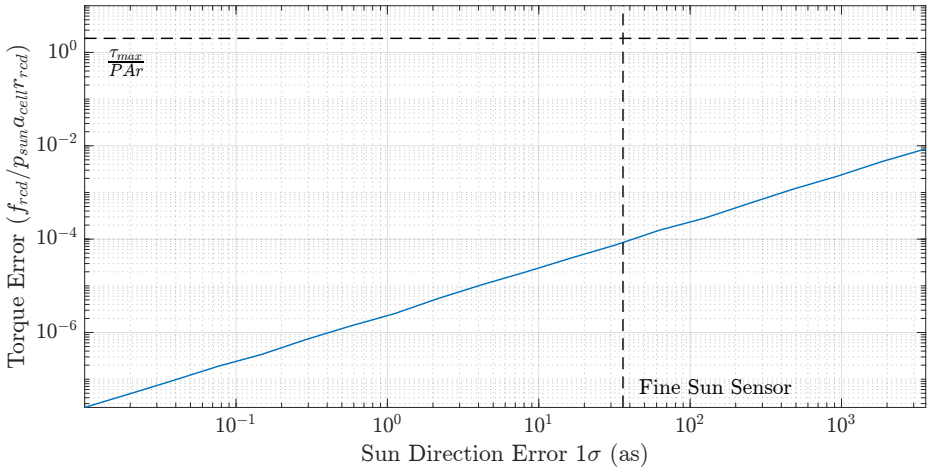

(b) Torque Error

Figure 4-27: Expected force and torque error from commanded output for a given standard deviation of Sun direction error.

Figure 4-27 shows the result of the Monte Carlo simulation. The values for the force and torque were normalized as a function of the Sun radiation pressure, p_{sun}, and RCD cell area a_{cell}. As the expected standard deviation of the Sun direction error increases, the force and torque error increases with it. In Figure 4-27a, the nominal

force was shown for reference while the maximum torque is shown in Figure 4-27b both in a black horizontal dashed line. For reference, the accuracy of a Commercial-Of-The-Shelf (COTS) fine Sun sensor for small satellites is given by the black vertical dash line[3]. Overall, the force and torque error produced by a Sun sensor error is at least two orders of magnitudes lower than the range of forces produced by the RCD configuration. Furthermore, the error can be diminished with an improved Sun sensor.

Similar analysis can be performed for errors from uncertainty in RCD placement location, uncertainty in RCD mounting angle, and the effective area can be performed. Furthermore, as solar activity changes the solar radiation pressure at SEL2 varies with respect to time, which may cause a source of error in the output force and torque from the configuration, and may even require recomputation of the nominal halo orbit.

4.3.2 Orbit Determination Error

One of the main challenges in performing orbit maintenance at SEL2 is that halo orbits are inherently unstable and any small errors if left unchecked move a satellite from its nominal orbit into a drift orbit. To overcome this challenge, there exists a need for high certainty in the position and velocity of the satellite.

Uncertainty in the knowledge of environmental variables such as the gravitational parameter, μ_{SE}, the solar radiation pressure, p_{sun}, as well as errors in measurements from range and tracking systems, contribute to errors in the orbit determination (OD) of satellites in SEL2 [136]. This OD error causes the satellite to slowly drift from a nominal orbit and in turn, requires a control input to return the satellite to the nominal halo orbit. The analysis presented in this section utilized commonly used OD error magnitudes from literature to determine the control magnitude needed to overcome these disturbances relative to the operational envelope of RCDs.

Improvement and analysis of orbit determination error in SEL2 is a rich field in the literature. Beckman presented results of different missions operating in the Lagrange

[3]Red Wire Space Fine Sun Sensor with 0.01° accuracy: `https://redwirespace.com/products/fine-sun-sensor-50/`

points and presented a novel algorithm of enhancing ground-based methods with celestial navigation for improvement in OD [137]. Gordon analyzed the effects of input error levels on the output OD error [136]. More recently, the JWST conducted several analyses on the impact of OD errors and its effect on correction maneuvers as part of the telescope's checkout procedure [138, 139]. Example values from these papers are given by Table 4.5. The values from Gordon were taken as an example

Table 4.5: Example of orbit determination errors for satellites in SEL2

Source	$\mathbf{x}^s$ $[km]$	$\mathbf{y}^s$ $[km]$	$\mathbf{z}^s$ $[km]$	$\dot{\mathbf{x}}^s$ $[mm/s]$	$\dot{\mathbf{y}}^s$ $[mm/s]$	$\dot{\mathbf{z}}^s$ $[mm/s]$
Gordon [136] (1σ)	1.46	2.65	4.81	1.40	1.85	2.49
Beckman [137] (1σ)	6.7	2.3	1.8	2.9	0.4	0.6
Yoon [139] (1σ)	0.6	6.55	9.95	2.1	5.3	5.4

of OD error levels for this analysis due to its extensive discussion on the impact of different filter parameters. Nevertheless, this is done without loss of generality, and additional analysis can be done from different sources of OD error.

The expected acceleration produced by this error can be computed by multiplying the OD state error by the translational feedback control law matrix k_{orb},

$$\delta\mathbf{a}_{OD,err} = K_{orb}\delta\mathbf{x}_{OD,err} \tag{4.29}$$

where $\delta\mathbf{x}_{OD,err}$ is the state error where each element is taken from a normal distribution with a standard deviation equal to the error values from Gordon in Table 4.5. The resultant standard deviation of the acceleration vector can then be computed by taking the standard deviation of $\delta\mathbf{a}_{OD,err}$ over many random values for the state error. In this analysis, one million randomly distributed values for $\delta\mathbf{x}_{OD,err}$ were taken to then compute the standard deviation for $\delta\mathbf{a}_{OD,err}$. The resultant value represents the standard deviation of the acceleration the controller would request in order to eliminate the estimated state error and bring the satellite to the nominal orbit. In other words, at each controller time step the magnitude of acceleration requested by the controller only due to OD error would have an expected a standard deviation of $\text{std}(\delta\mathbf{a}_{OD,err})$.

Figure 4-28 shows the magnitude of the expected acceleration due to OD distur-

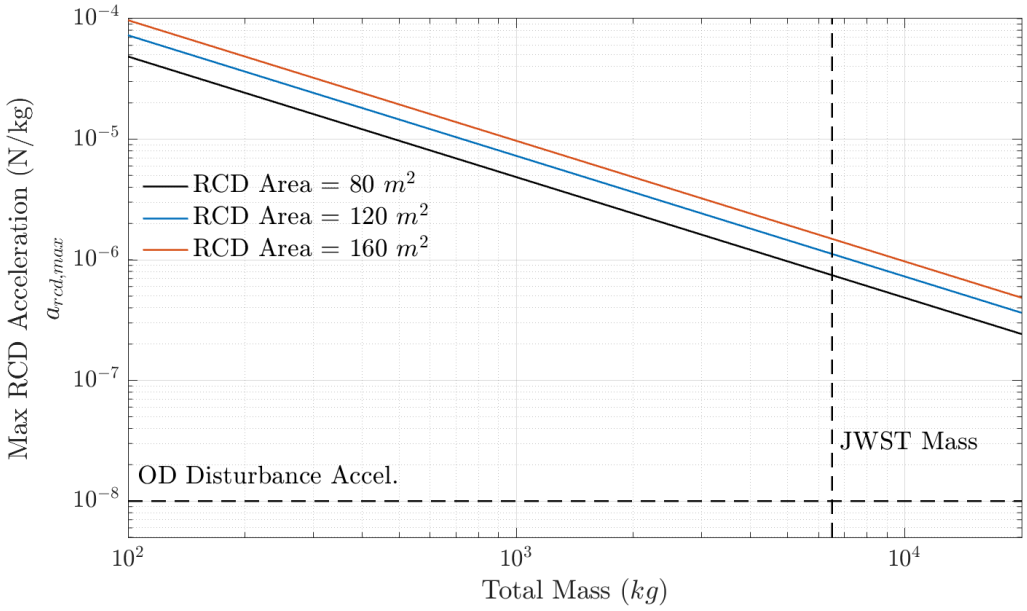

Figure 4-28: Comparison between maximum RCD acceleration and expected OD error disturbance acceleration as a function of satellite's mass.

bance value compared to the maximum acceleration that can be produced by RCDs as a function of the satellite's mass. The values are plotted on a logarithmic scale. The solid lines represent the *total* area for a given configuration. An eight-cell configuration is assumed so the black, blue, and red lines represent individual RCD cell areas of 10 m^2, 15 m^2, and 20 m^2, respectively. The expected acceleration due to OD error is shown in the horizontal dashed line and it is constant as a function the satellite's mass. The acceleration produced by the RCDs decreases linearly as a function of the satellite's total mass. Additionally, plotted for reference only is the total mass of the JWST telescope in the black dashed vertical line. For example, for a JWST-class telescope, the acceleration needed to overcome the OD error would correspond to less than 1% of the maximum possible force produced by an eight-cell RCD configuration with a total RCD area of 80 m^2.

Extending this result, an analysis is made to compare a satellite's mass and total RCD area with the force produced by OD error. This could aid in quickly sizing satellites where a certain percentage of actuator control has to be dedicated to this source of error. In Figure 4-29 the satellite's mass in kilograms is plotted against the

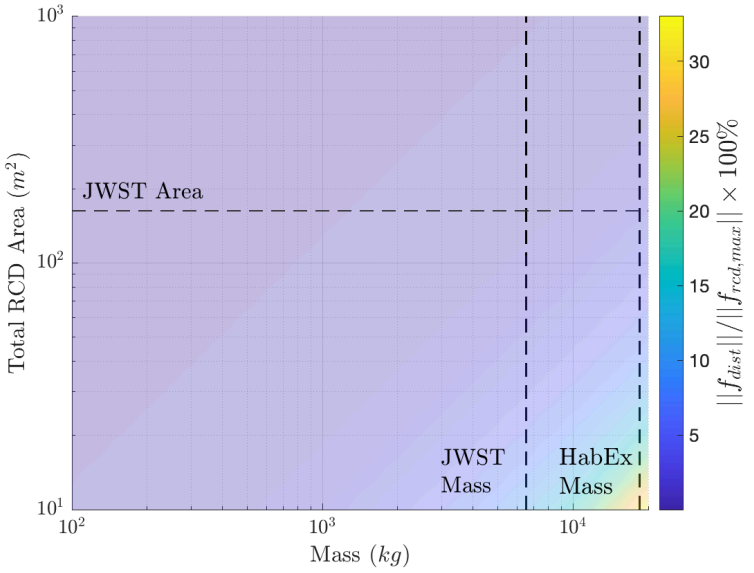

Figure 4-29: Percent utilization of RCD force authority by OD disturbance rejection over satellite's mass and total RCD area.

total area dedicated for RCDs in m^2. The color represents the amount of force in percentage that the OD disturbance represents compared to the maximum force that can be produced by the RCD configurations. The optimal 8-cell RCD configuration in Section 4.2 is utilized for this analysis. The mass of the JWST and the HabEx satellite are plotted in the black vertical line. Also, the JWST's sunshield area is plotted for reference. This result shows that a realistic RCD area can be designed for large-scale telescopes with enough disturbance rejection from errors in orbit determination, and can thus utilize the remaining control authority for operational needs.

4.3.3 Additional Satellite Uncertainties

The uncertainties presented in this section are not an exhaustive list of those expected in satellites with large sails or satellites operating in SEL2. The section instead presented a source of uncertainty that could be mitigated by an improvement in the sensor used in the satellite (Sun direction error), and another one that drives the mass and sizing of the entire satellite system (OD error). Additional uncertainties such as an error in the RCD placement location, the RCD mounting normal vector,

the center of mass of the satellite, the pressure of the sun, and the effective area of the RCD can contribute towards error in the desired force and torque produced by the RCD configuration. Furthermore, additional assumptions in the RCD force model including non-idealized sails as well as sail surface deformation are needed to gain more confidence in the design of a satellite mission. Previous work exists on analyzing the impact of some of these uncertainties on the maneuverability of sails [140, 141]. Furthermore, there exists uncertainty in the SRP value, p_{sun}, due to changes in the Sun's irradiance as a function of Solar activity [142]. Future work for this thesis would be to incorporate additional sources of uncertainties as well as produce a higher fidelity force model for RCDs including experimental data.

Distinctions between types of uncertainties and the effects it has on the control envelope or performance have been extensively covered in the literature [140, 143]. This section covers two of them to show how much the magnitude of such uncertainty compares against the force and torque authority of an RCD configuration. A similar analysis can be performed for additional disturbances to improve the model's fidelity.

4.4 A Case Study of Performance of RCDs on JWST

This section goes over a case study in which the JWST is imagined to be retrofitted with an optimal RCD configuration. Although this analysis represents a low-fidelity model with several assumptions, we are still able to highlight some potential benefits and drawbacks of utilizing RCDs in a satellite of the size of JWST are highlighted.

4.4.1 Satellite Parameters Model

This section presents the mass properties for both JWST and the RCD configuration. The mass parameters for the RCDs namely the density, thickness, and boom linear density, are taken from literature and are shown in Table 4.6. The values for RCD density, ϱ_{rcd}, are taken from Guerrant [144], and they represent a more conservative

value than those given by Okuizumi [145] which corresponded to a density of 1,500 $(\mathrm{kg/m^3})$.[4]

Table 4.6: RCD Mass Parameters.

Parameter	Unit	Value	Source
RCD density	$\mathrm{kg/m^3}$	3000	Guerrant [144]
RCD Thickness	μm	50	Okuizumi [145]

Each RCD is assumed to be a disk-shaped cell with 50 (μm) thickness. From this assumption, the inertia tensor of each RCD expressed in a local RCD frame is given by,

$$I_{rcd}^{rcd} = \begin{pmatrix} \frac{1}{12}m_{rcd}(3r_{0,rcd}^2 + \tau_{rcd}^2), & 0, & 0 \\ 0, & \frac{1}{12}m_{rcd}(3r_{0,rcd}^2 + \tau_{rcd}^2), & 0 \\ 0, & 0, & \frac{1}{2}m_{rcd}r_{0,rcd}^2 \end{pmatrix} \tag{4.30}$$

where $r_{0,rcd}$ is the radius of each cell, τ_{rcd} is the thickness, $m_{rcd} = \varrho_{rcd}(\pi r_{rcd}^2 \tau_{rcd})$ is the mass of the RCD. The local frame for the RCD has its origin at the geometric center of the cell, the z-axis being normal to the cell, and the x and y-axis coplanar to the cell forming a right-hand rule. Given that each RCD cell is canted and its location varies relative to the satellite's center of mass, the inertia tensor must be converted so that it is expressed in the telescopes's body frame and has its origin at the center of mass of the satellite.

Given an RCD cant angle θ_1 and an azimuth angle ϕ, the Euler-angles rotation matrix ${}^bR_{zyx}^{rcd}(\theta_1, \phi, 0)$ defines a rotation between the local RCD frame and the body frame. Let $\mathbf{r}_{rcd}$ be the vector from the satellite center of mass to the geometric center of the RCD. Then, using the parallel axis theorem, the inertia of an RCD cell about the satellite's CM expressed in the satellite body frame is given by,

$$I_{rcd}^{b} = {}^bR^{rcd} I_{rcd}^{rcdb} R^{rcd\ T} + m_{rcd}\left((\mathbf{r}_{rcd} \cdot \mathbf{r}_{rcd})\mathrm{eye}(3) - \mathbf{r}_{rcd}\mathbf{r}_{rcd}^T\right) \tag{4.31}$$

[4]The values given by [145] corresponded to the density of the RCD in the IKAROS spacecraft, however, this RCD density matched that of the rest of the sail despite being a different material; this is why the more conservative values on [144] were used.

where eye(3) is the identity matrix of size three.

The configuration utilized in this section corresponded to a 9.8 m^2 cell that uses the optimized RCD cant angles given by Table 4.1. It is assumed that each RCD cell is located so that it is covered by JWST's sunshield. The location, and orientation of the eight-cell RCD configuration for this analysis is shown in Table 4.7.

Table 4.7: RCD cell position and orientations for JWST test case.

Cell ID	θ_1 ($^\circ$)	ϕ ($^\circ$)	$\mathbf{r_x}$ (m)	$\mathbf{r_y}$ (m)
1	21.45	180.00	-1.64	4.90
2	21.45	360.00	1.64	4.90
3	21.45	90.00	12.25	1.64
4	21.45	270.00	12.25	-1.64
5	21.45	360.00	1.64	-4.90
6	21.45	180.00	-1.64	-4.90
7	21.45	270.00	-12.25	-1.64
8	21.45	90.00	-12.25	1.64

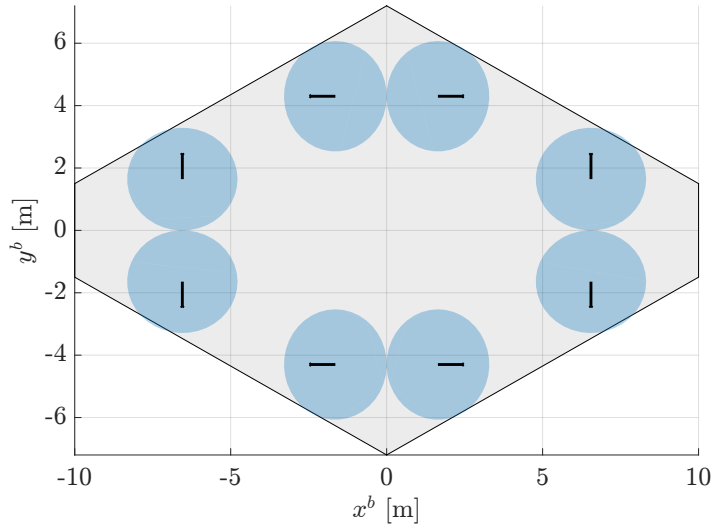

Figure 4-30: RCD cell position and sizes for the JWST example test case. Values are in meters, and each cell has a radius of 1.77 (m). JWST sunshield shown in the grey patch.

A visual representation of this configuration is shown in Figure 4-30. The aggregate RCD configuration is symmetric about the z^b-axis which outside the page. The grey patch corresponds to an approximation of JWST's sunshield dimensions [146]. The RCDs are assumed to be connected via the sunshield structural booms, and thus

the mass and inertia of the connections for the RCDs are not considered. The radius of the RCD cell was a compromise between having a larger lever arm along JWST's body axes and a larger cell area. Furthermore, there was the positional constraint that each RCD cell must not overlap with one another.

Given, the RCD configuration the total inertia corresponding to the aggregate RCD configuration can be computed using Equations (4.31),

$$I^b_{rcd} = \begin{pmatrix} 128.69 & 0.00 & -0.00 \\ 0.00 & 272.23 & -0.00 \\ -0.00 & -0.00 & 409.06 \end{pmatrix} \tag{4.32}$$

where the units for the inertia tensor are in (kgm^2). The total mass for the RCDs is given by m_{rcd} =11.76 (kg), respectively.

The parameters for JWST are given by [147],

$$I_{jwst} = \begin{pmatrix} 67946.00 & -83.00 & 11129.00 \\ -83.00 & 90061.00 & 103.00 \\ 11129.00 & 103.00 & 45821.00 \end{pmatrix} \ (kgm^2), \quad m_{jwst} = 6500 \ (kg) \tag{4.33}$$

The principal moments of inertia for JWST can be obtained through single value decomposition and are given by $I_{jwst,p} = \text{diag}([90061, 72575, 41191]^T)$ (kgm^2), therefore the aggregate RCD configuration corresponds to at most 1.02% of the inertia of JWST (using the minimum value of for the principal inertia tensor with the maximum value for the aggregate RCD configuration), while only accounting for 0.18% of the mass. For reference, the JWST carried approximately 133 kilograms of fuel [148] representing approximately 2.04 % of the mass of the satellite. The mass parameters derived in this section were utilized during this test case.

4.4.2 Scenario Description and Results

This section shows the results of the performance of a JWST-like satellite if it was also equipped with RCDs. The force and torque envelope are discussed and compared against the current JWST actuator performance, additionally the field of regard for this configuration is shown.

The RCD control envelope is shown in Figure 4-31. The force envelope, shown in Figure 4-31a, is expressed in the satellite's body-fixed frame in units of (mN). The solid blue lines in the background represent the shadow of the envelope against one of the body-axes planes for convenience. The magnitude of force generated on a similar

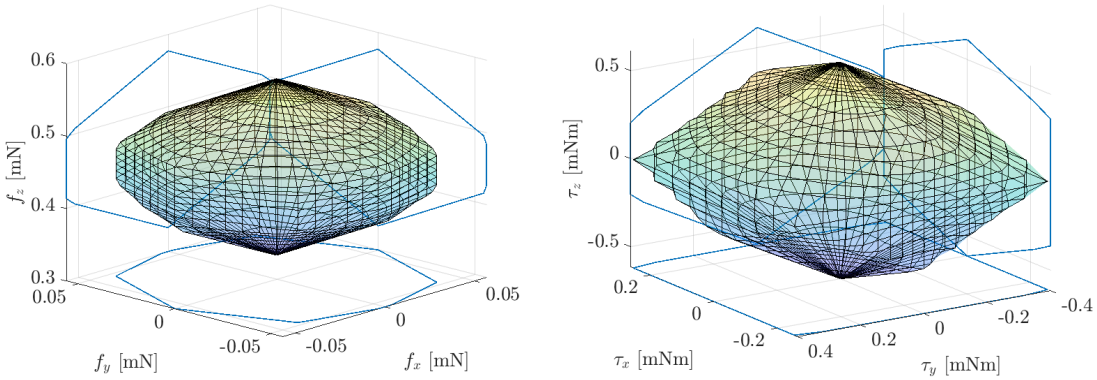

(a) Force Envelope (b) Torque Envelope

Figure 4-31: RCD control envelope of JWST case with a cell area of 9.8 (m^2).

order of magnitude as electrospray thrusters considered for HabEx [149].

The torque envelope, shown in Figure 4-31b, has units of (mNm). Figure 4-31b also has the shadows of the envelope in the background. It is estimated that angular momentum of up to 3 (Nms) can be accumulated in a span of 8 hours during observation by JWST [150]. This corresponds to a constant disturbance torque of less than 0.104 (mNm) which is within the torque that can be provided by RCDs.

The angular acceleration in the satellite's body axes can be computed by multiplying the envelope in Figure 4-31b by the pseudo-inverse of the satellite inertia. Figure 4-32, shows the resultant angular accelerations in units of ($^\circ/s^2$). This figure is a direct comparison of Figure 8 in [147] that shows the angular acceleration of JWST in body-fixed axes when using the reaction wheel assembly. Note the skewness in

the envelope corresponds to the principal axis of inertia for JWST not being aligned with the body-fixed axes. The reaction wheels assembly for JWST are designed to be

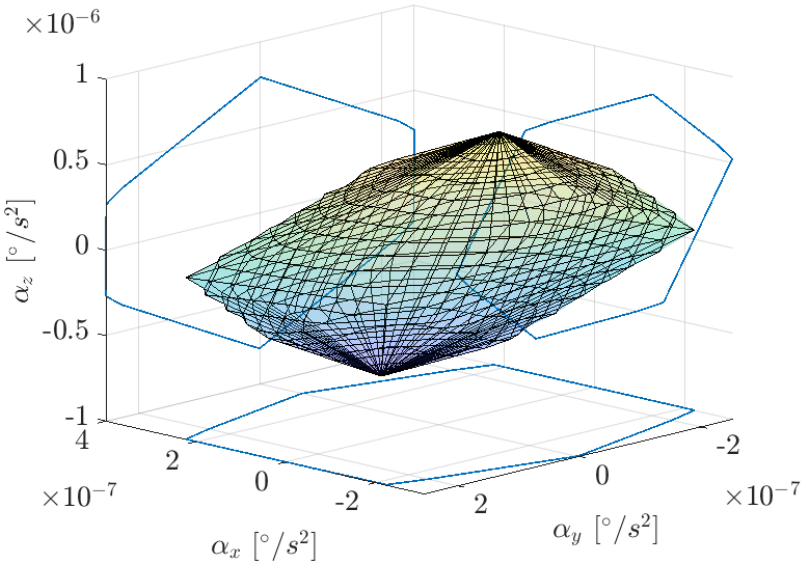

Figure 4-32: Angular acceleration envelope of JWST using only RCDs in $(^\circ/s^2)$.

capable of performing a 90-degree slew in under 56.5 minutes, and thus the maximum agility is close to 150 times that of the RCDs with a maximum angular acceleration of 0.90×10^{-4} $(^\circ/s^2)$ [150]. Therefore, RCDs are not capable of slewing JWST at the same rate as its reaction wheels assembly. However, since the magnitude of authority from RCD is higher than that of the SRP disturbance, the RCD configuration can be utilized to have a full zero-angular momentum system in JWST, or to allow attitude and orbit control to be maintained only with RCD during observations. The latter would ensure minimal disturbances compared to reaction wheels.

To view the operability of the aggregate RCD configuration on the JWST, the IFoR of JWST is shown in Figure 4-33. In Figure 4-33, the IFoR for a three-days imaging time is shown in the blue line. Additionally, JWST's equivalent IFoR is plotted by the black rectangle. For JWST, the IFoR is dominated by the sunshield's light keep-out zone, and it is shown here as the orientation that JWST's z^b-axis can point to ensure it maintains the instrument in the shadow of the sunshield [128]. Because JWST's optical axis is nor collinear to its z^b-axis, JWST has access to the

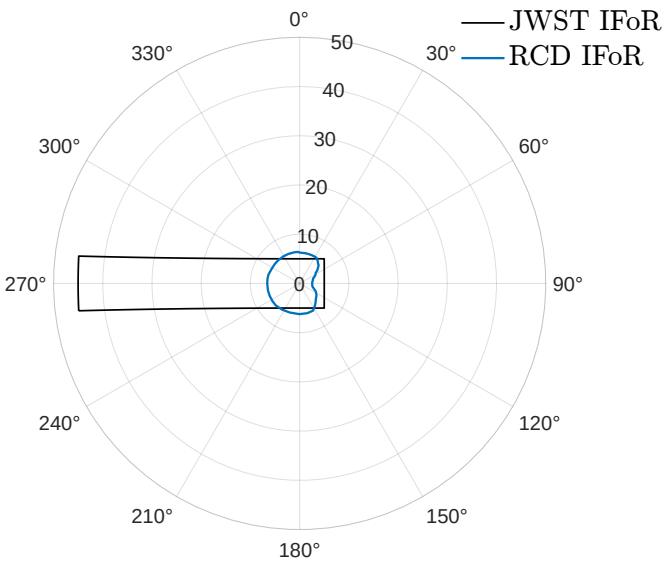

Figure 4-33: Comparison between JWST IFoR and JWST IFoR when using RCDs.

entire celestial sphere twice a year as shown in Section 4.1.2. Using RCDs in JWST leads to a smaller IFoR than JWST's current one. However, the addition of RCDs would mean that JWST would not have to spend fuel when the imaging targets lie inside the region for which the RCDs can operate. Furthermore, for observatories with a survey mission and fine steering mirrors, a slow continuous scan across the sky for the whole mission life is acceptable which can be accomplished with RCDs as long as the scan rate can be accomplished using the RCD's angular acceleration envelope. For JWST, the use of RWA would still be necessary for performing fast slews to new targets, however, RCDs could enhance JWST's operation by expanding the mission lifetime, and ensuring low disturbance from actuators during imaging.

Chapter Summary

This Chapter addresses the operability question from Contribution 2 by showing the field of regard for space telescopes utilizing RCDs as its main actuators. The field of regard region where both orbit and attitude control can be maintained is demonstrated including how this region translates into view access to the celestial

sphere. A methodology for optimizing the placement of RCDs is shown, leveraging the insight gained from simplified test cases. A discussion of how typical sources of disturbances affects the force and torque envelope for RCDs is shown demonstrating that design choices can result in disturbances becoming an insignificant portion of the control envelope. Finally, an analysis is presented that shows what the performance of an RCD configuration would be in the JWST that shows RCDs would be able to be operated during the imaging maneuvers and could reduce the amount of momentum unloading from SRP disturbances from the sunshield.

Chapter 5

Dynamics and Control Testbed for a Rotating Synthetic Aperture Satellite in LEO

Whereas Chapter 3 and Chapter 4 focus on the use of RCDs about the Sun-Earth Lagrange points, this chapter focuses on Low Earth Orbit environment. Particularly, this chapter seeks to demonstrate the concept of operation for RSA telescopes via a ground-based dynamics and controls testbed. The goal of this chapter is to verify the ability to control a CubeSat to smallsat size satellite in Low Earth Orbit by developing the GNC algorithm using a dynamically scaled testbed in 1-g as part of Contribution 3.

Section 5.1 goes over the development of the testbed including an overview of the capabilities, its main subsystems, and testing results for the FlatSat configuration[1]. Section 5.2 goes over the full results of the dynamics and control testbed, including the scaling laws developed to obtain similar behavior for a LEO and MEO satellite.

[1]Results from this section was presented in [4]

5.1 Dynamics and Control Testbed for RSA Telescopes

This section presents an overview of the testbed, including all of the main subsystems, as well as its performance in its flat satellite configuration. The testbed was designed to be able to accomplish the expected motion, or concept of operations, of an RSA satellite.[2]

5.1.1 Concept of Operations and Overall Testbed Requirements

RSA telescopes operate differently from traditional space telescopes, and thus require a different concept of operations (ConOps). This section goes over the ConOps for RSA telescopes, as well as the guiding factors in the design of the Dynamics and Control Testbed (DCT).

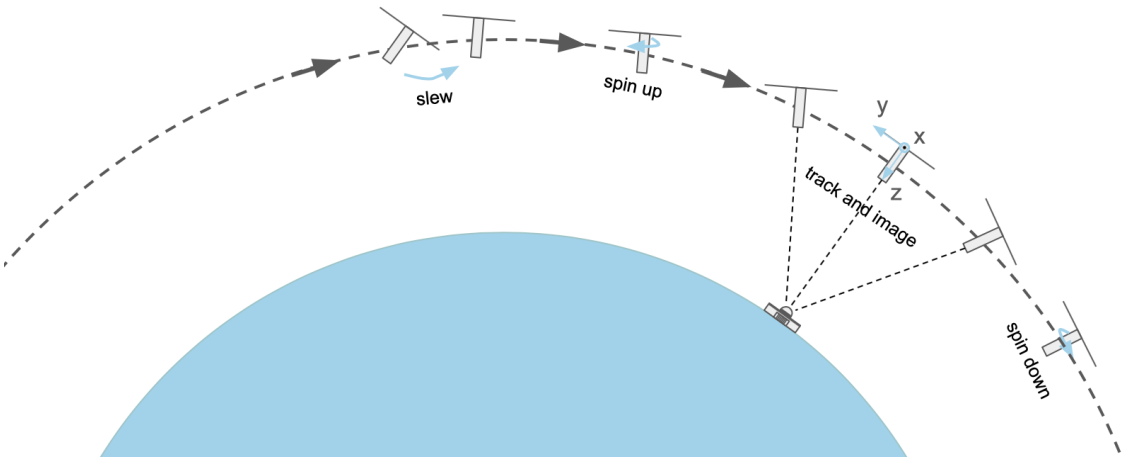

Figure 5-1: Typical Operating mission profile for imaging a ground-based target

[2]The author would like to acknowledge that the testbed was a product of a multi-year effort supervised by Dr. Rebecca Masterson and graduate students Alejandro Cabrales Hernandez, Evan Kramer, and Michael Fifield, as well as roughly a dozen of undergraduate researchers that were integral in helping the development and machining of the structural component of the DCT. The concept of the DCT was first brought up in MIT AeroAstro's 16.83/831 capstone class in 2018, and continued under a NASA APRA proposal co-led by Dr. Rebecca Masterson and Dr. Joseph Green. Many of the structural design choices for the resultant DCT come from that class.

A typical ConOps for an Earth-pointing RSA satellite is shown in Figure 5-1[3]. The main steps needed to perform a motion are

1. Slew to point the optical axis to a new ground target for the beginning of imaging
2. Spin up about the optical axis and maintain a constant rate required for imaging
3. Track the target by slewing about an axis normal to both the optical axis and the direction of the ground track
4. Spin down about the optical axis
5. Slew towards the new ground target

Note that in the above ConOps, the telescope spins up and down at the beginning and end of each target imaging maneuver. This is not necessary as the satellite may always maintain a spin about the optical axis for the entire duration and just slew to the new target while spinning. Whether the satellite maintains a constant spin throughout imaging and retargeting or not represents a trade study between two types of ConOps: a zero-angular momentum system, and a non-zero angular momentum system.

For a non-zero angular momentum system, the satellite rotates by means of external actuators such as thrusters or magnetorquers, or through perturbations such as gravity gradient torques. The optical axis of the satellite is always rotating at the rate that is needed to perform the imaging maneuver. To do so, an external torque, $\boldsymbol{\tau}_{ext}$, is required to move and point the angular momentum of the satellite,

$$\boldsymbol{\tau}_{ext} = \frac{D}{Dt}^{I} \mathbf{h}_{tot} \tag{5.1}$$

where $\frac{D}{Dt}^{I}$ represents the total derivative in an inertial frame. For an imaging maneuver and due to conservation of angular momentum, there is a need for a continuous torque to be applied on the system to keep the satellite's optical axis pointing at the

[3]Image Credit: MIT 16.831 Attitude Control Systems Team, 2018

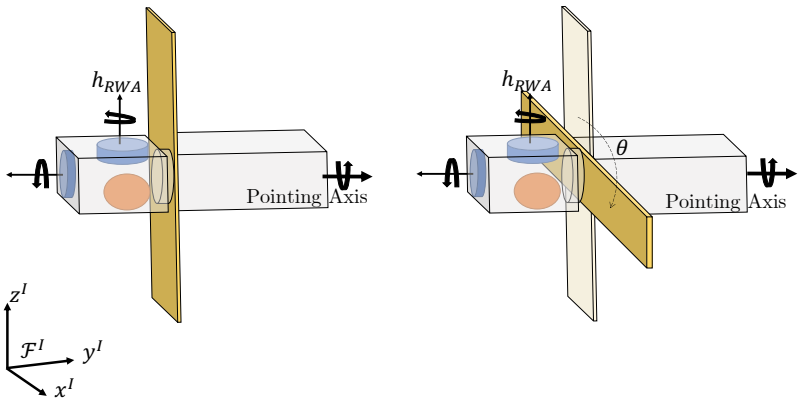

(a) Dual-Spinner RSA

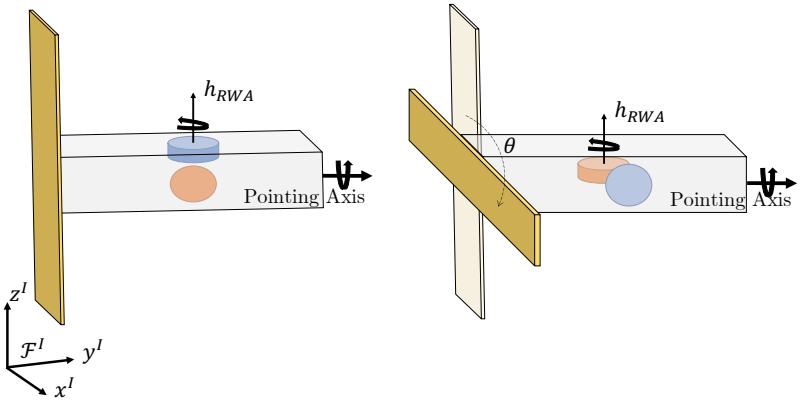

(b) Single-Spinner RSA

Figure 5-2: Example of zero angular momentum RSA configurations.

target, which would cause a large use of propellant for each maneuver if thrusters are used. Due to large fuel expenditure per imagining maneuver, non-zero angular momentum RSA telescopes are an undesirable configuration when the commanded spin rate is large. Furthermore, the control magnitude produced by orbital perturbations such as gravity gradient, magnetic field, or solar radiation pressure is not enough for controlling the satellites with large spin rates.

An alternative configuration is that of a zero angular momentum satellite. As mentioned in Section 2.1.1 there exists many types of zero-angular momentum spin satellites. Two of the main configurations are what are called single and dual spinners. Figure 5-2 shows examples of these two configurations. For each subfigure, the gold

rectangle represents the primary strip mirror of the RSA. The pointing axis is normal to the strip mirror and its spin direction is given by a black circular arrow. The reaction wheels are given by the blue and orange cylinders for both configurations. The dual-spinner in Figure 5-2a consists of two separate bodies connected via a slip ring. It is assumed in this configuration that all the optical system payload is in one of the bodies, while the ACS system is in the other. In the dual-spinner case, two configurations exits: the first configuration has the second spinner body rotates to counteract the momentum of the optical axis spin, and the second configuration has the angular momentum to counter the optical axes stored in a flywheel, allowing the second spinner body to appear quasi-stationary in the inertial frame. To maintain a zero angular momentum in the latter configuration, a larger flywheel or reaction wheel is needed to counteract the angular momentum of the spinning component. Performing attitude changes of the satellite is relatively simple, and it only requires the system's RWA to be commanded in the non-spinning body frame. For example, if a negative rotation of the satellite about the z^I axis is required, the blue RWA with its normal vector facing the z^I-axis in the figure needs to rotate to have an angular momentum in the z^I-axis.

The single spinner is shown in Figure 5-2b. In this system, the attitude control system is housed inside the spinning body. As the RSA rotates about its pointing axis, the RWA rotates with it. Changing the attitude of the single spinner is more challenging than the dual spinner, as the RW angular momentum required to perform the slew needs to be exchanged between the reaction wheels so that it is always pointing in the correct orientation. For example, if the same negative rotation about the z^I axis as in the dual spinner case is required, the angular momentum of the wheels must be exchanged between the blue and orange reaction wheels. As shown in Figure 5-2b, the angular momentum carried by the blue wheel must be completely exchanged to the orange wheel by the time the RSA rotates 90° about its pointing axis. This results in a more challenging controller, and an increase in power and torque requirements from the dual-spinner.

For the testbed, both the dual-spinner and the single-spinner were considered. De-

spite the increase in power requirements, the single spinner configuration was chosen for the testbed for several reasons. First, the torque from the reaction wheel actuators for the testbed was more than enough to allow for the exchange of momentum during the spinning operation. Reliable slip rings present a challenging design point as they are prone to failure, and a single spinner is a mechanically simpler design, and COTS components for a CubeSat are more readily available for the single-spinner configuration. A single-spinner testbed is a more flexible design as it allows testing for non-RSA satellite designs compared to a more specialized dual-spinner testbed. Finally, a zero or non-zero angular momentum configuration is expected for a large RSA satellite that operates in SEL2 at low spin rates.

The DCT was designed to meet several objectives including the ability to perform the operating profile for an RSA at different spin and slew rates that are consistent with those required for RSA imaging operations at different altitudes and given in Reference 110, to allow for the development of dynamically consistent scaling laws to allow for traceability in the performance of the testbed and a candidate RSA satellite, and be modular to allow for testing of different sensors, actuators, and GNC algorithms.

5.1.2 Overview of Testbed

This subsection gives an overview of the DCT, the subsystems, sensors, and actuators used, as well as the development of two intermediate testbeds used to validate all the subsystems.

The testbed was designed to allow for a limited three rotational degrees of freedom. To accomplish this the testbed rests on a hemispherical air bearing in the MIT Space Systems Laboratory. The testbed is shown in Figure 5-3 with the main components of the testbed labeled. The lab frame, taken to be a quasi inertial frame[4], is shown with black arrows in the top left side of the picture. The origin of the lab frame is

[4]The angular velocity of the Earth is approximately two orders of magnitudes below the IMU angular velocity resolution, and three orders of magnitude smaller than the commanded rates of the testbed. Also, due to the short time scale of each test, the frame can be assumed to be inertial for the purpose of this testbed.

at the center of the Optical camera in the ArUco board, the z^I-axis is normal to the ArUco board, the y^I-axis points to the right of the figure, parallel to one of the edges of the ArUco board, and the x^I-axis completes the right-hand coordinate frame. The hemispherical air bearing, and the location for the center of rotation of the testbed, sits on top of the aluminum column. The column is covered with 1.5" thick foam to reduce the impact force of the testbed with the air bearing. The structure of the testbed is machined out of aluminum with two concentric rings that lie below the air bearing connected via four aluminum threaded rods. The middle ring is for structural stability, while the lower ring is to safely limit the range of motion of the air bearing. As the testbed tilts the lower ring will make contact with the foam on the air-bearing column ensuring that the DCT will not over rotate and damage the air-bearing sytem. A set of counterbalance weights, coarse balance weights, and fine balance weights are

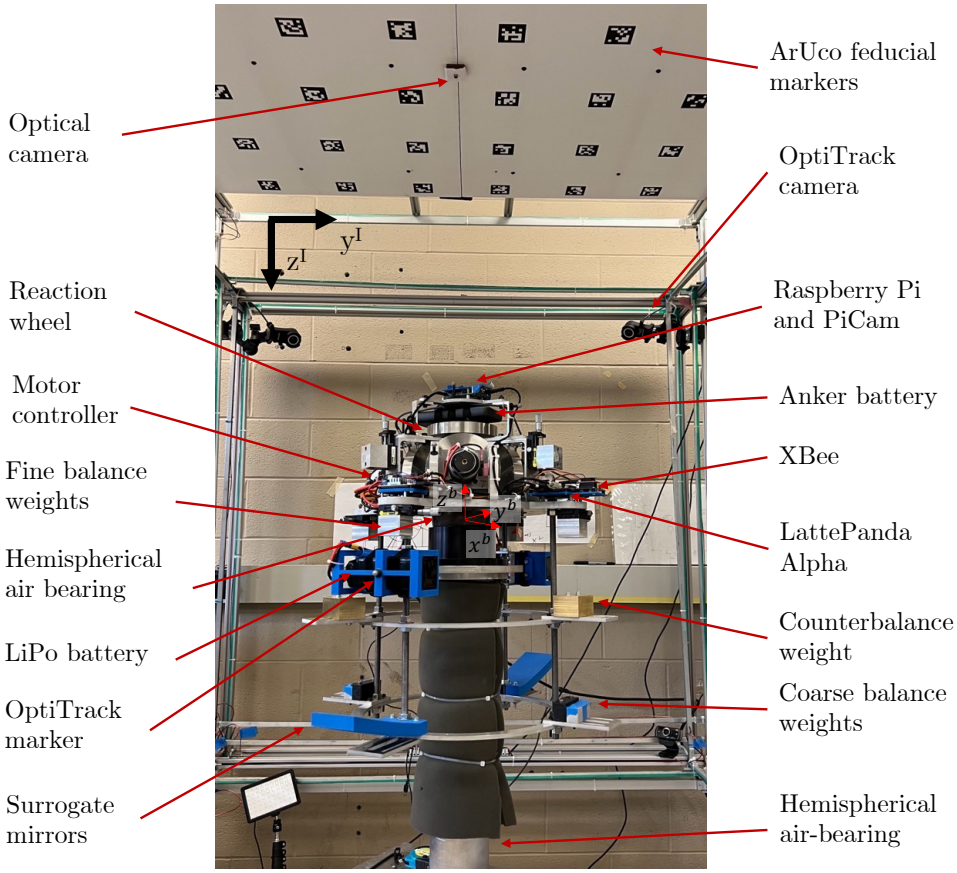

Figure 5-3: Annotated image of the Dynamics and Control testbed sitting on top of a 3 d.o.f. hemispherical air bearing.

placed throughout the testbed to reduce the offset between the center of rotation at the spherical air bearing, and the center of mass of the testbed.

Table 5.1: Sensor and actuator components for Dynamics and Control Testbed.

Component	**Subsystem**	**Description**
LattePanda Alpha	-	Single board computer running all GNC algorithms
Anker Battery	-	Battery used to power Raspberry Pi and LattePanda
Raspberry Pi 4	Est.	Single board computer for image processing
PiCam Module 2	Est.	Camera used for star tracker emulator
VectorNav 100	Est.	Inertial Measurement Unit
ArUco Board	Est.	Board with fiducial markers used by PiCam
XBee Radio	RWA	Wireless radio use for RWA emergency stop
Ametek ID23001	RWA	Brushed commutated DC motor
Roboclaw 2x30A	RWA	Motor Controller
Turnigy 6s 1.6Ah	RWA	LiPo Battery for RWA Motor

The sensor, actuators, and onboard computers are listed in Table 5.1. The testbed's Reaction Wheel Assembly (RWA) is composed of four reaction wheels each consisting of a brushed DC motor and an aluminum machined flywheel. Two BasicMicro Roboclaw motor controllers are used to command each pair of reaction wheels which are themselves powered by two 6S LiPo batteries at a nominal voltage of 25V. Additionally, an XBee radio is connected to both motor controllers to enable external commanding of a fail-safe emergency stop of the RWA assembly. For sensors, an Inertial Measurement Unit (IMU) is used to determine the testbed's angular velocity and magnetic field, and a Raspberry PiCam is used as a star tracker emulator to determine the testbed's orientation. The PiCam uses ArUco fiducial markers mounted at the top of the testbed enclosure to determine its orientation. Two onboard single-board computers are used to control the testbed. A fourth-generation Raspberry Pi is used to control the PiCamera, while a LattePanda Alpha single-board computer is used to command the motor controller and run the guidance, estimation, and control algorithms. The LattePanda Alpha was selected for its ability to operate any Linux-based operating system as well as its superior processing speed and storage compared to a Raspberry Pi.

The testbed used the Robot Operating System (ROS) to communicate between algorithms, sensors, and actuators. ROS is open-source software that handles communication across multiple programming languages and is widely used in robotics due to its ability to seamlessly integrate hardware and software as well as regulate

the rate at which information is published [151]. Each of the subsystems, sensor, or actuator is abstracted into what are called "nodes" that can receive (or "subscribe") to predefined messages (known as "topics") as well as send (or "publish") the messages. The nodes may publish the message at pre-defined rates without the user developing the low-level command and data handling. Note that although the user is able to pre-define the rate at which messages are sent and acted upon, ROS is a soft real-time system, and does not guarantee that messages are sent, or received.

To prevent damage to the air-bearing as well as to develop and test the GNC algorithms, two testbeds were created to ensure that the subsystems of the testbed successfully work before assembling the full DCT. One testbed was used to develop the algorithms for the RWA actuators, guidance and control algorithms, while the other testbed quantified the performance of the IMU and PiCam sensors. A system-wide overview of the DCT testbed is shown in Figure 5-4. Solid black lines correspond to communication using ROS, while blue dashed lines correspond to the interaction of actuators and sensors with the physical environment. The subsystems include Guidance, Controller, Reaction Wheel Assembly, Estimation, and Sensors. The subsystems are differentiated between hardware subsystem such as the RWA, IMU, and PiCam, and software subsystems such as the GNC algorithms. Each subsystem represent an individual ROS node. Finally, the Testbed Dynamics for the DCT represent the physical dynamics from the testbed and the real world. The communication between the ROS nodes is given by solid black lines, while the interactions with the environment are given by the dashed blue lines. The testbed was divided between the FlatSat, a guidance, control and actuator testbed, and the Attitude Determination and Control Testbed for the EKF and IMU.

The FlatSat testbed shown in Figure 5-5 consists of the four RW, the motor controllers, LiPo batteries, and the LattePanda single board controller. The RWAs were mounted on the main plate of the testbed for testing purposes, and are shown in the configuration that they are in the DCT. Three of the RWs are in an equilateral configuration that is coplanar with the xy^b-plane. The final RWA is mounted along the z^b-frame, however, for the FlatSat it was mounted at the side. Two emergency

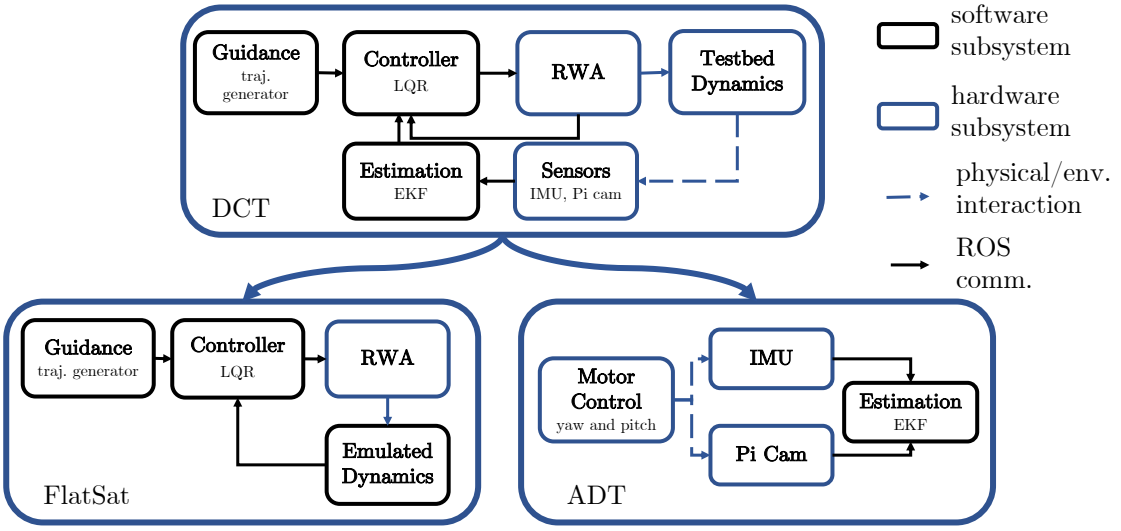

Figure 5-4: Overview of Dynamics and Control Testbed as the FlatSat and Attitude Determination Testbed. The diagram shows the communication between each subsystem and how they are incorporated into the respective Testbeds.

stop switches were utilized for safety considerations and served as a method to cut off power from the LiPo batteries. Results for the FlatSat configuration as well as the testing scheme are shown in Section 5.1.5.

The Attitude Determination Testbed is shown in Figure 5-6. The testbed consists of the PiCam and the IMU mounted on two-axis motors to provide yaw and roll motion. The frames of the PiCam are shown in green, with the origin at the center of the PiCam optical axis. The z-axis points outward from the optical axis, the y-axis points downward and is aligned towards the connection ports of the Raspberry Pi which corresponds to the y-axis of the DCT, and the x-axis completes the right-handed frame. The PiCam's frame is also the ADT body frame. The IMU axis are shown in red with the origin at the goemetric center of the IMU, the z-axis, pointing towards the camera's $-z$-axis, the x-axis pointing towards the camera's $-y$-axis, and the y-axis completing the right-handed coordinate system. Two DC motors provide motion about the ADT's z-axis, and about the axis normal to the top aluminum plate where the ADT is mounted. Also shown in the background is the same ArUco board that is used on the testbed. The sensor characterization of the ADT including is shown in Reference 110 and 4. The reader is referred to Kramer's master thesis for

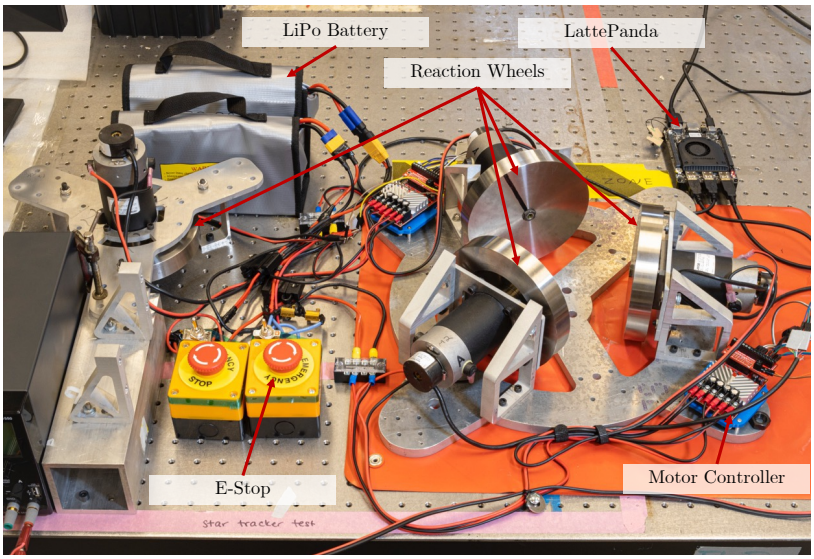

Figure 5-5: FlatSat testbed. Testbed shows the four reaction wheels utilized by the DCT testbed to achieve attitude control. Additionally, the motor controller and LattePanda single-board computer are shown. Image source from [4].

these results [110].

Results from the sensor characterization of the ADT was utilized to create sensor emulators for the FlatSat and incorporate them into its Emulated Dynamics block shown in Figure 5-4. The FlatSat, thus, represented our best estimate of the behavior of the DCT before assembling the testbed and operating in the hemispherical air-bearing.

5.1.3 Guidance Navigation and Control Subsystems

This subsection gives an overview of the main GNC algorithms and nodes that were developed for the DCT. For each subsystem, a description of the algorithm, available modes, and operating rates are described.

Before presenting the algorithms, a coordinate system for the testbed and its relation to an RSA satellite is presented. Figure 5-7 the coordinate system used by the RSA and the testbed. Each version contains two frames: an inertial frame $\mathcal{F}^I$, and a body-fixed frame $\mathcal{F}^B$. The body-fixed frame is defined as the z-axis pointing along the principal optical axis, the y-axis pointing along the long-axis of the strip mirror, and finally, the x-axis completes the right-handed frame. Unlike a RSA satellite, the

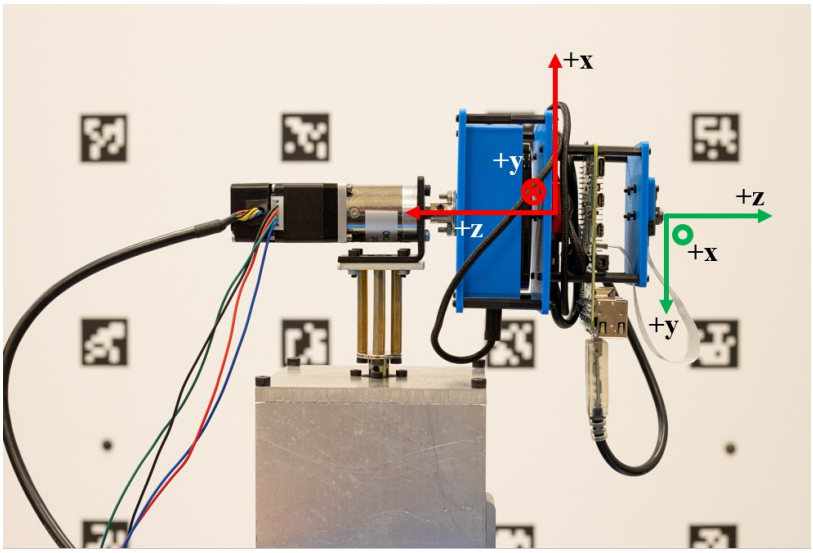

Figure 5-6: Attitude Determination Testbed including the ArUco board in the background. The testbed consists of two motors that provide two-axis degree of freedom. [4]

RSA testbed is constrained to only have three degree of freedom by the hemispheric air-bearing shown in orange. The origin for both the RSA and testbed is given by the center of mass. The pseudo-inertial frame of the testbed, as defined before, has its origin at the center of the ArUco board, the z^I-axis pointing downwards and it is collinear to the normal vector of the ArUco Board, the y^I-axis is parallel to one of the edges along the ArUco board, pointing to the right of the figure, and the x^I-axis completes the right-handed coordinate system.

Guidance

The Guidance subsystem node corresponds to the subsystem that provides the reference orientation and angular velocity of the testbed. The node generates kinematically consistent pairs of angular velocity and quaternion, by integrating an angular velocity profile and obtaining the quaternion. The quaternion is obtained by integrating the rate of change of the quaternion given in Equation 3.7

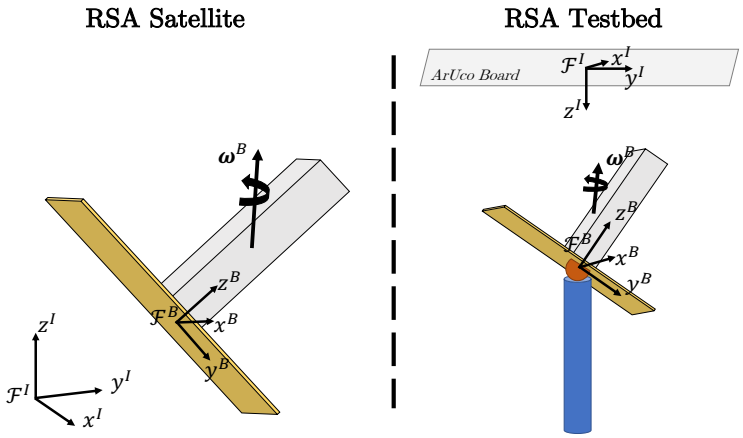

Figure 5-7: Frame definition for RSA satellite and equivalent testbed. $\mathcal{F}^I$ represents a frame in the inertial frame, $\mathcal{F}^B$ represents a body-fixed frame to the RSA mock satellite or testbed.

Thus, the angular reported by the quaternion is given by,

$$\begin{aligned} \boldsymbol{\omega}_{ref}(t,\Gamma) &= \mathbf{f}(t,\Gamma) \\ \mathbf{q}_{ref} &= \int \dot{\mathbf{q}}(\boldsymbol{\omega}_{ref})dt \end{aligned} \tag{5.2}$$

where $\mathbf{f}(t,\Gamma)$ is a function that generates an angular velocity profile as a function of time, and some specified parameters Γ, and $\mathbf{q}(\boldsymbol{\omega}_{ref})$ indicates that the rate of change of quaternion is dependent on the reference angular velocity.

Providing a smooth trajectory for the angular velocity and quaternion allows the controller to have a smoother control input profile, does not excite flexible modes, and reduces the amount of pointing error during the segment transitions [152, 153]. Due to this, the function $\mathbf{f}(t,\Gamma)$ was selected so that the reference quaternion was twice continuously differentiable, given by,

$$\boldsymbol{\omega}_{ref}(t,\Gamma) = \hat{\mathbf{e}}\Omega_{ref}(t,\Gamma) \tag{5.3}$$

where $\hat{\mathbf{e}}$ is the axis of the angular rotation, and $\Omega_{ref}(t,\Gamma)$ is a piecewise, continuously

differentiable scalar function given by

$$\Omega_{ref}(t,\Gamma) = \begin{cases} 0 & t \le t_0 \\ \alpha\tau_1^2/2 & t \le t_r/2 + t_0 \\ -\frac{\alpha}{4}\left(2\tau_1^2 - 4\tau_1 t_r + t_r^2\right) & t \le t_r + t_0 \\ \omega_s & t \le t_c + t_r + t_0 \\ \omega_s - \frac{\alpha}{2}\tau_2^2 & t \le \frac{3t_r}{2} + t_c + t_0 \\ \omega_s + \frac{\alpha}{4}\left(2\tau_2 - 4\tau_2 t_r + t_r^2\right) & t \le 2t_r + t_c + t_0 \end{cases} \tag{5.4}$$

and,

$$\begin{aligned} \tau_1 &= t - t_0, \\ \tau_2 &= t - t_0 - t_c - t_r \\ \alpha &= \frac{4\omega_s}{2t_r} \end{aligned} \tag{5.5}$$

where ω_s is the angular velocity change, t_0 is the initial ramp-up time, t_r is the duration of the ramp-up period, t_c is the coasting period at which the angular velocity is ω_s, $\alpha = 4\omega_s/t_r^2$ is the maximum angular acceleration attained during ramp up, and $\Gamma = [t_0, t_r, t_c, \omega_s]$. Note that t_r controls how smooth the function is, as more ramp-up time corresponds to a smoother trajectory.

Figure 5-8 shows an example of the smooth angular velocity trajectory. Note that the acceleration profile consists of two ramp sections at the beginning and end of the trajectory followed by a coast period. Since the angular acceleration and velocity is continuous, the trajectory for the quaternion is twice continuously differentiable.

In order to follow the mission profile shown in Figure 5-1, a combination of angular velocity in the inertial and body-fixed frame must be given. At each time step, the angular velocity described in the inertial frame corresponding to the tracking component must be converted to the body axis. Thus, the total angular velocity is given by,

$$\boldsymbol{\omega}_{total} = \boldsymbol{\omega}_{opt}^{B} + {}^{B}R^{I}({}^{B}\mathbf{q}^{I})\boldsymbol{\omega}_{track}^{I} \tag{5.6}$$

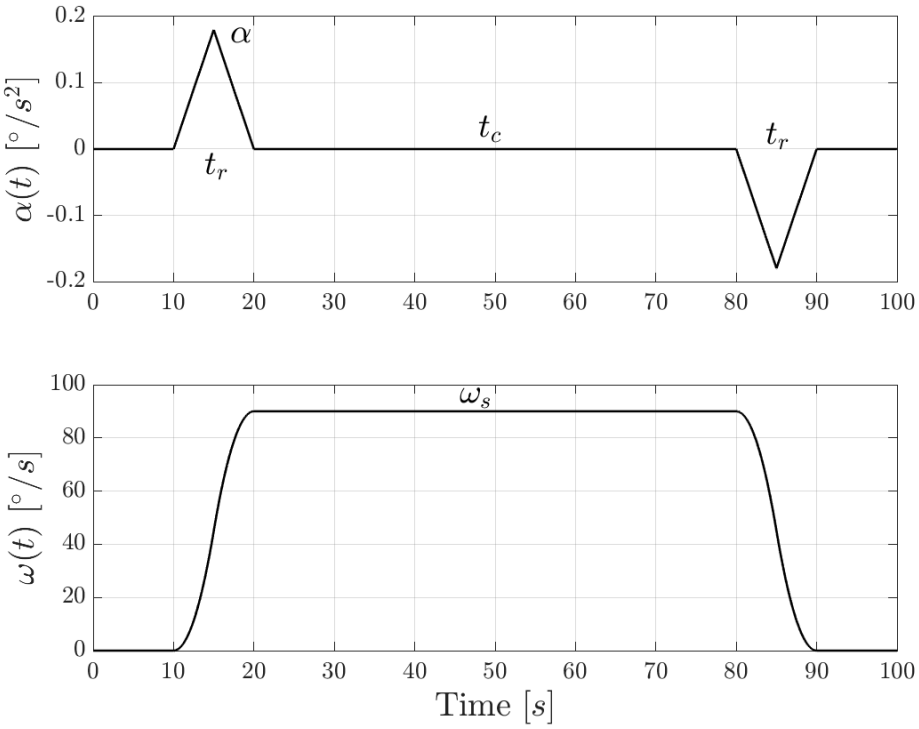

Figure 5-8: Example of angular velocity profile $\omega_{ref}(t)$ produced by the Guidance Node. Example case where $t_0 = 10$ (s), $t_r = 10$ (s), $\omega_s = 90$ $(^\circ/s)$.

where, $\boldsymbol{\omega}^B_{opt}$ corresponds to the angular velocity of the testbed about the principal optical axis, $\boldsymbol{\omega}^I_{track}$ is the angular velocity used for tracking expressed in the inertial frame, and ${}^B R^I({}^B\mathbf{q}^I)$ is the rotation matrix from inertial to body-fixed frame, generated by the attitude at the previous step assuming a discrete integration.

Equation (5.6) along with (5.2) are used for generating the reference angular velocity and quaternion for the testbed when performing the compound slew for the mission profile. The Guidance node publishes the reference state at a rate of $f_{guid} = 10$ Hz.

The possible modes for this subsystem are shown in Table 5.2. Five modes exist and are characterized by the angular velocity commanded. The "Hold" mode is primarily used to maintain a certain fixed attitude of the testbed and thus its angular velocity is always zero. The "Single Spin" implements the angular velocity from Equation (5.4), and was utilized mostly during the checkout procedure as a way to ensure that the testbed was controllable at relatively simple reference commands. The next

Table 5.2: Guidance Modes as a function of commanded angular velocity.

ID	Mode	Ang. Vel.	Description
1	Hold	$\mathbf{0}$	Holds attitude at desired attitude quaternion
2	Single Spin	$\omega\hat{e}_{\#}$	Smooth spin about a single axis given by $\hat{e}_{\#}$
3	Imaging Man.	$\boldsymbol{\omega}_{opt}^{B} + {}^{B}R^{I}({}^{B}\mathbf{q}^{I})\boldsymbol{\omega}_{track}^{I}$	Compound slew corresponding to an imaging maneuver. The angular velocity performs a single spin about the optical axis, while also performing a slew about an inertial axis
4	Safe Mode	$\omega_{safe}(t, \boldsymbol{\omega}_{init}, \mathbf{q}_{init}, \mathbf{q}_{safe})$	Combined slew that returns the DCT from its current state to the safe mode attitude
5	Change Angle	$\omega_{ang}(t, \Delta\boldsymbol{\theta})$	Command that allows for a change in roll-pitch-yaw of the satellite

mode "Imaging Maneuver" implements the compound slew in Equation (5.6), and is supposed to represent the motion shown in Figure 5-1. The "Safe Mode" as its name suggests is capable of designing an angular velocity trajectory from the testbed current angular velocity, $\boldsymbol{\omega}_{init}$, and quaternion, q_{init}, to the designated safe attitude for the testbed. The safe attitude is for the DCT testbed point upwards with the PiCam facing the axis normal to the ArUco board, and the testbed's y-axis, be parallel to the lab's y^I-axis. Finally, the "Change Angle" mode allows the testbed to be rotated by a desired delta angle, $\Delta\boldsymbol{\theta} = [\Delta\theta_{roll}, \Delta\theta_{pitch}, \Delta\theta_{yaw}]$, via a smooth single-axis slew. Appendix A provides the methodology of computing the angular velocity profiles for "Safe Mode" and "Change Angle" modes. The Guidance node subscribes to a message that controls which mode is active in the node.

Controller

The Controller node is responsible for providing the control command on the testbed actuators so that the testbed follows the profile given by the Guidance node. The algorithm for the controller is very similar to the Attitude controller presented in Section 3.4.2.

The controller is based on an extended version of the LQR controller that includes parameters to remove the integral error of the quaternion produced during complex maneuvers. To obtain the LQR controller, the linearized equations of motion must first be computed. Similar to Section 3.4.2 the Newton-Euler dynamics are used to

obtain the equations of the testbed:

$$\boldsymbol{\tau}_{ext} = \dot{\mathbf{h}}_{tot} + \boldsymbol{\omega}^b \times \mathbf{h}_{tot} \tag{5.7}$$

where $\boldsymbol{\tau}_{ext}$ is the external torque applied on the testbed, $\boldsymbol{\omega}^b$ is the angular velocity of the testbed relative to the inertial frame, and $\dot{\mathbf{h}}_{tot}$ is the total angular momentum given by

$$\mathbf{h}_{tot} = I_{dct}\boldsymbol{\omega} + \mathbf{h}_{RW} \tag{5.8}$$

where I_{dct} is the inertia tensor of the system (all the structural, electronics, optical, components) about the *center of mass*, and the angular angular momentum of the wheels is given by,

$$\mathbf{h}_{RW} = I_{rw}{}^B C^{RW} \boldsymbol{\omega}_{RW} \tag{5.9}$$

In Equation (5.9), I_{rw} is a scalar value of the moment of inertia of the reaction wheels about its spin axis, n_{RW} is the number of reaction wheels, $\boldsymbol{\omega}_{RW} \in \mathcal{R}^{n_{RW}\times 1}$ vector of speeds of the wheels, and ${}^B C^{RW}$ represents a 3 by n_{RW} matrix that transforms the wheel vector into the body-fixed frame.

The equation of motion for the testbed in terms of the rate of change of the angular velocity is given by,

$$\dot{\boldsymbol{\omega}} = -I_{dct}^{-1}\left[\boldsymbol{\omega} \times (I_s\boldsymbol{\omega} + \mathbf{h}_{RW}) - \boldsymbol{\tau}_c - \boldsymbol{\tau}_{ext}\right] \tag{5.10}$$

Note the similarity of Equation (5.10) with the equation of motion for a satellite in SEL2 given by Equation (3.6). The equations of motion are linearized about the equilibrium point $\boldsymbol{q} = [1,0,0,0]^T$, $\omega^b = [0,0,0]^T$, $h_{RW} = [0,0,0]^T$, and $\tau_c = \tau_{ext} = [0,0,0]^T$. The resultant A_{att}, and B_{att} matrices match that of Equation (3.34), but

are repeated here for convenience,

$$A_{att} = \begin{pmatrix} \mathbf{0}_{3\times3} & \frac{1}{2}\text{eye}(3) \\ \mathbf{0}_{3\times3} & \mathbf{0}_{3\times3} \end{pmatrix}$$

$$b_{att} = \begin{pmatrix} \mathbf{0}_{3\times3} \\ I_{sc}^{-1} \end{pmatrix}$$

Unfortunately, the LQR controller is not guaranteed to have zero steady-state error when the commanded reference trajectory is not constant. Thus, it is possible to concatenate the state vector to include integral in the attitude dynamics as follows

$$\delta\dot{\mathbf{x}}'_{err} = A_{int,DCT}\delta\mathbf{x}'_{err} + B_{int,DCT}\mathbf{u} \tag{5.11}$$

where $\delta\mathbf{x}'_{err} = [\int \mathbf{q}_{err,vec}, \mathbf{q}_{err,vec}, \boldsymbol{\omega}_{err}]^T$ and similar with the attitude controller for SEL2 the quaternion only contains the vector component. $A_{int,DCT}$ and $B_{int,DCT}$ given by,

$$A_{int,DCT} = \begin{pmatrix} eye(3) & \mathbf{0}_{3\times6} \\ \mathbf{0}_{6\times3} & A_{att} \end{pmatrix}, \quad B_{int,DCT} = \begin{pmatrix} \mathbf{0}_{3\times3} \\ B_{att} \end{pmatrix} \tag{5.12}$$

The $A_{int,DCT}$ and $B_{int,DCT}$ matrix can now be used to find the feedback controller using MATLAB's *lqrd* function,

$$K_{lqrd,DCT} = lqrd(A_{int,DCT}, B_{int,DCT}, Q_{att,DCT}, R_{att,DCT}, \Delta t_{ctrl}) \tag{5.13}$$

where $Q_{att,DCT} \in \mathcal{R}^{9\times9}$, $R_{att,DCT} \in \mathcal{R}^{3\times3}$ have the same function and properties as Q_{att} and R_{att} as in Sectionr 3.4.2.

The feedback controller law for the DCT is finally,

$$\mathbf{u}_{dct} = K_{lqr,DCT}\delta\mathbf{x}'_{err} - \boldsymbol{\omega}^b \times \mathbf{h}_{tot} + I_{dct}\dot{\boldsymbol{\omega}}_{ref} + \boldsymbol{\omega}_{ref} \times (I_{dct}\boldsymbol{\omega}_{ref}) \tag{5.14}$$

Where $\mathbf{u}_{dct}$ is the input torque on the RWA, the term $-\boldsymbol{\omega}^b \times \mathbf{h}_{tot}$ removes the ac-

cumulated system momentum (due to DCT disturbances), and the term $I_{dct}\dot{\boldsymbol{\omega}}_{ref} + \boldsymbol{\omega}_{ref} \times (I_{dct}\boldsymbol{\omega}_{ref})$ is a feedforward term of the desired trajectory and ensures that the error of the system is minimized due to the complex compound slew trajectory.

Having the input torque computed, the next step is translating the torque to commanded wheel speeds needed for the RWA node. This is simply done by discretizing the controller, and assuming a zero-order hold of the controller command,

$$\omega_{RW}^{+} = \omega_{RW}^{-} + \frac{1}{f_{ctrl} I_{RW}} {}^{B}C^{RW,\#}\mathbf{u}_{dct} \tag{5.15}$$

where ω_{RW}^{+} represents the new commanded wheel speed, ω_{RW}^{-} is the most recent RWA wheel speeds reported by the RWA node, f_{ctrl} is the rate for the Controller node, and the symbol # represents the pseudoinverse of a matrix.

In summary, the Controller node uses Equation (3.37) to compute the state error using the most recent values published by the Guidance, and Emulated Dynamics node. The error is then fed to Equation (5.14) to compute the torque needed by the controller, and finally, Equation (5.15) converts the torque to new commanded wheel speeds. The commanded wheel speeds are published at a rate $f_{ctrl} = 10$ Hz.

Table 5.3: Controller Modes for DCT and FlatSat testbeds.

ID	Mode	Algorithm	Description
1	None	N.A.	No Controller, the node does not publish any RWA speed command
2	Extended LQR	*LQR*	LQR-based algorithm with desired trajectory feedforward given by Equation (5.14)

The available modes for the Controller node are listed in Table 5.3. Currently, only two modes are implemented, the first one, "None" does not publish any command, and it is used for emergency stop as well as the initial mode for this node. The other mode "extended LQR" consist of the implementation of Equation (5.14) and publish the commanded reaction wheel speeds given by Equation (5.15). Similar to the Guidance node, the Controller node subscribes to a topic that sets its current mode.

Estimation

The Estimation node is responsible for taking the sensor readings from the IMU and Pi Cam and combining them to produce an adequate estimate of the state of the testbed. This testbed utilizes an Extended Kalman Filter (EKF) is used as the sensor fusion and estimation algorithm. The EKF relies on the use of a Taylor expansion about the current estimated state, and is better suited for nonlinear systems compared to the regular Kalman Filter [154]. The EKF has been used widely in attitude estimation for spacecraft systems [155, 156].

In its simplest form, the EKF uses two steps: a prediction and an update step. During the prediction step, the EKF propagates the estimate, known as *a priori*, using an internal model of the system. These steps also propagate the estimate covariance matrix. In the update step, the EKF utilizes the sensor measurements, along with their measurement noise covariances, to update the state, known as *posteriori*, and the covariance matrix.

Initialization

The state is initialized simply by letting the state vector be equal to $\hat{\mathbf{x}}_0 = [\mathbf{q}_0, \boldsymbol{\omega}_0, \mathbf{h}_{RW,0}]^T = [1,0,0,0,0,0,0,0,0,0]^T$. Where for the state of the testbed, the angular momentum of the reaction wheel was included. Additionally, the estimate measurement covariance is initialized as $P = I_{10x10}$.

Predict

The dynamics of the system are given by

$$\begin{aligned} \dot{\mathbf{q}} &= \mathbf{f}(t, \boldsymbol{\omega}), \text{ From Eq. (3.7)} \\ \dot{\boldsymbol{\omega}} &= \mathbf{f}(t, \boldsymbol{\omega}, \mathbf{h}_{RWA}), \text{ From Eq. (3.6)} \\ \mathbf{h}_{RWA} &= \boldsymbol{\tau}_c \text{ From Eq. (5.14)} \end{aligned} \tag{5.16}$$

where the $\boldsymbol{\tau}_c$ comes from the Controller Node. The discrete step $\hat{\mathbf{x}}_{k|k-1}$ is given by

$$\hat{\mathbf{x}}_{k|k-1} = \hat{\mathbf{x}}_{k-1} + 1/f_{est} \begin{pmatrix} \dot{\mathbf{q}} \\ \dot{\boldsymbol{\omega}} \\ \mathbf{h}_{RWA} \end{pmatrix} \tag{5.17}$$

and f_{est} is the rate of the estimator.

The estimate covariance measurement prediction is given by,

$$P_{k|k-1} = F_k P_{k-1} F_k^T + Q_k \tag{5.18}$$

where F_k is the jacobian of the equation of motion given by,

$$F_k = \left. \frac{\partial \mathbf{f}}{\partial \mathbf{x}} \right|_{x_{k-1}, u_k} \tag{5.19}$$

and, Q is the estimated process noise on the system.

Update

The update step begins when new measurements, either from the IMU, Pi Cam, or both arrive at the EKF node. Note that it is expected that a new IMU measurement arrives each time the EKF updates, while the Pi Cam arrives at a rate that is a *multiple* of the EKF rate. The residual of the function is given by,

$$\mathbf{r}_k = \mathbf{y}_k - H_t \hat{\mathbf{x}}_{k|k-1} \tag{5.20}$$

where the y_k is a column vector of size 3x1 or 7x1 where it depends as to whether measurement from the IMU, or IMU and Pi Cam are present. Furthermore, the measurement model matrix is given by,

$$H_t = \begin{cases} [0_{3x4}, I_{3x3}, 0_{3x3}] & \text{IMU only} \\ \begin{bmatrix} I_{4x4} & 0_{4x3} & 0_{4x3} \\ 0_{3x4} & I_{3x3} & 0_{3x3}] \end{bmatrix} & \text{Pi Cam and IMU} \end{cases} \tag{5.21}$$

The Kalman gain is then given by,

$$K_k = P_{k|k-1} H_k^T \left(H_k P_{k|k-1} H_k^T + R_k \right)^{-1} \tag{5.22}$$

where the sensor covariance is given by,

$$R_t = \begin{cases} R_{imu} & \text{IMU only} \\ \\ blkdiag(R_{pi\ cam}, R_{imu}) & \text{Pi Cam and IMU} \end{cases} \tag{5.23}$$

where $R_{pi\ cam}$, R_{imu} is the measurement covariance for the Pi Cam and IMU, respectively. and $blkdiag(A, B)$ is a block diagonal function. The *posteriori* state and covariance estimate are then given by,

$$\begin{aligned} \hat{\mathbf{x}}_k &= \hat{\mathbf{x}}_{k|k-1} + K_k \mathbf{r}_k \\ P_k &= I - K_k H_k P_{k|k-1} \end{aligned} \tag{5.24}$$

The EKF node publishes the estimate of the state given by Equation (5.24). The EKF is expected to run at 20 or 40 Hz.

Table 5.4: Estimation Modes for DCT and FlatSat testbeds.

ID	Mode	Algorithm	Description
1	None	N.A.	No estimation algorithm, the node does not publish the DCT state
2	EKF	EKF	The extended Kalman filter shown in this subsection publishes the current best testbed estimate.
3	IMU Only	Dead reckoning	The Estimator integrates only the IMU signal as a form of dead reckoning.

Table 5.4 shows the available modes for the Estimator subsystem node. Similar to the Guidance and Controller node, there exists a "None" mode in which the estimator does not publish anything. The Extended Kalman filter described in this section corresponds to mode "EKF" and it is the nominal mode used in the testbed. Additionally, a simpler estimator known as "IMU Only" uses the concept of dead reckoning where the estimated quaternion is computed from Equation (3.7) and reports the raw IMU angular velocity is used as the testbed's angular velocity. This mode is

not recommended as dead reckoning leads to drift and random walk of the quaternion but was implemented for debugging the Estimator node without the PiCam. Finally, the Estimator node subscribes to a mode command topic.

5.1.4 GNC Mode Manager and Testbed Safe Mode

An additional node not shown in Diagram 5-4 is a GNC Mode Manager (GMM) node. This ROS node is responsible for parsing User commands of the overall mode of the testbed, as well as autonomously commanding the safe mode.

Currently, the GMM has three operating modes implemented, "None" mode in which all the GNC Nodes are set to none, and the RWA commanding is disengaged, "Mission" mode in which the nominal mode for each subsystem is triggered, and the RWA node is engaged to receive commands, and "Safe" Mode which attempts to bring the testbed to its safe attitude. The Modes definition and IDs are shown in Table 5.5.

Table 5.5: GNC Mode Manager operating modes for DCT and FlatSat testbeds.

ID	Mode	Description
1	None	Initial mode the testbed enters when ROS starts. All subsystems are at None.
2	Mission	Main mode where all the GNC subsystems and actuators are able to operate and follow commanded reference trajectories.
3	Safe Mode	Mode used for a soft emergency, or to bring the testbed to a safe attitude. Safe mode may be triggered by the user or autonomously by GMM.

The GMM mode contains logic that allows the user to change the testbed between different operating modes. The flow logic is shown in Figure 5-9. When the DCT or FlatSat testbed is initialized by ROS the testbed is initialized at the None mode. Physically, this mode allows for the testbed operator to safely move the testbed without the GNC system fighting against it. The testbed will remain in this operating mode unless either the User commands the testbed to switch to a different operating mode (Mission, or Safe Mode), or the ROS system is shut down via a terminal command. In Mission operating mode, the guidance begins holding at the safe attitude unless the user specifies a different attitude for hold. The Controller node is set to the extended LQR controller, and the Estimator uses the EKF to determine its

position. In Mission mode, the RWA node is engaged which means it tries to match the commanded wheel speeds given by the controller. Mission mode is the intended

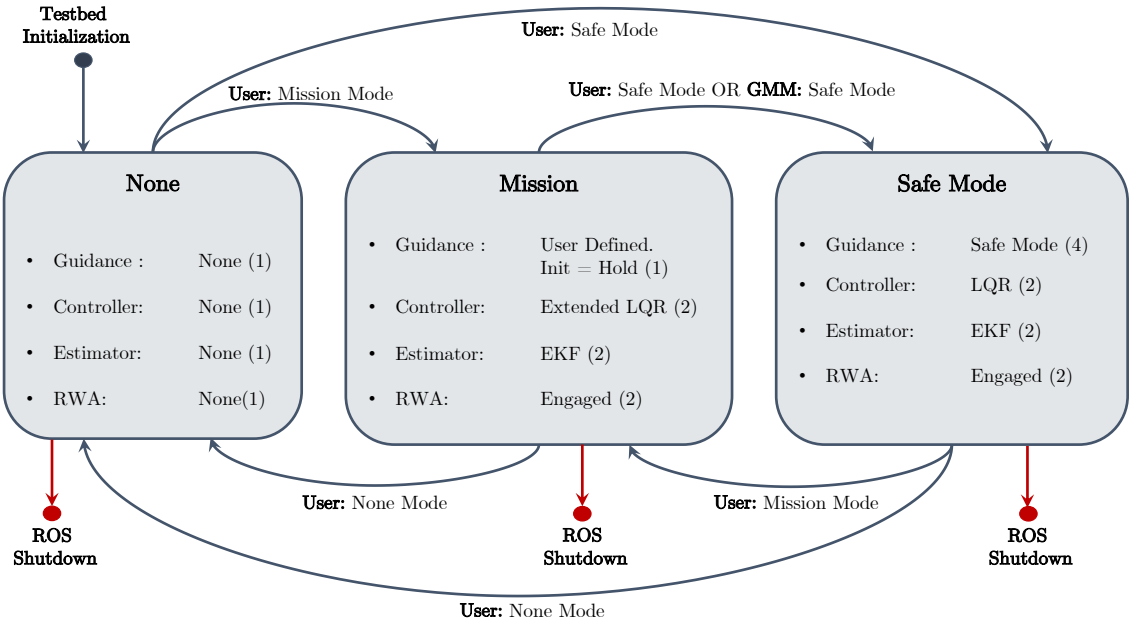

Figure 5-9: GNC Mode Manager modes flow

nominal mode of operation in which the user may command different Guidance reference trajectories using the modes in Table 5.2. The GMM has three methods for leaving the Mission mode: ROS is shut down, the User requests GMM to switch to None or Safe mode, and the GMM autonomously switches to Safe mode if the testbed triggers certain conditions as defined below. The last operating mode is Safe Mode which attempts to move and maintain the testbed at its safe attitude. The testbed accomplishes this by triggering the Guidance safe mode (4) and passing to the guidance the current state of the testbed. The GMM operating mode can change from Safe mode by either a User mode request or through ROS shutdown.

GMM Autonomous Safe Mode

As part of the GMM, there exists an autonomous safe mode logic that checks whether certain safety conditions of the testbed are violated. The GMM operates at $f_{gmm} = 2$ Hz, and subscribes to the RWA, Controller, and Estimator subsystem. The GMM keeps track of the current running sum fo the RWA,

$$\bar{\boldsymbol{\omega}}_{rwa} = \frac{1}{N_{sum}} \sum_{i=0}^{i=N_{sum}-1} \boldsymbol{\omega}_{rwa}[t - t_i] \tag{5.25}$$

where $\boldsymbol{\omega}_{rwa}[t-t_i]$ represents the vector of wheel speeds that the RWA node published, and t_i represents the time of the last RWA command. Thus, the GMM keeps track of the last N_{sum} RWA speeds. For the DCT $N_{sum} = 10$, which at the publish rate of the RWA node of $f_{rwa} = 20$ Hz, corresponds to roughly 0.5 seconds of data.

Another value that is kept track of is the angle between the testbed's z^b-axis and the -z^I-axis. Given the current quaternion of the testbed $\mathbf{q}_{dct}$ that describes the attitude from inertial to body frame, it is possible to express the z^b-axis in the inertial frame as,

$$\mathbf{z}^I_{dct} = \mathbf{q}_{dct} \otimes [0, \mathbf{z}^b]^T \otimes \mathbf{q}^{-1}_{dct} \tag{5.26}$$

where $\mathbf{a}\otimes\mathbf{b}$ represents the quaternion product. The angle between the inertial $-z$-axis and the body frame z-axis is then given by,

$$\theta_{z,dct} = \arccos([0, 0, -1]^T \cdot \mathbf{z}^I_{dct}) \tag{5.27}$$

The angle $\theta_{z,dct}$ is kept track by the GMM. The values for which the Auto Safe Mode triggers is shown in Table 5.6. When the angle from vertical reaches 10° a visual warning is issued on the ROS terminal, however, as the angle increase to 14°, Auto Safe Mode is triggered by the GMM. At this point, a visual red warning appears on the ROS terminal, the current state estimate is given to guidance, and its safe trajectory mode begins. The value of 14° was chosen as the hemispherical air bearing is capable of rotating at most 17°. Alternatively for the RWA subsystem, speeds visual warnings appear when any of the individual speeds reaches a value greater than 200 rad/s. Auto Safe Mode is triggered when either *at least one* reaction wheel speed crosses a magnitude of 250 rad/s, *or two or more* reaction wheels go above the 200 rad/s speed limit. The values for the wheels were chosen as the maximum wheel speed for the testbed were measured to be between $280 - 300$ rad/s depending on

the LiPo battery voltage. The values of Table 5.6 are set through an editable ROS parameter file.

Table 5.6: GNC Auto Safe Mode warning and emergency thresholds.

Value	Description	Warning	Emergency
$\theta_{z,dct}$	Angle from vertical	20°	25°
$\bar{\omega}_{rwa}$	Average RWA wheel speed	200 rad/s	250 rad/s

In addition to the Autonomous Safe Mode, there exists three additional safety mechanisms of the testbed. First, the user can command the safe mode command at any given time through the GMM. Second, the user may command the reaction wheels to disengage at any time outside the GMM, and upon ROS shutdown, the wheels are commanded to disengage automatically leading to a reduction in wheel speeds by friction only. Third, an Emergency Stop (E-Stop) exits that connect directly to the Basic Micro Roboclaw motor controllers, and is connected via a fail-safe XBee. This E-Stop resides outside the ROS framework and provides an alternative way to deactivate the wheels in the event ROS is unresponsive. Once pressed, the XBee will open the circuit between the motor controller input power, and the wheel speeds will go to zero by friction alone. No commands are accepted or acted upon by the motor controllers while the E-Stop is latched. This suite of safety mechanisms provides multiple ways for the testbed to be shut down and prevent damage to the air-bearing or the testbed.

5.1.5 FlatSat Results

This subsection covers two example cases and the capability of Monte Carlo simulations for the FlatSat.

The FlatSat emulated dynamics were those in Equation (5.10) with a disturbance torque corresponding to the torque from gravity from a CM-CR offset of 10 microns in the $-z^b$-direction. The testbed parameters used for FlatSat are shown in Table 5.7. The moments of inertia were the best estimates of the actual testbed based on a SolidWorks model. The rotation matrix from the reaction wheel frame is given by matrix ${}^{B}C^{RW}$. Note that the fourth wheel (last column of the matrix) is pointing

along the z^b axis.

Table 5.7: FlatSat simulation parameters

Parameter	**Description**	**Unit**	**value**
$I_s = [I_x, I_y, I_z]$	Inertia of FlatSat	kgm^2	[1.54, 1.05, 1.01]
I_r	Axial inertia of RWA	kgm^2	0.0075
${}^{B}C^{RW}$	RWA configuration	[-]	$\begin{bmatrix} 0, & 0.866, & -0.866, & 0 \\ -1, & 0.5, & 0.5, & 0 \\ 0, & 0, & 0, & 1 \end{bmatrix}$

The controller gain for the extended LQR used on the FlatSat simulation was given by,

$$K_{lqr,DCT} = \begin{pmatrix} -0.71 & 0.00 & 0.00 & -16.54 & 0.00 & 0.00 & -8.68 & 0.00 & 0.00 \\ 0.00 & -0.63 & 0.00 & 0.00 & -14.63 & 0.00 & 0.00 & -7.38 & 0.00 \\ 0.00 & 0.00 & -0.49 & 0.00 & 0.00 & -11.36 & 0.00 & 0.00 & -5.52 \end{pmatrix} \tag{5.28}$$

Three cases are shown in the FlatSat, namely the results for a single spin, a compound slew corresponding to the imaging maneuver in Figure 5-1, and a Monte Carlo simulation where the ability for the attitude controller to reject an initial attitude error was testbed far beyond the expected limits of the DCT.

The first example is shown in Figure 5-10. The testbed was commanded to perform a single-axis spin about the z^b-axis. On all four subplots, the horizontal axis represents the time published by ROS. The subplot plot where there is no data at $t = 0$ (s) corresponds to the GNC algorithms that have not been initialized. When ROS is launched on the FlatSat only the emulated dynamics and reaction wheels nodes are started. The controller, estimation, and guidance do not turn on until the user commands them to. Plotted is the RWA speed, the angular velocity, quaternion, and attitude error in Figure 5-10a, 5-10b, 5-10c, abd5-10d, respectively.

For the single-axis test, it was expected that only the fourth reaction wheel was active. This is confirmed in Figure 5-10a with RWA 4 having the highest angular speed. Due to the conservation of angular momentum, as the RWA 4 speed increases the angular velocity of the FlatSat in the z^b-axis increases at a rate proportional to

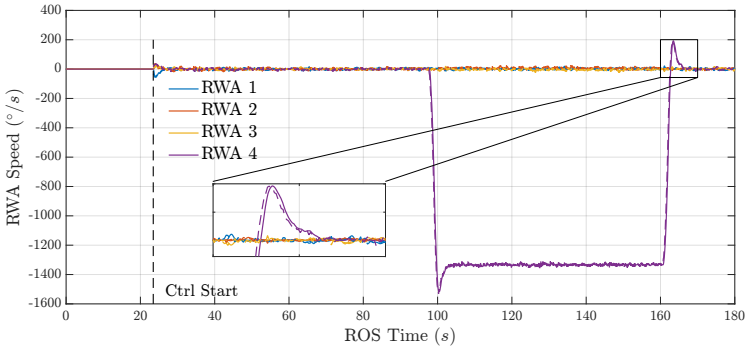

(a) RWA time history

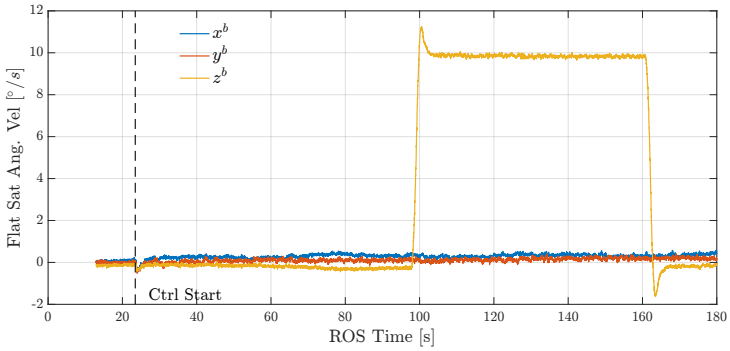

(b) Angular velocity time history

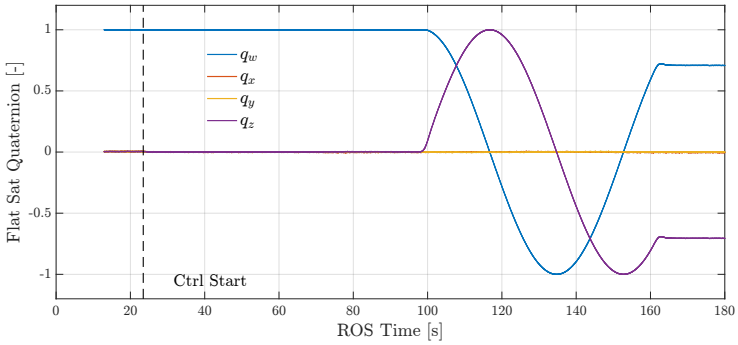

(c) Quaternion time history

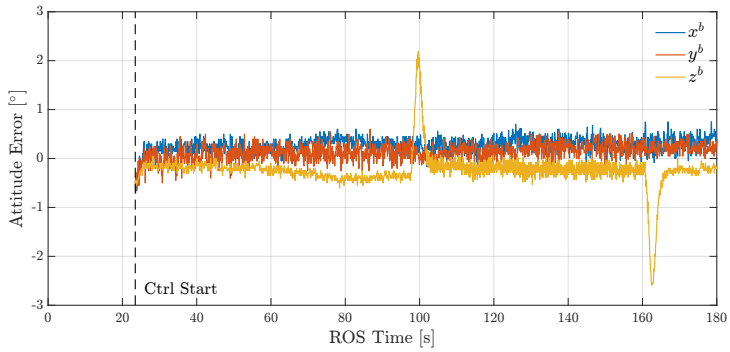

(d) Attitude error time history

Figure 5-10: FlatSat single axis closed-loop control test results.

the ratios of the inertia of the wheel and I_z. Also plotted in Figure 5-10a is an image inset of the wheel speeds at time $t \in [155, 165]$ (s). The purple dashed line seen in the inset corresponds to the *commanded* wheel speed. The difference in the commanded speed and reported wheel speed is due to a phase lag in the RWA motor controller.

Figure 5-10c shows the quaternion time history. As expected, the quaternion is smooth due to the twice differential reference trajectory is given by the Guidance node. Furthermore, only the scalar and z components of the quaternion move, which is consistent with a slew about the z^b-axis. Finally, figure 5-10d shows the attitude error, in degrees, during the single-axis spin. The attitude error remained within 1 degree in magnitude for all time except at the spin ramp-ups. This can be mitigated by modifying the argument t_r in the guidance command and increasing it to a longer ramp-up time period.

The next case corresponded to the imaging maneuver where a compound slew is required for an RSA to image a target. Figure 5-11 shows the FlatSat result for the imaging maneuver. The angular velocity of the testbed, the quaternion, and the attitude error are shown like in the single-spin case, however, rather than showing the reaction wheel time history, the reference angular velocity provided by the guidance subsystem was plotted in the first subplot. In Figure 5-11a, the reference trajectory begins with a spin up about the z^b-axis. The ramp time for this case was increased compared to the single-axis case, yielding a lower attitude error. The reference spin rate was set to $7^\circ/s$ since this rate is a realistic rate for a satellite in LEO [110]. At $t \in (80, 160)$ (s) the testbed slews about the inertial frame to a maximum rate of $2^\circ/s$ about the x^I-axis. The oscillation between the x^b and y^b-axis shown in the blue and red lines of Figure 5-11a, respectively, are due to the commanded angular velocity needing to change so it ensures that it is always pointing along the x^I-axis as the testbed spins about the z^b-axis. It is during this time period when the imaging is taken place, and it is highlighted in the figures in a light blue background.

The estimated angular velocity and quaternion are given in Figures 5-11b and 5-11c, respectively. Note that the angular velocity appears to match the reference angular velocity, although noise is present. The quaternion remains relatively smooth

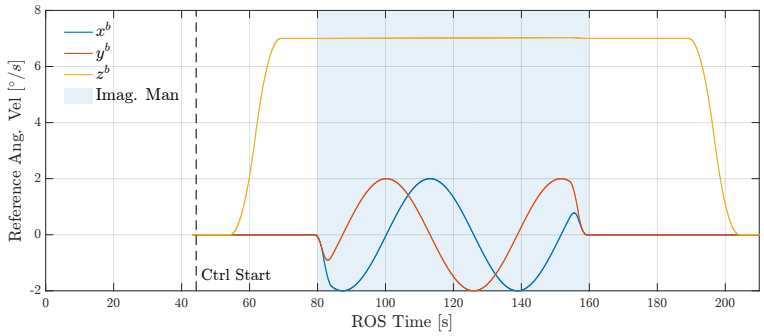

(a) Reference angular velocity time history

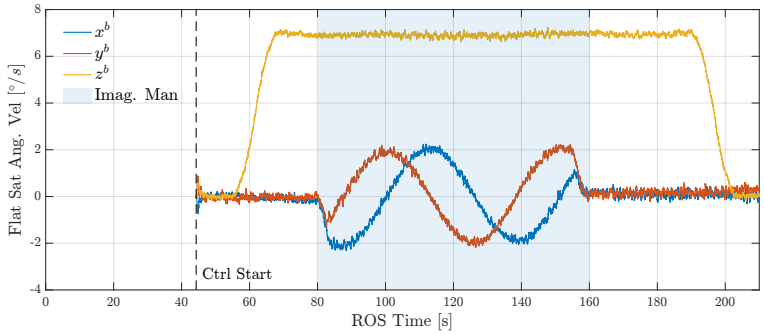

(b) Angular velocity time history

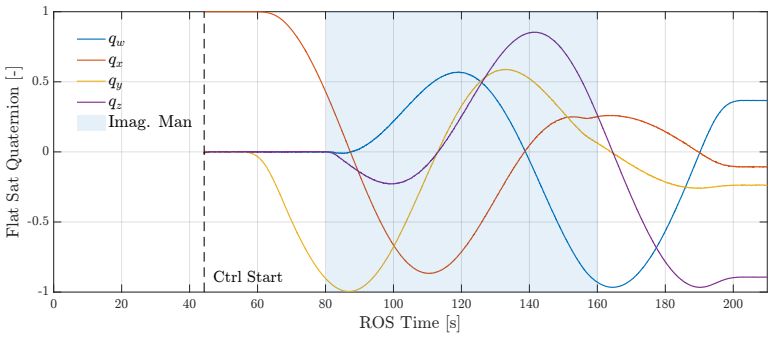

(c) Quaternion time history

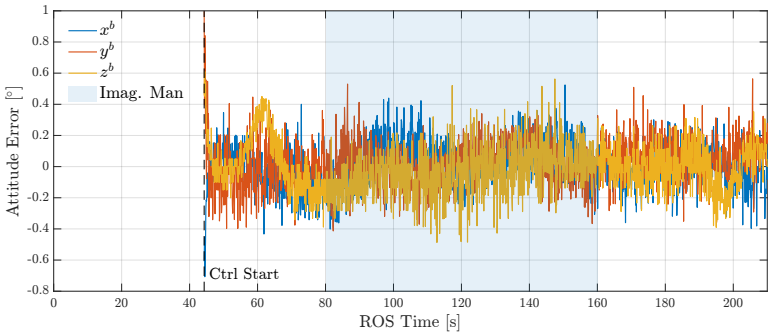

(d) Attitude error time history

Figure 5-11: FlatSat imaging maneuver closed-loop control test results. The blue area represents where imaging would occur.

and again it is due to the smooth trajectory design in the Guidance node. The attitude error is shown in Figure 5-11d in degrees. Note that similar to the single-axis spin case, there is two bumps in the z^b-axis during the ramp up and ramp down of the optical spin axis. During the actual imaging maneuver, the attitude error remains within 1 degree and has a zero mean. Overall, the FlatSat imaging maneuver demonstrates the ability of the GNC systems working together with the RWA actuators to maintain low attitude error during a complex maneuver.

The final case showing is the ability of the FlatSat testbed to perform hardware-in-the-loop Monte Carlo simulation. ROS allows for the creation of time-based scripts that trigger different GNC modes. As part of the testing of the FlatSat, a Monte Carlo simulation was performed in which the testbed had an initial state error, and the controller was commanded to reject the error. The results of the Monte Carlo simulation are shown in Figure 5-12a. All the simulations show that the attitude and rate error converges rapidly with an average error of less than one degree after 15 seconds. Furthermore, the actual DCT testbed is not expected to have attitude errors as those shown in this example case.

This subsection only covered three example test cases that were performed on the FlatSat satellite. Additional test cases not shown here was the ability to emulate sensor errors in the PiCam, as well as rigorous testing of the imagery maneuver at different CM-CR offset. The insights gained from the FlatSat testing allowed for a high degree of confidence in the subsystems and actuators before being placed in the air-bearing.[5]

This section covered the background and development of the Dynamics and Control Testbed in particular the combined hardware-in-the-loop testing performed for the FlatSat testbed. Presented in this section were the main GNC algorithms, the mode manager and autonomous safe mode, and example cases for the FlatSat testbed. The testbed was designed to be flexible allowing flexible implementation of additional

[5]The ROS code for the FlatSat, ADT, and DCT as well as a Wiki can be obtained at: `https://github.mit.edu/SSL/SpinAp`

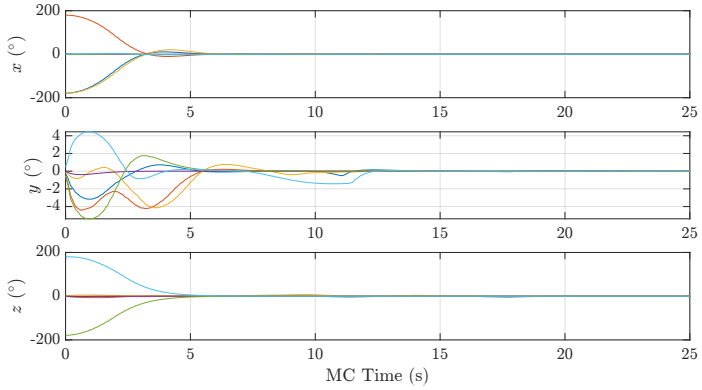

(a) Attitude Error

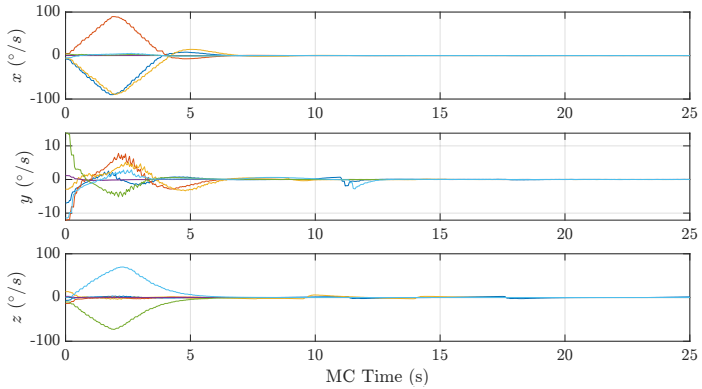

(b) Rate Error

Figure 5-12: FlatSat initial error rejection results.

guidance, estimation, or controller algorithms. Due to this, the DCT is not limited to testing RSA satellites and as such can be used as a general GNC testbed for satellites.

5.2 Results for a Dynamically Similar Testbed

This section presents the results for the DCT in the hemispherical air-bearing testing, the scaling laws used to convert from a testbed to a satellite in LEO, and the resultant expected behavior of RSA satellites in LEO and MEO via scaling of the DCT.

5.2.1 Full Dynamics and Control Testbed Results

This section presents the results of the Dynamics and Control Testbed. The testbed was mounted in the hemispherical air-bearing and all the GNC algorithms implemented in the FlatSat, including GMM, were running. Two examples are given, one representing a single spin similar to the test done for the FlatSat, and an imaging maneuver demonstrating the motion from Figure 5-1.

One of the first test cases to run to confirm that the DCT's subsystem worked was a single spin about the testbed z^b-axis. The commanded spin rate was only $5°/s$ compared to the $10°/s$ from of the FlatSat test case. The results are shown in Figure 5-13 where similar to the FlatSat case the reaction wheel time history, estimated angular velocity, quaternion time history, and attitude error are plotted. In all the subfigures, the horizontal axis represents the time of ROS since the reaction wheels node started, and a vertical black dashed line represents the time in which the extended LQR was activated.

The reaction wheel speeds reported by the encoders are shown in Figure 5-13a. At time $t = 70$ (s) the command for the single-axis spin is sent, leading to reaction wheel 4 spin in the clockwise direction (negative sign). However, during the first 70 seconds, the values for the three coplanar wheels increase. This is due to angular momentum accumulation from the wheels while they hold attitude. The main source of the accumulated angular momentum is the torque from gravity due to the CM-CR offset. Despite this external torque, the angular velocity of the testbed does

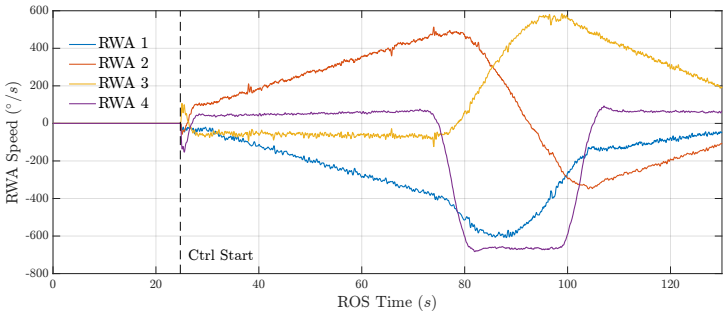

(a) RWA time history

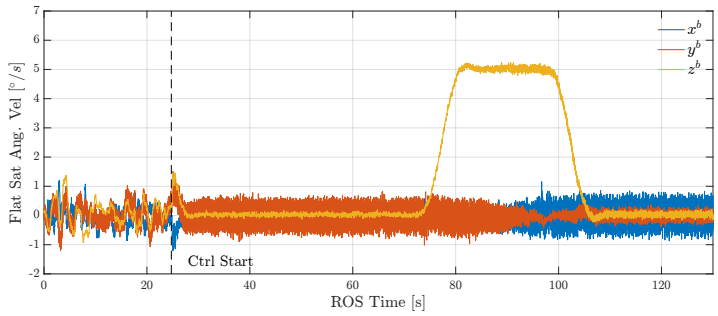

(b) Angular velocity time history

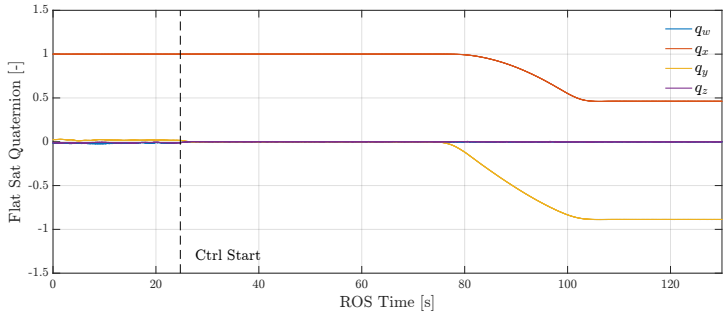

(c) Quaternion time history

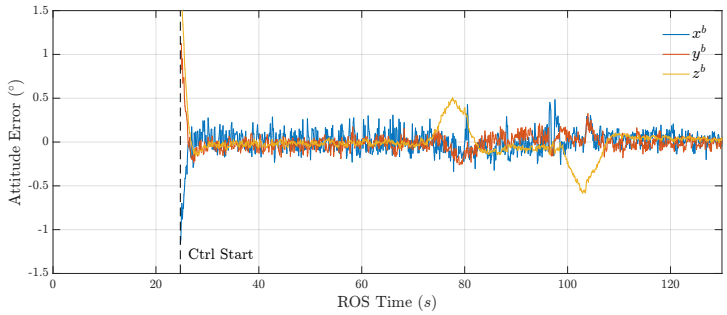

(d) Attitude error time history

Figure 5-13: DCT $5°/s$ sing-axis closed-loop control test results.

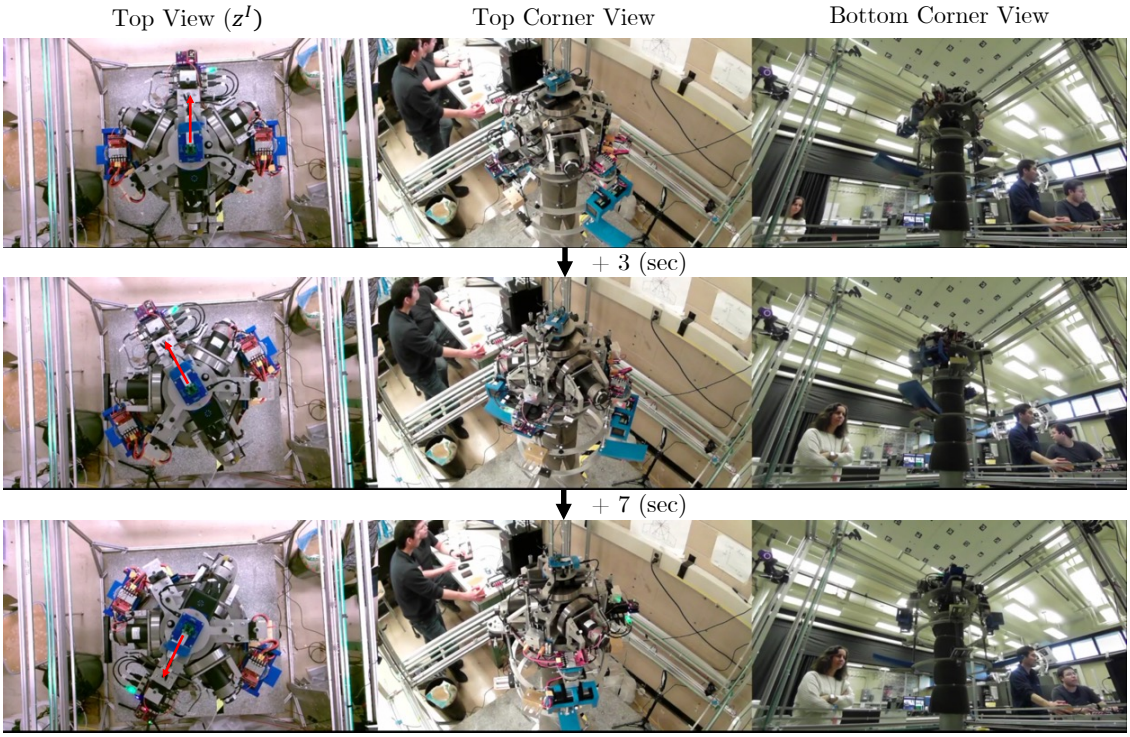

Figure 5-14: DCT single-axis $15°/s$ close loop test recording. Arrow pointing towards y^b-axis is shown in the Top View pictures

have a mean of zero before the spin command as seen in Figure 5-13b. From the amplitudes of the angular velocity of the RWA 4 and the testbed z-axis, it is possible to calculate the inertia ratio $I_z/I_{rwa} \approx 134$. The wheels are estimated to have an inertia of 0.0075 (kgm^2) [4] which would approximate the inertia of the testbed in the z^b-direction to be about 1.012 (kgm^2).

The quaternion for the single-spin case is given by Figure 5-13c. Similar to the FlatSat case, the quaternion is significantly smoother than the estimated angular velocity. This is due to the estimated angular velocity being mostly driven by the IMU which is noise, while the estimated quaternion comes from the combination of measurements from the PiCam and IMU. In terms of attitude error shown in Figure 5-13d, the error performance is better than the FlatSat. The error from the FlatSat from the emulated sensors included noise levels obtained from the ADT which were thought to be conservative, and thus this result is not unexpected.

Additionally, Figure 5-14 shows views from the recording cameras of the DCT

testbed area during a single-spin axis. The pictures shown are for a spin about the z^b-axis at $15^\circ/s$. Three views are shown, namely, a top view looking down from the center of the ArUco board, a top corner view looking down from the $-x^I$, $+y^I$ corner of the ArUco board, and a bottom corner view looking up. The three snippets shown occur in a span of 10 seconds. Also, shown in the Top View images is a post-processing overlay of the y^b-axis. The testbed rotates approximately 150° as expected.

An additional test performed in the DCT during the checkout process was to emulate an RSA imaging maneuver. This test is separate from the scaled results in Section 5.2.3 as the attempt was not to replicate a certain satellite in LEO or MEO, but rather was to confirm the ability of the testbed to do a full imaging maneuver. The results of this test are given in Figure 5-15. For all four subplots, the horizontal axis represents the ROS time as before. Additionally, the time at which the controller was active is shown by a black dashed line, The imaging maneuver in this test had three components, a slew of 7° about the $-x^b$-axis, represented by the light green region in the figures. This is followed by the spin while tracking part of the maneuver, which is represented by the light blue region. A user-issued safe mode command to bring the testbed pointing at the nominal attitude $\mathbf{q}_{nom} = [0, 1, 0, 0]^T$, and shown by the light magenta region.

The reference and estimated trajectory are given by Figures 5-15a, and 5-15b. The Safe Mode part of the trajectory had the highest angular velocity command out of all three trajectories. This is due to the requirement that the safe mode must be completed within 20 seconds. Note that before the controller being active, the estimated angular velocity was nonzero. The large noise in the angular velocity is due to IMU sensor noise, and structural vibration of the testbed. It was found via IMU, PiCam, and OptiTrack marker data, that the testbed itself had a mode at 15.3 Hz. This mode is suspected to be a structural mode of the lab itself.

Figure 5-15c shows the time history of the quaternion. After each segment the reference quaternion goes into hold mode which can be seen by the quaternion time history holding steady after each colored region. During the Imaging maneuver, the testbed slew a total of 17° around the inertial x-axis. During Safe Mode, the

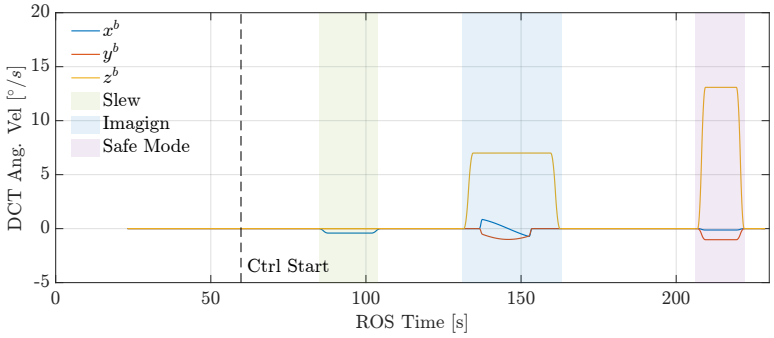

(a) Reference guidance time history

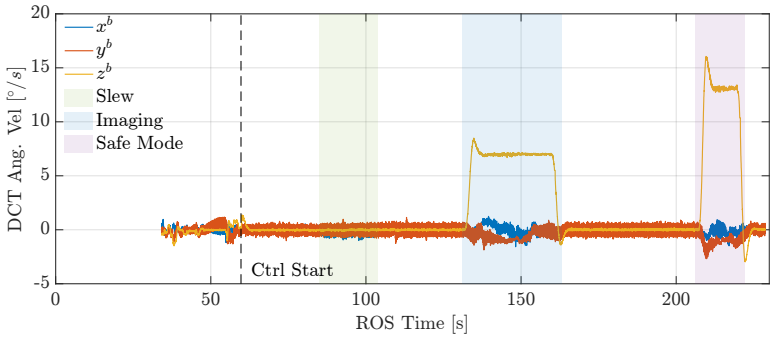

(b) Estimated angular velocity time history

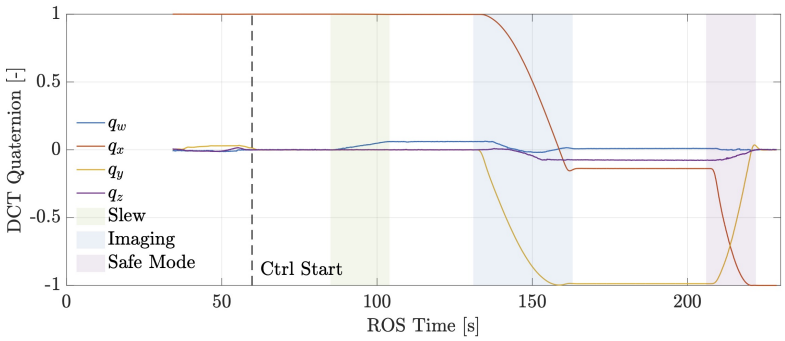

(c) Estimated quaternion time history

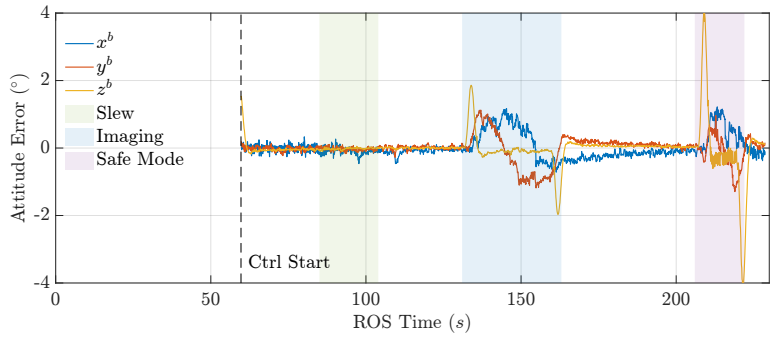

(d) Attitude error time history

Figure 5-15: DCT RSA imaging maneuver test results.

guidance trajectory commanded the quaternion to go to the attitude quaternion $[0, -1, 0, 0]$ which is the equivalent quaternion as the nominal attitude, $\mathbf{q}_{nom}$. The reason for choosing $[0, -1, 0, 0]$ was because this represented the shortest rotation from the testbed attitude at the start of Safe Mode.

The attitude error during the entire trajectory is given by Figure 5-15d. Note that during the slew aspect of the trajectory, the attitude error magnitude was below 0.2°. During, the imaging maneuver the attitude error increased close to a maximum error of 1.98° which happened during the optical axis spin down. Despite this increase in error, the testbed maintained stable attitude control, and between the Imaging maneuver and Safe mode, the attitude error converged to zero. During Safe mode, the attitude error was the highest. This is expected as the comanded rate was the highest during this period.

This subsection presented the results of the DCT on the hemispherical air-bearing. The tests shown in this section demonstrate the ability of the GNC systems to stabilize and control the testbed and follow a reference guidance trajectory that emulates the expected motion of an RSA satellite.

5.2.2 Scaling Laws

This section covers the scaling laws for the DCT for LEO and MEO type satellites. A sample problem is given to show how the scaling laws can be used.

The approach for generating the scaling laws follows that of Ciarcià [109] where the Buckingham-π theorem was used to emulate the motion of a formation flying satellite on a testbed. The Buckingham-π is one of the main theorems used for dimensional scaling and is a powerful method of generating scaling laws for dimensional analysis [157].

The Buckingham-π theorem relies on finding the number of parameters in a given problem and the number of fundamental units. For a satellite, the typical parameters present are,

$$t, m, I_x, I_y, I_z, \theta, \dot{\theta}, \ddot{\theta}, f, \tau \tag{5.29}$$

where the principal inertia values are given by $I = \text{diag}([I_x, I_y, I_z)$, the mass is given by m, the torque and force by τ and f, respectively, and the state variable and derivative given by θ, $\dot{\theta}$, and $\ddot{\theta}$. The dimensional base units are for the list of variables are then given by $[M]$, $[T]$, $[L]$ for mass, time, and length, respectively. In total, we have $n = 10$ parameters, and $k = 3$ base units, according to the Buckingham-π theorem we should expect $p = n - k = 7$ nondimensional parameters that allow us to scale between two similar systems. These parameters are called π parameters.

Whereas the Buckingham-π theorem states the minimum number of possible parameters needed for scaling, the method for finding those parameters is not explicitly stated. A method of obtaining the parameters is by creating a matrix that shows the relationship between the base units and the parameters. For example, the variable t has base units of $[T]^1$, mass m has $[M]^1$, inertia I has units of $[M]^1[L]^2$, force f has units of $[M]^1[L]^1[S]^{-2}$, torque τ has $[M]^1[L]^2[S]^{-2}$. Angles, however, do not have dimensions, and θ itself is a π parameter. The angular speed $\dot{\theta}$ does have units of $[T]^{-1}$, and angular acceleration $\ddot{\theta}$ has units of $[T]^{-2}$. The exponent values for each variable in Equation (5.29) are taken to produce a column vector and a matrix Π_{sat} can be generated and is given by,

$$\Pi_{sat} = \begin{pmatrix} 0 & 1 & 1 & 1 & 1 & 0 & 0 & 0 & 1 & 1 \\ 0 & 0 & 2 & 2 & 2 & 0 & 0 & 0 & 1 & 2 \\ 1 & 0 & 0 & 0 & 0 & 0 & -1 & -2 & -2 & -2 \end{pmatrix} \tag{5.30}$$

Note that in Equation (5.30) the rows represent the exponent of the base units $[M]$, $[L]$, and $[T]$, respectively for a given variable, while the columns represent each variable in the order given by Equation (5.29). The π parameters are a combination of the problem parameters such that their equivalent dimension is equal to zero. Thus, the goal is to obtain a vector $\boldsymbol{\zeta}$ such that

$$\mathbf{0} = \Pi_{sat}\boldsymbol{\zeta} \tag{5.31}$$

where the values in $\boldsymbol{\zeta}$ represent the set of exponents for which the satellite variables

are raised to. This is equivalent to finding the nullspace of matrix Π_{sat} and can be found by using MATLAB's null(Π_{sat}, 'r') where the argument 'r' forces the null vectors to be rationals. The nullspace matrix is given by,

$$\emptyset(\Pi_{sat}) = \begin{pmatrix} 0 & 0 & 0 & 1 & 2 & 4 & 2 \\ 0 & 0 & 0 & 0 & 0 & -1 & 0 \\ -1 & -1 & 0 & 0 & 0 & -1 & -1 \\ 1 & 0 & 0 & 0 & 0 & 0 & 0 \\ 0 & 1 & 0 & 0 & 0 & 0 & 0 \\ 0 & 0 & 1 & 0 & 0 & 0 & 0 \\ 0 & 0 & 0 & 1 & 0 & 0 & 0 \\ 0 & 0 & 0 & 0 & 1 & 0 & 0 \\ 0 & 0 & 0 & 0 & 0 & 2 & 0 \\ 0 & 0 & 0 & 0 & 0 & 0 & 1 \end{pmatrix} \tag{5.32}$$

where each column vector represents a null vector. For example, the first column corresponds to the $\pi_1 = \frac{I_y}{I_x}$, the second column to $\pi_2 = \frac{I_z}{I_x}$, etc. The full list of π parameters is then given by,

$$\begin{aligned} \pi_1 &= \frac{I_z}{I_x} & \pi_2 &= \frac{I_y}{I_x} & \pi_3 &= \theta \\ \pi_4 &= t\dot{\theta} & \pi_5 &= t^2\ddot{\theta} & \pi_6 &= \frac{t^4 f^2}{I_x m} \\ \pi_7 &= \frac{t^2 \tau}{I_x} \end{aligned} \tag{5.33}$$

The first two π parameters represent the inertia ratios of the testbed. The inertia ratios are the minimum set of values needed to obtain the shape of the Polhode of the system [158]. Parameter three is the angle value itself given that it is already nondimensionalized. Parameters four and five follow from basic integration: to obtain an angle the rate needs to be multiplied by time, and an angle scales with the square of the time multiplied by the angular acceleration. Parameter seven reflects the angular acceleration caused by a combination of torque and inertia (e.g. an increase in torque leads to an increase in acceleration, while an increase in inertia yields a

smaller acceleration).

Given the parameters, the scaling laws can be obtained by setting π parameters from the satellite and testbed equal to each other, hence,

$$\frac{I_{z,tb}}{I_{x,tb}} = \pi_1 = \frac{I_{z,sc}}{I_{x,sc}}$$

from this, a scaling factor law can be developed as

$$\lambda_{I_x} = \lambda_{I_y}$$

where $\lambda_{\#} = \frac{\#_{sc}}{\#_{tb}}$. The full scaling laws, are given by,

$$\begin{aligned}
&\lambda_{I_y} = \lambda_{I_x} \qquad \lambda_{I_z} = \lambda_{I_x} \qquad \lambda_\theta = 1 \\
&\lambda_{\dot{\theta}} = \frac{1}{\lambda_t} \qquad \lambda_{\ddot{\theta}} = \frac{1}{\lambda_t^2} \qquad \lambda_f^2 = \frac{\lambda_m \lambda_{I_x}}{\lambda_t^4} \\
&\lambda_\tau = \frac{\lambda_{I_x}}{\lambda_t^2}
\end{aligned} \tag{5.34}$$

For two systems to be dynamically similar all the scale laws in Equation 5.34 must be satisfied. Furthermore, the scale laws are not unique, and new scale laws can be formed by combining the terms in Equation (5.34).

Demonstration of scaling laws in 1-D case

To demonstrate the validity of the scaling laws a test case was made between two systems, one that correspond to a satellite and a testbed. The satellite and testbed equation of motion were expressed via a single degree of freedom to simplify the results. Both attitude dynamics were described using Newton-Euler, with the equations of motion for both systems given by,

$$I_{x,sc}\ddot{\theta}_{sc} = \tau_{sc} + L_g \qquad\qquad I_{x,tb}\ddot{\theta}_{tb} = \tau_{tb} \tag{5.35}$$

where, "sc" and "tb" corresponds to the values for the satellite and testbed, respectively, $I_{\#}$ corresponds to the inertia of the respective axis, τ is the torque on the

system, and L_g is the gravity gradient torque. As shown in Equation (B.1), the torque from gravity gradient is given by,

$$L_g = \frac{3\mu}{R^3}(I_{z,sc} - I_{y,sc}) \sin\theta_{sc} \cos\theta_{sc} = \frac{3}{2} n_{sc}^2 (I_{z,sc} - I_{y,sc}) \sin(2\theta) \tag{5.36}$$

where n_{sc} is the orbital rate of the satellite.

The scaling laws in Equation (5.34) were utilized which permits two free parameters. For example, by choosing the inertia about the x-axis of the testbed and the satellite, $I_{x,tb}$ and $I_{x,sc}$, the scaling law $\lambda_{I_x} = I_{x,sc}/I_{x,tb}$ is fully described. Additionally, by changing what the fundamental simulation time is Δt_{sc} and Δt_{tb}, the scaling factor $\lambda_t = \Delta t_{sc}/\Delta t_{tb}$ is set. All the other scaling laws in Equation (5.34) pertinent to the 1D motion depend upon these scaling factors with the exception of λ_θ which in itself is already defined to be equal to one. Therefore, when a satellite with parameters Δt_{sc}, $I_{x,sc}$, $I_{y,sc}$, $I_{z,sc}$, n_{sc}, are chosen, and a testbed with $I_{x,tb}$ and Δt_{tb} exits, all the other parameters for the testbed must match the scaling laws, and $I_{y,tb} = I_{y,sc}/\lambda_{I_x}$, $I_{z,tb} = I_{z,sc}/\lambda_{I_x}$, etc.

The dynamics in 5.35 were implemented in MATLAB with the testbed and satellite parameters given by Table 5.8. Note that all the parameters follow the scale laws in

Table 5.8: Parameters used for testbed-satellite scaling example

Parameter	**Unit**	**satellite**	**Testbed**
I_x	kgm^2	200	1
I_y	kgm^2	300	1.5
I_z	kgm^2	500	2.5
n	rad/s	$1.2e-4$	0.036
Δt	s	300	1

Equation (5.34). The simulation setup is shown in Figure 5-16. At each time step, an external torque and gravity gradient torque were applied to a satellite dynamical model. This resulted in a satellite output state of θ_{sc}, $\dot{\theta}_{sc}$. At the same time, the external force was scaled down using the scaling laws, while the gravity gradient torque was emulated given the testbed's current angle. These torques were applied to the testbed's dynamics which outputted the state θ_{tb} and $\dot{\theta}_{tb}$. The state was then

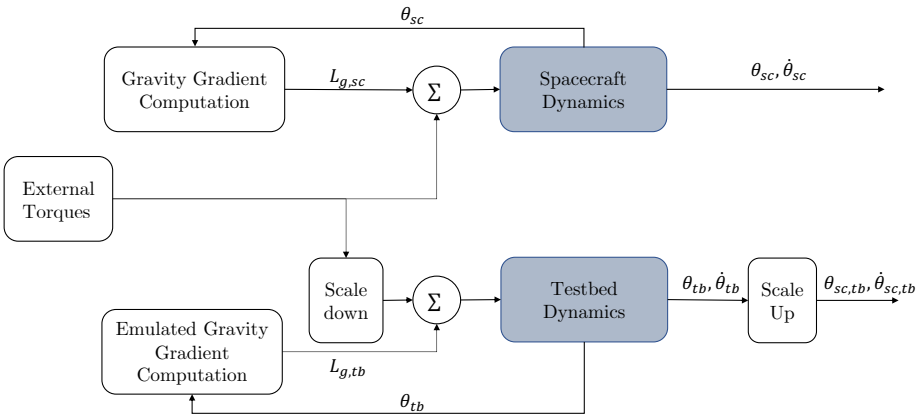

Figure 5-16: Configuration for Matlab-based sim for Buckingham-π 1-D testcase

scaled to obtain the predicted motion of a satellite $\theta_{sc,tb}$ and $\dot{\theta}_{sc,tb}$. For the example shown here, the external torque was set to zero for all time.

Figure 5-17 shows the result of this analysis. The state history of the testbed is shown in Figure 5-17a. The testbed angle and angular rate are shown in the subplots respectively. Note that the simulation for the testbed only lasted for 100 seconds. Figure 5-17b shows the result of the state history of the satellite dynamics. For the angle subplot, the satellite's state is shown in a solid blue line, the testbed state was plotted alongside in a red dash-dotted line, and the testbed's scaled-up angle were plotted in a dashed black line. For the angular rate, only the spacecraft and testbed's scaled-up angle were plotted. Note that the horizontal axis is different from the testbed as the fundamental time rate Δt_{sc} was 300 times that of the testbed. The testbed is shown to faithfully scale up and match the dynamics of a different system. This section covered the scaling laws for the Dynamics and Control Testbed that will be used for scaling the behavior of an RSA satellite in LEO and MEO

5.2.3 Scaling for LEO and MEO satellites

Given the scaling laws found in the previous section, it is possible to run a trajectory that would mimic the behavior of a satellite in LEO or MEO. As seen in the example before, there exist two parameters for which we can scale the testbed, namely, the

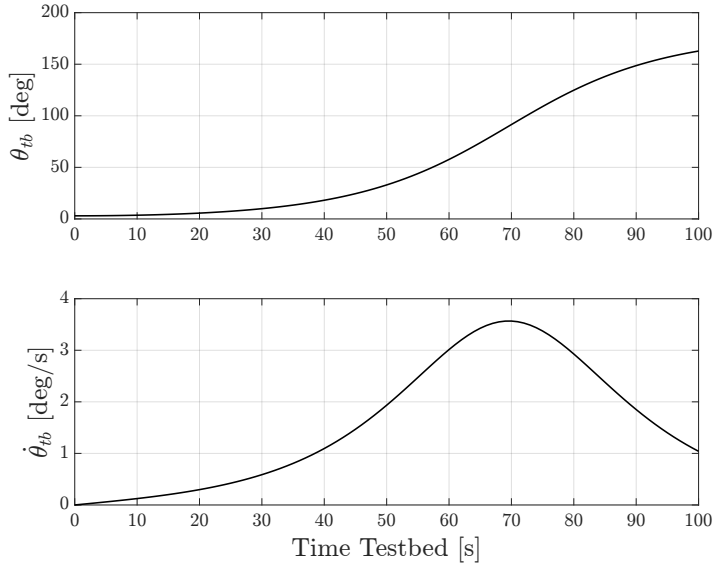

(a) Testbed State

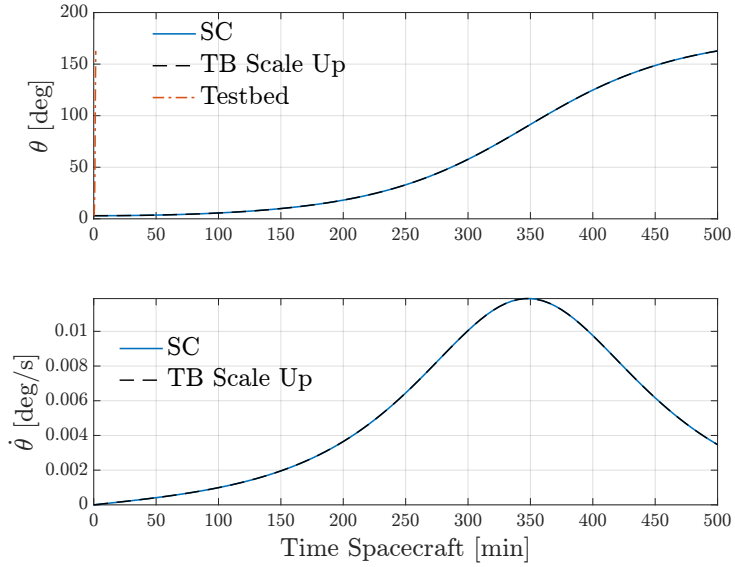

(b) Satellite and Emulated Testbed State

Figure 5-17: Results of utilizing Buckingham-π scaling analysis. Top two figures show the state of the testbed while bottom two figures show the state of a satellite as well as the scaled motion of the testbed using the scaling laws.

ratio between one of the inertias $\lambda_{I_\#}$, and the fundamental time constant λ_t. The latter indicates what a one-second in the DCT testbed translates to a length of time for the satellite simulation. When scaling the motion of an RSA, care must be made to ensure that the spin rate, slew rate, and expected torques followed that of a desired satellite.

Computing the spin and slew rate depends on several factors such as the integration time of the optics, the access time to the target on the ground, the lighting available, etc. [110]. The calculation derived in this work relied mainly on calculating the *minimum* angular spinning needed to complete an image maneuver based on the access window provided by the testbed. As mentioned earlier in the section, the testbed is only able to rotate inside a cone with a half angle of 17° before the testbed hits the safety foam barrier, thus for scaling a half angle of $\theta_{imag} = 12°$ was chosen for which the satellite would perform an imaging maneuver of the target. The imaging angle θ_{imag} represents the angle from the target at the surface of the Earth to the satellite in orbit passing overhead.

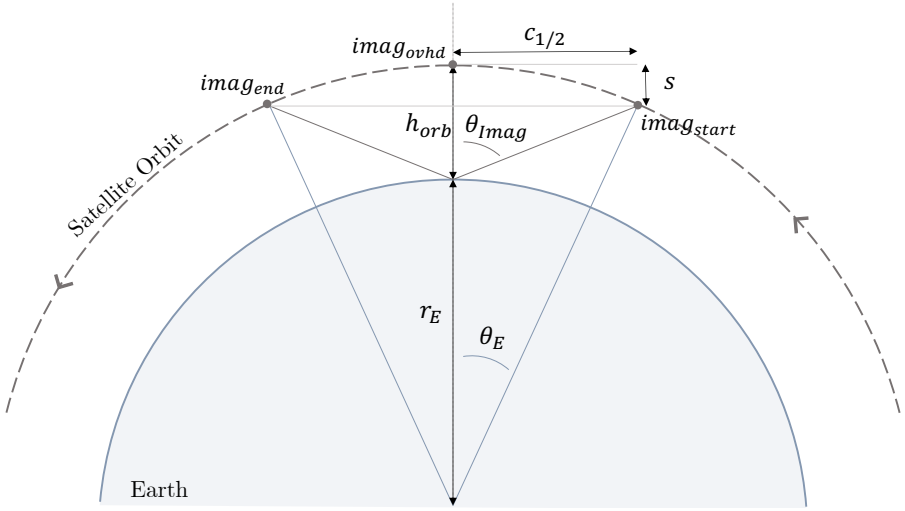

Figure 5-18: Diagram for simplified satellite slew derivation

Figure 5-18 shows a visual description of θ_{imag}. The satellite orbit is shown in a grey dashed line with the satellite moving counterclockwise. Three points, corresponding to the start of the image, img_{start}, point overhead, img_{ovhd}, and the end

of the imaging, img_{end}, are shown in a grey dot. The altitude of the orbit is shown given by h_{orb} and the radius of the earth is given by r_E. The duration of half the imaging maneuver is determine by the angle θ_E which is the angle that is formed from the points img_{ovhd}, the center of the earth, and img_{start}. Additionally shown in the diagram is the half distance of the cord, $c_{1/2}$ which is defined as the cord of a circle of radius $r_E + h_{orb}$ by and angle $2\theta_E$. Additionally, the sagitta is given by s, which is the distance between the cord and the point overhead of the orbit. The value of $c_{1/2}$ and s can be given by,

$$\begin{aligned} c_{1/2} &= (r_E + h_{orb})\sin(\theta_E) \\ s &= (r_E + h_{orb})(1 - \cos(\theta_E) \end{aligned} \tag{5.37}$$

The angle θ_{imag} can be found by the triangle formed between $c_{1/2}$ and $h_{orb} - s$,

$$\theta_{imag} = \frac{c_{1/2}}{h_{orb} - s} = \frac{(r_E + h_{orb})\sin(\theta_E)}{h_{orb} - (r_E + h_{orb})(1 - \cos(\theta_E)} \tag{5.38}$$

A Newton-method solver was used to find θ_E from Equation (5.38). The time for which a satellite moves from point $imag_{start}$ to $imag_{end}$ is given by,

$$t_{orb,imag} = \frac{2\theta_E}{n_{orb}} \tag{5.39}$$

where n_{orb} is the mean motion of the orbit. The slew rate can then be computed by,

$$\omega_{slew} = \frac{2\theta_{imag}}{t_{orb,imag}} \tag{5.40}$$

The spin rate can then be computed by the rate needed in order to complete a $n_{spin}\pi$ rotation during the orbit time, where n_{spin} is the number of desired full image caputures using the RSA assuming that it only takes 180° rotation about the optical axis in order to produce an image,

$$\omega_{spin} = \frac{n_{spin}\pi}{t_{orb,imag}} \tag{5.41}$$

Note that the configuration in Figure 5-18 has several assumptions including the

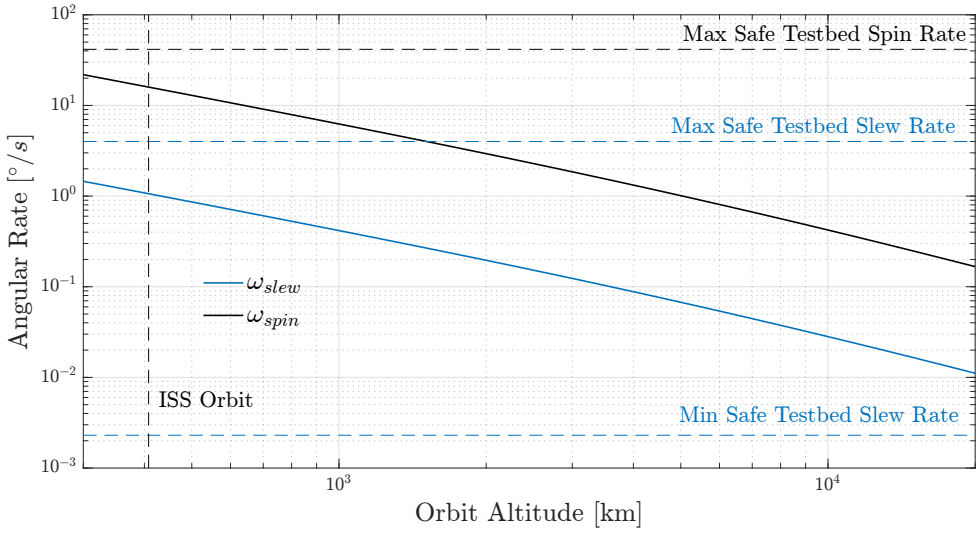

Figure 5-19: Slew and minimum spin rate for RSA satellite as a function of orbit altitude for $\theta_{imag} = 13°$.

satellite is assumed to pass directly overhead the target, the satellite is operating in a circular orbit, the Earth is assumed to be perfectly spherical, and the target and itself is not rotating. Depending on the altitude, these assumptions cause an error in pointing from 0.02° to almost 5° as the slew rate is dependent on the actual position of the orbit relative to the target and it is not constant. This can easily be mitigated by generating a time-based slew rate from a high-fidelity orbit simulation in STK, and feeding the scaled-down trajectory to the DCT view a new Guidance node mode.

Figure 5-19 shows the spin and slew rate for a requirement that $\theta_{imag} = 13°$. The horizontal axis is the orbit altitude, and the vertical axis is the angular rate in degrees. The solid black line represents the spin rate, while the solid blue line represents the slew rate. The maximum testbed spin and slew rate were plotted in the figure. The maximum spin rate of $42°/s$ is taken to be the spin rate that can be attained when the RWA 4 is operating at 75% of its momentum capacity and is plotted in a horizontal black dashed line. The maximum slew rate of $3°/s$ shown in the top blue dashed line was chosen to allow at least 5 seconds for the testbed to transverse half of the possible range of the spherical air bearing. The minimum slew rate at the current testbed's CM-CR balancing shown in the lower blue dashed line corresponds to the rate at

which the testbed is able to complete its 24° slew without the wheels saturating due to the torque from gravity. Finally, The ISS orbit was plotted for reference in the verical black dashed line.

As the simulation is scaled by λ_t, the commanded angular rate is multiplied by that value. For example, the ISS spin and slew rate are given by $16.2°/s$ and $1.08°/s$, if $\lambda_t = 3$ the scaled rates that the *testbed* needs to do is $48.6°/s$ and $3.24°/s$ both violating the testbed's maximum rates. Due to this, great care must be taken when selecting values of λ_t such that they are physically realizable in the testbed.

Another factor to consider when scaling is how the torque of the testbed is scaled for a given satellite size, and λ_t. The only current actuators for the DCT are the reaction wheels which are driven by the BasicMicro Roboclaw motor controllers. The motor controller has a finite quantized value for which it can command wheels speed and is constrained by the number of quadrature values in the encoder. Additionally, due to the LiPo's battery voltage and brushed motor electromechanical properties, it has the maximum torque possible. For our actuators, the motor controller can command the reactions wheels with a minimum equivalent quantized torque of $2.33e-4$ (Nm), and a maximum torque of 0.8 (Nm). These values are shown in Table 5.9.

Table 5.9: DCT's minimum and maximum commanded RWA torque ranges

Minimum (Nm)	**Maximum (Nm)**
2.33e-4	0.8

In terms of disturbance torque, the main one present and measurable in the DCT is the CM-CR offset. Great care has been made to make sure that the testbed is balanced, however, even small movements of cables can affect the balancing and move the CM-CR offset. For example, a two-gram object (such as cable locations) on the testbed moving by 1 mm will move the CM-CR offset by about 0.1μm. Table 5.10 shows different examples of CM-CR offset for the testbed and the corresponding minimum and maximum torque produced during the 24° rotation for an imaging maneuver. The current estimated testbed CM-CR offset is given by the second row. The

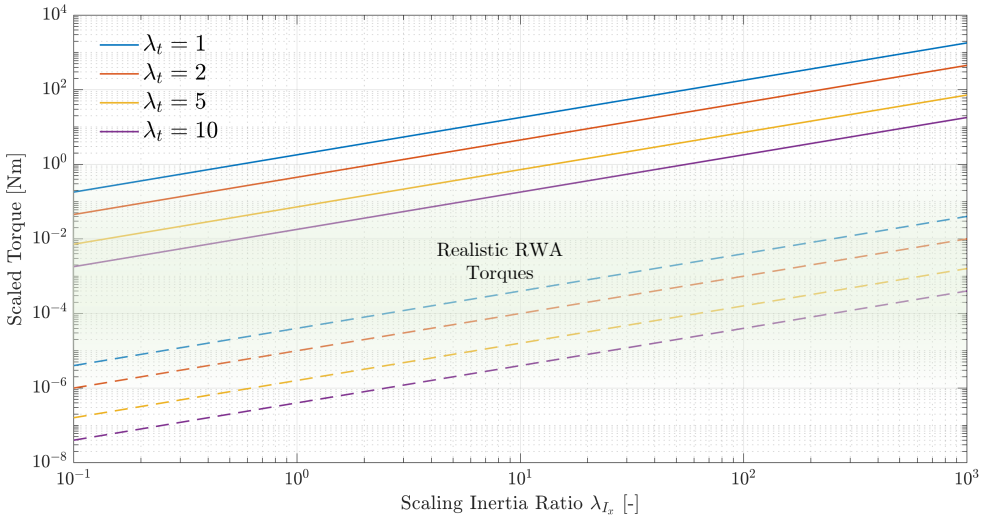

Figure 5-20: Scaled maximum and minimum possible torque of DCT as a function of scaling ratio λ_{I_x} and λ_t. Solid line represents maximum torque, dashed lines represent minimum torque.

last row represents an ideal CM-CR offset for the testbed that could be accomplished by additional balancing procedure iterations. When scaling the results of the DCT, it is useful to scale the maximum disturbance torque to see if it is realistic in terms of expected orbital disturbances for a satellite.

Table 5.10: DCT's minimum and maximum CM-CR offset torque in testbed operating range

CM-CR Offset (μm)	**Minimum (Nm)**	**Maximum (Nm)**
$[2, 2, -343]^T$	$8.3e-4$	$2.2e-2$
$*[-1.1, -0.6, -2.2]^T$	$3.3e-4$	$1.6e-4$
$[0.1, 0.1, -1]^T$	$4.16e-5$	$9.9e-5$

Figure 5-20 shows how the choice of the inertia ratio λ_{I_x} and fundamental time ratio λ_t scales the minimum and maximum torque of the DCT shown in Table 5.9. For a choice of λ_{I_x} and λ_t the scaled torque for a satellite is given by $\tau_{sc} = \tau_{tb}\lambda_{I_x}/\lambda_t^2$. The horizontal axis is the inertia scaling ratio. The vertical axis shows the scaled torque in units of Nm. Each color, representing a different value of λ_t has the maximum and minimum value of the torque shown in the solid and dashed line, respectively. As λ_t increases, the range of torque increases with it. Unfortunately, for a large scaling

Table 5.11: DCT test cases for LEO and MEO scaling

	Satellite						Testbed		
	Altitude (km)	$\boldsymbol{\omega}_{slew}$ ($^\circ/s$)	$\boldsymbol{\omega}_{spin}$ ($^\circ/s$)	$\boldsymbol{\lambda}_t$ (-)	$\boldsymbol{\lambda}_{I_x}$ (-)	$\boldsymbol{\tau}_{cm-cr}$ (mNm)	$\boldsymbol{\omega}_{slew}$ ($^\circ/s$)	$\boldsymbol{\omega}_{spin}$ ($^\circ/s$)	$\boldsymbol{\Delta t}_{image}$ (s)
1	450	0.97	7.2	1	1	11.6	0.96	7.2	24.9
2	450	0.96	7.2	2	10	29.1	1.92	14.4	12.5
3	2000	0.20	1.46	4	1	0.7	0.78	5.87	30.6
4	2000*	0.20	1.46	4	100	72.8	0.78	11.74	30.6
5	10,000	0.03	0.21	10	50	5.8	0.28	2.12	85

inertia ratio, the effectively scaled torque is physically impossible for a satellite to have. Typical satellite reaction wheels have a maximum possible torque on the order of 10 to 100s mN and are shown on the green gradient region. Increasing a λ_t would allow for the scaled torque to be of magnitude of those that are available for RWA actuators, however, large values of λ_t increase the spin rate which may violate the testbed slew rates shown in Figure 5-19. These competing requirements limit the possible scalability of the testbed.

Table 5.11 shows the test cases that were run to demonstrate the ability to scale the DCT. For each test case, a satellite altitude was picked with the slew and spin rate of that altitude corresponding to the values given in Figure 5-19. The value of λ_{I_x} was picked which corresponds to the overall inertia scaling of the testbed. For example, the first test has a scaling value of λ_{I_x} which means that the satellite's inertia is the DCT inertia from Table 5.7. The value for λ_t was chosen so that the slew and spin rates were within the safe region from those given in Figure 5-19. The scaled gravity gradient torque $\boldsymbol{\tau}_{cm-cr}$ was computed when the CM-CR offset was $[2, 2, -343]^T$ (μm). For the testbed, the scaled slew and spin rate were computed by $\omega_{slew,tb} = \omega_{slew,sc}\lambda_t$ and $\omega_{spin,tb} = \omega_{spin,sc}\lambda_t$. Respectively. Finally, the expected time for the imaging duration for the testbed was computed. Note that the disturbance torque for some of the test cases, particularly for Tests 4 and 5 is larger than what is normally expected on satellites at those altitudes. Finally, Test 4 is highlighted because the spin rate is twice the spin rate needed, corresponding to an RSA being able to take two full images per target.

Figure 5-21 shows the scaling for Test 1. Since both scaling ratios were equal to one, the testbed results were effectively not scaled. On each figure, two sets of axes are overlayed on top of each other. The black axes given by the lower horizontal and left vertical axis correspond to units of the Satellite. The blue axes are given by the top horizontal and right vertical axis which correspond to the units of the DCT testbed. Figure 5-21a shows the angle from overhead, defined as the angle from the target, or the imaging angle in Figure 5-18. A zero angle indicates that the satellite is directly overhead the target. The horizontal axis represents time with the top axis

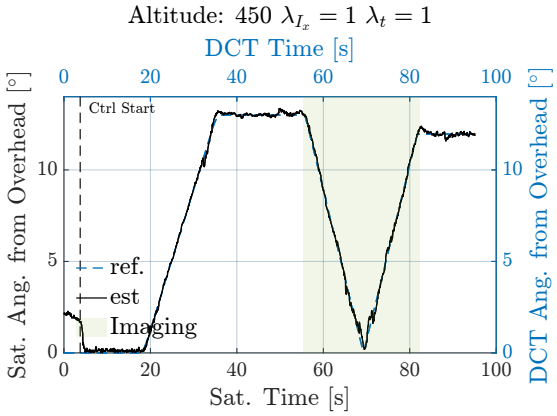

(a) Angle from overhead

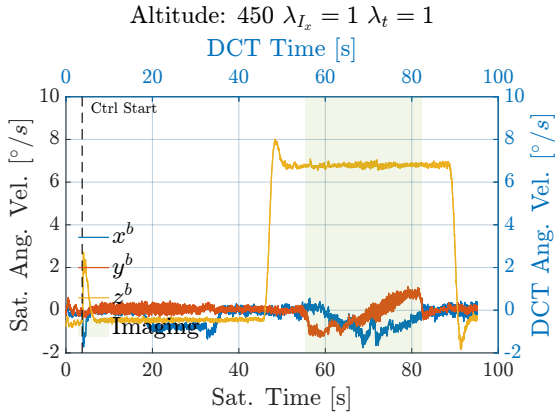

(b) Angular velocity

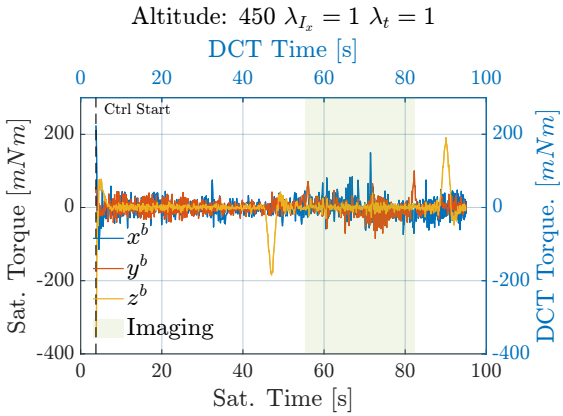

(c) Torque

Figure 5-21: DCT Scaling results for satellite with altitutde 450 km, $\lambda_t = 1$, $\lambda_{I_x} = 1$.

being the DCT time, and the lower axis being the scaled satellite time. The vertical axis is the angle from overhead in degrees. Note the axes limits for both time and angle are the same due to $\lambda_t = 1$, $\lambda_{I_x} = 1$. The vertical black dashed line corresponds

to the time at which the GNC controller started. The reference angle and estimated angle are shown by the dashed blue and solid black lines, respectively. Finally, the green area highlighted in the figure represents the time when imaging would occur, or when the RSA satellite would be spinning and slewing. During this green region. Halfway through the imaging, the satellite would be directly overhead.

Figure 5-21b shows the angular velocity of the testbed and satellite. Similar to Figure 5-21a, the horizontal axis represents time, however, the vertical axis represents the satellite and DCT angular velocity in degrees per second. The angular velocity about the x^b, y^b, and z^b axis are represented by blue, red, and yellow colors, respectively. Note that during the imaging spin the angular velocity about the x and y axis appear to be oscillating. This behavior can be also seen in Figure 5-15a. Finally, the torque for both the satellite and DCT are shown in Figure 5-21c. As in the previous figures, the horizontal axis represents time, while the vertical axis represent the torque of the satellite and DCT both in units of (mNm). Note that the largest amount of torque happens during and immediately after the imaging period. This is expected as the DCT must exchange the angular momentum of the testbed between the RWAs in order to slew while spinning. The x^b-axis and y^b-axis torque are out of phase with each other during this time.

Figure 5-22 shows all the test cases in Table 5.11. Each row represents one test case, each with three plots corresponding to the angle overhead, the angular velocity, and torque as the results shown for Test case 1. The test cases for higher altitudes have a longer imaging time as expected, with the longest imaging time corresponding to Test 5, in which the DCT slew for 85 seconds, corresponding to over 14 minutes for the satellite. The test cases with the lower spin rate, notable Test 3 and Test 5 correspond to the test cases with the lowest angle error which can be seen in Figure 5-22d and 5-22j where the reference angle and estimated angle matched more closely. This is expected as the DCT torque required for the imaging maneuver in both cases have the lowest magnitude. Furthermore, due to the longer time, it takes for the satellite to spin, the testbed has more time to fully exchange the angular momentum between the wheels. Test 3, corresponding to a satellite with the same

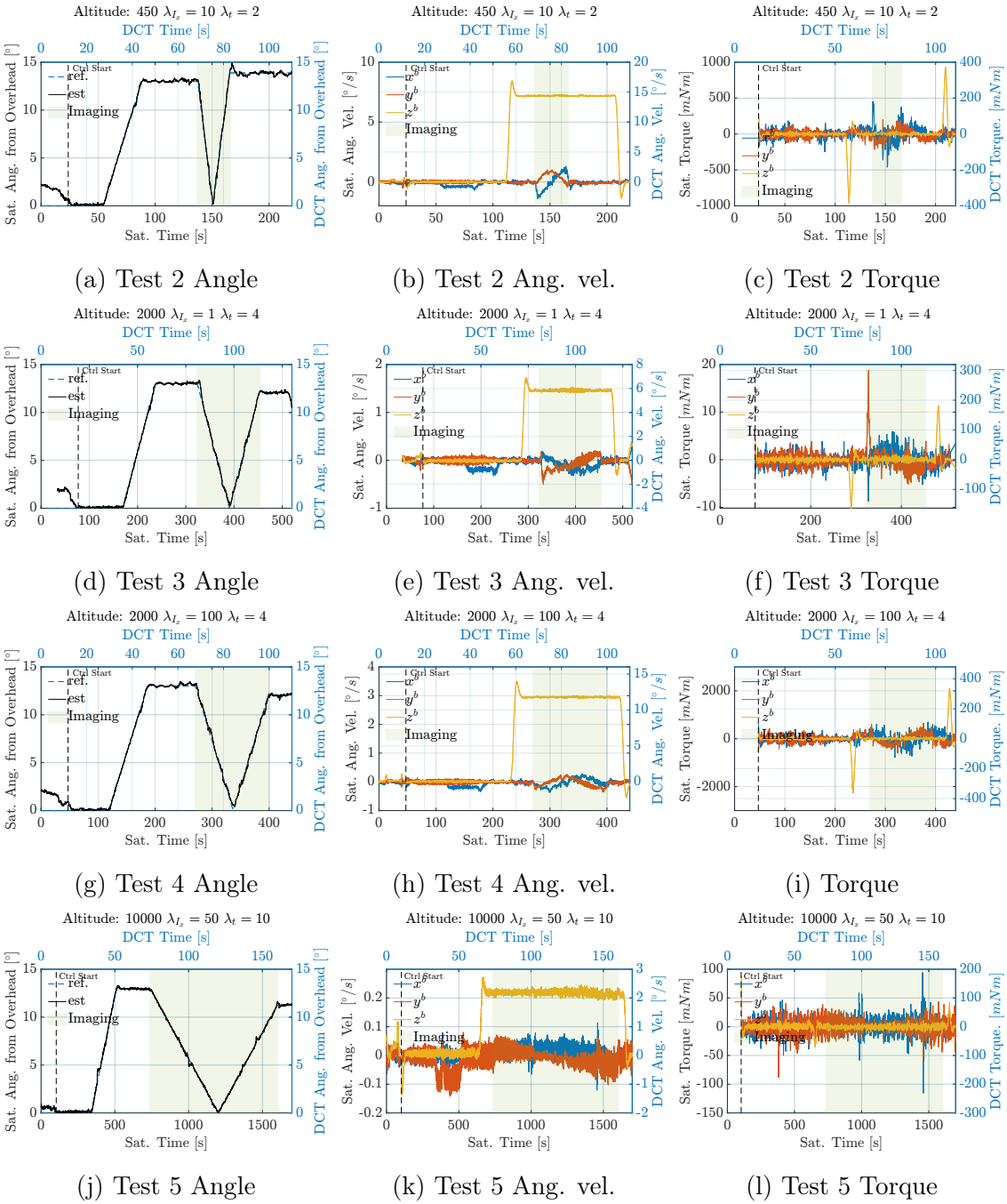

(a) Test 2 Angle (b) Test 2 Ang. vel. (c) Test 2 Torque

(d) Test 3 Angle (e) Test 3 Ang. vel. (f) Test 3 Torque

(g) Test 4 Angle (h) Test 4 Ang. vel. (i) Torque

(j) Test 5 Angle (k) Test 5 Ang. vel. (l) Test 5 Torque

Figure 5-22: DCT scaling results for Table 5.11 test cases.

mass properties as the DCT, requires the lowest amount of scaled Torque to operate. This lower magnitude of torque is expected as the satellite operates at an altitude of 2,000 (km) and has to spin and slew at a slower rate than the nominal case of 450 (km). Overall, the testbed is able to effectively emulate the motion of the satellite at different orbital regimes in LEO and MEO, and at different mass properties scaling.

This section covered the process for scaling the dynamics and control testbed using the scaling laws presented in Section 5.2.2, the limitations based on the DCT hardware, and results for scaling at different orbit altitudes and satellite sizes. The main restriction for scaling the DCT is the center-of-mass (CM) to center-of-rotation offset resulting in a large torque from gravity. Despite this limitation, it was shown that it is possible to obtain results that present reasonable torque requirements for satellites that could aid in sizing and designing RSA systems.

5.2.4 Scaling for SEL2 Satellites and Recommended DCT Improvements

One of the main challenges when scaling for higher orbit altitudes is the ability to faithfully scale the magnitude of torques from the RWA, and the CM-CR disturbance. Currently, the testbed is unable to be scaled for SEL2 satellites, to either test RSA satellites with reaction wheels, or with RCDs. This section goes over recommended DCT improvements, and a discussion of possible avenues to test RCD-like behavior for SEL2 satellites in the DCT.

One of the challenges with RCDs is that they provide external torques, and themselves create a non-zero angular momentum system, unlike RWAs. Putting RCDs in the testbed would be fruitless as the force produced by them would be completely negligible and unmeasurable. Therefore, a mock RCD actuator is needed. Actuators such as cold-gas canisters used in SPHERS [159] are not recommended due to them being expendable, and the torque provided would not be sensitive enough when scaled. Instead, one of the recommendations provided here is to use magnetorquers.

Currently, the DCT is mounted on top of a Helmholtz cage capable of generating a magnetic field with a magnitude of up to 6.5 Gauss about any axis. Magnetorques such as the New Space Systems's NCTR-M016 could provide up to 0.01 (Nm) in torque which would be adequate to scale the torque produced by RCD in SEL2 [6]. For this actuator to be useful, however, the CM-CR offset must be at the ideal value of $[0.1, 0.1, -1]^T$ (μm) from Table 5.10. Therefore, the DCT must at least have an improvement in balancing, and the incorporation of magnetorquers in order to allow for torque scaling of SEL2 satellites, and RCDs.

Additional recommendations for the DCT are improvements in overall sensors, actuators, and laboratory isolation for the hemispherical air-bearing. Currently, the reaction wheel assembly utilizes brushed DC motors with a rough encoder of only 4000 encoder counts per revolution. Replacing the motors for brushless DC motors with higher encoder counts would allow for finer control. Additionally, brushless DC motors tend to be more power and weight-efficient allowing for a reduction in the overall DCT testbed mass by reducing the structural mass, as well as the LiPo batteries size. A reduction in mass would also reduce the magnitude of the torque from gravity. Further improvements for the RWA subsystem would be to incorporate current control of the wheel speeds to allow for more realistic RWA behavior compared to flight attitude control systems, and allow a reduction in the phase lag from the RWA commanded speed to its current speed.

In terms of sensors, additional PiCams could allow for further reduction in knowledge error by utilizing sensor fusion from the EKF. An improved mounting of the ArUco board would also allow for better testing of truth using the OptiTrack system, which is currently not possible. Finally, sensor tests show that the testing environment has a constant 15.2 Hz disturbance in the IMU readings. The current hypothesis is that this noise level is due to the structural disturbance of the building itself. By having the hemispherical air-bearing, testbed, and ArUco mounting cage mounted seismically on air springs, the environmental disturbances can be reduced. Furthermore, to increase the capabilities of the testbed it is recommended to design a method

[6] `https://satsearch.co/products/newspace-systems-nctr-m012-magnetorquer-rod`

of easily changing the inertia ratios. This can be performed either by having a fixed set of masses and mechanical elements that can be attached to the DCT increasing the DCT's principal inertia values or by adding more coarse balance that can be finely tuned to increase or decrease the system's inertia. A methodology must be created to have the ability to increase the inertia independently from the CM-CR offset,

Chapter Overview

This chapter presented an overview of the Dynamics and Control Testbed including the formulation of its subsystems and testing results in order to address the scalability of RSA for Contribution 3. The DCT was designed to allow for testing motions for rotating synthetic aperture satellites, and due to this similarity laws were obtained between the DCT and RSA satellites at LEO and MEO. Constraints for scaling from the testbed achievable angular rates and scaled torques were also shown. Results for the scaled satellites are presented which demonstrate the ability to achieve scaling of some subsystems despite the presence of large disturbances from CM-CR misalignment. Finally, the chapter presented recommendations for improvement of the DCT as well as the addition of magnetorques that would allow for the testing of mock RCD actuators for satellites in SEL2.

Chapter 6

Conclusion and Future Work

This chapter reviews the contributions and presents some potential research avenues for future work.

6.1 Review of Contributions

This thesis developed the methodology for utilizing reflectivity control devices for orbit and attitude control of rotating and non-rotating space-based aperture satellites. The contributions encompassed the development of the controllability of satellites utilizing RCDs, the operability of these devices on space-based telescopes, as well as the scalability from the development of a hardware-based testbed for RSA telescopes.

Chapter 3 demonstrated Contribution 1 which showed the methodology for achieving full six DOF control using RCDs as its only actuator while using the dynamics in the CR3BP with Solar radiation pressure. Previous works had only achieved the ability of up to five DOF freedom, requiring an extra actuator such as reaction wheels or thrusters to control about the axis normal to the surface where the RCDs are placed in a sail. The allocation algorithm for selecting the reflectivity coefficients based on the singular value decomposition is shown. An analysis of the force and torque envelopes, as well as how those envelopes change with the Sun direction is also shown. Finally, the reference halo orbit found in the modified CR3BP with SRP as well as the orbit and attitude controller is derived in this chapter.

Chapter 4 went over the operability of these actuators when used in space-based aperture satellites which addresses Contribution 2. This chapter developed the idea of field-of-regard for RCD satellites which is defined as the region of operation where both orbit and attitude control can be maintained. This region would correspond to target locations that a rotating telescope such as an RSA can image. This is also extended to non-rotating telescopes such as the JWST or the future HWO. As part of Contribution 2, this chapter demonstrated the ability to optimize RCD configurations so that they maximize the control envelopes discussed in Chapter 3. Finally, this chapter concluded with a discussion of how some expected disturbances compare to the authority provided by RCDs and gives a case study of how the JWST would perform if it was retrofitted with an optimal aggregate RCD configuration. Results from this case study demonstrated that although some RCD configurations would not achieve the required slew rates, RCDs are capable of maintaining orbit and attitude control during imaging portions which could aid in a reduction of disturbances present during science data gathering.

Chapter 5 presented results for a hardware-based dynamics and control testbed for rotating synthetic aperture satellites as part of Contribution 3. An overview of the DCT's subsystems including several test cases is presented. The testbed was designed to be modular with the ability to easily modify any of the GNC algorithms or replace sensors or actuators. A set of scaling laws that allow for the similarity between the DCT and an RSA telescope was also shown in this chapter. Finally, hardware-based results of the testbed that are scaled for different RSA telescopes operating at LEO and MEO were shown. The chapter concluded with an overview of suggested improvements that would allow the DCT to be scaled for satellites operating in SEL2 including the type of actuators that it would need to scale the forces generated by certain RCD configurations.

Overall, this thesis showed that low-disturbance, long-mission lifetime missions can be achieved using RCDs as actuators for both rotating and non-rotating space-based telescopes.

6.2 Future Work

Several further research avenues can be explored from this research. The research avenues are divided between the use of RCDs in the Sun-Earth Lagrange points, and the further development of the DCT testbed and RSA telescopes operating in LEO and MEO.

In the first category, there exist several research avenues that would allow higher-fidelity modeling of RCDs. First, a non-idealized higher fidelity model of RCDs can be explored that would yield higher confidence in the results presented in this Thesis. This would include the expected power requirements needed to operate RCDs. Additionally, one assumption made in this research is the ability to seamlessly switch between a fully reflective and fully absorptive state. Current RCD technology has shown that it is possible to transition between the two states, however, work needs to be done to demonstrate with hardware the ability to switch to a specific desired reflectivity value and maintain it for long periods of time, as well as understanding the life cycles for these systems. An improvement in the optimization of RCD placement can also be made so it scales well with an arbitrarily large number of RCD cells in a given configuration.

There are additional research avenues for the operability of space-based telescopes. For situations where additional actuators are needed in agile space telescopes, a hand-off algorithm must be developed that allows switching the control between the two actuator modes. This includes the ability to still utilize RCDs during the period where they are not the main actuator as a way to reduce the angular momentum accumulation. Furthermore, another possible avenue is to develop an algorithm that estimates the current CM-CR offset of the entire observatory and biases the RCDs to have a close to net zero angular momentum system. This avenue could include the regeneration of reference halo orbit that ensures a wider possible range of operation for RCDs. Finally, RCDs can be dually utilized for both orbit and attitude control as well as thermal management. Previous work has dealt with the use of electrochromic panels for thermal control, and incorporating the results of this thesis for a combined

ACS and thermal control system could allow for additional capabilities for future telescopes.

For the DCT, there are several future works and improvements that can be done to allow for a capable testbed. Improvements in sensors and actuators such as engineering models of RWAs could allow for a reduction in the overall attitude control error of the testbed. This could additionally translate to a reduction in the overall mass of the system, reducing the disturbance due to the center of mass to the center of rotation offset, and an improvement in the performance of the testbed. The use of magnetorquers could allow for the emulation of RCD actuators when scaled using the similarity rations developed. However, isolation from laboratory environment disturbances must first be made in order for the magnetorquers to be effectively scaled. Additional nonlinear actuators such as sliding masses might improve the testbed attitude error if the actuator dynamics are also modeled. Further work for RSA satellites operating in LEO and MEO is to analyze different orbital perturbations such as magnetic fields to see if it is possible to operate RSA satellites using them. The addition of magnetorques on the DCT could allow for testing of this perturbation on the testbed.

Appendix A

Guidance Function Generation Utilized in this Work

This Appendix covers the methodology for generations of reference guidance trajectories for use in both the Dynamics and Control Testbed and satellites operating on SEL2 utilizing reflectivity control devices. All the trajectory generation relies on the principle of providing a twice continuously differentiable reference quaternion for the respective controllers. Providing smooth reference trajectories allows for a lower magnitude of commanded torques, reducing attitude error. This is of particular concern to the Thesis where a large magnitude of torque will saturate the RCD's capability, and a large torque control for the DCT would lead to a large error and could potentially damage the testbed.

This Appendix is divided into two sections. Section A.1 covers the trajectory generation for the DCT including the Guidance node Safe Mode and Change of Angle mode. Section A.2 covers the reference trajectory for SEL2. This trajectory allows for slew generation for pointing in the inertial and synodic frame.

The trajectory generation for all the above solutions relies on the use of Equation (5.3) and (5.4) repeated here,

$$\boldsymbol{\omega}_{ref}(t,\Gamma) = \hat{\mathbf{e}}\Omega_{ref}(t,\Gamma) \tag{A.1}$$

where $\hat{\mathbf{e}}$ is the axis of the angular rotation, and $\Omega_{ref}(t,\Gamma)$ is a piecewise, continuously differentiable scalar function given by

$$\Omega_{ref}(t,\Gamma) = \begin{cases} 0 & t \leq t_0 \\ \alpha\tau_1^2/2 & t \leq t_r/2 + t_0 \\ -\frac{\alpha}{4}\left(2\tau_1^2 - 4\tau_1 t_r + t_r^2\right) & t \leq t_r + t_0 \\ \omega_s & t \leq t_c + t_r + t_0 \\ \omega_s - \frac{\alpha}{2}\tau_2^2 & t \leq \frac{3t_r}{2} + t_c + t_0 \\ \omega_s + \frac{\alpha}{4}\left(2\tau_2 - 4\tau_2 t_r + t_r^2\right) & t \leq 2t_r + t_c + t_0 \end{cases} \tag{A.2}$$

where,

$$\tau_1 = t - t_0,$$

$$\tau_2 = t - t_0 - t_c - t_r$$

$$\alpha = \frac{4\omega_s}{2t_r}$$

and the parameters Γ given by,

$$\Gamma = [t_0, t_r, t_c, \omega_s] \tag{A.3}$$

A.1 Reference Guidance Trajectory for DCT

This section covers the Safe Mode and Change of Angle trajectory for the DCT's guidance node.

A.1.1 Safe Mode Trajectory

The goal of Safe Mode is to take the DCT from its current state to a desired "safe" attitude as soon as possible. The method utilized in the DCT is to perform two maneuvers, one that arrests the current angular velocity of the DCT to a user-defined tolerance, and another to bring the satellite to the desired safe quaternion via a single-axis slew. The initial input of the trajectory is the state of the testbed at the moment

Safe Mode was triggered,

$$\begin{aligned} \boldsymbol{\omega}_0 &= \boldsymbol{\omega}(t_{cur}) \\ \boldsymbol{q_0} &= \boldsymbol{q}(t_{cur}) \end{aligned} \tag{A.4}$$

The guidance proceeds to Maneuver 1 *if* the magnitude of angular velocity is greater than the threshold ω_{tresh}, otherwise, it moves to Maneuver 2.

Maneuver 1: Arresting Initial Angular Velocity

The first step for performing the arresting of the initial angular velocity is to compute the parameters Γ to use Equation (A.1). The values for the parameters $\Gamma = [t_0, t_r, t_c, \omega_s]$

The axis $\hat{\boldsymbol{e}}$ is given by,

$$\hat{\boldsymbol{e}} = \frac{\boldsymbol{\omega}_0}{||\boldsymbol{\omega}_0||} \tag{A.5}$$

The initial time for this component of Safe mode to start the simulation is $t_0 = 0.1\ (s)$ seconds after the mode is called. The ramp-up time is set to

$$t_r = \frac{||\boldsymbol{\omega}_0||}{\omega_{max,safe}} \tag{A.6}$$

where $\omega_{max,safe}$ is the maximum magnitude of angular velocity that the testbed will achieve, and it is user-defined. For the DCT. the max safe norm of the angular velocity was set to $12°/s$. There is no coasting time $t_c = 0\ (s)$. Finally,

$$\omega_s = -||\boldsymbol{\omega}_0|| \tag{A.7}$$

Having the parameters set, safe modes command the reference angular velocity and reference quaternion from Equation (5.2) repeated below,

$$\begin{aligned} \boldsymbol{\omega}_{ref}(t, \Gamma) &= \mathbf{f}(t, \Gamma) \\ \mathbf{q}_{ref} &= \int \dot{\mathbf{q}}(\boldsymbol{\omega}_{ref}) dt \end{aligned} \tag{A.8}$$

This continues until $\boldsymbol{\omega}_{ref}(t, \Gamma) \leq \omega_{tresh}$, at which point the current reference an-

gular velocity, $\boldsymbol{\omega}$, and quaternion, $\boldsymbol{q}$, are used at the begining of Maneuver 2.

Maneuver 2: Single Axis Slew to $\boldsymbol{q}_{safe}$

Maneuver 2 starts when either the initial testbed velocity is equal to zero or at the end of Maneuver 2. In both occasions, it is assumed that the current reference angular velocity and quaternion are given by $\boldsymbol{\omega}_{ref,0}$ and $\boldsymbol{q}_{ref,0}$.

This maneuver also utilizes the reference trajectory generation form Equation (A.1), and thus requires the computation of the same parameters $\Gamma = [t_0, t_r, t_c, \omega_s]$. For the single-axis slew, two user-defined parameters are set, namely the time of ramp up, $t_{r,safe}$, and the final time of completion of the slew $t_{f,slew}$ given by 2.5 (s), and 15 (s), respectively.

Given the ramp-up time, the final time, and the total slew angle, the coasting time t_c can be computed by,

$$t_c = t_{f,safe} - 2t_{r,safe} \tag{A.9}$$

The next step is to compute the delta quaternion that the testbed must rotate in order to reach $\boldsymbol{q}_{safe}$ with a zero angular velocity. This can be computed by,

$$\Delta\boldsymbol{q} = \boldsymbol{q}_{safe} \otimes \boldsymbol{q}_{ref,0} \tag{A.10}$$

The total angle corresponding to this quaternion can be computed by,

$$\Delta\theta = 2\arccos(\Delta\boldsymbol{q}_w) \tag{A.11}$$

where $\Delta\boldsymbol{q}_w$ corresponds to the scalar component of the quaternion. Since we want to perform the shortest slew we need to account for the case when $\Delta\theta$ is greater than 180° and change the values,

$$\Delta\theta = \begin{cases} \Delta\theta & \Delta\theta < 180^\circ \\ 2\pi - \Delta\theta & \Delta\theta \geq 180^\circ \end{cases} \tag{A.12}$$

Given the total rotation angle, the magnitude of the slew ω_s can be computed as,

$$\omega_s = -\frac{\Delta\theta sgn(\Delta \boldsymbol{q}_w)}{t_{f,safe} - t_{r,safe}} \tag{A.13}$$

where $sgn(\Delta \boldsymbol{q}_w)$ is a modified sign function that equals one when the value is zero,

$$sgn(\Delta \boldsymbol{q}_w) = \begin{cases} +1 & \Delta \boldsymbol{q}_w) \geq 0 \\ -1 & \Delta \boldsymbol{q}_w) < 0 \end{cases} \tag{A.14}$$

Finally, the angle $\hat{\boldsymbol{e}}$ is given by,

$$\hat{\boldsymbol{e}} = \frac{1}{\sin(\frac{1}{2}\Delta\theta)}[\Delta \boldsymbol{q}_x, \Delta \boldsymbol{q}_y, \Delta \boldsymbol{q}_z]^T \tag{A.15}$$

Similar to Maneuver 1, the reference angular velocity and quaternion are propagated via Equation (A.8).

A.1.2 Change Angle Trajectory

Another important trajectory generation mode used in the Guidance node is that of the Change Angle trajectory. This allows the user to select angle rotation about the body axis performing a Roll-Pitch-Yaw Euler angle sequence.

For this mode, the user requests a command with rotation angles $\boldsymbol{\theta} = [\theta_x, \theta_y, \theta_z]^T$ and a desired ramp up and final time t_r, and t_f, respectively. Similar to the Safe Mode case the trajectory provided by Equation (A.1) will be used with its associated Γ parameters

The coasting time can be computed as,

$$t_c = t_f - 2t_r \tag{A.16}$$

Given the set of angles, the desired quaternion rotation Δq, can be obtained by,

$$\Delta \boldsymbol{q} = angle2quat([\theta_x, \theta_y, \theta_z]) \tag{A.17}$$

where *angle2quat* is the implementation of MATLAB's function of the same name. Given the desired change in angle, the rest of the reference angular velocity function parameters follow the same steps as Maneuver 2 of Safe Mode.

The total angle of rotation is given by,

$$\Delta\theta = 2\arccos(\Delta \boldsymbol{q}_w) \tag{A.18}$$

Similarly to the Safe Mode, the shortest rotation is obtained by finding the angle theta that is of magnitude less than 180°,

$$\Delta\theta = \begin{cases} \Delta\theta & \Delta\theta < 180^\circ \\ 2\pi - \Delta\theta & \Delta\theta \geq 180^\circ \end{cases} \tag{A.19}$$

The angular velocity change ω_s and axis angle $\hat{\boldsymbol{e}}$ is given by,

$$\omega_s = -\frac{\Delta\theta sgn(\Delta \boldsymbol{q}_w)}{t_f - t_r} \tag{A.20}$$

and,

$$\hat{\boldsymbol{e}} = \frac{1}{\sin(\frac{1}{2}\Delta\theta)}[\Delta \boldsymbol{q}_x, \Delta \boldsymbol{q}_y, \Delta \boldsymbol{q}_z]^T \tag{A.21}$$

Given all the reference trajectory function parameters, the angular velocity and quaternion time history are given via Equation (A.8).

A.2 Reference Guidance Trajectory for Sats in SEL2

For Chapter 3 and 4, there is a need to create smooth reference trajectories for satellites switching between inertially pointing towards targets and pointing parallel to the Sun-Earth line in the synodic frame. This section covers the methodology used to generate the trajectories shown, for example, in Figure 3-15.

A.2.1 Slew Generation in Inertial and Synodic Frame

This section goes over four main segments of trajectories needed for satellites in SEL2: transfer to inertial pointing, inertial pointing, slewing to the Sun-Earth line, and maintaining Sun-Earth line pointing.

Transfer to inertial pointing

The first segment corresponds to a transfer from a satellite initially pointing along the Sun-Earth line to a target in the inertial plane. This transfer utilizes the technique used in Appendix A.1.2. It is assumed that the target point is about an azimuth and elevation θ_{az}, θ_{el} where the angles are defined in the same way as those in Section 3.4.

A rotation matrix is first generated using the desired azimuth and elevation angle,

$$^{tar}R^{bd} = angle2dcm(\theta_{az}, \theta_{el}, 0, \text{`}ZYX\text{'}) \tag{A.22}$$

where the function *angle2dcm* is given by MATLAB's Aerospace Toolbox. The pointing vector of the satellite's z^b axis is computed in this target frame,

$$\mathbf{z}^{tar} = {}^{tar}R^{bd}\mathbf{z}^b = {}^{tar}R^{bd}[0,0,1]^T \tag{A.23}$$

The delta quaternion used to make the satellite's z^b axis to be pointing to z^{tar} can be obtained as follows

$$\Delta\boldsymbol{q}_w = 1 + \left(\mathbf{z}^{bd} \cdot \mathbf{z}^{tar}\right) \tag{A.24}$$

and the vector component of the quaternion is given by,

$$[\Delta\boldsymbol{q}_x, \Delta\boldsymbol{q}_y, \Delta\boldsymbol{q}_z] = \mathbf{z}^{bd} \times \mathbf{z}^{tar} \tag{A.25}$$

The delta quaternion must be normalized so that it equals to one,

$$\Delta\boldsymbol{q} = \frac{\Delta\boldsymbol{q}}{||\Delta\boldsymbol{q}||} \tag{A.26}$$

The user chooses the transfer and final time t_r, and t_f, respectively. Equations

(A.18) and (A.21) are utilized to find the trajectory parameters Γ, and the reference angular velocity and quaternion are given via Equation (A.8).

Inertial pointing

Inertial pointing is the most basic trajectory that is generated. Throughout this trajectory the reference angular velocity is strictly zero $\boldsymbol{\omega} = \mathbf{0}$, and the reference quaternion is the quaternion produced at the end of the Transfer to inertial pointing.

Slewing to Sun-Earth line

The slewing to the Sun-Earth line maneuver is based on the DCT's Safe Mode. Unlike Safe Mode where the angular velocity is first arrested before slewing to a stationary attitude, this motion does the opposite as it starts at a stationary attitude (with respect to the inertial frame), and tries to achieve an angular velocity and attitude so that it ends aligned with the Sun-Earth line.

This trajectory generation can be divided into two parts: a ramp-up to the Sun-Earth line (Maneuver 2), and a slewing towards ramp-up (Maneuver 1). Maneuver 1 occurs before Maneuver 2, however, as will be shown here the generation and description of the overall trajectory will follow Maneuver 2 and then Maneuver 1. For the overall maneuver the user selects a total time for which the trajectory must be completed $t_{f,total}$, as well as the ratio of the time spent between Maneuver 1 and 2, ϵ_{s-e}. The initial condition of the satellite is that it starts pointing inertially, with a state $\boldsymbol{\omega}_0$, and $\boldsymbol{q}_0$.

Maneuver 2: Ramp-up to the Sun-Earth line

Maneuver 2 leverages the technique used in Safe Mode where the satellite's reference angular velocity is set to zero from an initial state. We will use the same technique by assuming that the satellite's initial state is the *final* state desired for the overall maneuver. That is, the "initial state" here is the state at which the satellite is following the Sun-Earth line with the correct angular velocity which is the angular velocity of the synodic frame relative to the inertial frame expressed in the satellite's body axis.

The first step is to compute the angle between the inertial and synodic frame at the end of the overall trajectory,

$$\theta_{syn} = n_{sun}\left(t_{start} + t_{f,total}\right) \tag{A.27}$$

where n_{sun} is the angular rate of the synodic frame relative to the inertial frame, and t_{start} is the start time of this overall trajectory. The rotation matrix between the synodic frame and inertial frame can be obtained by,

$${}^{syn}R^{I} = \begin{pmatrix} \cos(\theta_{syn}) & \sin(\theta_{syn}) & 0 \\ -\sin(\theta_{syn}) & \cos(\theta_{syn}) & 0 \\ 0 & 0 & 1 \end{pmatrix} \tag{A.28}$$

The rotation matrix from the satellite nominal attitude to the synodic frame is given by,

$${}^{bd}R^{syn} = \begin{pmatrix} 0.000 & 0.000 & 1.000 \\ 0.000 & -1.000 & 0.000 \\ 1.000 & 0.000 & 0.000 \end{pmatrix} \tag{A.29}$$

Therefore the quaternion representing the desired attitude of the satellite at the end of the overall trajectory so that it is pointing along the Sun-Earth line can be obtained by,

$$\boldsymbol{q}_{s-e} = dcm2quat({}^{bd}R^{syn}\ {}^{syn}R^{I}) \tag{A.30}$$

where $\boldsymbol{q}_{s-e}$ represents the quaternion from the inertial frame to the body-axis frame of the satellite, and MATLAB's *dcm2quat* function was utilized. The desired angular velocity of the spacecraft at this time is then,

$$\boldsymbol{\omega}_{syn}^{bd} = {}^{bd}R^{syn}[0, 0, n_{syn}]^{T} \tag{A.31}$$

The same trajectory from Safe Mode can be utilized by finding the axis of rotation,

$$\hat{\boldsymbol{e}} = \frac{\boldsymbol{\omega}_{syn}^{bd}}{||\boldsymbol{\omega}_{syn}^{bd}||} \tag{A.32}$$

The duration of this trajectory is the portion dedicated for this maneuver and it is also the ramp-up time, $t_r = \epsilon_{s-e} t_{f,total}$. The coasting time and initial time are set to zero, $t_c = 0$ and $t_0 = 0$, since the trajectory should be performed as quickly as possible. Finally, $\omega_s = n_{syn}$.

The values of $\Gamma = [t_0, t_r, t_c, \omega_s]$ alongside $\hat{\boldsymbol{e}}$ are used for the reference guidance function for a duration of t_r. The commanded angular velocity and quaternion are obtained via Equation (A.8).

After t_r time, let $\boldsymbol{q}_{man\ 2}$ be the reference quaternion from propagation of Equation (A.8).

Maneuver 1: Slew from target to start of ramp-up attitude

Maneuver 1 goal is to slew from the start of the overall reference trajectory's state $\boldsymbol{\omega}_0$, and $\boldsymbol{q}_0$ to reach the quaternion attitude where the ramp up to Sun-Earth lines begins, $\boldsymbol{q}_{man\ 2}$. This is done through a single-axis slew.

Similar to all the other trajectories the values $\Gamma = [t_0, t_r, t_c, \omega_s]$ have to be defined.

The ramp-up time corresponds to half of the remaining time between the overall trajectory,

$$t_r = \frac{1}{2}(1 - \epsilon) t_{f,total} \tag{A.33}$$

This trajectory's initial time is set to zero as well as the coasting time $t_c = 0$ and $t_0 = 0$. The delta quaternion for this part of the trajectory can be computed as,

$$\Delta \boldsymbol{q} = \boldsymbol{q}_0^{-1} \otimes \boldsymbol{q}_{man\ 2} \tag{A.34}$$

where the superscript -1 corresponds to the quaternion inverse. Similar to the transfer to inertial pointing trajectory, Equations (A.18) and(A.21) are utilized to find the trajectory parameters Γ, and the reference angular velocity and quaternion are given via Equation (A.8).

The overall trajectory is then produced by the combination of Maneuver 1 and the *time inversion* of Maneuver 2. At the end of this maneuver the satellite will be pointing along the Sun-Earth line with an angular velocity equal to that angular velocity relative to the synodic and inertial frame expressed in the satellite's body

axes.

Maintaining Sun-Earth line pointing

The final type of trajectory is that produced in order to continue pointing along the Sun-Earth. For this trajectory, it is assumed that the satellite is already pointing along the Sun-Earth line with an angular velocity given by $\boldsymbol{\omega}_{syn}^{bd}$.

To generate this trajectory the current angle between the synodic and inertial frame is computed,

$$\theta_{syn} = n_{syn}(t + t_0) \tag{A.35}$$

where $n_{syn}t_0$ is the initial angle of the synodic frame relative to the inertial frame at the start of the simulation. The rotation matrix between the synodic and inertial frame can be obtained through Equation (A.38). The desired testbed quaternion can then be computed by,

$$\boldsymbol{q}_{s-e} = dcm2quat({}^{bd}R^{syn\ \ syn}R^{I}(t)) \tag{A.36}$$

and the angualr velocity continues being,

$$\boldsymbol{\omega}_{syn}^{bd} = {}^{bd}R^{syn}[0, 0, n_{syn}]^T \tag{A.37}$$

This trajectory can be computed analytically and does not require any integration.

A.2.2 Incorporation of RSA Rotation to Trajectory Generation

Incorporating the rotation about the optical axis for an RSA satellite can be done trivially. The trajectory generation shown in Appendix A.2.1 do not change. Instead a new frame on top of the body frame is defined. Let the frame $\mathcal{F}^{rsa}$ be a frame with its origin coincident with the origin of the satellite's body-fixed axes origin. The z^{rsa}

axes is collinear with z^b. This new frame is allowed to rotate about the $z^b = z^{rsa}$ axis, and its nominal angle is such that the x^{rsa} and y^{rsa} axis are collinear to the body-axis counterparts. If the RSA satellite has an optical axis spin rate of ω_{spin}, then the rotation matrix between the RSA frame and the body-fixed frame is symply,

$$ {}^{rsa}R^{bd} = \begin{pmatrix} \cos(\omega_{spin}(t-t_0)) & \sin(\omega_{spin}(t-t_0)) & 0 \\ -\sin(\omega_{spin}(t-t_0)) & \cos(\omega_{spin}(t-t_0)) & 0 \\ 0 & 0 & 1 \end{pmatrix} \tag{A.38} $$

where $\omega_{spin}t_0$ is the initial angle offset between the two frames. If the non-rotating satellite has a commanded angular velocity and quaternion of $\boldsymbol{\omega}^{bd}$ and ${}^{bd}\boldsymbol{q}^I = {}^{bd}R^I$, respectively[1], the corresponding commanded angular velocity and quaternion for an RSA satellite is,

$$ \begin{aligned} \boldsymbol{\omega}^{rsa} &= \left({}^{rsa}R^{bd}\ \boldsymbol{\omega}^{bd}\right) + [0, 0, \omega_{spin}]^T \\ {}^{rsa}\boldsymbol{q}^I &= dcm2quat\left({}^{rsa}R^{bd}\ {}^{bd}R^I\right) \end{aligned} \tag{A.39} $$

This Appendix showed the derivations of guidance reference trajectories that were used throughout the Thesis. For the DCT, new guidance modes can be easily created corresponding to either new formulations or permutaions to the maneuvers shown in this case. For the SEL2 case, the main guidance trajectories needs for motions of RSA and non-RSA satellites were also presented.

[1]The formulation ${}^{bd}\boldsymbol{q}^I$ means that the quaternion represents an attitude rotation from the inertial frame to the body frame.

Appendix B

Torque Free Solution for RSA Motion Utilizing Gravity Gradient

This Appendix presents an example of the motion of an RSA satellite obtained only through the use of a gravity gradient in LEO. This Appendix is separate from Chapter 5 as it focuses on non-zero momentum satellites. Instead, the spinning about the optical axis is done only through external disturbance.

For this problem, a rigid body was placed on an orbit around earth as shown in Figure B-1. The system contains three frames: 1) an inertial frame $\mathcal{F}^I$, a Local Vertical Local Horizontal $\mathcal{F}^{lvlh}$, and a body-fixed frame $\mathcal{F}^b$. The inertial frame and represents an Earth-Centered Inertial Frame (ECI) J200 frame where the origin is at the center of Earth, the x-axis points to the mean equinox, the z-axis is aligned with the celestial North pole, and the y-axis completes the right-handed coordinate system. The LVLH frame is defined by the origin fixed at the satellite center of mass CM, the z-axis point radially outwards from Earth to the satellite, the x-axis points towards the orbit velocity, and the y-axis completes the right-hand plane and points towards the orbit normal [112]. Finally, the body-fixed frame corresponds to a framed fixed at the satellite body with the z-axis pointing in the direction of the principal pointing axis, the y-axis along the satellite aperture length, and the x-axis about the aperture width such that it completes a right-handed frame.

The gravity gradient for such a satellite is given by [160],

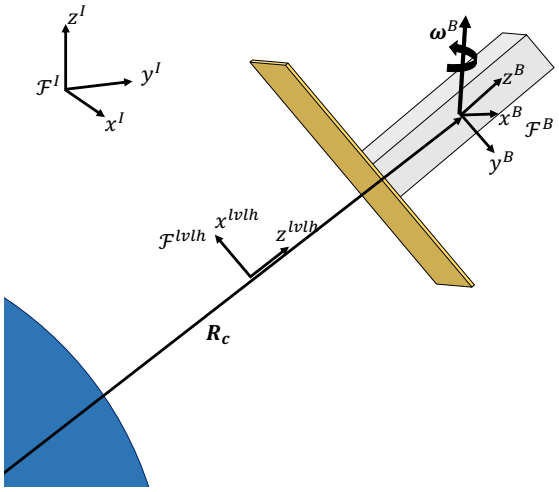

Figure B-1: Definition of LVLH frame, inertial frame, and body frame.

$$\mathbf{L}_G = \frac{3\mu}{\|\mathbf{R}_c\|^5}\mathbf{R}_c \times ([I]\mathbf{R}_c) \tag{B.1}$$

where μ is the gravitational parameter, $[I]$ is the inertia tensor of the system, and $\mathbf{R}_c$ is distance from the satellite CM to the origin of the primary.

Equation B.1 is independent on the coordinate system. A body frame can be chosen that is aligned with the principal axis of inertia i.e.

$$I = \begin{pmatrix} I_x & 0 & 0 \\ 0 & I_y & 0 \\ 0 & 0 & I_z \end{pmatrix} = diag([I_x, I_y, I_z]) \tag{B.2}$$

To simplify the analysis the assumption will be made that the system is axisymmetric in the sense of an inertial tensor about the z-axis, $I_x = I_y$. Additionally, taking from concepts from formation flying, it is well known there exists a set of initial conditions between a series of satellites such that their orbit, in an LVLH frame, forms a circle, known as a circle in space orbit [161]. In this orbit, it is expected that an axisymmetric satellite would experience no internal forces as each point in the rigid body rotates concerning each other. The condition of the orbit can be completely defined by the angle between the orbit normal and the z-axis of the LVLH frame as shown in Figure

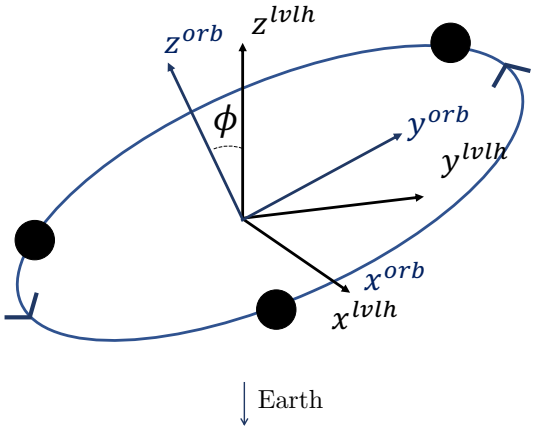

Figure B-2: Condition for "circle in orbit" trajectory. At a condition defined by angle ϕ about the x^{lvlh} axis it is possible for a number of satellites to form a perfect circle when viewed in LVLH frame.

B-2.

Given this condition, and assuming that there exists an axisymmetric object in the plane of the orbit such as a thin disk, it is possible to define a rotation matrix between the body and the LVLH axes,

$$ {}^{B}R^{lvlh} = \begin{pmatrix} 1 & 0 & 0 \\ 0 & \cos\phi & \sin\phi \\ 0 & -\sin\phi & \cos\phi \end{pmatrix} \tag{B.3} $$

Therefore, the position of the satellite can be given by,

$$ \mathbf{R}_C^b = {}^{B}R^{lvlh}\mathbf{R}_C^{lvlh} = \begin{pmatrix} 0 \\ R_c\sin\phi \\ R_c\cos\phi \end{pmatrix} $$

This yields a gravity gradient torque of

$$ \mathbf{L}_G = \frac{3\mu}{\|\mathbf{R}_c\|^5}\mathbf{R}_c \times ([I]\mathbf{R}_c) = 3n^2(I_z - I_x)\sin\phi\cos\phi \tag{B.4} $$

where $\mu/||R_c||^3 = n^2$ or the orbital rate for a circular orbit. To study stability of the

rigid body placed in this configuration, the rigid body is perturbed about each body axis given by,

$$^{ptb}R^{B} = R_z(\theta_3)R_y(\theta_2)R_x(\theta_1) \tag{B.5}$$

where θ_1, θ_2, and θ_3 are small angle perturbations about the axis. Note that this rotation matrix is applied to the body-fixed axis.

The combined angular velocity of the system is taken as,

$$\boldsymbol{\omega}_{tot} = \boldsymbol{\omega}_{bd} + \boldsymbol{\omega}_{lvlh} \tag{B.6}$$

where $\boldsymbol{\omega}_{bd}$ is the perturbed angular velocity of the rigid body *relative* to the LVLH and $\boldsymbol{\omega}_{lvlh}$ is the angular velocity of the LVLH frame relative to the inertial frame. Since the angular velocity of the LVLH frame is in the direction of the orbit normal, we obtain assuming small angle approximations

$$\boldsymbol{\omega}_{lvlh} = {}^{ptb}R^{B}\ {}^{B}R^{lvlh} \begin{pmatrix} 0 \\ n \\ 0 \end{pmatrix} = \begin{pmatrix} n\theta_2 \sin(\phi) + n\theta_3 \cos(\phi) \\ n\cos(\phi) - n\theta_1 \sin(\phi) \\ -n\sin(\phi) - n\theta_1 \cos(\phi) \end{pmatrix} \tag{B.7}$$

The term $\boldsymbol{\omega}_{bd}$ corresponds to the angular velocity from the small perturbations as well as from the satellite spinning due to the "circle in space" motion. Let the spin of the rigid body, on the z-axis be $\Omega_s\hat{\mathbf{z}}$. The total angular velocity of the system from Equation (B.6) is given by,

$$\boldsymbol{\omega}_{tot} = \begin{pmatrix} \dot{\theta}_1 + n\theta_2 \sin(\phi) + n\theta_3 \cos(\phi) \\ \dot{\theta}_2 + n\cos(\phi) - n\theta_1 \sin(\phi) \\ \dot{\theta}_3 + \Omega_s - n\sin(\phi) - n\theta_1 \cos(\phi) \end{pmatrix} \tag{B.8}$$

Plugging the total angular velocity into the NewtonEuler equation results in,

$$I\dot{\omega} + \boldsymbol{\omega} \times I\boldsymbol{\omega} = \mathbf{L}_G \tag{B.9}$$

$$
\begin{aligned}
Ix\ddot{\theta}_1 + \big[(2I_x - Iz)\, n \sin\phi + I_z\Omega_s \big]\dot{\theta}_2 + I_z n\dot{\theta}_3 \cos\phi + \big[(I_x - I_z)n^2 \cos 2\phi - \\
I_z\Omega_s n \sin\phi\big]\theta_1 + 4(I_x - I_z)n^2 \cos\phi \sin\phi + I_z n\Omega_s \cos\phi = 0 \\
I_x\ddot{\theta}_2 + \big[(I_z - 2I_x)n \sin\phi - I_z\Omega_s\big]\dot{\theta}_1 + \big[(I_z - I_x)n^2 \sin^2\phi - Iz\Omega_s n \sin\phi\big]\theta_2 \\
\big[(I_z - I_x)n^2 \cos\phi \sin\phi - I_z\Omega_s n \cos\phi\big]\theta_3 = 0 \\
I_z\ddot{\theta}_3 + \big[(I_z - 2I_x)n \sin\phi - I_z\Omega_s\big]\dot{\theta}_1 + \big[(I_z - I_x)n^2 \sin^2\phi - I_z\Omega_s n \sin\phi\big]\theta_2 \\
\big[(I_z - I_x)n^2 \cos\phi \sin\phi - I_z\Omega_s n \cos\phi\big]\theta_3 = 0
\end{aligned}
\tag{B.10}
$$

In order to look for equilibrium points, let $\ddot{\theta}_1 = \ddot{\theta}_2 = \ddot{\theta}_3 = 0$ and $\dot{\theta}_1 = \dot{\theta}_2 = \dot{\theta}_3 = 0$. Using the first line from Equation (B.10) for the case in which the perturbations are set to zero, we obtain ,

$$
4(I_x - I_z)n^2 \cos\phi \sin\phi + I_z n\Omega_s \cos\phi
$$

which yields the equilibrium condition for the angle ϕ to,

$$
\sin\phi = \frac{I_z\Omega_s}{4(I_z - I_x)n} \tag{B.11}
$$

Equation (B.11) represents the condition for which an axisymetric rigid body, with inertias $I_x,\ I_z$ with a spin Ω_s about the z-axis, spins without any required torque. This condition was checked by running a full nonlinear high-fidelity satellite simulation of a spinning rigid body.

The stability condition about this point can be found by plugging Equation (B.11) on Eq. (B.10), and assuming a thin disc condition $I_x = 1/2I_z$[1] yielding,

[1] was done to simplify the results, however, the general condition without loss of generality can be found as well

$$\frac{1}{2}\ddot{\theta}_1 + \Omega_s\dot{\theta}_2 + n\cos\phi\dot{\theta}_3 + [-\frac{1}{2}n^2\cos 2\phi - \Omega_s n\sin\phi]\theta_1 = 0$$

$$\frac{1}{2}\ddot{\theta}_2 - \Omega_s\dot{\theta}_1 + \left(\frac{1}{2}n^2\sin^2\phi - \Omega_s n\sin\phi\right)\theta_2 + \left(\frac{1}{2}n^2\cos\phi\sin\phi - \Omega_s n\cos\phi\right)\theta_3 = 0$$

$$\ddot{\theta}_3 - n\cos\phi\dot{\theta}_1 = 0 \tag{B.12}$$

Note that $\left(\frac{1}{2}n^2\sin^2\phi - \Omega_s n\sin\phi\right) = -\frac{3}{8}\Omega_s^2$ and $\left(\frac{1}{2}n^2\cos\phi\sin\phi - \Omega_s n\cos\phi\right) = \frac{3}{4}n\Omega_s\cos\phi$, It is possible to find the poles of the system. Which are given by $\sigma = \pm in,\ \pm i\Omega_s$. Therefore, linear stability analysis cannot tell us about the stability of the system and nonlinear analysis must be used.

Bibliography

[1] Lori Keesey. The next generation of telescopes are almost impossibly accurate. *NASA*, 2016.

[2] Rafanelli G Haeri M Polidan R, Bauermeister A. A rotating synthetic aperture (rsa) space telescope for future uv/opt/ir astronomical missions, 2015.

[3] Gerard L Rafanelli, Christopher M Cosner, Susan B Spencer, Douglas Wolfe, Arthur Newman, Ronald Polidan, and Supriya Chakrabarti. Revolutionary astrophysics using an incoherent synthetic optical aperture. In *UV/Optical/IR Space Telescopes and Instruments: Innovative Technologies and Concepts VIII*, volume 10398, page 103980P. International Society for Optics and Photonics, 2017.

[4] Alejandro D Cabrales Hernandez, Evan L Kramer, and Rebecca A Masterson. Development of a hardware-in-the-loop testbed for rotating synthetic aperture telescopes. In *2022 IEEE Aerospace Conference (AERO)*, pages 1–16. IEEE, 2022.

[5] Anthony J Manna. 25 years of tiros satellites. *American Meteorological Society, Bulletin*, 66:421–423, 1985.

[6] Bill Emery and Adriano Camps. *Introduction to satellite remote sensing: atmosphere, ocean, land and cryosphere applications*. Elsevier, 2017.

[7] Sabrina Stierwalt. Why Do We Put Telescopes in Space? *Scientific American*, 2018.

[8] Harley A. Thronson, Nicholas Siegler, Ronald Polidan, Matthew Greenhouse, John Grunsfeld, Howard Macewen, Bradley M. Peterson, and Rudranarayan Mukherjee. Future capabilities in space servicing and assembly: Opportunities for future major astrophysics missions. *2018 AIAA SPACE and Astronautics Forum and Exposition*, (September):1–8, 2018.

[9] Jonathan P Gardner, John C Mather, Mark Clampin, Rene Doyon, Kathryn A Flanagan, Marijn Franx, Matthew A Greenhouse, Heidi B Hammel, John B Hutchings, Peter Jakobsen, et al. The james webb space telescope. In *Astrophysics in the Next Decade*, pages 1–29. Springer, 2009.

[10] Tyler Robinson, BS Gaudi, Sara Seager, Bertrand Mennesson, Alina Kiessling, and Keith Warfield. The habitable exoplanet observatory. In *American Astronomical Society Meeting Abstracts# 233*, volume 233, pages 222–01, 2019.

[11] Matthew R Bolcar, Julie Crooke, Jason E Hylan, Ginger Bronke, Christine Collins, James Corsetti, Joe Generie, Qian Gong, Tyler Groff, William Hayden, et al. The large uv/optical/infrared surveyor (luvoir): decadal mission study update. In *Space telescopes and instrumentation 2018: optical, infrared, and millimeter wave*, volume 10698, pages 232–244. SPIE, 2018.

[12] Matthew R Bolcar, Kunjithapatham Balasubramanian, Mark Clampin, Julie Crooke, Lee Feinberg, Marc Postman, Manuel Quijada, Bernard Rauscher, David Redding, Norman Rioux, et al. Technology development for the advanced technology large aperture space telescope (atlast) as a candidate large uv-optical-infrared (luvoir) surveyor. In *UV/Optical/IR Space Telescopes and Instruments: Innovative Technologies and Concepts VII*, volume 9602, page 960209. International Society for Optics and Photonics, 2015.

[13] LUVOIR Team et al. The luvoir mission concept study final report. *arXiv preprint arXiv:1912.06219*, 2019.

[14] Daniel Clery. Future nasa scope would find life on alien worlds. *Science (New York, NY)*, 379(6628):123–124, 2023.

[15] Engineering National Academies of Sciences, Medicine, et al. *Pathways to Discovery in Astronomy and Astrophysics for the 2020s*. 2021.

[16] Stephen D Creech. Nasa's space launch system: Launch capability for lunar exploration and transformative science. In *2020 IEEE Aerospace Conference*, pages 1–13. IEEE, 2020.

[17] Xu Boqian, Yu Funan, AS Shugarov, ME Sachkov, IS Savanov, Gao Yan, Wang Shuaihui, Ju Guohao, Zhang Chunyue, and Kuang Ye. Conceptual design of the chinese-russian on-orbit-assembling space telescope (oast). *Solar System Research*, 54(7):685–689, 2020.

[18] Lee D Feinberg, Jason G Budinoff, Howard A MacEwen, Gary W Matthews, and Marc Postman. Modular assembled space telescope. *Optical Engineering*, 52(9):091802, 2013.

[19] William David Sanchez, Keenan Eugene Sumner Albee, Rosemary Katherine Davidson, Ryan de Freitas Bart, Alejandro Cabrales Hernandez, and Jeffrey A Hoffman. A preliminary architecture optimization for in-space assembled telescopes. 2019.

[20] WR Oegerle, LR Purves, JG Budinoff, RV Moe, TM Carnahan, DC Evans, and CK Kim. Concept for a large scalable space telescope: in-space assembly. In *Space Telescopes and Instrumentation I: Optical, Infrared, and Millimeter*,

volume 6265, page 62652C. International Society for Optics and Photonics, 2006.

[21] William D Sanchez, Keenan Albee, Rosemary Davidson, Ryan De Freitas Bart, Alejandro Cabrales Hernandez, and Jeffrey Hoffman. A Preliminary Architecture Optimization for In-Space Assembled Telescopes. (October), 2019.

[22] Yuchen She, Shuang Li, Yufei Liu, and Menglong Cao. In-orbit robotic assembly mission design and planning to construct a large space telescope. *Journal of Astronomical Telescopes, Instruments, and Systems*, 6(1):017002, 2020.

[23] Máximo A Roa, Korbinian Nottensteiner, Gerhard Grunwald, Pablo Lopez Negro, Aurelian Cuffolo, Sabrine Andiappane, Mathieu Rognant, Antoine Verhaeghe, and Vincent Bissonnette. In-space robotic assembly of large telescopes. In *Proc. 15th Symp. Advanced Space Technologies Robotics and Automation (ASTRA)*, 2019.

[24] Ariadna Farres, Cassandra Webster, Jennifer Donaldson, and Dave Folta. Orbital maintenance for the wide field infrared survey telescope: The effects of solar radiation pressure and navigation accuracies on station keeping. In *2018 AAS/AIAA Astrodynamics Specialist Conference*, number GSFC-E-DAA-TN59701, 2018.

[25] Gabriel Soto, Dean Keithly, Daniel Garrett, Christian Delacroix, and Dmitry Savransky. Optimal starshade observation scheduling. In *Space Telescopes and Instrumentation 2018: Optical, Infrared, and Millimeter Wave*, volume 10698, page 106984M. International Society for Optics and Photonics, 2018.

[26] Fernando Mier-Hicks and Paulo C Lozano. Electrospray thrusters as precise attitude control actuators for small satellites. *Journal of Guidance, Control, and Dynamics*, 40(3):642–649, 2017.

[27] Gerard L Rafanelli and Mark J Rehfield. Full aperture image synthesis using rotating strip aperture image measurements, September 7 1993. US Patent 5,243,351.

[28] JJ Green and Bobby R Hunt. Super-resolution in a synthetic aperture imaging system. In *Proceedings of International Conference on Image Processing*, volume 1, pages 865–868. IEEE, 1997.

[29] Rebecca Masterson and Joseph Green. Demonstration of pointing stability to enable astrophysics with rotating synthetic aperture telescopes. 2019.

[30] Gabriele Facciolo, Carlo De Franchis, and Enric Meinhardt-Llopis. Automatic 3d reconstruction from multi-date satellite images. In *Proceedings of the IEEE Conference on Computer Vision and Pattern Recognition Workshops*, pages 57–66, 2017.

[31] Jeroen Klomp. Economic development and natural disasters: A satellite data analysis. *Global Environmental Change*, 36:67–88, 2016.

[32] GL Rafanelli, A Newman, JJ Green, S Chakrabarti, C Mendillo, and R Polidan. Potential benefits of rotating synthetic apertures (rsas) for astronomical and astrophysical observatories. *The Space Astrophysics Landscape for the 2020s and Beyond*, 2135:5009, 2019.

[33] Green J. Masterson R. Demonstration of pointing stability to enable astrophysics with rotating synthetic aperture telescopes. In *NASA Research Opportunities in Space and Earth Sciences 2018*, 2018. NASA ROSES: NNH18ZDA001N-APRA.

[34] Donald J Dichmann, Cassandra Alberding, and Wayne Yu. James webb space telescope (jwst) stationkeeping monte carlo simulations. In *International Symposium on Space Flight Dynamics*, number GSFC-E-DAA-TN14534, 2014.

[35] Paweł Zagórski. Modeling disturbances influencing an earth-orbiting satellite. *Pomiary Automatyka Robotyka*, 16(5):98–103, 2012.

[36] Yuichi Tsuda, Osamu Mori, Ryu Funase, H Sawada, T Yamamoto, T Saiki, T Endo, and Jun'ichiro Kawaguchi. Flight status of ikaros deep space solar sail demonstrator. *Acta astronautica*, 69(9-10):833–840, 2011.

[37] Osamu Mori, Hirotaka Sawada, Ryu Funase, Mutsuko Morimoto, Tatsuya Endo, Takayuki Yamamoto, Yuichi Tsuda, Yasuhiro Kawakatsu, Jun'ichiro Kawaguchi, Yasuyuki Miyazaki, et al. First solar power sail demonstration by ikaros. *Transactions of the Japan Society for Aeronautical and Space Sciences, Aerospace Technology Japan*, 8(ists27):To_4_25–To_4_31, 2010.

[38] Hulya Demiryont, Kenneth Shannon III, and Rengasamy Ponnappan. Electrochromic devices for satellite thermal control. In *AIP Conference Proceedings*, volume 813, pages 64–73. American Institute of Physics, 2006.

[39] Cornelius J Dennehy and Oscar S Alvarez-Salazar. A survey of the spacecraft line-of-sight jitter problem. In *AAS Annual Guidance and Control Conference*, number NF1676L-32261, 2019.

[40] O De Weck, D Miller, and H Guiterrez. Structural dynamics and control for ngst-a preliminary study. In *LIA Colloq. 34: The Next Generation Space Telescope: Science Drivers and Technological Challenges*, volume 429, page 269, 1998.

[41] Rebecca A Masterson, David W Miller, and Robert L Grogan. Development and validation of reaction wheel disturbance models: empirical model. *Journal of sound and vibration*, 249(3):575–598, 2002.

[42] Aron Wolf and Neil Dennehy. Applications of microthrusters on astrophysics missions with demanding jitter requirements. *Bulletin of the American Astronomical Society*, 51(7):168, 2019.

[43] Thibault LB Flinois, Cameron Haag, Milan Mandic, William Sanchez, Oscar Alvarez-Salazar, and John Ziemer. Microthruster-based control for precision pointing of next-generation space telescopes. 2022.

[44] Nicholas Belsten, Leonid Pogorelyuk, Christian Haughwout, Eric Cady, and Kerri Cahoy. Strategies for high order wavefront sensing and control (howfsc) computation on future space telescopes. In *Techniques and Instrumentation for Detection of Exoplanets X*, volume 11823, pages 477–490. SPIE, 2021.

[45] Kerri Cahoy, James Clark, Gregory Allan, Yinzi Xin, Ewan Douglas, Jennifer Lumbres, and Jared Males. Space-based laser guide star mission to enable ground and space telescope observations of faint objects. *NAS APC White Paper*, 2019.

[46] Joseph W Goodman. I synthetic-aperture optics. In *Progress in Optics*, volume 8, pages 1–50. Elsevier, 1970.

[47] Nicholas J Miller, Matthew P Dierking, and Bradley D Duncan. Optical sparse aperture imaging. *Applied Optics*, 46(23):5933–5943, 2007.

[48] Ettien Kpré, Cyril Decroze, Moctar Mouhamadou, and Thomas Fromenteze. Computational imaging for compressive synthetic aperture interferometric radiometer. *IEEE Transactions on Antennas and Propagation*, 66(10):5546–5557, 2018.

[49] Markus E Testorf and Michael A Fiddy. Superresolution imaging—revisited. *Advances in Imaging and Electron Physics*, 163:165–218, 2010.

[50] Müjdat Çetin, Ivana Stojanović, N Özben Önhon, Kush Varshney, Sadegh Samadi, William Clem Karl, and Alan S Willsky. Sparsity-driven synthetic aperture radar imaging: Reconstruction, autofocusing, moving targets, and compressed sensing. *IEEE Signal Processing Magazine*, 31(4):27–40, 2014.

[51] Silvia Masi. Lecture notes in methods in space astrphysics, 2005.

[52] Howard Curtis. *Orbital mechanics for engineering students*. Butterworth-Heinemann, 2013.

[53] Peter W Likins. Effects of energy dissipation on the free body motions of spacecraft. 1966.

[54] Stephen Andrews and James O'Donnell. Map attitude control system design and flight performance. In *AIAA Guidance, Navigation, and Control Conference and Exhibit*, page 4580, 2002.

[55] Peter AR Ade, Nabila Aghanim, Monique Arnaud, M Ashdown, J Aumont, C Baccigalupi, M Baker, A Balbi, AJ Banday, RB Barreiro, et al. Planck early results. i. the planck mission. *Astronomy & Astrophysics*, 536:A1, 2011.

[56] Craig Tooley. Nasa's magnetospheric multiscale (mms) mission. In *2015 University of North Dakota Space Studies Colloquium*, number GSFC-E-DAA-TN22485, 2015.

[57] Anton H De Ruiter, Christopher Damaren, and James R Forbes. *Spacecraft dynamics and control: an introduction*. John Wiley & Sons, 2012.

[58] Li-Sheng Wang, Kuang-Yow Lian, and Po-Tuan Chen. Steady motions of gyrostat satellites and their stability. *IEEE transactions on automatic control*, 40(10):1732–1743, 1995.

[59] Alan Title. Observations of the sun from space. In *The Sun as a Guide to Stellar Physics*, pages 387–417. Elsevier, 2019.

[60] Evan Dale Wise. *Design, analysis, and testing of a precision guidance, navigation, and control system for a dual-spinning Cubesat*. PhD thesis, Massachusetts Institute of Technology, 2013.

[61] William Blackwell, G Allen, C Galbraith, Timothy Hancock, R Leslie, Idahosa Osaretin, L Retherford, Michael Scarito, C Semisch, Michael Shields, et al. Nanosatellites for earth environmental monitoring: The micromas project. In *2012 12th Specialist Meeting on Microwave Radiometry and Remote Sensing of the Environment (MicroRad)*, pages 1–4. IEEE, 2012.

[62] Anne D Marinan, Ayesha Georgina Ayesha Georgina Iwalanai Hein, Zachary T Lee, Ashley K Carlton, Kerri Cahoy, Adam B Milstein, Michael W Shields, Michael T DiLiberto, and William J Blackwell. Analysis of the microsized microwave atmospheric satellite (micromas) communications anomaly. 2018.

[63] Angela Crews, W Blackwell, R Vincent Leslie, Michael Grant, Idahosa Osaretin, Michael DiLiberto, Adam Milstein, and Kerri Cahoy. Calibration and validation of small satellite passive microwave radiometers: Micromas-2a and tropics. In *Active and Passive Microwave Remote Sensing for Environmental Monitoring II*, volume 10788, page 107880Y. International Society for Optics and Photonics, 2018.

[64] Oscar S Alvarez-Salazar. Pointing architecture of smap's large spinning antenna. In *AIAA Guidance, Navigation, and Control (GNC) Conference*, page 4560, 2013.

[65] Todd S Brown and Tina S Sung. In-flight pointing accuracy assessment and gnc commissioning overview for the dual-spinning smap (soil moisture active passive) spacecraft. 2017.

[66] Damon D Phinney. Slip ring experience in long duration space applications. *2dh Aerospace*, 1986.

[67] JB Mondier, F Sirou, and P Mäusli. Life test of the scarab instrument slipring units. In *9th European Space Mechanisms and Tribology Symposium*, volume 480, pages 99–106, 2001.

[68] PA Mäusli, A Gisiger, and JM Gavira. Long-life, elevated-velocity slip-ring contacts investigation. In *6th European Space Mechanisms and Tribology Symposium*, volume 374, page 21, 1995.

[69] Lúcia V Santos, Vladimir J Trava-Airoldi, Evaldo J Corat, Jadir Nogueira, and Nélia F Leite. Dlc cold welding prevention films on a ti6al4v alloy for space applications. *Surface and Coatings Technology*, 200(8):2587–2593, 2006.

[70] F Avino, B Gaffinet, D Bommottet, A Howling, and I Furno. Slip ring test assembly with increased breakdown voltage limit for high-voltage bus satellites. *IEEE Aerospace and Electronic Systems Magazine*, 35(8):32–36, 2020.

[71] Shumei Cui, Zhi Bie, Jiantao Zhang, Kai Song, Chunbo Zhu, et al. A redundancy design of wireless power transfer system for satellite slip ring with high reliability. In *2021 IEEE 4th International Electrical and Energy Conference (CIEEC)*, pages 1–6. IEEE, 2021.

[72] Brent J Bos, Pamela S Davila, Matthew Jurotich, Gurnie Hobbs, Paul A Lightsey, James Contreras, and Tony Whitman. The james webb space telescope instrument suite layout: optical system engineering considerations for a large deployable space telescope. In *Optical, Infrared, and Millimeter Space Telescopes*, volume 5487, pages 734–745. International Society for Optics and Photonics, 2004.

[73] Guy Nir, Barak Zackay, and Eran O Ofek. A possible advantage of telescopes with a noncircular pupil. *The Astronomical Journal*, 158(2):70, 2019.

[74] Joseph J Green, Samuel Case Bradford, Thomas Gautier, Michael Rodgers, Erkin Sidick, and Gautam Vasisht. Architecture for space-based exoplanet spectroscopy in the mid-infrared. In *Space Telescopes and Instrumentation 2018: Optical, Infrared, and Millimeter Wave*, volume 10698, page 106981C. International Society for Optics and Photonics, 2018.

[75] Y-W Chiang and BJ Sullivan. Multi-frame image restoration using a neural network. In *Proceedings of the 32nd Midwest Symposium on Circuits and Systems,*, pages 744–747. IEEE, 1989.

[76] Xiyang Zhi, Shikai Jiang, Lei Zhang, Dawei Wang, Jianming Hu, and Jinnan Gong. Imaging mechanism and degradation characteristic analysis of novel rotating synthetic aperture system. *Optics and Lasers in Engineering*, 139:106500, 2021.

[77] Lyle E Wiggins. Relative magnitudes of the space-environment torques on a satellite. *Aiaa Journal*, 2(4):770–771, 1964.

[78] Colin R McInnes. *Solar sailing: technology, dynamics and mission applications*. Springer Science & Business Media, 2004.

[79] Marc Jorba-Cusco, Ariadna Farrés, and Àngel Jorba. On the stabilizing effect of solar radiation pressure in the earth-moon system. *Advances in Space Research*, 67(9):2812–2822, 2021.

[80] Colin R McInnes, Alastair JC McDonald, John FL Simmons, and Ewan W MacDonald. Solar sail parking in restricted three-body systems. *Journal of Guidance, Control, and Dynamics*, 17(2):399–406, 1994.

[81] Hexi Baoyin and Colin R McInnes. Solar sail orbits at artificial sun-earth libration points. *Journal of Guidance, control, and dynamics*, 28(6):1328–1331, 2005.

[82] James D Biggs, Colin R McInnes, and Thomas Waters. Control of solar sail periodic orbits in the elliptic three-body problem. *Journal of Guidance, Control, and Dynamics*, 32(1):318–320, 2009.

[83] John Bookless and Colin McInnes. Control of lagrange point orbits using solar sail propulsion. *Acta Astronautica*, 62(2-3):159–176, 2008.

[84] Kailash Chandra Pande. *Attitude control of spinning satellites using environmental forces*. PhD thesis, University of British Columbia, 1973.

[85] Bong Wie. Solar sail attitude control and dynamics, part 1. *Journal of Guidance, Control, and Dynamics*, 27(4):526–535, 2004.

[86] He Huang and Jun Zhou. Solar sailing cubesat attitude control method with satellite as moving mass. *Acta Astronautica*, 159:331–341, 2019.

[87] Shahin Firuzi and Shengping Gong. Attitude control of a flexible solar sail in low earth orbit. *Journal of Guidance, Control, and Dynamics*, 41(8):1715–1730, 2018.

[88] Feng Zhang, GONG Shengping, GONG Haoran, and Hexi Baoyin. Solar sail attitude control using shape variation of booms. *Chinese Journal of Aeronautics*, 35(10):326–336, 2022.

[89] John R Scull. Guidance and control of the mariner planetary spacecraft. *IFAC Proceedings Volumes*, 2(1):97–107, 1965.

[90] Keum W Lee and Sahjendra N Singh. Three-axis l 1 adaptive attitude control of spacecraft using solar radiation pressure. *Proceedings of the Institution of Mechanical Engineers, Part G: Journal of Aerospace Engineering*, 229(3):407–422, 2015.

[91] Camilla Colombo, Charlotte Lücking, and Colin R McInnes. Orbit evolution, maintenance and disposal of spacechip swarms through electro-chromic control. *Acta Astronautica*, 82(1):25–37, 2013.

[92] EB Franke, CL Trimble, Mathias Schubert, John A Woollam, and JS Hale. All-solid-state electrochromic reflectance device for emittance modulation in the far-infrared spectral region. *Applied physics letters*, 77(7):930–932, 2000.

[93] Hulya Demiryont and David Moorehead. Electrochromic emissivity modulator for spacecraft thermal management. *Solar Energy Materials and Solar Cells*, 93(12):2075–2078, 2009.

[94] Junshan Mu, Shengping Gong, and Junfeng Li. Reflectivity-controlled solar sail formation flying for magnetosphere mission. *Aerospace Science and Technology*, 30(1):339–348, 2013.

[95] Junshan Mu, Shengping Gong, Junfeng Li, and Hexi Baoyin. Coupled attitude–orbit dynamics and control of reflectivity modulated solar sail for geosail formation flying. *Advances in Solar Sailing*, pages 791–810, 2014.

[96] Junshan Mu, Shengping Gong, and Junfeng Li. Coupled control of reflectivity modulated solar sail for geosail formation flying. *Journal of Guidance, Control, and Dynamics*, 38(4):740–751, 2015.

[97] James D Biggs and Alessio Negri. Orbit-attitude control in a circular restricted three-body problem using distributed reflectivity devices. *Journal of Guidance, Control, and Dynamics*, 42(12):2712–2721, 2019.

[98] Markus Wilde, Casey Clark, and Marcello Romano. Historical survey of kinematic and dynamic spacecraft simulators for laboratory experimentation of on-orbit proximity maneuvers. *Progress in Aerospace Sciences*, 110:100552, 2019.

[99] Corey Whitcomb. Crowell. *Development and analysis of a small satellite attitude determination and control system testbed.* Massachusetts Institute of Technology, Department of Aeronautics and Astronautics, 2011.

[100] Muhammad Faisal, Florian Wolz, Felix Dengel, and Sergio Montenegro. A testbed for a three dimensional pico-sphere satellite-simulator (t3dpilare). In *2021 IEEE International IOT, Electronics and Mechatronics Conference (IEMTRONICS)*, pages 1–6. IEEE, 2021.

[101] A Tavakoli, A Faghihinia, and A Kalhor. An innovative test bed for verification of attitude control system. *IEEE Aerospace and Electronic Systems Magazine*, 32(6):16–22, 2017.

[102] David Miller, A Saenz-Otero, J Wertz, A Chen, G Berkowski, C Brodel, S Carlson, D Carpenter, S Chen, S Cheng, et al. Spheres: a testbed for long duration satellite formation flying in micro-gravity conditions. In *Proceedings of the*

AAS/AIAA space flight mechanics meeting, volume 105, pages 167–179. Clearwater, Florida, January, 2000.

[103] Maria Bualat, Jonathan Barlow, Terrence Fong, Chris Provencher, and Trey Smith. Astrobee: Developing a free-flying robot for the international space station. In *AIAA SPACE 2015 Conference and Exposition*, page 4643, 2015.

[104] K Saulnier, D Pérez, R.C Huang, D Gallardo, G Tilton, and R Bevilacqua. A six-degree-of-freedom hardware-in-the-loop simulator for small spacecraft. *Acta astronautica*, 105(2):444–462, 2014.

[105] Richard Zappulla, Josep Virgili-Llop, Costantinos Zagaris, Hyeongjun Park, and Marcello Romano. Dynamic air-bearing hardware-in-the-loop testbed to experimentally evaluate autonomous spacecraft proximity maneuvers. *Journal of Spacecraft and Rockets*, 54(4):825–839, 2017.

[106] Bahman. Zohuri. *Dimensional Analysis and Self-Similarity Methods for Engineers and Scientists*. Springer International Publishing, Cham, 1st ed. 2015. edition, 2015.

[107] Bahman. Zohuri. *Dimensional Analysis Beyond the Pi Theorem*. Springer International Publishing, Cham, 1st ed. 2017. edition, 2017.

[108] Ayansola D Ogundele, Bautista R Fernandez, Josep Virgili-Llop, and Marcello Romano. A tip-tilt hardware-in-the-loop air-bearing test bed with physical emulation of the relative orbital dynamics. *Adv Astronaut Sci*, 168(2019):3781–3799, 2019.

[109] Marco Ciarcià, Roberto Cristi, and Marcello M Romano. Emulating scaled clohessy–wiltshire dynamics on an air-bearing spacecraft simulation testbed. *Journal of Guidance, Control, and Dynamics*, 40(10):2496–2510, 2017.

[110] Evan Laith Kramer. *Towards the Advancement of Rotating Synthetic Aperture Space Telescope Technology*. PhD thesis, Massachusetts Institute of Technology, 2022.

[111] Robert Willard Farquhar. *The utilization of halo orbits in advanced lunar operations*, volume 6365. National Aeronautics and Space Administration, 1971.

[112] J Prussing and B Conway. *Orbital Mechanics*. Oxford University Press. Problems are normally assigned every week and due . . . , 1993.

[113] Robert W Farquhar and Ahmed A Kamel. Quasi-periodic orbits about the translunar libration point. *Celestial mechanics*, 7(4):458–473, 1973.

[114] Ariadna Farres and Jeremy Petersen. Solar radiation pressure effects on the orbital motion at sel2 for the james webb space telescope. *UMBC Faculty Collection*, 2019.

[115] Alejandro D Cabrales Hernandez. Real-time quasi-analytical trajectory generation for docking with tumbling objects. Master's thesis, Massachusetts Institute of Technology, 2020.

[116] Kathleen Howell. Three-dimensional, periodic, halo orbits. *Celestial mechanics*, 32(1):53–71, 1984.

[117] David L Richardson. Analytic construction of periodic orbits about the collinear points. *Celestial mechanics*, 22(3):241–253, 1980.

[118] M. B. Blanke, M.and Larsen. *Satellite Dynamics and Control in a Quaternion Formulation (2nd edition)*. Department of Electrical Engineering, Technical University of Denmark. Kongens Lyngby, Denmark, 2010.

[119] Bong Wie. *Space vehicle dynamics and control*. Aiaa, 1998.

[120] Shengping Gong and Junfeng Li. Solar sail halo orbit control using reflectivity control devices. *Transactions of the Japan Society for Aeronautical and Space Sciences*, 57(5):279–288, 2014.

[121] Vincent R Marcopoli and Stephen M Phillips. Control strategies for systems with limited actuators. Technical report, 1994.

[122] Peter J Wiktor. Minimum control authority plot-a tool for designing thruster systems. *Journal of Guidance, Control, and Dynamics*, 17(5):998–1006, 1994.

[123] Dimitris Bertsimas and John N Tsitsiklis. *Introduction to linear optimization*, volume 6. Athena scientific Belmont, MA, 1997.

[124] F Landis Markley, Reid G Reynolds, Frank X Liu, and Kenneth L Lebsock. Maximum torque and momentum envelopes for reaction wheel arrays. *Journal of Guidance, Control, and Dynamics*, 33(5):1606–1614, 2010.

[125] Toshihiro Chujo and Yuki Takao. Synodic resonant halo orbits of solar sails in restricted four-body problem. *Journal of Spacecraft and Rockets*, pages 1–19, 2022.

[126] Karl J. Astrom and Richard M. Murray. *Feedback systems : an introduction for scientists and engineers.* Princeton : Princeton University Press, c2008., 2008.

[127] Alexander V Prokhorov, Raju U Datla, Vitaly P Zakharenkov, Victor Privalsky, Thomas W Humpherys, Victor I Sapritsky, Albert C Parr, and Lev K Issaev. Spaceborne optoelectronic sensors and their radiometric calibration. terms and definitions.

[128] JWST User Documention. Moving target field of regard, 2017.

[129] NAIF. An overview of reference frames and coordinate systems in the spice context, 2022.

[130] Charles H Acton Jr. Ancillary data services of nasa's navigation and ancillary information facility. *Planetary and Space Science*, 44(1):65–70, 1996.

[131] B. Scott Gaudi, Sara Seager, Bertrand Mennesson, and et al. The habitable exoplanet observatory (habex) mission concept study final report. 2020.

[132] Jaroslaw Sobieszczanski-Sobieski. Overcoming the bellman's curse of dimensionality in large optimization problems. In *Pan American Congress of Applied Mechanics*, number NAS 1.15: 102662, 1990.

[133] Jeffery T King. Increasing agility in orthogonal reaction wheel attitude control systems. *Acta Astronautica*, 177:673–683, 2020.

[134] Zuliana Ismail and Renuganth Varatharajoo. A study of reaction wheel configurations for a 3-axis satellite attitude control. *Advances in Space Research*, 45(6):750–759, 2010.

[135] Kalyanmoy Deb. *Multi-objective optimisation using evolutionary algorithms: an introduction*. Springer, 2011.

[136] S Gordon. Orbit determination error analysis and comparison of station-keeping costs for lissajous and halo-type libration point orbits and sensitivity analysis using experimental design techniques. In *NASA Conference Publication*, pages 395–395. NASA, 1993.

[137] Mark Beckman. Orbit determination issues for libration point orbits. In *Libration Point Orbits and Applications*, pages 1–17. World Scientific, 2003.

[138] Donald J Dichmann, Cassandra M Alberding, and Wayne H Yu. Stationkeeping monte carlo simulation for the james webb space telescope. In *International Symposium on Space Flight Dynamics 2014*, number GSFC-E-DAA-TN14095, 2014.

[139] Sungpil Yoon, Jose Rosales, and Karen Richon. James webb space telescope orbit determination analysis. In *International Symposium on Space Flight Dynamics*, number GSFC-E-DAA-TN14105, 2014.

[140] Kenshiro Oguri, Takumi Kudo, and Ryu Funase. Design criteria of reflectivity control system under uncertainty in sail property for maneuverability requirement of spinning solar sail. In *AIAA/AAS Astrodynamics Specialist Conference*, page 5674, 2016.

[141] Xiyao Huang, Xiangyuan Zeng, Christian Circi, Giovanni Vulpetti, and Dong Qiao. Analysis of the solar sail deformation based on the point cloud method. *Advances in Space Research*, 67(9):2613–2627, 2021.

[142] Judit Pap, Martin Anklin, Claus Fröhlich, Christoph Wehrli, Ferenc Varadi, and Linton Floyd. Variations in total solar and spectral irradiance as measured by the virgo experiment on soho. *Advances in Space Research*, 24(2):215–224, 1999.

[143] Nicolas Croisard, Matteo Ceriotti, and Massimiliano Vasile. Uncertainty modelling in reliable preliminary space mission design. In *International Joint Conference on AI (IJCAI)*, 2007.

[144] Dan Guerrant and Dale Lawrence. Heliogyro solar sail blade twist stability analysis of root and reflectivity controllers. In *AIAA Guidance, Navigation, and Control Conference*, page 4842, 2012.

[145] Nobukatsu Okuizumi, Yasutaka Satou, Osamu Mori, Hiraku Sakamoto, and Hiroshi Furuya. Analytical investigation of global deployed shape of a spinning solar sail membrane. *AIAA Journal*, 59(3):1075–1086, 2021.

[146] Ryan A Fellini and Yury L Kropp. James webb space telescope sunshield: Challenges in analysis of gossamer structures. *Technology Review*, page 17, 2008.

[147] Mark Karpenko, Jeffrey T King, Cornelius J Dennehy, and I Michael Ross. Agility analysis of the james webb space telescope. *Journal of Guidance, Control, and Dynamics*, 42(4):810–821, 2019.

[148] Alise Fisher. Nasa's james webb space telescope fully fueled for launch, 2021.

[149] Nathaniel R Demmons, Zack Wood, and Nereo Alvarez. Characterization of a high thrust, pressure-fed electrospray thruster for precision attitude control applications. In *AIAA Propulsion and Energy 2019 Forum*, page 3817, 2019.

[150] L Petro, W Kinzel, W Rumpl, D Jones, and R Rager. The angular momentum of jwst in a schedule of the science operations–design reference mission. JWST mission internal report 556. Zimmerman, L., Asson, D., 2002. SPIKE: A ..., 2005.

[151] Morgan Quigley, Brian Gerkey, Ken Conley, Josh Faust, Tully Foote, Jeremy Leibs, Eric Berger, Rob Wheeler, and Andrew Ng. Ros: an open-source robot operating system. In *Proc. of the IEEE Intl. Conf. on Robotics and Automation (ICRA) Workshop on Open Source Robotics*, Kobe, Japan, May 2009.

[152] Morris Frayman and R Strunce. Spacecraft slewing/guidance algorithm for hyperspectral imagers. In *AIAA Fifth Responsive Space Conference*. Citeseer, 2007.

[153] Guido Fracchia, James D Biggs, and Matteo Ceriotti. Analytical low-jerk reorientation maneuvers for multi-body spacecraft structures. *Acta Astronautica*, 178:1–14, 2021.

[154] Rudolph Emil Kalman. A new approach to linear filtering and prediction problems. 1960.

[155] Ern J Lefferts, F Landis Markley, and Malcolm D Shuster. Kalman filtering for spacecraft attitude estimation. *Journal of Guidance, Control, and Dynamics*, 5(5):417–429, 1982.

[156] James K Hall, Nathan B Knoebel, and Timothy W McLain. Quaternion attitude estimation for miniature air vehicles using a multiplicative extended kalman filter. In *Proceedings of IEEE/ION PLANS 2008*, pages 1230–1237, 2008.

[157] John H Evans. Dimensional analysis and the buckingham pi theorem. *American Journal of Physics*, 40(12):1815–1822, 1972.

[158] Roger R Bate, Donald D Mueller, Jerry E White, and William W Saylor. *Fundamentals of astrodynamics*. Courier Dover Publications, 2020.

[159] John Enright, Mark Hilstad, Alvar Saenz-Otero, and David Miller. The spheres guest scientist program: Collaborative science on the iss. In *2004 IEEE Aerospace Conference Proceedings (IEEE Cat. No. 04TH8720)*, volume 1. IEEE, 2004.

[160] Hanspeter Schaub and John L Junkins. *Analytical mechanics of space systems*. AIAA, 2003.

[161] Kyle T Alfriend, Srinivas R Vadali, Pini Gurfil, Jonathan P How, and Louis Breger. *Spacecraft formation flying: Dynamics, control and navigation*, volume 2. Elsevier, 2009.